

# Proceedings of the Fifth International Symposium on Ultrasonic Doppler Methods for Fluid Mechanics and Fluid Engineering

ETH Zurich, Switzerland  
12 – 14 September 2006

## Editors:

Beat H. Birkhofer  
Shaik A. K. Jeelani  
Erich J. Windhab

Laboratory of Food Process Engineering  
Institute of Food Science and Nutrition  
Building LFV E21  
ETH Zurich  
Switzerland

## Scientific Committee:

Prof. Dr. M. Aritomi (Tokyo Institute of Technology, Fluid/Nuclear Engineering)  
Dr. G. De Cesare (EPFL Lausanne, Hydraulics)  
Prof. Dr. J.A. Jensen (Technical University of Denmark, Medical Ultrasound Signal Processing)  
Dr. G. King (Warwick University, Physics)  
Dr. M. Mori (TEPCO, Industrial Applications)  
Prof. Dr. Y. Takeda (Hokkaido University, Fluid Engineering/Mechanics)  
Prof. Dr. Tokuhiro (University of Missouri, Nuclear Engineering)  
Prof. Dr. E.J. Windhab (ETH Zurich, Food Process/Fluid Engineering)

## Organizing Committee:

B. Birkhofer  
Dr. S.A.K. Jeelani  
Dr. P. Fischer  
Prof. Dr. E.J. Windhab  
Prof. Dr. Y. Takeda  
Dr. H. Kikura



Copyright © 2006 by Laboratory of Food Process Engineering (ETH Zurich)  
All rights reserved

**Proceedings of the 5th International Symposium on Ultrasonic  
Doppler Methods for Fluid Mechanics and Fluid Engineering**

ISBN: 3-905609-29-0

Published and distributed by:

Laboratory of Food Process Engineering  
Institute of Food Science and Nutrition  
ETH Zurich  
Building LFV E21  
8092 Zurich  
Switzerland

<http://www.isud.ethz.ch/>  
<http://www.ilw.agrl.ethz.ch/vt/>

Printed in Germany by:

Kerschensteiner Verlag GmbH  
Mörikestrasse 4  
93138 Lappersdorf  
Germany



# Table of Contents

## Keynote Lectures

<b>Ultrasonic velocity profiler – from present to future</b> Yasushi Takeda	1
<b>Vector blood velocity estimation in medical ultrasound</b> Joergen Arendt Jensen, Fredrik Gran, Jesper Udesen, Michael Bachman Nielsen, Kristina Rue Nielsen	3
<b>Characterization of dispersions by ultrasound spectroscopy</b> Laurent P. Adjadj, Alexander K. Hipp, Giuseppe Storti, Massimo Morbidelli	9

## Signal processing and methodology

<b>A new velocity estimation method using spectral identification of noise</b> Stéphane Fischer, Philippe Schmitt, Denis Ensminger, Fares Abda, Anne Pallares	15
<b>Velocity vector profile measurement using multiple ultrasound transducers</b> Seiji Kon, Kouhei Yamaguchi, Hironari Ohbayashi, Yuji Tasaka, Yuichi Murai, Yasushi Takeda	19
<b>Application of ultrasonic multi-wave method for two-phase flow</b> Hideki Murakawa, Hiroshige Kikura, Masanori Aritomi	23
<b>A custom-designed ultrasound echo particle image velocimetry system: Initial experiments</b> Lingli Liu, Hairong Zheng, Logan Williams, Jean Hertzberg, Craig Lanning, Robin Shandas	27

## Fundamental Flow

<b>Ultrasonic visualization of thermal convective motion in liquid Gallium layer</b> Yuji Tasaka, Masataka Yoshida, Yasushi Takeda, Takatoshi Yanagisawa	31
<b>Characteristics of echo signal of pulse ultrasound on boiling two-phase flow</b> Daisuke Ito, Hiroshige Kikura, Masanori Aritomi	35
<b>Velocity profile of non-magnetic fluid and magnetic fluid sloshing</b> Shinichi Yoshida, Kenji Tomita, Andrea Benvenuti, Tatsuo Sawada, Masaaki Motozawa	39

## Applied flow

<b>UVP measurement of a turbulent channel flow containing large bubbles</b> Yuichi Murai, Hideki Fujii, Yuji Tasaka, Yasushi Takeda	43
<b>ADV measurements in a flotation tank with bubble containing water</b> Lennart Jönsson	47
<b>Determination of the flow structure in bubble-driven liquid metal flows using ultra-sound Doppler method</b> Chaojie Zhang, Sven Eckert, Gunter Gerbeth	51
<b>Velocity measurement around a large bubble rising in stagnant water in a round pipe using the UVP (2nd Report: The effect of bubble length and pipe diameter)</b> Hisato Minagawa, Tsuyoshi Fukazawa, Yoshiyuki Nakazawa, Satoshi Yamada, Yoichi Shiomi	55
<b>Spatial-temporal variation of turbulence characteristics in sewer flow</b> Vojtech Bares, Jakub Jirak, Jaroslav Pollert	59
<b>Simultaneous UVP and PIV measurements related to bed dunes dynamics and turbulence structures in circular pipes</b> A. Herimonja Rabenjafimanantsoa, Rune W. Time, Arild Saasen	63
<b>PIV and UDM measurements of axial and circumferential flow modes between rotating disks</b> Masato Furue, Jiro Funaki, Katsuya Hirata	69
<b>Flow visualisation inside a flip-flop using UVP</b> Jiro Funaki, Katsuya Hirata, Tatsuya Inoue, Hiroyuki Matsuda, Hirochika Tanigawa	73
<b>An investigation in using UVP for assisting in rheological characterisation of mineral suspensions</b> Rainer Haldenwang, Reinhardt Kotze, Paul Slatter, Olivier Mariette	77
<b>Flow measurement of lead bismuth eutectic in spallation target model loop</b> Hironari Obayashi, Kenji Kikuchi, Yasushi Takeda	81
<b>Flow velocity measurements in a large amplitude meandering flume using an acoustic doppler velocity profiler</b>  Mafalda Piraino, Donatella Termini	85
<b>From fundamental investigations towards industrial application of ultrasound based in-line rheometry</b> Boris Ouriev, Klaus-Jochen Lisner, Erich Windhab	87

## Flow metering

- A study of ultrasonic propagation for flow rate measurement using ultrasonic flow meter** 89  
Yuto Inoue, Hiroshige Kikura, Masanori Aritomi, Michitsugu Mori
- Stability of anomalous modes on Taylor-Couette vortex flow in magnetic fluid** 93  
Toshikazu Kotaka, Daisuke Ito, Hiroshige Kikura, Masanori Aritomi, Shuichiro Hirai
- Improving acoustic Doppler velocimetry in steady and unsteady flow by means of seeding with hydrogen bubbles** 97  
Tobias Meile, Giovanni De Cesare, Koen Blanckaert, Anton Schleiss
- Calibration tests of pulse-Doppler flow meter at National Standard Loop** 101  
Michitsugu Mori, Kenichi Tezuka, Takeshi Suzuki, Yasushi Takeda
- Application of ultrasonic pulse-Doppler flow meter for hydraulic power plant** 105  
Kenichi Tezuka, Michitsugu Mori, Takeshi Suzuki, Toshimasa Kanamine
- Theoretical and experimental investigation of effects of flow fluctuations on UDV signals** 109  
Volkan Köseli, Yusuf Uludag

## Environmental flow

- Flow velocity measurements using ultrasound Doppler method – 10 years experience in hydraulic modeling** 113  
Giovanni De Cesare, Jean-Louis Boillat
- UVP measurement for flows accompanying free surface** 117  
Shinya Kojima, Yuji Tasaka, Yuichi Murai, Yasushi Takeda
- Flow pattern visualization of combined sewer overflow** 121  
Vojtech Bares, Jaroslav Pollert, Petr Srnicek
- Interface tracking and velocity profile in an oil-water two-phase flow** 125  
Azin Amini, Giovanni De Cesare, Anton Schleiss
- Flow field investigation in a rectangular shallow reservoir using UVP, LSPIV and numerical model** 129  
Sameh Kantoush, Erik Bollaert, Giovanni De Cesare, Jean-Louis Boillat, Anton Schleiss

<b>Flow measurements in a suction sump by UVP</b>	<b>135</b>
Katsuya Hirata, Masakatsu Hattori, Masashi Neya, Jiro Funaki, Hiroya Tanigawa	
<b>Measurements of bubble jets by 3D PTV and UVP</b>	<b>139</b>
Atsushi Shintani, Jiro Funaki, Katsuya Hirata	
<b>Discharge estimation by continuous measurement of water velocity by Doppler instrument</b>	<b>143</b>
Andrej Vidmar, Luka Štravs, Simon Rusjan, Sašo Petan, Mitja Brilly	

## **In-line rheometry**

<b>Application of in-line ultrasound Doppler based UVP-PD method to concentrated model and industrial suspensions</b>	<b>145</b>
Johan Wiklund, Mats Stading	
<b>Monitoring of fat crystallization process using UVP-PD technique</b>	<b>149</b>
Beat Birkhofer, Shaik A.K. Jeelani, Erich Windhab, Boris Ouriev, Klaus-Jochen Lisner, Peter Braun, Yuantong Zeng	
<b>In-line ultrasonic device for flow and rheology measurements of complex fluids</b>	<b>155</b>
Robert L. Powell, Nihan Dogan, Michael J. McCarthy	

# Author Index

Abda F. ....	15
Adjadj L. ....	9
Amini A. ....	125
Aritomi M. ....	23, 35, 89, 93
Bachman Nielsen M. ....	3
Bares V. ....	59, 121
Benvenuti A. ....	39
Birkhofer B. ....	149
Blanckaert K. ....	97
Boillat J. ....	113, 129
Bollaert E. ....	129
Braun P. ....	149
Brilly M. ....	143
De Cesare G. ....	97, 113, 125, 129
Dogan N. ....	155
Eckert S. ....	51
Ensminger D. ....	15
Fischer S. ....	15
Fujii H. ....	43
Fukazawa T. ....	55
Funaki J. ....	69, 73, 135, 139
Furue M. ....	69
Gerbeth G. ....	51
Gran F. ....	3
Haldenwang R. ....	77
Hattori M. ....	135
Hertzberg J. ....	27
Hipp A. ....	9
Hirai S. ....	93
Hirata K. ....	69, 73, 135, 139
Inoue T. ....	73
Inoue Y. ....	89
Ito D. ....	35, 93
Jeelani S. ....	149
Jensen J. ....	3
Jirak J. ....	59
Jönsson L. ....	47
Kanamine T. ....	105
Kantoush S. ....	129
Kikuchi K. ....	81
Kikura H. ....	23, 35, 89, 93
Kojima S. ....	117
Kon S. ....	19
Kotaka T. ....	93
Kotze R. ....	77
Köseli V. ....	109
Lanning C. ....	27
Lisner K. ....	87, 149
Liu L. ....	27
Mariette O. ....	77
Matsuda H. ....	73
McCarthy M. ....	155
Meile T. ....	97
Minagawa H. ....	55
Morbidelli M. ....	9
Mori M. ....	89, 101, 105
Motozawa M. ....	39
Murai Y. ....	19, 43, 117
Murakawa H. ....	23
Nakazawa Y. ....	55
Neya M. ....	135
Nielsen K. ....	3
Obayashi H. ....	81
Ohbayashi H. ....	19
Ouriev B. ....	87, 149
Pallares A. ....	15
Petan S. ....	143
Piraino M. ....	85
Pollert J. ....	59, 121
Powell R. ....	155
Rabenjafimanantsoa A. ....	63
Rusjan S. ....	143
Saasen A. ....	63
Sawada T. ....	39
Schleiss A. ....	97, 125, 129
Schmitt P. ....	15
Shandas R. ....	27
Shintani A. ....	139
Shiomi Y. ....	55
Slatter P. ....	77
Srnicek P. ....	121
Stading M. ....	145
Storti G. ....	9
Štravs L. ....	143
Suzuki T. ....	101, 105
Takeda Y. ....	1, 19, 31, 43, 81, 101, 117
Tanigawa H. ....	73, 135
Tasaka Y. ....	19, 31, 43, 117
Termini D. ....	85
Tezuka K. ....	101, 105
Time R. ....	63
Tomita K. ....	39
Udesen J. ....	3
Uludag Y. ....	109
Vidmar A. ....	143
Wiklund J. ....	145
Williams L. ....	27
Windhab E. ....	87, 149
Yamada S. ....	55
Yamaguchi K. ....	19
Yanagisawa T. ....	31
Yoshida M. ....	31
Yoshida S. ....	39
Zeng Y. ....	149
Zhang C. ....	51
Zheng H. ....	27



# Ultrasonic Velocity Profiler - from present to future

Yasushi Takeda

Div. Energy and Environmental Engineering, Hokkaido University, Sapporo, Japan

Past and current activities related to UVP; physical and engineering fluid mechanics, industrial applications and development of methodology are surveyed. A general trend of its use and development is overviewed and future of UVP is discussed.

**Keywords:** UVP

## 1 UVP

After UVP was first applied to general fluid mechanical study in mid-80's [1], its application has been steadily broadening in wide variety of flow configurations. From beginning, the following three advantages are featured for UVP;

- Spatio-temporal information of flow fields,
- Applicable to opaque liquids
- Efficient flow mapping.

Both for physics study and engineering work, these advantages attracted a great deal of interest of researchers in physics as well as engineering.

Development of UVP and its applications up to present will be surveyed on these two coordinates. Based on this, a future of the method and equipments will be discussed.

## 2 UVP TO PRESENT

### 2.1 Fields and configurations

By literature survey where UVP method is investigated and applied, fields and configurations are categorized, as shown in Table 1, by two coordinates of advantages and research fields. They do not include work for biomedical applications, civil engineering etc. More than 200 journal papers were found easily in the fields of physics and engineering fluid mechanics.

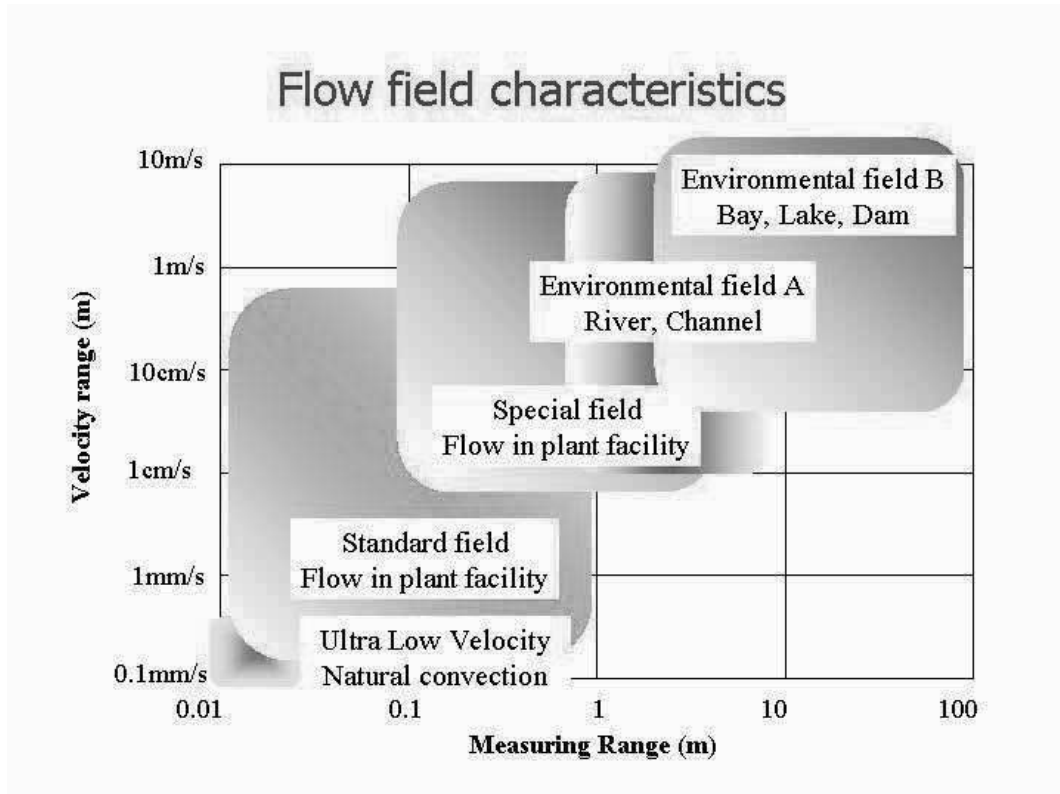
Physics study was made being related to flow instability. [2,3] This is due to a characteristics of problems where the change of spatial distribution appears prior to temporal changes, and because UVP is superior in detecting such changes in the flow fields. For investigation of turbulence, the present time and space resolution of the equipment is not sufficient that investigations for improving these weakness were attempted. [4]

More effectively, UVP is used for flow investigation of liquid metals. The liquid is Gallium [5] and the flow configuration is related to a geofluid dynamics such as mantle convection or astrophysical dynamics. [6] Especially effective is to investigate Magneto-Hydro-Dynamics using liquid sodium. [7] Ultrasound is the only possible wave to be used in such media. In the similar manner, many of the non-Newtonian liquids are opaque and UVP is used to investigate flow behavior for Rheology. [8]

As physics study has been and still is under way, more engineering applications has become popular. This is presumably because the method has been established and accepted by fluid mechanists and engineers through the investigations by physicists. Industrial application has also been made in flow metering.[9] The accuracy of flow rate measurement has been made breakthrough, improving its level down to 0.1%. A commercial product of novel type flowmeter using UVP principle has been developed and now available in the market.[10]

Table 1 Fields and configurations of UVP applications

	Physics	Engineering
Spatio-temporal	Instability and nonlinear problems flow transition and turbulence	Velocity profiling in devices Flow metering
Opaque liquids	Geoscience MHD and magnetic effect, Rheology	Liquid metal and food flows Material processing
Flow mapping	Measurement of distributions of stream function and vorticity	CFD code validation Design of flow and thermal devices Environmental flow



## 2.2 Trends

By viewing these accumulated results of investigations, a general trend can be found such that more and more engineering applications will be made and also industrial applications might take a larger part of the activity in near future.

Especially, applications in medical engineering and civil/environmental engineering, although they are not mentioned in the present survey, are foreseen with a considerable growing rate

## 3 UVP FOR FUTURE

As seen above, the applicable flow field ranges in enormous breadth. It is not only the measurement range in space but also its velocity levels, as depicted in Figure 2. The measurement length would be from a couple of mm for boundary layer flow to a couple of 10 m for a coastal flow. The velocity level also ranges from 1 mm/s for natural convection flow to a several or 10 m/s in the environmental and industrial flow fields.

The preset measurement systems have been developed for a standard flow field that is anticipated to be found in laboratory experiments, [11] and because of it, they cannot cover the whole range of flow field and velocity level. In one hand, different systems must be provided, or a flexible system to adjust those measurement ranges to the required characteristics of flow fields. Moreover, physics research are seriously concerned about

spatial and temporal resolution. Signal processing algorithms which can realized such requirement have been made and further development is expected. This is also the case for multi-component measurement of flow velocity vector. [12]

On other hand, an industrial application requires less flexibility of system parameters. Each application has its specific ranges of depth and velocity of limited scale. It is required therefore the system be robust against poor reflection of ultrasound. These were found in the course of development of novel type of flow meter. Their experience would be used for other applications too.

A challenge in physics study using UVP is under way into the space. Marangoni convection will be investigated using UVP in the Japanese mission of ISS, JEM. [13]

## REFERENCES

- Here only representative literatures are cited.
- [1] Takeda, Y., *Int. J. Heat & Fluid Flow*, **7** (1986) 313
  - [2] Takeda, Y. et al., *Exp. in Fluids*, **13** (1992) 199
  - [3] Le Gal, P. et al., *Phys. Fluids*, **8** (1996) 2097
  - [4] Ozaki, Y. et al., *Exp Therm. Fluid Sci.*, **26** (2002) 253
  - [5] Brito, D. et al., *Exp in Fluids* **31** (2001) 653
  - [6] Aubert, J. et al., *Phys. earth & planet. int.*, **128** (2001) 51
  - [7] Brawn, B.E. et al., *Chaos*, **15** (2005) 41104
  - [8] Ouriev, B., *Colloidal Journal*, **64** (2002) 740
  - [9] Mori, M. et al., *Exp in Fluids*, **32** (2002) 153
  - [10] [http://www.fic-net.jp/products/flow\\_ultra/top.html](http://www.fic-net.jp/products/flow_ultra/top.html)
  - [11] <http://www.met-flow.com/>
  - [12] Ohbayashi, N. et al., *ISUD-4* (2004)
  - [13] [http://iss.sfo.jaxa.jp/utiliz/surp/surpdoc4\\_e.html](http://iss.sfo.jaxa.jp/utiliz/surp/surpdoc4_e.html)

## Vector blood velocity estimation in medical ultrasound

Jørgen Arendt Jensen, Fredrik Gran

Ørsted•DTU, Building 348, Technical University of Denmark, DK-2800 Kgs. Lyngby, Denmark

Jesper Udesen, Michael Bachmann Nielsen, Kristina Rue Nielsen

Department of Radiology, Section of Ultrasound, Rigshospitalet, Blegdamsvej 9, DK-2100 Copenhagen Ø, Denmark

Two methods for making vector velocity estimation in medical ultrasound are presented. All of the techniques can find both the axial and transverse velocity in the image and can be used for displaying both the correct velocity magnitude and direction. The first method uses a transverse oscillation in the ultrasound field to find the transverse velocity. In-vivo examples from the carotid artery are shown, where complex turbulent flow is found in certain parts of the cardiac cycle. The second approach uses directional beam forming along the flow direction to estimate the velocity magnitude. Using a correlation search can also yield the direction, and the full velocity vector is thereby found. An examples from a flow rig is shown.

**Keywords:** Medical ultrasound, vector velocity estimation, directional beam forming.

### 1 INTRODUCTION TO VECTOR VELOCITY ESTIMATION

Imaging of the blood velocity has been made for the last 20 years. The original paper by Kasai et al. [1] demonstrated that the velocity could be estimated in the direction of the ultrasound beam. This often gives problems, since the vessel run along the skin surface and the ultrasound beam is, thus, perpendicular to the flow direction. This can be corrected by tilting the beam, but often the geometry of the vessels is complicated and a single correction is not sufficient. There is therefore a real need in medical ultrasound for vector flow techniques. This paper will present two techniques for vector flow imaging developed in our laboratory.

Many authors have developed techniques for vector velocity estimation. Fox [1,2] developed the crossing beams technique, where the velocity is found along two beam directions. The approach is, however, difficult to use for imaging, as it is difficult to get crossing beams simultaneously over the full image. Another approach is speckle tracking [3], where two images acquired at different times are correlated to find the vector motion. A number of other techniques have also been introduced, but none have so far made it into commercial products.

### 2 TRADITIONAL VELOCITY ESTIMATION

Traditional velocity estimation is performed by emitting a pulsed field a number of times in the same direction as shown in Fig. 1. Here the left graph shows the received signal for a single scatterer moving away from the transducer. The consecutive signals are shown with an increasing y-axis offset. The signal is sampled at the depth of interest resulting in the signal on the right. The frequency of this signal is proportional to the velocity as [4]

$$f_p = \frac{2|v| \cos \Theta}{c} f_0 = \frac{2v_z}{c} f_0 \quad (1)$$

where  $\Theta$  is the flow angle between the ultrasound beam and the velocity vector,  $|v|$  is the velocity magnitude,  $v_z$  is the axial blood velocity,  $c$  is the speed of sound, and  $f_0$  is the emitted ultrasound center frequency. A larger velocity will, thus, give a larger shift between signals and a higher frequency. The generating mechanism is the oscillation in the ultrasound signal and the shift in position between pulse emissions.

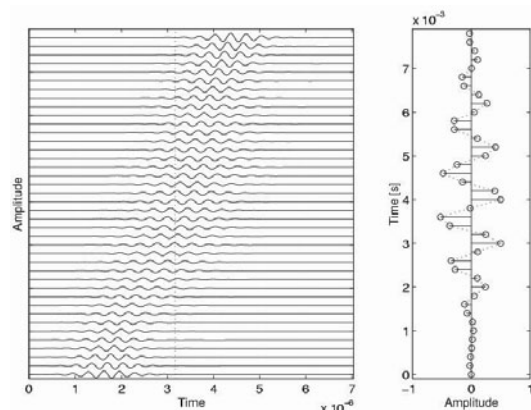


Figure 1: Received RF signal for a single scatterer moving away from the transducer. The left graph shows the individual traces received after each pulse emission and the right graph shows the sampled signal obtained at the dashed line in the left graph at 3.2  $\mu$ s (from [4]).

Figure 2 shows the major problem with this approach. The velocity has here been determined at a number of places in the image from the frequency given by (1). A blue color shows velocity towards the transducer and a red color away from the transducer. The jugular vein and carotid artery in the neck has been scanned. A change in color is seen

around the green line. This is due to the  $\cos \Theta$  factor in (1) as the flow angle changes along the green line. This is easily detected in this image, but very difficult to compensate for in more complicated flow patterns. A major problem is also that the projected velocity is shown. This will always make the velocity lower than the true velocity, and this makes quantitative velocity imaging difficult.

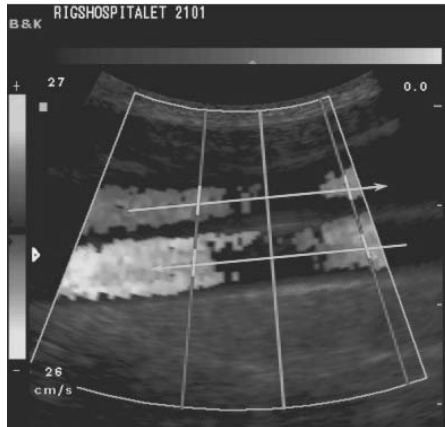


Figure 2: Velocity image of the jugular vein (top) and carotid artery (bottom). The blue color indicates velocity towards the transducer and red away from it. The change in color along the blue center line is due to the change in angle between the ultrasound beam and the velocity direction (from [16]).

### 3 TRANSVERSE OSCILLATION APPROACH

The important feature for estimating the velocity in traditional systems is the sinusoidal pulse in the axial directions. This generates the received frequency and makes it possible to determine the velocity. The transverse velocity cannot be estimated, since there is no corresponding transverse oscillation, as shown in Fig. 3. Here the point spread function (psf) is depicted with a black value corresponding to a negative pressure and a white value is positive pressure. A scatterer going through the psf in the axial direction will give an oscillation as described in the previous Section with a frequency given by (1). A corresponding lateral movement will give the signal shown in the right graph in Fig. 3. Here no oscillation is seen and the mean frequency of this signal will be zero.

The basic idea in the transverse oscillation approach [5, 13] is to introduce a lateral oscillation in the field as shown in Fig. 4. A lateral motion will then give the signal shown in the right graph in Fig. 4, with an oscillation frequency proportional to the lateral velocity as

$$f_l = \frac{v_x}{\lambda_x} \quad (2)$$

where  $v_x$  is the lateral oscillation and  $\lambda_x$  is the lateral

oscillation period in the signal. Such a transverse oscillation can be introduced by splitting the transducer aperture in two and emitting waves from each part as shown in Fig. 5. The two fields will then interfere and generate a transverse oscillation.

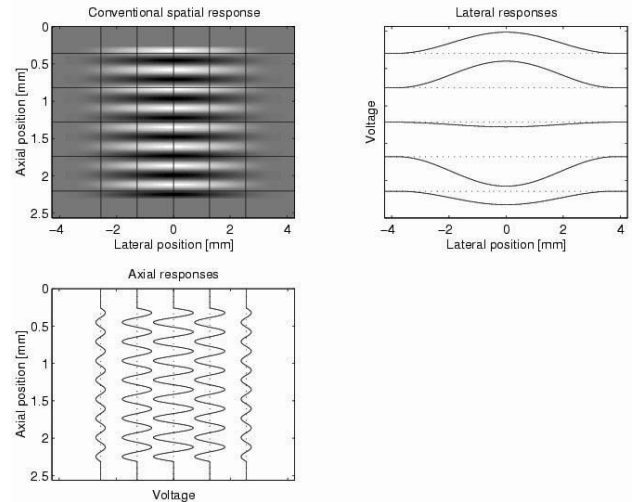


Figure 3: Point spread function (psf) for ordinary ultrasound velocity estimation. The top left graph shows the psf and the lower graph shows the response from a scatterer transversing the field in the axial direction. The right graph shows the signal for the scatterer transversing the field in the lateral direction (from [5]).

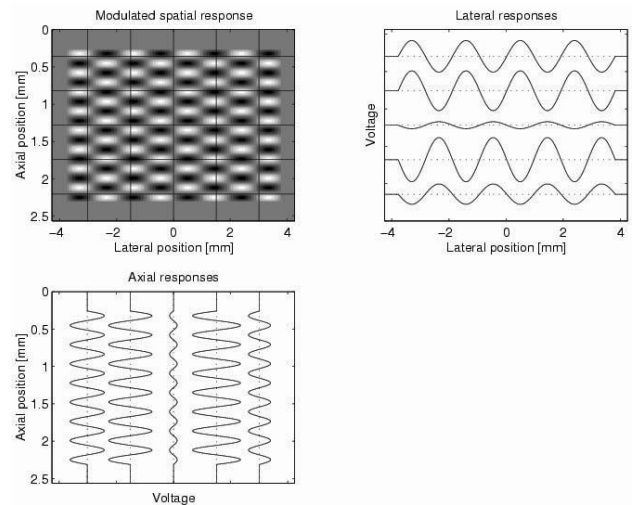


Figure 4: Point spread function (psf) for transvers oscillation method. The top left graph shows the psf and the lower graph shows the response from a scatterer transversing the field in the axial direction. The right graph shows the signal for the scatterer transversing the field in the lateral direction (from [5]).

The received signal can then be processed to yield both the axial and lateral velocities independently as described in [6].

An example of such an image is shown in Fig. 6, which has been measured on the carotid artery of a human volunteer. A 128 element, 7 MHz linear array

probe was used connected to the RASMUS experimental ultrasound scanner [14]. The data was stored in the scanner and then processed in a Linux cluster to estimate both the axial and lateral velocities. The image shows the velocity magnitude as a red color with the magnitude corresponding to color intensity. The arrows on the image indicate both direction and magnitude. The flow angle is nearly 90 degrees and an estimate of the velocity is obtained. For this simple case the ultrasound beam could just be tilted to give an estimate with the conventional method, but this is not possible for more complex patterns.

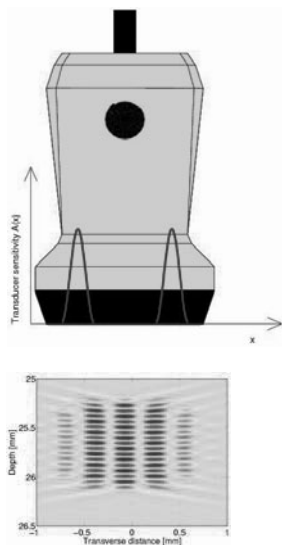


Figure 5: Transducer aperture used for transmission and the corresponding field as simulated by the Field II program [12].

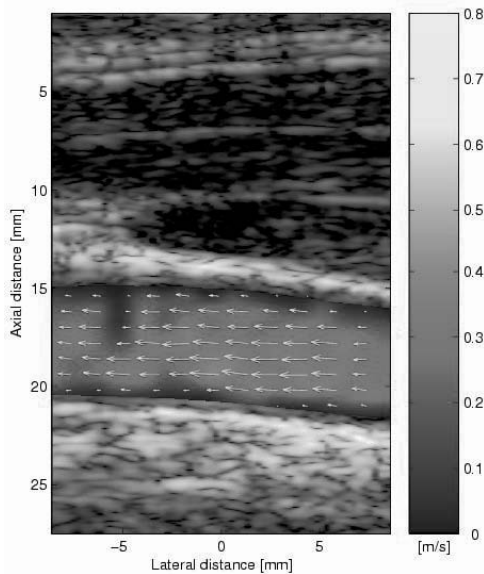


Figure 6: Vector velocity image of the carotid artery. The color indicates velocity magnitude and arrows indicate both velocity direction and magnitude (from [7]).

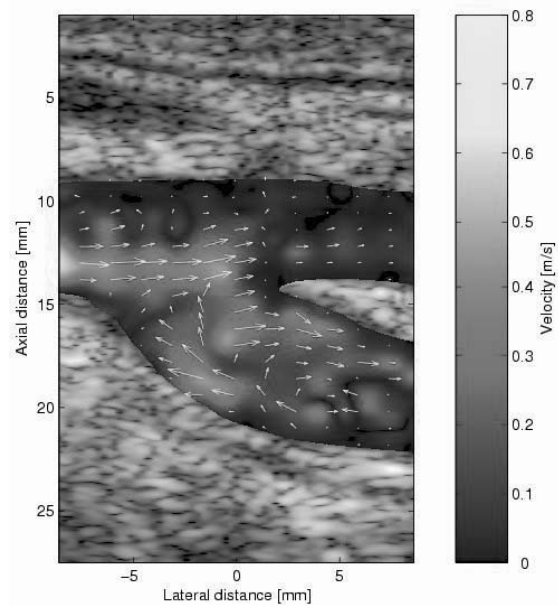
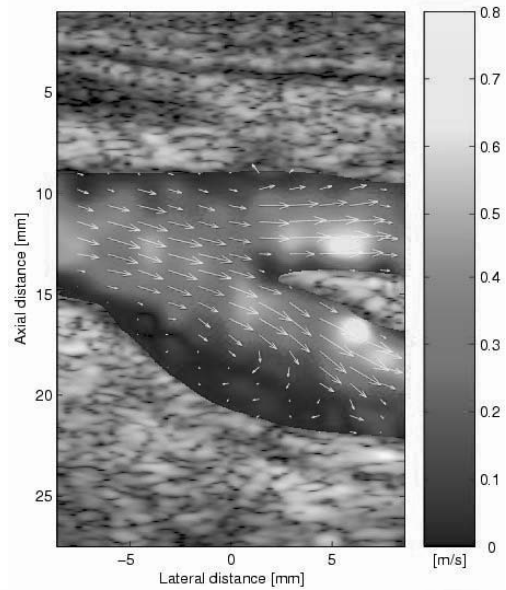


Figure 7: Vector velocity image of the carotid artery bifurcation at peak systole (top) and 0.1 s after peak systole. (from [7]).

This is demonstrated in Fig. 7, where the flow patterns in the carotid bifurcation are shown around the maximum contraction of the heart. The flow at peak systole is fairly laminar with a lower velocity at the lowest part of the vessel, whereas there is a very disturbed, rotating flow right after peak systole. The velocity arrows here rotate full circle within 100-200 ms demonstrating the importance of showing the full velocity vector to capture and display the very complex flow patterns in the human body.

#### 4 DIRECTIONAL BEAMFORMING APPROACH

There are also other methods for finding the velocity vector. The directional beam forming approach uses focusing along the flow direction to find the velocity

vector [8,9]. Here a normal focused ultrasound field is emitted and the scattered signal is sampled from all the receiving elements. The direction of the flow is determined from the B-mode image and signals are then focused along this direction as shown in Fig. 8. The process is repeated and a number of signals are found and the signals are cross-correlated to yield the shift in position between the signals. The spatial shift will be equal to the velocity magnitude times the time between the signals. Finding the shift and dividing by the time will then yield the velocity. This is the principle in the directional beam forming method.

An example of such an image is shown in Fig. 9. It was made using a circulating flow rig with a mass flow meter as reference. A 128 element, 7 MHz linear array probe was used connected to the RASMUS experimental ultrasound scanner and 20 pulse echo lines were acquired for each of the 65 imaging lines. The velocity was then found by focusing lines perpendicular to the ultrasound beam, cross-correlating them, and then finding the velocity.

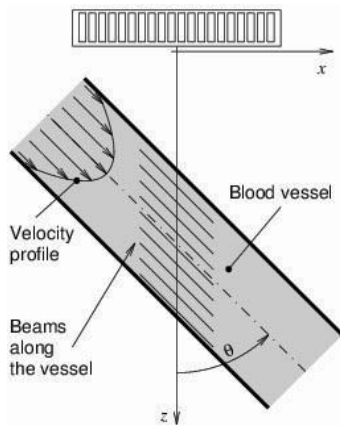


Figure 8: Directional focusing along the flow direction (from [10]).

The standard deviation across the parabolic profiles is 4.3% relative to the peak velocity in the vessel, which is comparable to the accuracy obtained in traditional scanners, that here would show no velocity at 90 degrees.

The angle for the flow can also be determined for this approach. This is done by beam forming in a number of directions and then find the velocity and normalized peak cross-correlation for the different angles. The highest correlation coefficient then denotes the correct angle, since the signals will decorrelate for others angles as the velocity is different in different parts of the directional signal. Such an approach has been investigated in [15].

## 5 SUMMARY

Two different methods for vector velocity estimation have been presented. It has been shown that conventional techniques can lead to cross errors in

determining the correct velocity and that vector velocity techniques are needed in order to display the full complexity of flow in the human body.

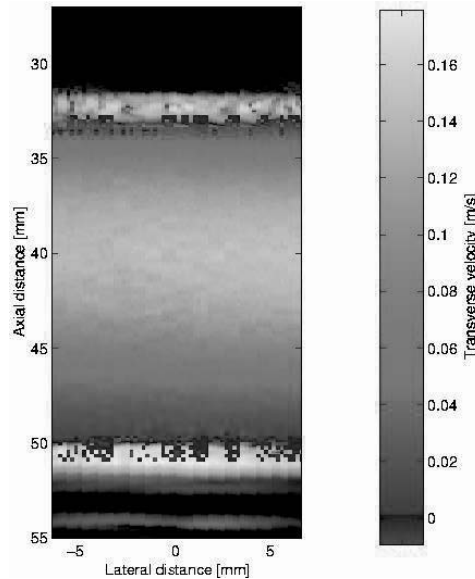


Figure 9: Velocity image at 90 degrees in a flow rig (from [9]).

## ACKNOWLEDGEMENT

This work was supported by grant 9700883, 9700563 and 26-04-0024 from the Danish Science Foundation, the Academy of Technical Sciences, the Ministry of Science, Technology and Innovation, and by B-K Medical A/S.

## REFERENCES

- [1] M. D. Fox. Multiple crossed-beam ultrasound Doppler velocimetry. *IEEE Trans. Son. Ultrason.*, SU-25:281-286, 1978.
- [2] B. Dunmire, K. W. Beach, K-H Labs., M. Plett, and D. E. Strandness. Cross-beam vector Doppler ultrasound for angle independent velocity measurements. *Ultrasound Med. Biol.*, 26:1213-1235, 2000
- [3] G. E. Trahey, J. W. Allison, and O. T. von Ramm. Angle independent ultrasonic detection of blood flow. *IEEE Trans. Biomed. Eng.*, BME-34:965-967, 1987.
- [4] J. A. Jensen. Estimation of Blood Velocities Using Ultrasound: A Signal Processing Approach. Cambridge University Press, New York, 1996
- [5] J. A. Jensen and P. Munk. A new method for estimation of velocity vectors. *IEEE Trans. Ultrason., Ferroelec., Freq. Contr.*, 45:837-851, 1998.
- [6] J. A. Jensen. A new estimator for vector velocity estimation. *IEEE Trans. Ultrason., Ferroelec., Freq. Contr.*, 48(4):886-894, 2001.
- [7] J. Udesen, M. B. Nielsen, K. R. Nielsen, J. A. Jensen. Blood vector velocity estimation using an autocorrelation approach: In vivo Investigation., *IEEE Ultrasonics Symposium 2005*, pp 162-165, 2005
- [8] J. A. Jensen. Directional velocity estimation using focusing along the flow direction: I: Theory and simulation. *IEEE Trans. Ultrason., Ferroelec., Freq. Contr.*, pages 857-872, 2003.

- [9] J. A. Jensen and R. Bjerggaard. Directional velocity estimation using focusing along the flow direction: II: Experimental investigation. *IEEE Trans. Ultrason., Ferroelec., Freq. Contr.*, pages 873-880, 2003.
- [10] J. A. Jensen and S. I. Nikolov. Directional synthetic aperture flow imaging. *IEEE Trans. Ultrason., Ferroelec., Freq. Contr.*, pages 1107-1118, 2004.
- [11] J. A. Jensen and N. B. Svendsen. Calculation of pressure fields from arbitrarily shaped, apodized, and excited ultrasound transducers. *IEEE Trans. Ultrason., Ferroelec., Freq. Contr.*, 39:262-267, 1992.
- [12] J. A. Jensen. Field: A program for simulating ultrasound systems. *Med. Biol. Eng. Comp.*, 10th Nordic-Baltic Conference on Biomedical Imaging, Vol. 4, Supplement 1, Part 1:351-353, 1996b.
- [13] M. E. Anderson. Multi-dimensional velocity estimation with ultrasound using spatial quadrature. *IEEE Trans. Ultrason., Ferroelec., Freq. Contr.*, 45:852-861, 1998.
- [14] J. A. Jensen, O. Holm, L. J. Jensen, H. Bendsen, S. I. Nikolov, B. G. Tomov, P. Munk, M. Hansen, K. Salomonsen, J. Hansen, K. Gormsen, H. M. Pedersen, and K. L. Gammelmark. Ultrasound research scanner for real-time synthetic aperture image acquisition. *IEEE Trans. Ultrason., Ferroelec., Freq. Contr.*, 52 (5), May 2005.
- [15] J. Kortbek and J. A. Jensen. Determination of velocity vector angles using the directional cross-correlation method. In *Proc. IEEE Ultrason. Symp.*, pages 1339-1343, 2005.
- [16] P. Munk, J. A. Jensen, Performance of a vector velocity estimator, *IEEE Ultrasonics Symposium Proceedings*, pp 1489-1493, IEEE, 1998



# Characterization of dispersions by ultrasound spectroscopy

Laurent P. Adjadj, Alexander K. Hipp\*, Giuseppe Storti and Massimo Morbidelli

Institute for Chemical and Bioengineering, ETH Zurich, 8093 Zurich, Switzerland

\*The Dow Chemical Company, 8810 Horgen, Switzerland

In this work, a review of our main theoretical and experimental results in particle sizing of colloidal dispersions using ultrasound spectroscopy is given, with special emphasis on polymeric materials. Both low and high-concentration systems are analyzed. In the first case, a single particle literature model is shortly presented and the key problem of model parameter evaluation is addressed. With this respect, a specific approach to the direct evaluation of the intrinsic attenuation of bulk, solid materials is also mentioned. For high concentration systems, a semi-empirical modeling approach is described and validated by comparison with experimental data. A few conclusive remarks and perspectives are finally given.

**Keywords:** ultrasound spectroscopy, dispersion, emulsion, particle size, polymer latexes

## 1 INTRODUCTION

Among the different ultrasonic techniques used to characterize particle dispersions, ultrasound spectroscopy (US) shows a large potential because of two main reasons: (i) the ability to penetrate opaque systems (i.e. at high concentration) and (ii) the ability to cover huge range of particle diameter, virtually from tens of nanometers to millimeters. Both aspects are very promising with respect to on-line applications to processes where the control of the particle size is important.

The measurement principle is based on the different sound attenuation exhibited by waves at different frequency values when traveling through dispersion containing particles at various sizes. Thus, by measuring sound energy loss at multiple frequency values (so called attenuation spectrum), the size distribution of the particles can be estimated. A modeling tool is essential to properly extract the particle size and different models, suitable for different conditions, are available to this aim.

While different commercial equipments appeared in the last years, full validation of the technique is still missing, in particular with reference to popular dispersions like those involving polymer particles. In this presentation, we focus on the application of US to sizing different aqueous dispersions of spherical particles or droplets made of inorganic (silica) and organic materials (oils, polymers). In all cases, the particle diameter was in the range from 0.1 to 1  $\mu\text{m}$ , thus limiting the analysis to colloidal dispersions. Different modeling approaches suitable for diluted and concentrated systems are shortly presented and validated by comparison with experimental data.

## 2 DILUTED SYSTEMS

### 2.1 Modeling

The propagation of sound waves through

heterogeneous media is characterized by changes in amplitude and phase of the wave due to scattering and irreversible energy dissipation. While scattering is fully equivalent to that of light (lossless redirection), the irreversible dissipation is due to different mechanisms, mainly intrinsic, visco-inertial and thermal. Intrinsic losses are due to molecular interactions and, therefore, are always present, even in homogeneous systems. When dealing with heterogeneous systems, the discontinuity between suspending and suspended phases results in additional dissipations, related to particle vibrations (visco-inertial losses) and temperature-pressure coupling (thermal losses). A comprehensive theory accounting for these dissipation mechanisms was proposed by Epstein and Carhart for liquid-liquid systems [1] and extended to solid-liquid systems by Allegra and Hawley [2]. Such a model (below indicated as ECAH model) is used here because of its generality.

The model development can be summarized as follows: (i) wave equations are derived from the conservation laws of mass, momentum and energy; (ii) these equations are solved analytically as an infinite series of spherical Bessel functions, Legendre polynomials and unknown expansion coefficients, so-called "scattering coefficients",  $A_n$ ; (iii) these coefficients can be evaluated after the introduction of the boundary conditions for the problem, i.e. the continuity of normal and tangential velocity, of normal and tangential stress and of temperature and heat flow at the interface particle phase-continuous phase. A set of linear equations can be written for each order  $n$  of the expansion coefficients; therefore, as many sets of scattering coefficients as required are independently evaluated. The complete set of equations for the coefficients is omitted here; full details can be found in the original references [2].

From the scattering coefficients, the wavenumber

characteristic of the whole dispersion,  $K$ , is readily evaluated. It is defined as  $\omega/c_{\text{eff}} + i\alpha_{\text{eff}}$ , being  $\omega$  the angular frequency of sound and  $c_{\text{eff}}$  and  $\alpha_{\text{eff}}$  the “effective” sound speed and attenuation of the dispersion. The relationship for  $K$  in terms of scattering coefficients is as follows:

$$\left(\frac{K}{k}\right)^2 = 1 - \frac{24i\phi}{k^3 d^3} \sum_{n=0}^{\infty} (2n+1)A_n \quad (1)$$

where  $k$  is the wavenumber of the continuous phase,  $\phi$  the volume fraction of the dispersed phase and  $d$  the particle diameter. While the first few coefficients are required for small particles ( $<1 \mu\text{m}$ ), large numbers of them might be required for large particles ( $\gg 1 \mu\text{m}$ ). Eq.(1) is intended for isolated particles, therefore can be applied to dilute dispersions, where the volume fraction of the dispersed phase is not larger than few percents for high the density contrast case (large density difference between the two phases) and around 20% for low density contrast case.

Eq.(1) is intended for a single value of the particle size. In the general case of particle size distribution, based on the linearity of the acoustic field, the corresponding expression of the dispersion wavenumber is readily obtained by superimposing the contributions of each particle size weighted according to their concentration. Then, Eq.(1) becomes:

$$\left(\frac{K}{k}\right)^2 = 1 - \frac{24i\phi}{k^3} \int_0^{\infty} \frac{F(d)}{d^3} \sum_{n=0}^{\infty} (2n+1)A_n(d)dd \quad (2)$$

where  $F(d)$  indicates the probability density of having particles in the size range from  $d$  to  $d+dd$ . Such probability density function is normalized to unity and different model distributions (such as Gamma and log-normal) are usually adopted, the characteristic parameters of which are estimated by fitting the experimental attenuation data.

The equations for the scattering coefficients involve several physical properties of both continuous and dispersed phase: density, shear viscosity (liquids) or modulus (solids), speed of sound, intrinsic attenuation, heat capacity, thermal conductivity and thermal expansion. This means that accurate values of seven properties have to be known for each phase to calculate the overall wavenumber. While such properties are usually well known for the continuous, liquid phase (water in all our cases), their evaluation can be quite demanding in case of the dispersed phase and, in particular, of polymers. Actually, this evaluation problem could be a major limitation with respect to the reliability of the technique when used for sizing.

With this respect, a sensitivity analysis could be always carried out to estimate the impact of parameter uncertainties on the reliability of the model predictions. Accordingly, a smaller number of

key parameters is usually identified and direct evaluation of the most important ones could be also a reasonable option, as it will be shown in the next section.

## 2.2 Applications

Different examples of particle sizing using US are now shown with reference to diluted dispersion of different materials. More specifically, particle size distribution,  $F(d)$  (i.e. the corresponding characteristic parameters, average size and distribution broadening) and, occasionally, particle concentration,  $\phi$  are evaluated from attenuation spectra (attenuation vs. frequency) using the model presented above. All measurements of sound absorption were carried out using the commercial equipment Ultrasizer (Malvern Ltd, UK), covering the frequency range from 1 to 100 MHz.

**Silica in water** [3]. This is an example of a system characterized by large density contrast. Under this conditions, and if small particles are considered, the attenuation is expected to be fully dominated by the viscoinertial mechanism, i.e. coefficient  $A_1$  in Eq.(1). Particles in the size range from 0.1 to 0.5  $\mu\text{m}$  were analyzed, always under highly diluted conditions (solid weight fraction around 1%). The results are summarized in Table 1 in terms of median diameter,  $d_{50}$ , and standard deviation,  $\sigma$ . Notably, different sizing techniques have been compared: electron microscopy (SEM/TEM) and dynamic light scattering (DLS/PCS). Keeping in mind that comparative analyses of different sizing methods are always difficult (for example, the average diameter and the distribution broadening estimated by DLS/PCS are not the same as those evaluated using the two other methods), a reasonable agreement is found in the two monomodal cases being the differences below 10%. On the other hand, both US and DLS/PCS do not see the first mode in the bimodal case. In the DLS/PCS case, this is an intrinsic limitation, since large particles “obscure” small ones. However, the sizing performance of US could be largely improved by selecting different model distributions, e.g. suitable for multimodal distributions. Finally, it should be mentioned that repeated measurements were found to be quite well reproduced, thus indicating a significant robustness of the ultrasonic technique.

**Polymer latexes** [4] [5]. A colloidal dispersion of polymer particles in water is called latex. Many industrial polymers are produced in this form and, in some cases, this is also the final product. Several end-use properties of polymer latexes are determined by particle size and the monitoring of the size distribution during the synthesis could be an extremely helpful tool. Many polymers exhibit density values not too far from that of water, so that thermal losses (and not only viscoinertial ones),

determine the attenuation behavior of such dispersions. We analyzed by US different polymers, from high (polytetrafluoroethylene, PTFE) to medium (polyvinylchloride, PVC) and low density contrast (polystyrene, PS and polymethyl methacrylate, PMMA).

Let us focus on the PVC case. A preliminary sensitivity analysis showed that, differently from the silica case, thermal properties are also important. Examples of sizing are shown in Figure 1, where PVC latexes at three different particle diameters were considered (0.2, 0.3 and 0.5  $\mu\text{m}$ ). The three different attenuation spectra (experimental and calculated) and the calculated particle size distribution as well, are shown in the figure. The sizing performance is indeed satisfactory: diameter values of 0.215, 0.325, 0.508  $\mu\text{m}$  and 0.202, 0.315, 0.502  $\mu\text{m}$  were estimated by US and DLS, respectively.

Despite the good results, some discrepancies in the low frequency range (< 20 MHz) can be noticed.

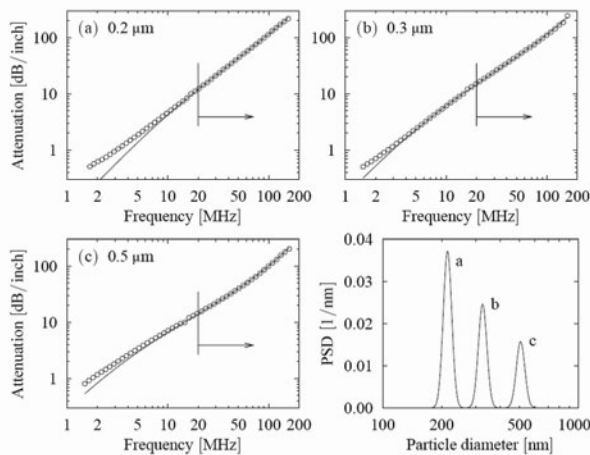


Figure 1: Attenuation spectra of different PVC latexes (a = 0.2  $\mu\text{m}$ ; b = 0.3  $\mu\text{m}$ ; c = 0.5  $\mu\text{m}$ ) and resulting particle size distributions. Symbols are experimental data and solid curves model results. The dashed lines represent attenuation of pure water.

This behavior was actually found quite systematically, also in the case of different polymers, such as PS and PMMA. Such discrepancies were initially imputed to system "impurities" (emulsifier or residual monomer) or to gas micro-bubbles formed in-situ. However, the negligible impact of impurities was checked experimentally while careful sample treatments aimed to prevent bubble formation were not affecting the discrepancy. Then, the evaluation procedure for the different parameters was carefully reconsidered. Using the ECAH model, the different physical properties were ranked in terms of

relevance to the model predictions. Among the main parameters, the intrinsic attenuation of the polymer was identified. Such property has to be known as a function of frequency with accuracy, which is very rarely the case for polymers. Therefore, a procedure to measure directly the intrinsic attenuation of polymer slabs has been developed based on the same equipment used to measure the attenuation spectra of dispersions [5]. By using these directly measured values of the polymer attenuation, the agreement between experimental and predicted attenuation values was improved significantly with respect to the case where literature values were considered, as it is shown in Figure 2.

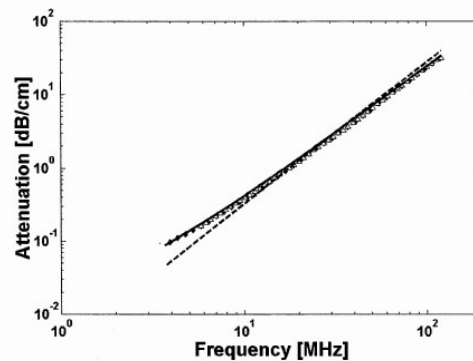


Figure 2: Attenuation spectra for PS latexes (particle diameter = 70 nm; polymer weight fraction = 0.035). Symbols are experimental data and curves model results. Solid line: measured intrinsic attenuation; dashed line: intrinsic attenuation from literature [2].

### 3 CONCENTRATED SYSTEMS

#### 3.1 Modeling

One of the most attractive features of US is its applicability to high concentration, opaque systems, a decisive advantage with respect to light scattering techniques when on-line applications are considered. Even though the measurements are readily feasible, the extraction of the particle size distribution from the experimental spectra cannot be based on the model discussed above, limited to highly diluted systems. When dealing with concentrated systems, sound attenuation is exhibiting highly nonlinear dependence upon the particle concentration, a behavior not explained by Eq.(1), where linear dependence is invariably predicted. With the aim of using the same modeling framework originally proposed for isolated particles, a new semi-empirical model has been proposed for concentrated systems based on the core-shell concept [6].

The deviations from the linear dependence can be imputed to two main effects, lossless redirections due to multiple scattering and particle-particle interactions modifying the absorption mechanism at the single particle level. While the first effect has been proved to be negligible in polymer latexes [8], the second one was expected to be important

because of the very small particle separation distances typical of such colloidal dispersion at high concentration. Therefore, a core-shell model was proposed where the original polymer particle is embedded into a shell of pure continuous phase (water in our cases) which is in turn immersed in a kind of "effective medium". Being the system description still based on a single particle, the same fundamental conservation laws of the ECAH model were adapted and analytically solved. However, the introduction of a third phase causes the number of scattering coefficients to increase from 6 to 12 for each  $n$  value. Again, these coefficients need to be evaluated in order to compute the attenuation of the dispersion using Eq. 3:

$$\alpha_{eff} = -\frac{12\phi}{k^2 d^3} \sum_{n=0}^{\infty} (2n+1) \text{Re}(A_n) + \alpha_B \quad (3)$$

where  $\alpha_B$  is the background attenuation (volume-average of the intrinsic attenuations of continuous and dispersed phase) and  $A_n$  are the scattering coefficients characterizing the waves leaving the particle surface inside the shell, those affecting the measured total attenuation. This equation, originally proposed in the literature for diluted systems [1] [2], was used instead of the more comprehensive Eq.(1) because of its improved numerical stability [6].

Finally, the evaluation of the additional quantities of the core-shell model with respect to the original single-particle model deserves few comments. The size of the shell has been evaluated as a function of the particle concentration so as to fill the free, interparticle space. Therefore, it is a given function of the particle diameter when the particle concentration is known. Moreover, the values of the physical properties of the fictitious, effective medium have been estimated as volume average of the properties of the original phases, with the exception of viscosity, which is always assumed the same as that of the continuous phase. Despite the large empiricism involved in this choice, this approach resulted quite effective for most examined systems, as it is shown in the next section.

### 3.2 Applications

The core-shell model has been validated by sizing different aqueous dispersions of solid particles (silica and polytetrafluoroethylene, PTFE) and droplets (corn oil) [7]. The case of PTFE is shown in Figure 3.

The significant improvement introduced by the core-shell approach is quite evident and the nonlinear dependence of the attenuation upon the particle concentration is properly predicted. The sizing performance of the two models is compared in Figure 4, where the size predictions for all mentioned systems are compared. The core-shell model is clearly suppressing the drift with

concentration of the predicted particle size, a clear artifact introduced by the ECAH model when applied to concentrated systems.

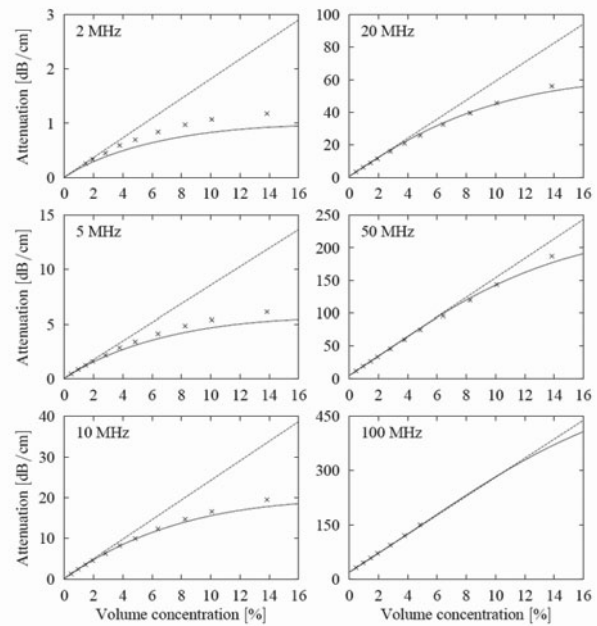


Figure 3: Attenuation vs. particle volume concentration for a PTFE latex (particle diameter 0.2  $\mu\text{m}$ ) at different frequency values. Solid line: core-shell model; dashed line: ECAH model.

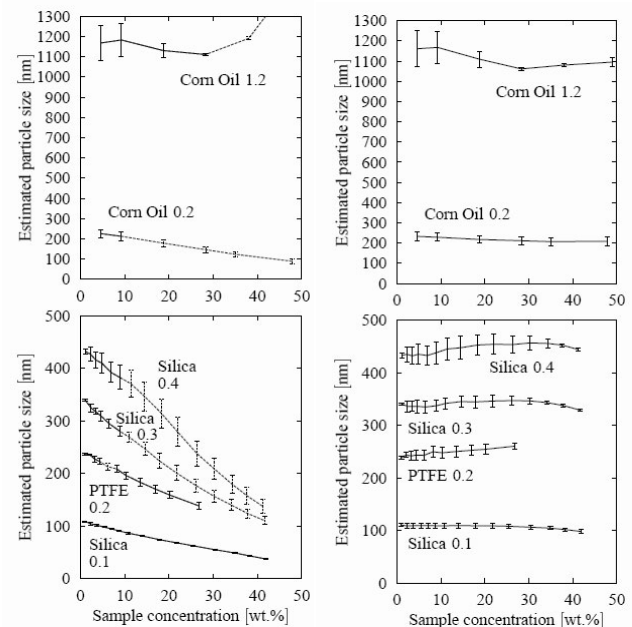


Figure 4: Particle sizing using ECAH model (left) and core-shell model (right). Average particle diameter and distribution variance were predicted at given particle concentration (numbers indicate the approximate average diameter in  $\mu\text{m}$ ).

#### 4 CONCLUDING REMARKS

The reliability of the particle sizing based on sound attenuation measurements has been explored with reference to solid-liquid and liquid-liquid dispersions. Even though different models covering remarkably large ranges of concentration are available, the evaluation of the many required physical properties could be a significant limitation. This is even all the more true when analyzing systems containing materials the properties of which are not well defined or changing in time due to reaction processes. A sensitivity analysis of the model predictions with respect to such parameters was found quite helpful in ranking them according to their relevance with respect to sizing and, therefore, to identify the required accuracy of the corresponding value.

Even though colloidal dispersions (submicron particle diameters) were analyzed in this work, the same technique and the same modeling tools can be applied to systems involving larger particles. Examples in this direction are given in the literature with reference to the monitoring of crystallization processes (crystal size around 100  $\mu\text{m}$ , [9]) and of three-phase gas-liquid-liquid systems (droplet size around 100  $\mu\text{m}$ , gas bubble size around 1 mm, [10]).

Finally, it could be mentioned that further advances in the equipment technology are continuously appearing towards the miniaturization of the apparatus and, in particular, of the measuring cell. Such advances could open major perspectives with respect to on-line applications for process monitoring where the quality control of particulate products is the main requirement.

[7] Hipp AK, Storti G, Morbidelli M: Acoustic Characterization of Concentrated Suspensions and Emulsions. 2. Experimental Validation. *Langmuir* 18 (2002) 405-412.

[8] Hipp AK, Storti G, Morbidelli M: On Multiple-particle Effects in the Acoustic Characterization of Colloidal Dispersions. *J. Phys. D: Appl. Phys.* 32 (1999) 568-576.

[9] Hipp AK, Storti G, Morbidelli M: In-situ Monitoring of Batch Crystallization by Ultrasound Spectroscopy. *Ind. Eng. Chem. Res.* 39 (2000) 783.

[10] Cents AHG, Brilman DWF, Versteeg GF, Wijnstra PJ, Regtien PPL: Measuring Bubble, Drop and Particle Sizes in Multiphase Systems with Ultrasound. *AIChE J.* 50 (2004) 2750-2762.

Table 1: Comparison of sizing results on aqueous dispersions of silica using ultrasound spectroscopy (US), microscopy (SEM/TEM) and light scattering (DLS/PCS) (from [3]).

	US	TEM/SEM	DLS/PCS
Silica 0.1 $\mu\text{m}$			
$d_{50}$ (PCS: $d_{PCS}$ ) (nm)	82	81	112
$\sigma$ (PCS: $Pd$ )	0.09	0.19	0.10
Silica 0.3 $\mu\text{m}$			
$d_{50}$ (PCS: $d_{PCS}$ ) (nm)	314	346/354	355
$\sigma$ (PCS: $Pd$ )	0.05	0.05	0.06
Silica 0.2/0.5 $\mu\text{m}$ (bimodal)			
$D_{50}$ (PCS: $d_{PCS}$ ) (nm)	432	215/483	419
$\sigma$ (PCS: $Pd$ )	0.05	0.18/0.22	0.16

#### REFERENCES

[1] Epstein PS, Carhart RR: The Absorption of Sound in Suspensions and Emulsions. I. Water Fog in Air. *J. Acoustic. Soc. Am.* 25 (1953) 553.

[2] Allegra JR, Hawley SA: Attenuation of Sound in Suspensions and Emulsions: Theory and Experiments. *J. Acoustic. Soc. Am.* 51 (1972) 1545.

[3] Hipp AK, Storti G, Morbidelli M: Particle Sizing in Colloidal Dispersions by Ultrasound. Model Calibration and Sensitivity Analysis. *Langmuir* 15 (1999) 2338-2345.

[4] Storti G, Hipp AK, Morbidelli M: Monitoring Latex Reactors by Ultrasonics. *Polymer Reaction Eng.* 8 (2000) 77-94.

[5] Adjadj LP, Storti G, Morbidelli M: Ultrasound Attenuation in Polystyrene Latexes. *Langmuir* 19 (2003) 3953-3957.

[6] Hipp AK, Storti G, Morbidelli M: Acoustic Characterization of Concentrated Suspensions and Emulsions. 1. Model Analysis. *Langmuir* 18 (2002) 391-404.



# A New Velocity Estimation Method using Spectral Identification of Noise

Stéphane FISCHER, Philippe SCHMITT, Denis ENSMINGER, Fares ABDA, and Anne PALLARES

Institut de Mécanique des fluides et des Solides, 2 rue Boussingault, 67000-Strasbourg, France

In all measurement techniques one seeks accuracy and precision. In ultrasonic Doppler velocimetry, those qualities strongly depend on signal-to-noise ratio of the Doppler signal and on the performance of the velocity estimator. The most widely used estimation method in ultrasonic Doppler velocimetry is the Pulse Pair method. Its success is due to the computation efficiency of the algorithm combined to an unbiased estimator. Unfortunately, in a wide range of experimental fluid flows, the pulse pair estimation is less efficient, especially in clear water or concentrated mud where the signal-to-noise ratio can be very low, or in highly turbulent flows where the Doppler signal has a broad spectrum. Our approach is based on the treatment of the Doppler Spectral Information. It uses a simple parametric identification inspired by theoretical models and experimental observations. It acts through noise subtraction and subsequent cutting. Thus, we have developed a fast velocity estimation algorithm superior to the Pulse Pair in terms of accuracy. Robustness of the method was evaluated by adding different levels of white Gaussian noise to an experimental Doppler signal. Results demonstrate an increase of noise immunity up to one decade compared to the Pulse Pair method.

**Keywords:** frequency estimation, Doppler signal, spectral analysis, variance

## 1 INTRODUCTION

There are several methods for flow velocity evaluation. One of the commonly used is the pulsed ultrasound technique: the estimation of the flow velocity at different depths along a profile can be obtained by Doppler evaluation from the backscattered acoustic signals [1]. In this approach, every sample volume is defined by the ultrasound beam geometry and the range gate of the pulse [2]. The ultrasonic signal is the result of reflection on moving scatterers in the insonified volume. This pulsed ultrasound technique generates, after coherent quadrature demodulation, a vector of samples for each depth volume in the profile. This signal is a complex Gaussian process, with addition of complex white Gaussian noise in first approximation.

Velocity in the depth volume is obtained by extraction of the Doppler information, estimated by the first spectral moment of the signal. The difficulty is mainly due to the random fluctuation of the Doppler frequency associated with each particle in the considered sample volume, even if there is no noise. The most used technique to estimate the moment of this complex signal is so called the Pulse Pair technique, which computes the autocovariance in order to extract the spectral mean frequency [3]. This estimator is in addition the maximum likelihood solution under Gaussian assumption.

Nevertheless, acoustic signal might present multiplicative noise, and data acquisition systems might introduce perturbation that deteriorates the performance of the Pulse Pair technique, and implies that the estimation variance can be larger than the Cramer-Rao lower bound. In this context, a new estimation method [4], based on the

identification of the spectrum of the Doppler signal can be of great interest. The aim of this paper is to compare the new spectral method with the Pulse Pair in the case of white Gaussian noise conditions.

This paper is organized as follow. First, a model for moving scatterers in the insonified volume is presented, taking into account beam width and velocity distribution of the particles. Second, a novel method of first moment estimation is presented based on the identification of signal and noise in the spectrum. Finally, simulation results are discussed, presenting the noise range where this method is of interest.

## 2 DESCRIPTION OF THE METHOD

### 2.1 Doppler signal model

This study uses a basic time model corresponding to a Gaussian Doppler spectrum. The assumption of such a Gaussian spectrum is widely used [5-6] and is experimentally observed [7-8]. We consider a set of particles uniformly distributed in the fluid. Each particle appears in the Doppler signal as a wavelet when crossing the ultrasonic beam [7]. The complete signal is the sum (equ. 1) of those wavelets randomly delayed ( $\tau_i$ ). Each single wavelet is the product of a complex exponential function with a Gaussian shape (with a standard deviation  $\sigma$  and amplitude  $a$ ).

$$s_D(t) = \sum_{i=1}^N a \cdot \exp\left[-\frac{(t - \tau_i)^2}{2\sigma^2}\right] \cdot \exp j(2\pi f_D t + \varphi_i) \quad (1)$$

The Doppler frequency  $f_D$  of this demodulated signal is proportional to the particles velocity and the

corresponding phase  $\varphi_i$  is a random uniform variable.

## 2.2 Algorithms description

The Pulse Pair method was first introduced by [3]. It is the most widely used for the Doppler velocity estimation. This method supposes a white Gaussian noise and is based on a correlation calculation:

$$f_D = \frac{f_e}{2\pi} \arctan \frac{\text{Im}(R(1/f_e))}{\text{Re}(R(1/f_e))} \quad (2)$$

where  $f_e$  is the sampling frequency equal to the Pulse Repetition Frequency (PRF) and  $R$  is the autocovariance function of the complex Doppler signal.

The newly proposed velocity estimation method is based on the identification of the spectrum by a Gaussian model:

$$M(f) = A_s \cdot \exp\left(-\frac{(f - f_D)^2}{2\sigma_D^2}\right) + A_N \quad (3)$$

This approach is similar to that proposed in [4] which use the Levenberg-Marquard non-linear regression. The evolution of the algorithm is optimized in term of calculation efficiency and is forty time faster than the previous one but stay ten times slower than the Pulse Pair. The algorithm act as follow (see fig. 1):

- In the first step the Doppler spectrum is calculated from the square of the Fast Fourier Transform (FFT) magnitude.
- This spectrum is smoothed by a third order FIR (Finite Impulsion Response) filter until one can extract a single peak when cutting the spectrum at the first third of its magnitude.
- The forth step consist in the estimation of the mean  $f_D$  and the standard deviation  $\sigma_D$  of a Gaussian function cutting the spectrum at the same points.
- The linearization of the data is then done by the use of a new variable  $f'$ :

$$f' = \exp\left(-\frac{(f - f_D)^2}{2\sigma_D^2}\right) \quad (4)$$

- This allows to estimate the parameters  $A_s$  and especially  $A_N$  by least square.
- The noise is then suppressed by a simple subtraction of the  $A_N$  value from the spectrum and all the values out of the  $[f_D - 3\sigma_D; f_D + 3\sigma_D]$  interval are set to

zero. This operation gives an estimate of the spectral density of the Doppler signal  $D_s(f)$ .

- The last step is to estimate the mean frequency of the Doppler Signal by the calculation of the spectral first moment:

$$f_D = \frac{\sum f \cdot D_s(f)}{\sum D_s(f)} \quad (5)$$

The estimation can be enhanced by cumulating the magnitude-squared FFT of a few observed Doppler signals [9] before the smoothing step.

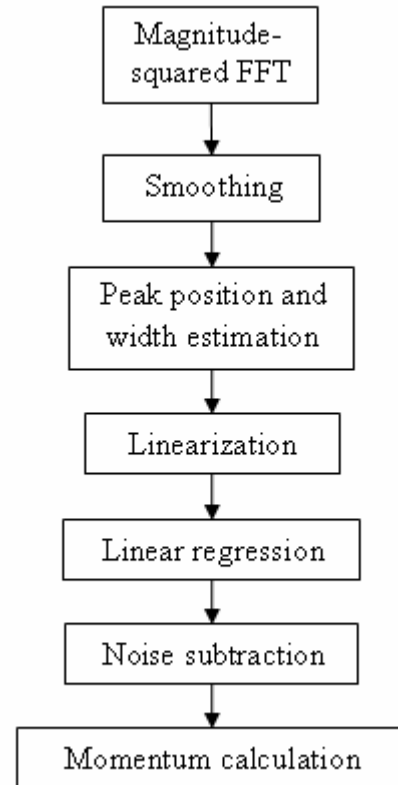


Figure 1: Steps of the spectral estimation method

## 3 PERFORMANCE

### 3.1 Simulation and estimation procedure

Several simulations for performance evaluation were conducted. We focused our attention on the comparison of the two methods by calculating the bias and the variance of each estimator for different SNRs. We varied the Doppler frequency to be estimated and the spectral width. The latter is related to the wavelet duration.

The simulated signal duration consisted of 5x64 samples. Depending on the used method, we calculated the mean value of the autocorrelation or the magnitude squared spectrum averaged over the 9 blocs of 64 samples. Indeed, in order to improve

the performance of the estimation process, we use an overlapping of 32 samples between two adjacent blocs.

Normalization is done by dividing the bias and standard deviation on the frequency estimation by the length of the frequency range (corresponding to the PRF). In the different figures, the Doppler frequency is normalized by the PRF:

$$f = \frac{f_D}{f_e} \quad (6)$$

The normalized width  $w$  is driven by the duration of the Doppler wavelet directly linked to the beam width. This spectral width is chosen equal to:

$$w = \frac{6 \cdot \sigma_D}{f_e} \quad (7)$$

with  $\sigma_D = (2\sqrt{2\pi}\sigma)^{-1}$  the standard deviation of the Gaussian function modeling the Doppler spectrum of the signal described by equation (1).

### 3.2 Model validation

The first step of this work is the validation of the signal model in comparison with the experimental data. This validation consists in the observation of the estimator behavior when the signal-to-noise ratio decreases. In this procedure, a portion of an experimental Doppler signal with a low noise level is selected. This signal has a normalized central frequency of 0.88 and a normalized spectral width (at 6 sigma) of 0.18. Then a signal is simulated with the same properties of mean frequency and spectral width, according to the model described by equation (1). Finally, noise is progressively added to those vectors of samples.

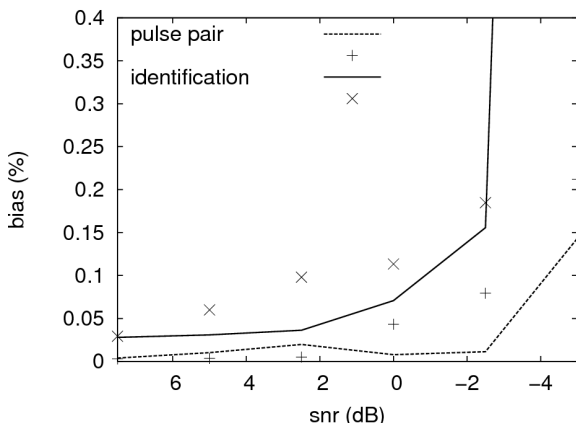


Figure 2: Comparison of the bias for the two methods with experimental data (points) and simulated data (lines).

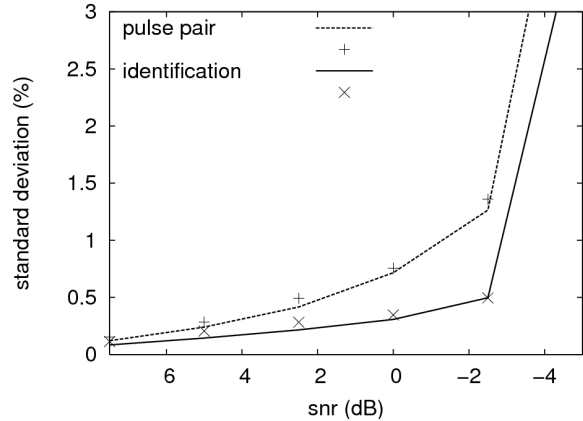


Figure 3: Comparison of the standard deviation for the two methods with experimental data (points) and simulated data (lines)

Figures (2) and (3) present the variation of the bias and the standard deviation while adding noise. In both cases the difference between the experimental signal and the simulated one is less than 0.1%. This validates the use of the model for the comparison of the two estimators. Nevertheless, the simulation results are a bit more optimistic than the simulated data.

### 3.3 Simulation results

The normalized bias and standard deviation of the two estimates are shown in figures (4) and (5) for different values of frequencies and for a normalized spectral width of 0.16.

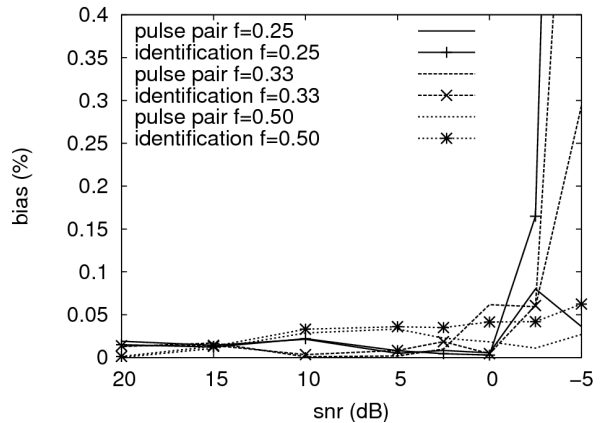


Figure 4: Comparison of the bias at different normalized frequencies.

The bias is less than 0.05 percent for any signal to noise ratio greater than 0 db. The results for the two methods are quite similar but for low signal to noise ratio, the pulse pair is globally more efficient.

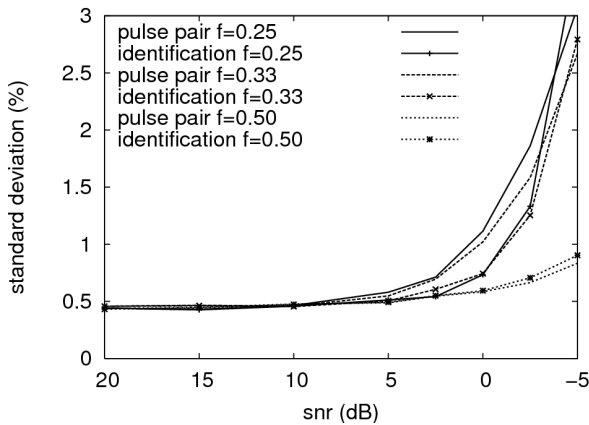


Figure 5: Comparison of the standard deviation at different frequencies.

As shown in figure (5), the main difference between the two methods is in term of standard deviation. It can be up to 40% greater for the Pulse Pair than for the identification method. This difference greatly depends on the central Doppler frequency  $f_D$  and mostly grows up with the frequency reduction.

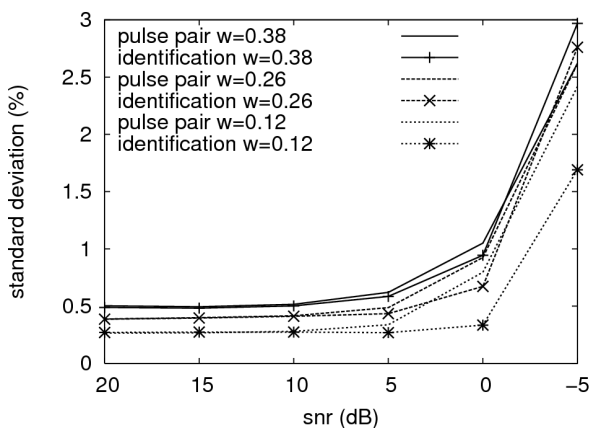


Figure 6: standard deviation comparison for different spectral widths.

Figure (6) present the results of the two methods for different width of the Doppler spectrum.

Those results show a significant improvement of the standard deviation when using the identification method, especially for narrow spectra. The identification method can be up to two times more precise.

#### 4 SUMMARY

A novel estimation algorithm, based on spectral identification, has been evaluated. Compared to the traditional Pulse Pair, this method has globally the same bias, but is better in term of standard deviation. This method delivers better standard deviation for a signal to noise ratio in the range going from 10 to 0 dB.

Moreover, this novel method is more robust for experimental signals, especially when the data contain additional perturbations. Simulations with those kinds of perturbations (asymmetry between in-phase and quadrature signals, non Gaussian or/and coloured noise) have still to be done.

#### REFERENCES

- [1] Takeda Y: Velocity profile measurement by ultrasonic Doppler Method, *Experimental Thermal and Fluid Science*, 10 (1995) 444-453.
- [2] Yu ACH et al.: Transit-time broadening in pulsed Doppler ultrasound: a generalized amplitude modulation model, *53-3(2006) 530- 541*.
- [3] Miller KS, Rochwarger MM: A covariance approach to spectral moment estimation, *IEEE Transactions on Information Theory* 18 (1972) 588-596.
- [4] Fischer S. et al.: *Suppression du bruit par identification en vélocimétrie ultrasonore pulsée*, Instrumentation - aspects fondamentaux, Hermes (2004).
- [5] Bendat JS, Piersol AG: *Random Data Analysis and Measurements Procedures*, Wiley-Interscience (1971).
- [6] Torp H et al.: Autocorrelation Techniques in Color Flow Imaging, Signal model and statistical properties of the Autocorrelation estimates, *IEEE Transactions on Ultrasonics, Ferroelectrics, and Frequency Control*, 41- 5 (1994) 604-612.
- [7] Garbini JL et al.: Measurement of fluid turbulence based on pulsed ultrasound techniques Part 1 & 2, *Journal of Fluid Mecanics* 118 (1982) 445-505.
- [8] Guidi G et al.: Intrinsic spectral broadening (ISB) in ultrasound Doppler as a combination of transit time and local geometrical broadening, *Ultrasound in Med. & Biol.*, 26 (2000), 853-862.
- [9] Fischer S: *Développement d'une instrumentation ultrasonore pour la mesure des vitesses des liquides au-delà de la limite de Nyquist par une approche spectrale*, Université Louis Pasteur (2004).

## Velocity Vector Profile Measurement using Multiple Ultrasound Transducers

Seiji Kon\*, Kohei Yamaguchi\*, Hironari Ohbayashi\*\*, Yuji Tasaka\*,  
Yuichi Murai\* and Yasushi Takeda\*

\*Division of energy and environmental system, School of engineering, Hokkaido University  
N13W8, Sapporo, Hokkaido, 060-8628, Japan, E-mail: kon@ring-me.eng.hokudai.ac.jp

\*\*Japan Atomic Energy Agency  
2-4, Shirane, Shirakata, Tokai-mura, Ibaraki-ken, 319-1195, Japan  
E-mail: obayashi.hironari@jaea.go.jp

Unit of Vector-UVP system, which is an advanced UVP system to measure three directional velocity components on a line by using multiple transducers, was developed. Obtaining information of acoustic field is very important for optimizing Vector-UVP system. We attempted to study it experimentally but found that it is time consuming to measure acoustic field by scanning a hydrophone. Moreover, the measurement result could involve some problems like space resolution and a problem of echo from any surrounding experimental apparatuses. To obtain more accurate data effectively and estimate the influence of existence of a wall, acoustic field under the developed system was calculated by solving two-dimensional wave equation and then the measurement volume and measurement area were estimated to optimize the system. The system applied to measure two directional velocity components of Kármán vortices in a wake of a cylinder as an example of unsteady flow. From the measurement data, vortices were observed and vorticity distribution of cylinder wake was calculated by using Taylor's frozen hypothesis.

**Keywords:** UVP, Velocity vector measurement, Spatio-temporal velocity profile, Unsteady flow

### 1 INTRODUCTION

Ultrasonic Velocity Profiler (UVP) has been applied to experimental study of fluid dynamics and fluid engineering. The objective of this study is to develop an advanced UVP system named Vector-UVP that enables us to obtain three directional velocity components of the fluid flow on a line.

The velocity vector of fluid flow is expressed by functions for three velocity components of three directions of space and time. Therefore, in the experimental study for fluid dynamics, it is a goal to obtain such information. Recently, such ideal measurement may be realized by drastic progress of Particle Image Velocimetry (PIV). But PIV cannot be applied to the opaque fluids and an opaque apparatus. On the other hand, Ultrasonic Velocity Profiler (UVP) is a very effective tool for velocity profile measurement of opaque fluids. But UVP gives only one directional velocity component on a measurement line and it is less informative in comparison with velocity vector field given by PIV.

The purpose of this study is to overcome this disadvantage of the conventional UVP by expanding the dimension of velocity vector. We call this velocimetry Vector-UVP.

An idea and concept of Vector-UVP has been reported by Lemmin. [1-4], which is apparently not

suitable for fluid dynamic study since measurement volume is too large. So we advance its concept to be applied to the experiment of fluid dynamics as shown in Fig.1.

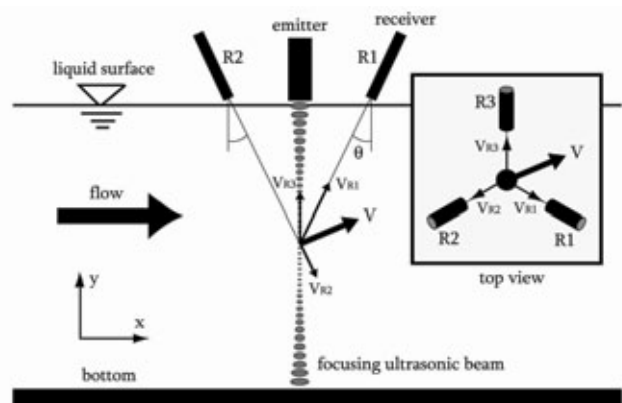


Fig. 1 Schematic illustration of concept of Vector-UVP; multiple ultrasonic receivers are surrounding ultrasonic emitter to take multi-directional information of the velocity vector of the fluid flow

It consists of a central emitter, symmetrically surrounded by three receivers, R1 to R3. An ultrasonic pulse is emitted into fluid from the emitter, and surrounding receivers receive the echo reflected from tracer particles. By analyzing these received echo waves, three directional velocity components can be obtained in the same manner

as in the conventional UVP for each receivers and three-dimensional velocity vector can be formed. Since these receivers have a certain spatial range of receivable area, it can receive the echo from each point on the ultrasonic beam in this range. Therefore, this system can obtain the profile of the three-dimensional velocity vector on the ultrasonic beam. In order to reduce spatial uncertainties of the measurement position, a focusing TDX (F-TDX) that is able to decrease the diameter of ultrasonic beam by using acoustic lens was employed as an emitter in Vector-UVP.

In 4<sup>th</sup> ISUD, Ohbayashi *et al.* presented their achievement of Vector-UVP measurement of flow in the rotating cylinder as an example of steady flow. [6] So in this study, as an example of unsteady flow, two directional velocity components of Kármán vortices in a wake of a cylinder were measured. And as a preparation for optimum design of its experimental apparatus, we calculated sound field made by ultrasonic transducer by solving wave equation and estimated the measurement volume and measurable area.

## 2 SOUND FIELD MEASUREMENT

For optimizing the V-UVP system, sound field is one of the most important characteristics. Measurement of sound field generated by 8 MHz F-TDX was performed by using a needle hydrophone. (Toray engineering, NH8028, active diameter 0.5 mm) The experimental setup is shown in Fig. 2. The received signal was observed using a spectrum analyzer to record a sound pressure. The measured field spans from 0.5 to 32.0 mm to x-direction and -5.0 to 5.0 mm to y-direction. The interval of each grid was set to  $dx = 0.5$  mm and  $dy = 0.5$  mm. The medium was water.

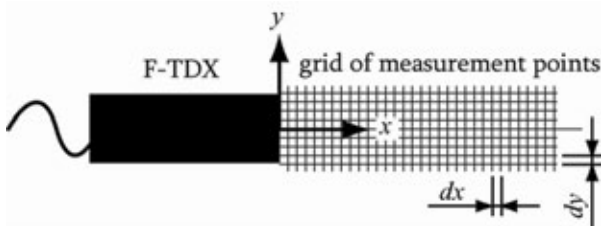


Fig. 2 Experimental setup for measurement of sound pressure made by F-TDX

The measurement result of the sound field and the maximum sound pressure on the centerline of the transducer is shown in Fig. 3. Focusing of ultrasonic beam is clearly shown. The beam diameter is defined as the FWHM of radial intensity distribution of ultrasound beam. The narrowest point of beam diameter is considered as focal point. Therefore, focal point is  $x = 25$  mm, which is almost same as the nominal value given by TDX manufacturer. It should be noted, first, that the space resolution is not high enough. Because the active diameter of needle hydrophone is almost

three times as large as wave length of ultrasound. Second, the measurement value includes the influence of echo from surrounding walls.

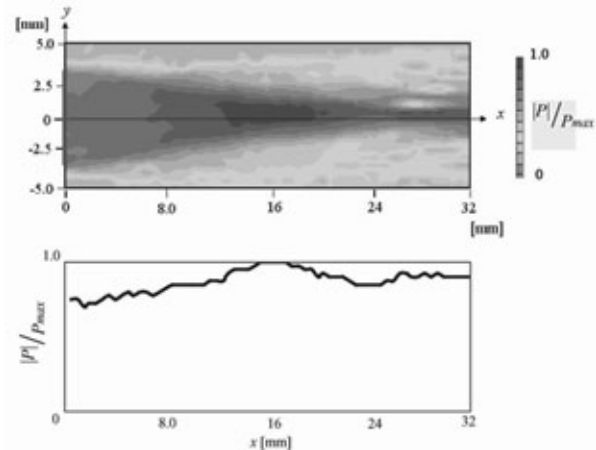


Fig. 3 Experimental results of sound field generated by 8 MHz F-TDX and the maximum sound pressure on the centerline

## 3 SOUND FIELD CALCULATION

To know sound field effectively without the problem of space resolution and influence of echo from surrounding apparatuses, the sound field was calculated from the following two-dimensional wave equation.

$$\frac{\partial^2 P(x, y, t)}{\partial t^2} = c(x, y)^2 \left\{ \frac{\partial^2 P(x, y, t)}{\partial x^2} + \frac{\partial^2 P(x, y, t)}{\partial y^2} \right\}$$

In practice, TDX generates ultrasound by oscillation of circular piezoelectric element. In this calculation, sound field made by ultrasonic transducer was substituted with superposition of ultrasound made by point sound source. In this calculation, acoustic lens whose curvature radius was 30 mm was attached to the top of TDX in the same way as actual F-TDX. Sound speed of acoustic lens is 2630 m/s. Intervals of spatial step and time step were chosen as 1/10 of ultrasonic wavelength and 1/50 of the period of oscillation of ultrasound. A medium was water whose sound speed is 1480 m/s at 20 °C. 8 MHz F-TDX which has 7 mm effective diameter is employed as an emitter in Vector-UVP. Calculation result of instant sound field and maximum sound pressure on the centerline of the transducer for 8 MHz F-TDX is shown in Fig. 4. By acoustic lens attached to the top of TDX, focal point of this F-TDX becomes 25.7 mm from transducer. Beyond this point, sound pressure distribution becomes smooth. The nominal focal point is 24.96 mm. That is to say, difference between value of this calculation and nominal value is 0.7 mm that is less than spatial resolution of UVP. So this calculated results can be accepted as accurate enough to estimate the sound field.

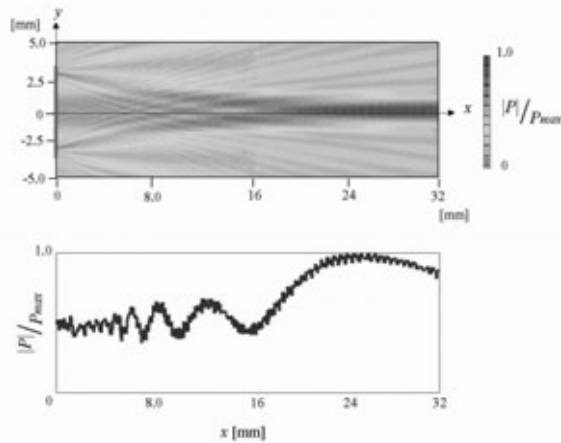


Fig. 4 Sound field generated by 8 MHz F-TDX and maximum sound pressure on the centerline

In many cases, TDX is set outside the wall. The inclusion of a wall will alter ultrasonic beam characteristics. The influence of an inclusion between TDX and working fluid on sound field was investigated by this calculation. As preparation for measurement of Kármán vortices in a wake of a cylinder, the sound field made by 8 MHz F-TDX set on the other side of acrylic wall was calculated. The thickness of acrylic wall was 0.2 mm and sound speed is 2700 m/s. The working fluid was silicone oil whose sound speed is 995 m/s at 20°C. The calculation result is shown in Fig. 5.

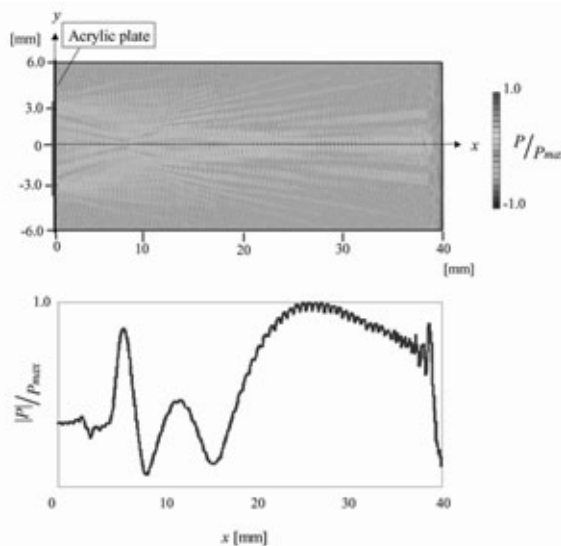


Fig. 5 Sound field generated by 8 MHz F-TDX set up on the other side of acrylic wall and maximum sound pressure on the centerline

By the reflection on surface of acrylic wall, on the whole, sound pressure is lower than the case without the wall. In a range of 15 mm from 0 mm, the maximum sound pressure on the centerline has different characteristic from the case without the wall. This difference would be made by the influence of multiple reflection echo. But over 15 mm, the

maximum sound pressure characteristic is similar to the case without the wall. From this calculation result, the focal point is considered as  $x = 26.7$  mm.

In the other condition, for example, the thickness of wall is 3 mm, and the distance between the top of TDX and the wall isn't 0 mm, the flow field was calculated. From these results, as far as possible, the inclusion should be thin. And TDX should be set upped as the top of TDX directly contact with the inclusion to reduce the influence of inclusion.

## 4 MEASUREMENT OF KÁRMÁN VORTICES IN A WAKE OF A CYLINDER

### 4.1 Experimental setup

Measurement of two directional velocity components of Kármán vortices in the wake of a cylinder was performed as an example of unsteady flow measurement. The cylinder with diameter  $d = 10$  mm is mounted in a channel, which has 160 mm in width and 40 mm in height, at 1700 mm downstream from the inlet of the channel. Working fluid is silicone oil. Ultrasonic transducers, an emitter and a receiver, are mounted on the top of the channel behind the acrylic plate of 0.2 mm in thickness (Fig. 6). Setting of the transducers is optimized based on the results of the numerical simulation for the ultrasonic beam described in the last section: An intersection of the axes of the transducers was chosen to be at the focal point of the emitter, 26.7 mm from the front of the emitter, which is determined by the numerical simulation. The receiver is fixed inclining with 25 degree. An distance of the measurement line from the cylinder,  $l_x$ , is chosen as  $2.75d$  or  $3.75d$ .

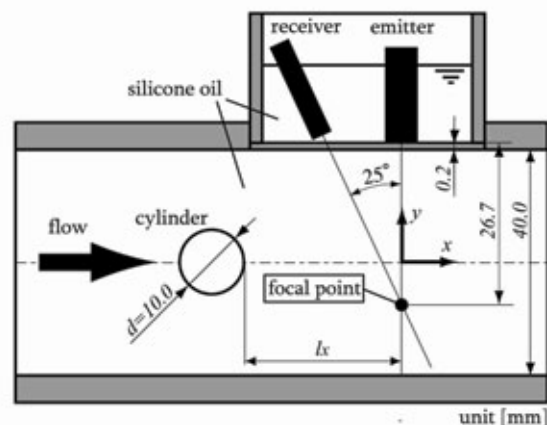


Fig. 6 Experimental setup to measure Kármán vortices in a wake of a cylinder

In this experiment, Reynolds number is defined by following formula.

$$Re = \frac{u_m d}{\nu}$$

where  $u_m$  is a mean stream velocity in the channel, and  $\nu$  is kinematic viscosity of silicone oil. The

measurement was performed for 4 measurement conditions given in Table 1.

Table 1 Experimental conditions, where  $l_x$  expresses a distance of the measurement line from the cylinder

$Re$	$l_x/d$	
	2.75	3.75
150	(A)	(B)
250	(C)	(D)

#### 4.2 Results and discussions

As one of the results of the measurement, temporal variation of the velocity vector profile obtained for the measurement condition specified (B) in Table 1 is shown in Fig. 7, where the sampling period is 30 msec and the profiles are arranged inversely to measurement time (from right to left). In the area enclosed with a black line in Fig. 7, two large vortices can be observed. Since the channel does not have enough height in comparison with the diameter of the cylinder, vortex shedding seems symmetric to the center of the channel unlike Karmann vortex street. But the shedding is periodic and the measured velocity vector profiles express it well.

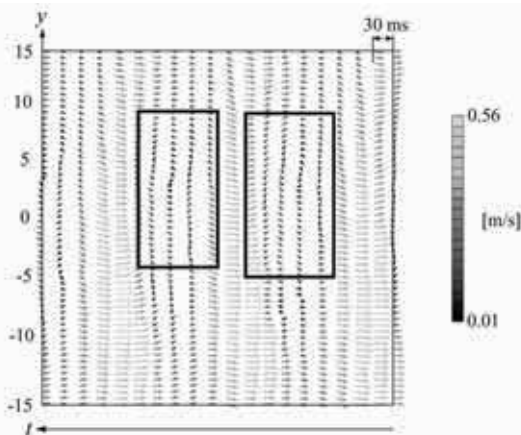


Fig. 7 Two-dimensional velocity vector map of cylinder wake ( $Re = 150$ ,  $l_x/d = 3.75$ )

Velocity vector distribution of the cylinder wake  $\mathbf{v}(x,y)$  is determined from the temporal variation of the velocity vector profiles with applying Taylor's frozen hypothesis, where the spatial value  $x$  is determined by following equation,

$$x = u_m t .$$

Vorticity distribution  $\omega(x,y)$  ( $= \partial v/\partial x - \partial u/\partial y$ ) is computed from the velocity vector distribution (Fig. 8). We can see an alternating vortex shedding from the top and the bottom of the cylinder even though we cannot confirm that in the temporal variation of the velocity vector profile (Fig. 7). It may be caused by less temporal resolution of the profile (30 msec in

temporal resolution corresponds to 4.5 mm in spatial resolution. This value is comparable with the size of the vortex.)

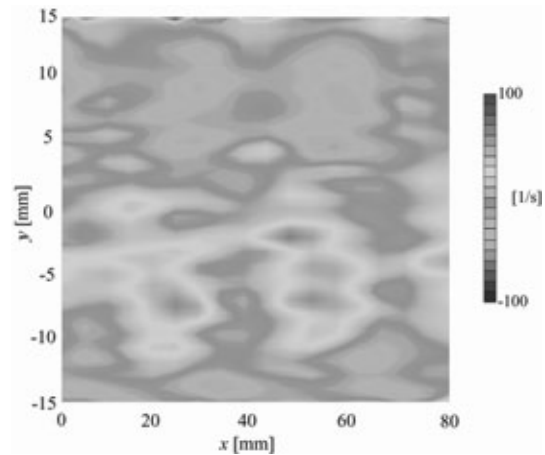


Fig. 8 Vorticity distribution of cylinder wake determined from temporal variation of velocity vector profile ( $Re = 150$ ,  $l_x/d = 3.75$ )

#### 5 CONCLUSIONS

We established the measurement technique for velocity vector profile using ultrasound named Vector-UVP. To design and optimize the system of Vector-UVP, we estimated the measurement volume and measurable range by calculating sound field made by ultrasonic transducer by solving two-dimensional wave equation.

Optimized Vector-UVP system was applied to measure two directional velocity vector profile of unsteady flow, vortex shedding in the wake of a cylinder. The vortex shedding was well reproduced in the vorticity distribution by applying Taylor hypothesis to the temporal variation of velocity vector profile obtained by Vector-UVP.

#### REFERENCES

- [1] R.Lhermitte, U.Lemmin, 1993, "Turbulent flow microstructures observed by sonar" *Geophysical research letters* Vol. 20 No.9, pp.823-826.
- [2] C.Shen and U.Lemmin, 1996, "Ultrasonic measurements of suspended sediments: a concentration profiling system with attenuation compensation", *Meas. Sci. Technol.*7 pp.1191-1194.
- [3] C.Shen and U.Lemmin, 1997, "A two-dimensional acoustic sediment flux profiler", *Meas. Sci. Technol.*8, pp.880-884.
- [4] D.Hurther and U.Lemmin, 1998, A constant-beam-width transducer for 3D acoustic Doppler profile measurements in open-channelflows, *Meas. Sci. Technol.*9 pp.1706-1714.
- [5] Y.Takeda, 1991, "Experimental measurements of 2D velocity vector field using ultrasonic velocity profile monitor (UVP)", *J. Exp. Numer. Flow visualization* 128 pp.47-59.
- [6] H.Ohbayashi, Y.Takeda, K.Yamaguchi, 2004, "Fundamental study for development of Vector-UVP (1) Concept and time information" *proc. 4th Int. Symp. Ultrasonic Doppler Method on Fluid Mech. and Fluid Eng.*, pp.125-128.

# Application of Ultrasonic Multi-wave Method for Two-phase Flow

Hideki Murakawa, Hiroshige Kikura and Masanori Aritomi

Research Laboratory for Nuclear Reactors, Tokyo Institute of Technology, 2-12-1-N1-13, Ookayama, Meguro-ku, Tokyo, 152-8550 Japan

In order to obtain both liquid and liquid-gas interface velocities simultaneously, the authors developed a new measurement system referred to as multi-wave ultrasonic method. The measurement employs a unique ultrasonic transducer. In the present study, the characteristic of the multi-wave TDX was investigated. In order to apply the technique for flow measurement, incident angle of the TDX is one of the important parameter. Therefore, the ultrasonic intensity distributions at back of inclined acrylic plate and pipe are measured. From the results, appropriate incident angle and ultrasonic field for the measurements are obtained. Furthermore, the technique is applied to measuring bubbly and slug flows. Compared with the results of the multi-wave method and high-speed camera, it is confirmed that the technique can separate information of liquid and gas phases.

**Keywords:** multi-wave, ultrasonic intensity distribution, bubble, slug, cross-correlation, UTDC, UVP

## 1 INTRODUCTION

The authors had developed a unique ultrasonic transducer (TDX) referred to as multi-wave TDX. This TDX consists of two ultrasonic elements. Its use permits the emission of two types of ultrasonic wavelengths simultaneously and in the same positions. As an initial trial, measurements of bubbly flow in vertical pipes were carried out with the UDM-UDM measurement system [1]. The UDM-UDM measurement system ensured that both ultrasonic elements are connected to the UVP monitors. The velocity distributions of liquid and gas were then obtained. However, the flow conditions were too limited for this technique (mean Reynolds number:  $Re_m=8000$ , superficial gas velocity:  $J_G=0.00310$ ). Hence, ultrasonic time-domain cross correlation (UTDC) method was applied to the multi-wave method for measuring bubble rising velocity in order to overcome the limitation [2]. Furthermore, the technique enabled to separate the liquid and gas velocity information. The rising velocities of the bubbles were obtained at 2 MHz of ultrasound and the liquid velocity distributions were obtained at 8 MHz by means of the UTDC.

In this study, the technique was applied to measuring both bubbly and slug flow. In order to compare the measured velocity and the interface position, high-speed camera was synchronized with the measurements.

## 2 MULTI-WAVE ULTRASONIC METHOD

### 2.1 Multi-wave Ultrasonic Transducer

Fig.1 shows a schematic diagram of the multi-wave TDX. A piezoelectric element of 8-MHz basic ultrasonic frequency with 3 mm diameter is installed in the center of the TDX. Furthermore, a piezoelectric element of 2-MHz basic ultrasonic frequency with hollow shape is set along the central axis. The inner diameter is 3 mm and the outer

diameter is 10 mm. The each element is connected with BNC via lead wires. The piezoelectric elements are made of composite oscillator with PZT and plastic. An epoxy resin with half thickness of the wavelength  $\lambda$  is used as acoustic matching layer. Since the composite oscillator has low acoustic impedance, the energy loss is low at acrylic wall surface comparing with the other materials. Furthermore, the element has an advantage that is difficult to decrease the sensitivity. The multi-wave TDX emits ultrasonic beams independently for basic frequencies of 2 and 8 MHz, respectively. Using the multi-wave TDX, two types of ultrasonic beam diameter ( $D_{US}$ ) can be obtained for multi-phase flow measurements using a single ultrasonic probe.

### 2.2 Measurement of Ultrasonic Intensity Distribution

The multi-wave TDX has a unique shape. Therefore, it is important to obtain the characteristics of the TDX, particularly for the 2-MHz ultrasound. Using a hydrophone method, measurement of ultrasonic pressure fields were carried out for the multi-wave TDX.

The measurement system consisted of automatic xyz-stage and a stage controller (Sigma Koki Co., Ltd.), a pulser/receiver (DPR300, JSR Co., Ltd.), an A/D board (PCI-5112, National Instrument Co., Ltd.), a PC and a water box. The A/D board was installed in a PC. The xyz-stage and the A/D board were controlled with the PC. An ultrasonic TDX was connected with the pulser/receiver. An ultrasonic



Figure 1: Schematic diagram of a multi-wave TDX.

hydrophone (NH8040, Toray techno Co., Ltd.) was traversed by the xyz-stage in order to measure the ultrasonic signal at each measuring point. The measurements were carried out in three dimensionally in order to prevent the inclination of the TDX. The signals were recorded at an A/D board, with a sampling rate of 100 MS/s. A maximum and minimum value was calculated from the 50 average ultrasonic signals. The peak-to-peak between the maximum and minimum of the signal was considered as the ultrasonic signal-intensity at the point. The minimum resolution of the measuring point was set at 0.5 mm. As the distance from the surface of the TDX, the resolution was increased from 0.5 to 5 mm in a longitudinal direction, from 0.5 to 2 mm in a radial direction. The total measuring point was 233 (radial plane)  $\times$  59 (longitudinal direction). The experiments were carried out in three conditions. The first condition was that the ultrasonic pressure distribution in water without any disturbance. The others were the pressure at back of an acrylic plate and pipe. The TDX was set at back of the pipe or plate with contact angle of 45° as shown in Fig. 2.

### 2.3 Characteristics of Multi-wave TDX

The results are shown in Fig. 3(a) and (b). Because of the intrusive between the TDX and the plate or pipe, it is impossible to measure the nearfield area. Therefore, the graphs start at 20 mm from the TDX surface. The gray-scale plots were normalized by the maximum value of the results without any plate. Therefore, the gray-scale represents the relative intensity in between the no-plate condition and pipe-condition. In each measurement condition, there are not any differences between them except the maximum intensity of ultrasonic. With setting the acrylic plate or pipe, the ultrasonic intensity weakens. However, it is not observed that the ultrasonic bend or wider because of the plate/pipe effect. Based on the results of maximum intensity in each condition, the intensity of the ultrasonic with 8-MHz wavelength weakens if it passes the acrylic plate or pipe. The decreases of the intensity are larger than the results of 2 MHz. Therefore, the 8-MHz basic frequency is strongly affected by the wall material where the TDX is set more than the 2-MHz

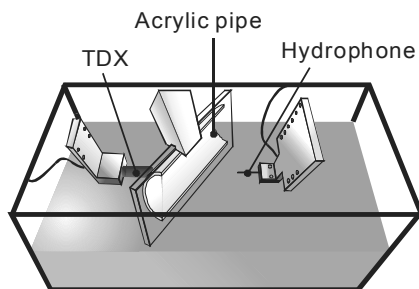


Figure 2: Schematic diagram of a experimental apparatus of ultrasonic intensity distributions at back of an acrylic pipe.

frequency.

From the above investigations, it is found that the multi-wave TDX can be used for measuring bubbly flow. Furthermore, the difference of measurement volume in each frequency is confirmed. Therefore, characteristic of the ultrasound based on the measurement volume is expected.

## 3 EXPERIMENTAL FACILITIES AND SIGNAL SETTING

### 3.1 Experimental Apparatus

The measurement system includes two ultrasonic pulsers/receivers (DPR35+, JSR Co., Ltd. and TB-1000, Matec) in order to emit and receive ultrasonic pulses. Both 2-MHz and 8-MHz ultrasonic elements were connected to the pulsers/receivers. The echo signals received in each pulser/receiver were recorded on an A/D board (PCI-5112, National Instrument Co., Ltd.), with a sampling resolution of 8 bit and a sampling rate of 100 MS/s at two channels. The A/D board was installed in a PC. The A/D board and the pulsers/receivers were connected to each other and synchronized. Therefore, both the 2-MHz and 8-MHz ultrasonic echo signals were simultaneously recorded. The recorded data were calculated by the PC using the correlation method and the velocities were obtained. The signal acquisitions and calculations were simultaneously carried out.

In each channel, 101 consecutive signals were recorded continuously at a sampling rate of 1,000 Hz. The sampling rate and spatial resolution are related to each other. It is well known that the sound velocity in water at 19.5 °C is 1,480 m/s. Therefore, the channel width, which represents the spatial resolution, was set at 0.74 mm. When the sampling rate is set at 100 MS/s, the number of acquisition data in each channel is 100. The velocity resolution, maximum velocity along the TDX, and search

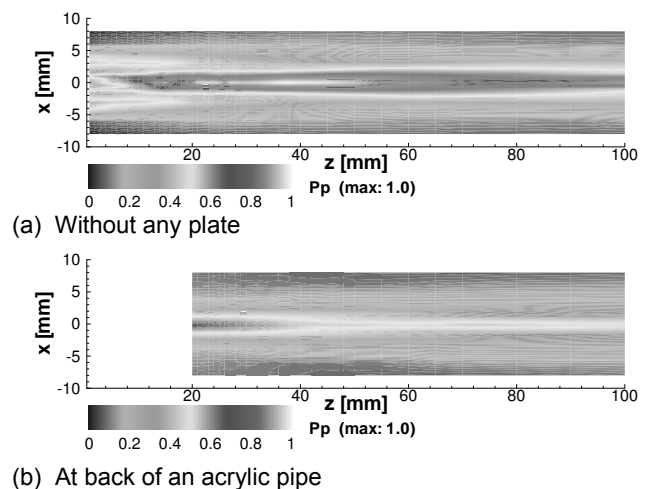


Figure 3: Measurement results of ultrasonic intensity distributions in 2 MHz of multi-wave TDX.

window for the UTDC calculation are related to each parameter. Therefore, the maximum velocity was set as 0.74 m/s, and the velocity resolution was set at 100 divisions of the maximum velocity. The measurement test section was vertical pipe with an inner diameter of 50 mm. The multi-wave TDX was installed on the outer surface with a contact angle of 45°. The measurements were conducted at downstream at a distance of 67D from a bubble generator.

Based on the above setting, 100 velocity distributions were calculated for acquiring 101 continuous echo signals. In these experiments, the acquisitions of the signals were repeated 100 times. A total of 10,000 velocity distributions were obtained.

### 3.2 Signal Setting

Since the echo signals of the ultrasonic beam reflected by the bubbles are stronger than those reflected by particles, the particles signals can be easily eliminated from the recorded data at an ultrasonic wavelength of 2 MHz. Therefore, the bubble-rising velocity distributions are easily obtained. However, the bubble data must be eliminated from the measured data at 8 MHz in order to calculate the liquid velocity distribution. If the signal at 8 MHz includes echo signals reflected by the bubble, the signal can be recorded at 2 MHz as well. Based on this concept, it is possible to obtain only liquid data using an 8-MHz signal.

Fig. 4 shows a schematic diagram of the measurement of the two-phase bubbly flow using a multi-wave TDX. Ultrasonic measuring volumes of 2-MHz and 8-MHz signals are overlapped in the test section. If the echo signals reflected by the particles are eliminated from the measured signals of a 2-MHz beam, the bubble and particle positions can be divided into three patterns. Based on the presence of the particles and bubbles, a combination of the echo signals at 2 MHz and 8 MHz can be divided into 3 groups. These combinations are as follows: Pattern A—echo signals appear at 2 MHz and no echo signal appear at 8 MHz; Pattern B—echo signals appear at both ultrasonic wavelengths; Pattern C—no echo signal at 2 MHz and echo signals appear at 8 MHz. Based on the signal

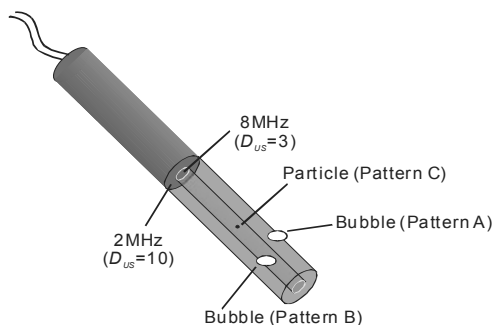


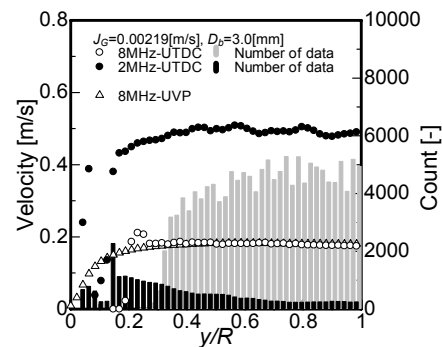
Figure 4: Schematic diagram of two-phase flow measurement using the multi-wave TDX.

setting, the bubble and liquid velocity distributions can be divided. Bubble-rising velocities are obtained using the echo signals recorded at 2 MHz that yield Pattern A and B. On the other hand, by subtracting the data for Pattern B from the recorded signals at 8 MHz, liquid velocity distributions are obtained.

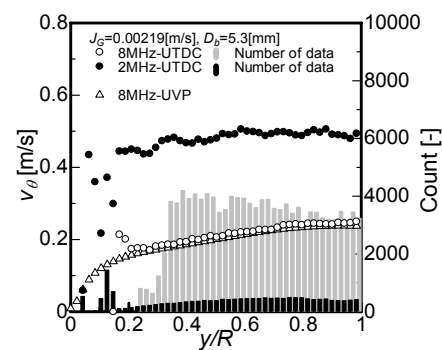
## 4 EXPERIMENTAL RESULTS

### 4.1 Measurement of Bubbly Flow

Figs. 5 show the measurement results at  $J_G=0.00219$  m/s and  $Re_m=8,000$ . The results of the liquid velocity distribution are compared with the data measured using the UVP monitor. The circles represent the distributions measured using the UTDC. The black and gray bars represent the data of the 2-MHz and 8-MHz ultrasonic wavelengths measured in each channel position. It can be clearly seen that the data distributions are affected by the void-fraction distributions. When the void fraction is small, the data of the bubble-rising velocity is extremely low. Since the data was not sufficient for calculating the bubble-rising velocity, the time average gas velocity distribution fluctuates. On the other hand, the data for the liquid velocity is sufficient for the calculation. Since smaller bubbles tended to rise near the wall region, the data acquisition of bubbles the near wall region is larger than that in other areas. On the contrary, the number of data of the liquid is larger when  $y/R > 0.3$ . In general, the calculation of the liquid velocity



(a)  $D_b=3.0$ mm: wall-peak condition



(b)  $D_b=5.3$ mm: core-peak condition

Figure 5: Average liquid and interface velocity distributions in bubbly flow.

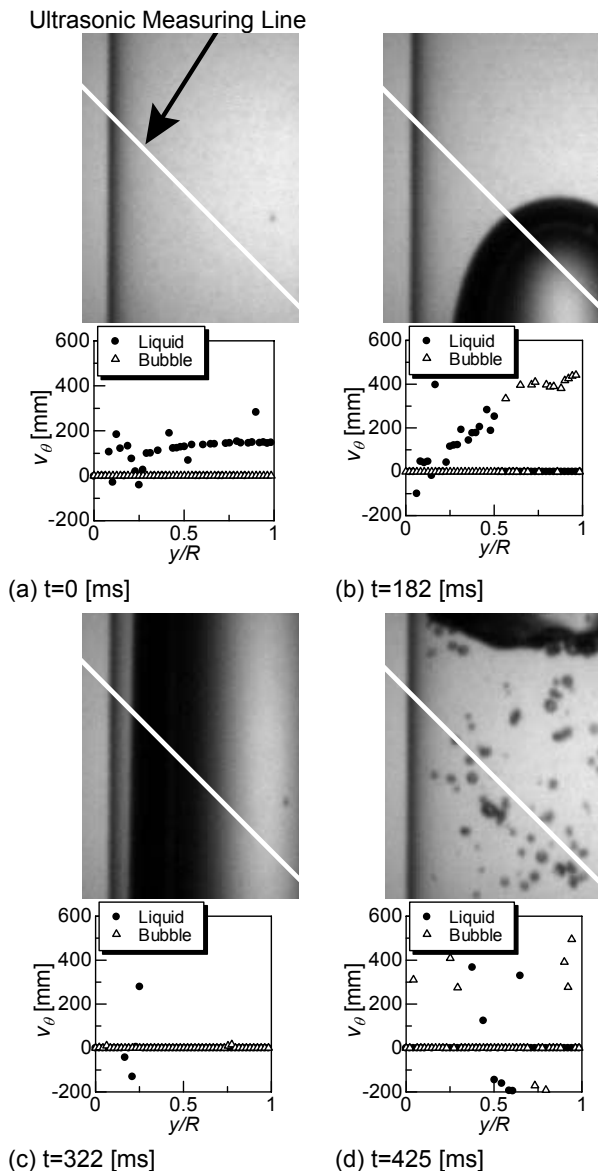


Figure 6: Pictures and velocity distributions of slug flow by using ultrasonic and high-speed camera.

distribution is more difficult than that of the bubble-rising velocity because the echo signals reflected by the particles have less intensity. However, the results of the velocity distributions are in good agreement with that measured using a UVP monitor. The liquid velocity distribution has a larger error particularly near the wall region. This is because some liquid data include the bubble-rising velocity. Furthermore, data on the liquid velocity around the region is insufficient. This implies that the bubble data could not be completely eliminated from the data measured by using the 8-MHz ultrasonic wavelength. It is confirmed that the bubble-rising velocity data varies and that it is larger near the wall region. This is an effect of the beams overlapping the area between the wall region and the ultrasonic measuring volume.  $D_{US}$  of the 2-MHz ultrasonic wavelength is comparatively large. The wider region overlaps with the wall of the test section.

#### 4.2 Measurement of Slug Flow

The results of measuring slug flow are shown in Fig. 6. Simultaneous measurements with high-speed camera and ultrasonic were carried out, in order to synchronize the picture and the measured velocity. The figures represent the rising process of a slug bubble under the condition of  $Re_m=4,000$ .

When the time ( $t$ ) is 0, the liquid velocity distribution was obtained by the data of 8-MHz ultrasonic wavelengths. When the slug bubble crosses the ultrasonic measuring line, the liquid velocity is accelerated by the bubble motion. The time resolution obtaining a velocity distribution was set at 1 ms, which is higher than that of UVP. Therefore, the motion of slug bubble could be obtained by using both the ultrasonic and high-speed camera. The interfacial velocity is obtained by the 2-MHz ultrasonic wavelength at  $t=182$ ms. Furthermore, both velocities distributions are completely distinguished. When the bubble rises the ultrasonic measuring line, ultrasonic cannot penetrate the gas phase. Therefore, only the liquid film velocity was obtained. However, the calculation of the cross-correlation has relatively large error, in particular, near wall region. The result might include the error velocity. After the bubble passes the measuring line, complex velocity distributions appear, because the leading bubble induce the wake turbulence. In order to evaluate the accuracy of the measurement, further improvement of the technique is necessary.

#### 5 SUMMARY

The multi-wave method was applied for two-phase flows, *i.e.* bubbly and slug. The developed phase separation technique can detect the liquid-gas interface at a slug bubble. The main advantage of this method is that it enables the simultaneous acquisition of two target velocity distributions at the same position. For further improvement in the measurement accuracy, this method can be applied for the clarifications of the flow structure in the wake region behind a slug bubble, interaction mechanism between the liquid and bubble, and monitoring of a bioreactor.

#### ACKNOWLEDGMENT

The author gratefully acknowledges the financial support by Japan Society for the Promotion of Science for Young Scientists (JSPS Research Fellow).

#### REFERENCES

- [1] Murakawa, H., Kikura, H., Aritomi, M.: Application of ultrasonic Doppler method for bubbly flow measurement using two ultrasonic frequencies, *Exp. Therm. Fluid Sci.*, 29(2005) 843-850.
- [2] Murakawa, H., Kikura, H., Aritomi, M.: Application of Multi-wave TDX for multi-phase flow measurement, 4<sup>th</sup> ISUD, 111-114, Sapporo, Japan(2004).

# A Custom-Designed Ultrasound Echo Particle Image Velocimetry System: Initial Experiments

Lingli Liu, Hairong Zheng, Logan Williams and Jean Hertzberg

Department of Mechanical Engineering, University of Colorado, Boulder, CO.

Craig Lanning and Robin Shandas

Department of Mechanical Engineering, University of Colorado, Boulder, CO; Department of Pediatrics, The Children's Hospital, Denver, CO.

Echo-PIV is a novel contrast-based ultrasonic technique for measuring multi-component velocity vectors in opaque flows. Ultrasound contrast microbubbles are used as flow tracers, and digitally acquired RF-data are converted into B-mode images. A pair of sequential images is cross-correlated to determine particle displacement, using algorithms derived from optical particle image velocimetry (PIV). The resulting data provides temporally and spatially resolved two-dimensional velocity fields of two velocity components. This technique has been successfully implemented using off-the-shelf clinical ultrasonic imaging systems, but such systems currently lack sufficient control and frame rates. A customized system is being developed with extended capabilities. To date, excellent temporal ( $<0.6$  msec) and spatial resolution ( $<0.4$ mm) resolution has been achieved. Both phased-array and mechanically scanned systems are being developed. The system performance parameters and limitations are described. Examples of measurements of velocity fields from several flows including steady and transient vortexes are presented.

**Keywords:** PIV, particle image velocimetry, echo, B-mode, hemodynamics, vascular imaging,

## 1 INTRODUCTION

Non-invasive assessment of cardiovascular hemodynamics is an important part of the comprehensive clinical examination of both adult and pediatric patients. The ability to obtain multi-component blood flow velocity data non-invasively would have a number of immediate benefits. Vascular investigators would be able to compute various shear stress parameters to quantitatively examine factors related to intimal hyperplasia, restenosis after stenting, arteriosclerotic plaque development, venous and arterial thrombus formation, vascular aneurysms, and other disease conditions where shear stress (both within the fluid and along the wall) has been shown to play an important role in amplifying or attenuating a disease process. Cardiologists could more comprehensively characterize flow within the coronary arteries, evaluate shear stress parameters within the atrium and ventricle, quantify diastolic filling more accurately, and measure the multiple components of flow through prosthetic heart valves.

A variety of methods have been examined for measurement of multiple blood velocity components *in vivo*. Magnetic resonance imaging (MRI) velocimetry provides multiple components of velocity with good spatial resolution; however, the method is cumbersome to use since it requires breath-holds, collection of data over multiple cycles for ensemble averaging, and possesses relatively poor temporal resolution [i,ii] Ultrasound Doppler

measurement of local velocity has also been examined [iii,iv]. Although this method provides greater temporal resolution, it is dependent on the angle between the ultrasound beam and the local velocity vector, only provides velocity along the ultrasound beam (1-D velocity), and has difficulty in measuring flow near the blood-wall interface.

The recent development of microbubbles to enhance ultrasound backscatter provides a potential ultrasound-based imaging solution for velocimetry of vascular and other opaque flows. This solution is based on the synthesis of two existing technologies: particle image velocimetry (PIV) and brightness-mode (B-mode) contrast ultrasound echo imaging. We have termed this Echo PIV. Figure 1 illustrates the schematic of the general Echo PIV technique. In the method, B-mode image frames are first obtained by sweeping a focused beam of ultrasound through the desired field of view. The ultrasound beam is scattered by contrast microbubbles, resulting in a clear image of the particle positions. Two sequential image frames are then subjected to PIV analysis: the images are divided into interrogation windows (sub-windows); a cross-correlation is performed on the sub-window images to provide the local displacement of the particles; extension of the cross-correlation to all sub-windows over the entire frame allows the velocity vector field to be determined since the time between images ( $\Delta t$ ) is known.

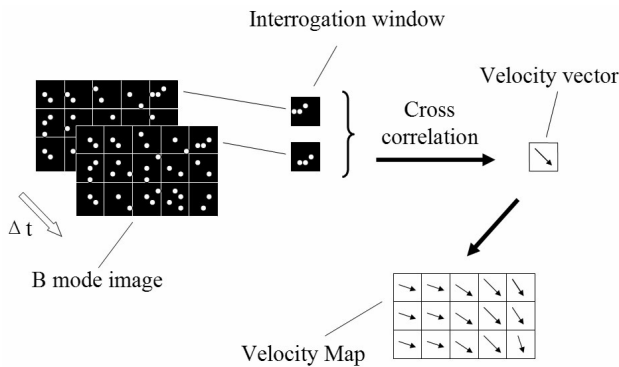


Figure 1: Schematic of the Echo PIV technique

The application of PIV analysis to echo images was first reported by Crapper et al. [v], who used a medical ultrasound scanner to image kaolin particles in a study of sediment-laden flows. PIV algorithms were applied to B-mode video images, and speeds of up to 6 *cm/s* were obtained. Others have used 2D ultrasound speckle velocimetry (USV), a combination of classical ultrasonic Doppler velocimetry and 2D elastography techniques, for flow imaging [vi,vii, viii]. The USV technique can provide velocity vectors by analyzing the acoustic speckle pattern of the flow field, which is seeded with a high concentration of scattering particles. However, this technique is limited by the requirement for extremely fast acquisition systems, heterogeneous signals caused by polydispersed particles, and high noise induced by high concentration of scattering particles. The inherent necessity of very high scatterer particle concentrations in particular, seriously limits the application of USV in hemodynamics measurement in living creatures [ii].

We first implemented Echo PIV algorithms on image data obtained from a commercial clinical ultrasound apparatus [ii]. The maximum achievable frame rate of the commercial system was 500 image frames per second (fps) at reduced imaging window size. Using such frame rates, we were able to raise the measurable maximum velocity 50 *cm/sec*, with axial resolution up to 1.2 *mm* and lateral resolution of 1.7 *mm*. Although these studies were useful in that they showed the potential for Echo PIV, both the velocity range and spatial resolution were insufficient to meet the full range of vascular blood flow imaging requirements.

## 2 NEXT GENERATION SYSTEM DESIGN

Accurate measurements of velocity fields using Echo PIV depend on a number of interdependent parameters, which must be optimized for each application. Our initial target for Echo PIV is peripheral vascular imaging, including blood velocity measurements in vessels such as the carotid, brachial, femoral, popliteal, illiac, aortic, and renal arteries, as well as central and peripheral veins. A rectangular field of view is used, which requires a

linear array transducer (sector images can be used, but coordinate transformations result in a loss of resolution and accuracy). To measure velocity profiles and shear stress accurately, we estimate 20 vectors will need to be measured across the vessel lumen [ix]. Thus, for a 1.0 *cm* vessel, the minimum resolution perpendicular to the vessel would be 0.5 *mm*. This will then dictate transducer firing characteristics such as pulse length, bandwidth, etc.

Considering the key requirements for vascular velocimetry, a custom echo imaging system from the Tetrad Corp. was designed with a 128-element 1D linear ultrasound array transducer, novel control and receiver system, and signal processing. This was then combined with our Matlab-based Echo PIV processing and display software. The linear array transducer has a 7.8 *MHz* center frequency and a 73% fractional bandwidth (6 *dB*), so it can efficiently transmit and receive ultrasound pulses in a 5-10 *MHz* frequency range. The processing system allows flexible control of system parameters, such as the size of imaging widow, focal depth, imaging frequency, beam line density (BLD, detailed later), power level, etc. Besides allowing display of real-time B-mode images, the system also enables separate acquisition of the summed RF signal into a high-resolution (16 bit) data acquisition (DAQ) card (Gage Applied Technologies, Inc., Canada), so that B-mode images can be generated selectively for Echo PIV analysis.

Figure 2 shows the signal collecting and processing procedures for the customized Echo PIV system. First the linear array transducer scans through the field of view by transmitting and receiving ultrasound pulses sequentially. Backscattered ultrasound is then received by transducer elements and turned into voltage signals which undergo amplification, time gain compensation (TGC) and digitization (analog-to-digital conversion). Then the echo voltages (RF data) pass through digital delay lines to accomplish the focusing functions and be summed together to produce the resulting scan line. The data acquisition (DAQ) card saves selected summed RF data, which are then used to generate B-mode images for PIV analysis.

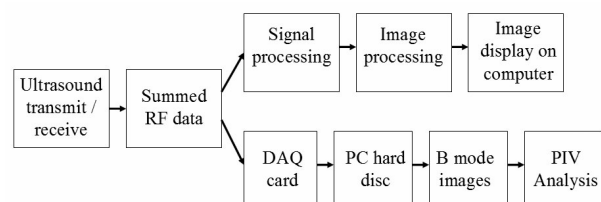


Figure 2: Data path schematic.

Based on the transducer characteristics, the lateral resolution ranges approximately from 0.5 *mm* to 1 *mm*, and the axial resolution is about 0.23 *mm* when

the transducer operates at its center frequency.

The total field of view (FOV) required will be based on how much of the vessel geometry needs to be included within the Echo PIV imaging window. However, the larger the FOV, the longer the image takes to acquire, which then reduces not only the overall time resolution, but significantly impacts the dynamic range (i.e. the range of measurable velocities) as follows. In order to get a successful cross correlation between interrogation windows, the same particles must be in view in both windows. For simple PIV processing algorithms, this requires that the particles move across no more than  $\frac{1}{4}$  of the interrogation window  $[x]$  in the interval between images. Thus,  $\frac{1}{4}t$  dictates the maximum measurable velocity. To avoid this stringent limitation, current optical PIV systems employ window offsetting techniques to move the second window to capture the particle motion, which dramatically extends the dynamic range. However, the results presented here do not employ such techniques, and thus represent a conservative estimate of the system performance.

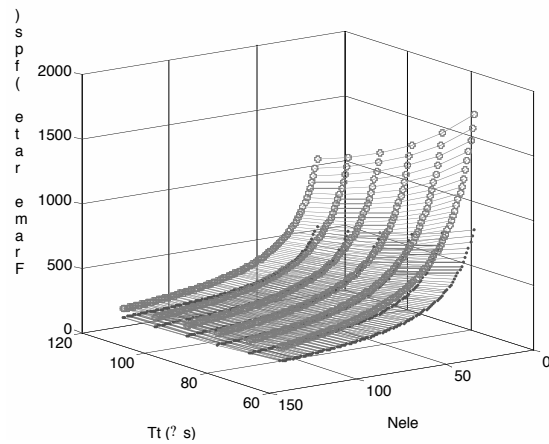


Figure 3: Frame rate as a function of FOV for BLD = 0.5 (red) and 1 (blue).

The maximum frame rate (which is  $1/\frac{1}{4}t$ ) is estimated as follows.  $BLD$  is the number of scan lines generated within one transducer element width ( $W_{ele}$ ) in the B-mode image; options for the custom Echo PIV system are 0.5, 1, 2 and 4. The hardware response time  $T_h$  is the time period between receipt of the most distant echo and transmission of the next beam, and is set by system hardware to be 3  $\mu$ s, which is small compared to the typical ultrasound round-trip time for each beam. The width ( $W_{FOV}$ ) of the FOV is determined by  $W_{ele}$  and the number of activated transducer elements ( $N_{ele}$ ), which ranges from 16 to 128. The length of the FOV is determined by the imaging depth ( $D$ ) required, which ranges from 30 cm to 90 cm. Total

$$FR = \frac{1}{T_f} = \frac{1}{BLD \times T_t \times N_{ele}}$$

where  $T_t$  is the total time per beam and  $c$  is the speed of sound;  $T_t = 2cD + T_h$ . Calculated values

of FR are shown as a function of FOV in Figure 3.

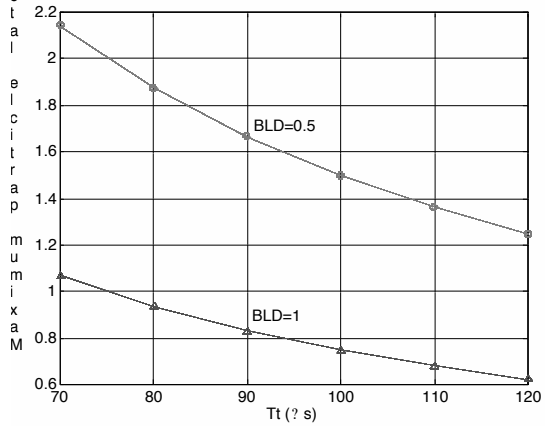


Figure 4: Maximum lateral velocity as a function of image depth.

The maximum frame rate can then be translated into an estimated maximum measurable lateral particle velocity  $V_{lmax}$  by assuming that the entire field of view is used for a single interrogation window, and that particles may convect no farther than  $\frac{1}{4}$  of the window during  $\frac{1}{4}t$ . This case may be useful when a local wall shear stress is of primary interest. Since both the window width and the frame rate are proportional to the number of elements,  $V_{lmax}$  is actually independent of  $N_{ele}$ , and depends only on image depth,  $W_{ele}$  and  $BLD$ :

$$V_{lmax} = \frac{W_{FOV}/4}{T_f} = \frac{W_{ele}}{4 \times BLD \times T_t}$$

Figure 4 illustrates this dependence. However, when multiple adjacent subwindows are used across the width of the image,  $V_{lmax}$  will be reduced by a factor equal to the number of windows.

### 3 INITIAL MEASUREMENTS

Initial measurements using the custom Echo PIV system were made on a steady rotating flow and a transient jet flow. The rotating flow was generated in a thin plastic 55 mm diameter beaker using a

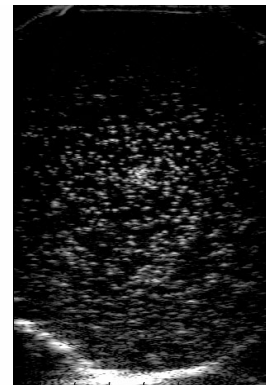


Figure 5: Echo PIV (B-mode) image of dilute contrast agent in a rotating flow.

magnetic stirrer. A 0.012 ml volume of commercially available ultrasound contrast microbubbles, Optison® (Amersham, UK), was injected in the beaker for each measurement. Figure 5 shows one B-mode frame of the microbubbles with a 46 mm focal depth. Figure 6 shows the resultant Echo PIV velocity vector map using an interrogation window size of 3 mm \_ 3 mm with a 60% overlap of windows.

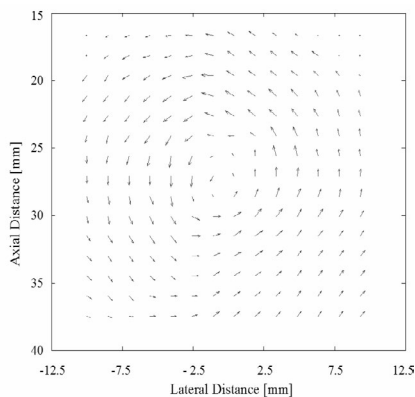


Figure 6: Velocity vectors resulting from Echo PIV processing of the image in Fig. 5.

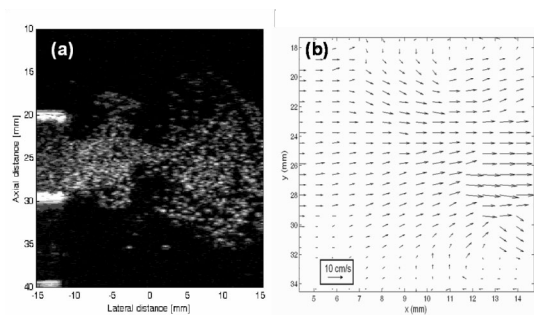


Figure 7: Jet flow measurement using Echo PIV: (a) B-mode particle imaging of the whole flow field; (b) Velocity field of the vortex ring at the head of the jet.

A transient, suddenly started jet, which mimics ventricular filling, was also imaged by Echo PIV (Fig 7). Such a flow is typically difficult to capture using ultrasound Doppler or MRI velocimetry due to the inherently transient nature of the flow, the existence of multi-component velocity vectors and high velocity gradients. Data were obtained at a frame rate of 90 fps using 104 ultrasound beams with focal depth of 24 mm and FOV of 40mm. The sub-window size was 20x20 pixels. Echo PIV provided clear delineation of the velocities in the two vortex rings.

The optimum microbubble concentration was determined by quantitatively evaluating data quality using the cross-correlation index (CCI), which is produced by the cross-correlation function and indicates the effectiveness of the pattern-matching between the two sub-windows. Optimal local bubble concentration was found at  $1\sim 2 \cdot 10^3/\text{ml}$ . This concentration is about 100 times lower than suggested clinical upper limits for conventional

contrast imaging. The CCI can also be used as a real time indicator of optimal bubble concentration during *in vivo* imaging.

#### 4 CONCLUSION

Echo PIV is a promising new non-invasive technique for vascular flow imaging. Estimates spatial resolution and dynamic velocity range were derived based on transducer specifications and controllable system parameters. Successful initial measurements were made in rotating and transient flows.

#### REFERENCES

- [i] Zananiri FV, Jackson PC, Halliwell M, Harris, RA, Hayward JK, Davies ER, Wells PNT (1993): A comparative-study of velocity-measurements in major blood-vessels using magnetic-resonance-imaging and doppler ultrasound, *Brit. J. Radiology*, **66**, pp. 1128-1133.
- [ii] Kim HB, Hertzberg JR, Shandas R. (2004): Development and validation of echo PIV', *Exp. Fluids*, **36**, pp. 455-462.
- [iii] Samijo SK, Willigers JM, Barkhuysen R, Kitslaar, PJEHM, Reneman RS, Brands PJ, Hoeks APG (1998): Wall shear stress in the human common carotid artery as function of age and gender, *Cardio. Res.* **39**, pp. 515-522.
- [iv] Forsberg F, Morvay Z, Rawool NM, Deane CR, Needleman L (2000): Shear rate estimation using a clinical ultrasound scanner, *J. Ultrasound Med.* **19**, pp. 323-327.
- [v] Crapper M, Bruce T, Gouble C (2000): Flow field visualization of sediment-laden flow using ultrasonic imaging, *Dyn. Atm. and Oceans*, **31**, pp. 233-245.
- [vi] Manneville S, Sandrin L, Fink M (2001): Investigating a stretched vortex with ultrafast two-dimensional ultrasonic speckle velocimetry, *Phys. Fluids*, **13**, pp. 1683-1690.
- [vii] Sandrin L, Manneville S, Fink M (2001): Ultrafast two-dimensional ultrasonic speckle velocimetry: A tool in flow imaging, *Appl. Phys. Ltrrs*, **78**, pp. 1155-1157.
- [viii] Gharib M, Beizaie M. (2003): Correlation between negative near-wall shear stress in human aorta and various stages of congestive heart failure, *Annals Biomed. Engr.*, **31**, pp. 678-685
- [ix] Kim HB, Hertzberg JR, Lanning C, Shandas R. (2004): Noninvasive measurement of steady and pulsating velocity profiles and shear rates in arteries using echo PIV: In Vitro validation studies. *Annals Biomed. Engr.*, v 32, n 8, August, 2004, p 1067-1076
- [x] Keane RD, Adrian, RJ (1990): Optimization of Particle Image Velocimeters .1. Double Pulsed Systems, *Meas. Sci. & Tech.*, **1**, pp. 1202-1215

# Ultrasonic Visualization of Thermal Convective Motion in Liquid Gallium Layer

Yuji Tasaka, Masataka Yoshida, Yasushi Takeda

Division of Energy & Environmental System, School of Engineering, Hokkaido University, N13-W8, Kita-ku, Sapporo 060-8628, Japan, E-mail: tasaka@eng.hokudai.ac.jp

Takatoshi Yanagisawa

Institute for Research on Earth Evolution, Japan Agency for Marine-Earth Science & Technology, Yokosuka 237-0061, Japan

For low Prandtl number fluid, which is liquid metal, optical methods cannot be used and we attempted to visualize a convective motion in a liquid gallium layer by measuring a velocity profile in the fluid layer using UVP. Spatio-temporal behavior of a large-scale convective motion in turbulent convection was observed as a temporal variation of the velocity profile. Furthermore, simultaneous 2-axes measurement of instantaneous velocity showed axial motion of the convection roll similar to the wavy motion predicted by a stability analysis of Rayleigh-Bénard convection for low Prandtl number fluid.

**Keywords:** Thermal convection, Liquid metal, Low Prandtl number, Visualization

## 1 INTRODUCTION

Thermal convection induced by a vertical temperature gradient in a shallow fluid layer is one of the fundamental problems in fluid dynamics, thermal engineering and geophysics, but it is not well known for low Prandtl number ( $Pr$ ) fluids. In a phase diagram constructed by Krishnamurti [1], it is expected that the convection of low  $Pr$  fluid easily changes from two-dimensional steady state to turbulent state via three-dimensional state and time dependent state. A temperature measurement of the convection of mercury supports this expectation. On the other hand, Rossby [2] reported that the convection of mercury has a periodic variation of Nusselt number even in the transition state at the phase diagram. Yamanaka *et al.* [3] showed that the variation is induced by a periodic fluctuation of temperature in a fluid layer in their experimental study using liquid gallium. Such periodic phenomenon might be related to a large-scale convective motion in the fluid layer. These studies, however, cannot clarify what type of the convective motion exists because the studies were made only temperature measurement at a point. Almost all studies of low  $Pr$  convection relied on such a temperature measurement because optical visualization cannot be used to observe the convective motion of opaque fluids such as liquid metal. In this study, we attempted to visualize the convective motion of low  $Pr$  fluid by measuring velocity profile in the fluid layer using ultrasonic velocity profiler (UVP).

We measured instantaneous velocity profiles in a rectangular container filled with liquid gallium, which has around 0.03 of  $Pr$ , heated from below and cooled from above. Comparison of temporally averaged velocity profiles measured at a higher or a lower position of the container told us that the

convective motion is similar to two-dimensional roll as a convective motion at extremely low Rayleigh number but the rotation of the roll is not rigid as the two-dimensional roll. A spatio-temporal velocity map represented two different temporal behaviors of the rolls; one is meandering motion with keeping its size and another one is repetition of expansion and contraction. The period of such a convective motion agrees with the temperature variation in the fluid layer measured by a thermistor. Furthermore, simultaneous two-axes measurement of the instantaneous velocity profile clarified the phase delay of the temporal behavior on the roll axis.

## 2 EXPERIMENTAL

### 2.1 Liquid gallium

We used liquid gallium as low  $Pr$  fluid in this study. An advantage of using liquid gallium as working fluid is its safety. It has a lower vapor pressure than mercury and does not react with water like sodium. Table 1 shows physical properties of liquid gallium given by Brito *et al.* [4]

UVP measurement requires suspending Ultrasonic reflection particles in a fluid. We use  $ZrB_2$  fine powder, which has 50  $\mu m$  diameter and 6.17  $kg/m^3$  density. It was also used in other work of UVP measurement of a liquid gallium flow and gave good results [5].

### 2.2 Experimental setup

A container for the liquid gallium layer consists of three parts, the lateral wall, the top plate and the bottom plate. Figure 2 shows a schematic diagram of the container. The container has large aspect ratio, i.e. height  $L$  is 50 mm, width 200 mm ( $= 4L$ ) and depth 50 mm ( $= L$ ). This shape of the fluid layer may be restrictive for a convective flow pattern appearing in the fluid layer. We expected that roll

Table 1 Physical properties of liquid gallium [4], where almost all value is determined at 30 °C, which is slightly larger than melting temperature, ~ 29.0 °C.

	Symbol	Unit	Value
Density	$\rho$	kg/m <sup>3</sup>	6.095
Bulk modulus	$\beta$	K <sup>-1</sup>	1.26×10 <sup>-4</sup>
Thermal diffusivity	$\kappa$	m <sup>2</sup> /s	1.18×10 <sup>-5</sup>
Kinematic viscosity	$\nu$	m <sup>2</sup> /s	3.22×10 <sup>-7</sup>
Prandtl number	$Pr$		0.025
Acoustic impedance	$Z$	kg/(m <sup>2</sup> s)	17.4×10 <sup>6</sup>

pattern would appear with a rotating axis parallel to  $y$  axis. The lateral wall of the container is Pyrex glass, which can be wet with liquid gallium very well. As acoustic impedance of Pyrex glass,  $Z = 13.1 \times 10^6$ , is very close to that of liquid gallium, an ultrasonic pulse passes easily through the lateral wall. Furthermore, faces of the both ends at which US transducer is mounted have smaller thickness, 5 mm, than other faces, 10 mm in order to reduce attenuation of ultrasound. The top and the bottom plates are made of copper and the plates are put together with 25 mm thickness acrylic plate. There is a circular channel with 12 mm diameter at the boundary of the plates. Temperatures of flowing waters in these channels were controlled by thermostatic bathes, AS-One model CH-202 and AS-One model LTB400. These water flows kept surface temperatures at the both plates constant. We kept cooling temperature  $T_1$  at 32 °C, which is higher than the melting temperature of gallium, and varied Rayleigh number in a range of  $R = 200$  to  $800R_c$  by changing heating temperature  $T_2$ , where Rayleigh number  $R$  is defined as

$$R = g\beta(T_2 - T_1)L^3/(\kappa\nu) \quad (1)$$

and  $R_c$  is the critical Rayleigh number of R-B convection in a shallow fluid layer,  $R_c = 1707.7$ .

An ultrasonic transducer was held at an end and normal to the fluid container and Ultrasonic burst emitted by the transducer propagates in the gallium layer parallel to  $x$  direction. The burst has 4 MHz basic frequency and 5 mm effective diameter. Received ultrasonic echo was analysed by UVP, UVP monitor model Duo (Met-Flow S. A.).

### 3 RESULTS AND DISCUSSIONS

#### 3.1 Flow pattern

Since liquid gallium is opaque, it is difficult to make a direct comparison between measured velocity profile and actual convective pattern. We attempt to confirm that UVP can measure convective motion, which has  $O(1)$  mm/s of velocity, in transparent glycerol solution.

Figure 2 shows the results of the measurement for 28 wt % glycerol solution. Fluid layer has 200

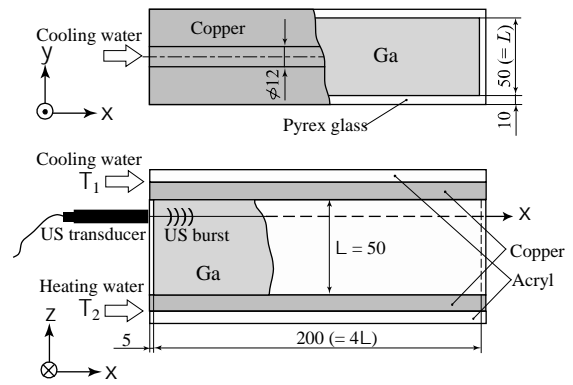


Figure 1: Schematic diagram of the experimental apparatus for the liquid gallium layer, where unit of the scale is mm

mm width, 30 mm depth and 20 mm height. The lateral wall is Plexiglas, and the top and the bottom plate are aluminum and copper. Flowing waters, whose temperature is controlled by a thermostatic bath, keep surface temperatures constant at the top and the bottom boundary of the fluid layer. Rayleigh number determined from the temperatures at the both boundary is around  $800R_c$ . Figure 2 (a) is a temporally averaged velocity profile obtained from 1024 instantaneous profiles, where  $u_x$  represents velocity component on  $x$  axis. Figure 2 shows location of the transducer and illustration of observed convection pattern. As shown in the figure, a formed convection pattern is quasi-two dimensional roll, which has the rotating axis on the vertical direction of the larger lateral wall. Convective motion is unsteady and its size temporally changes, however, the width of the roll has never become larger than the height of the fluid container. Measured velocity varies gently on the measurement direction and alternately has positive and negative value. In comparison with the observed convection pattern, such variation between positive and negative value corresponds to

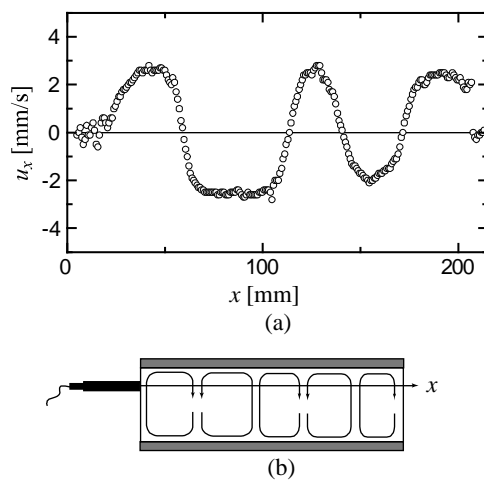


Figure 2: (a) Temporally averaged velocity profile, and (b) Sketch of observed convective motion in glycerol solution

individual motion of the roll. The obtained velocity profile should show flat distribution without boundary between the rolls if the rotation of the roll is similar to the rigid body motion. The obtained velocity, however, contains both a flat profile and a sinusoidal profile, therefore some rolls take rotation being different from a rigid body motion.

Figure 3 shows temporally averaged velocity profiles measured at higher or lower position of the fluid layer, where the horizontal axis  $x$  represents distance from the ultrasonic transducer. Sampling period of the profile is 80 msec and the number of profiles for the averaging is 1024. Spatial resolution on the  $x$  axis is 1.44 mm. Rayleigh number is  $770R_c$  at which convective motion is turbulent.

At a lower position of the fluid layer, velocity varies with two periods on the measurement direction. Magnitude of measured velocity is in the range from 0 to  $\pm 10$  mm/s. At a higher position, velocity also varies oscillatory and a measured velocity profile is approximately symmetrical to that measured at the lower position. Furthermore, range of magnitude of velocity is similar.

We can easily draw a flow pattern from these velocity profiles; there are two pairs of roll arranged parallel to  $y$  direction. This flow pattern agrees with what is expected. At the Rayleigh number,  $R = 770R_c$ , state of convection is turbulence according to the flow régime diagram drawn by Krishnamurti [1]. However, such large-scale convective motion exists stably. The velocity fluctuation should contain small-scale motion but it does not appear on the measured velocity. It is difficult to detect such a motion because convective motion is too slow.

### 3.2 Spatio-temporal behavior

UVP can measure an instantaneous velocity profile, and we can investigate spatio-temporal variation of large-scale convective motion. Figure 4 shows spatio-temporal velocity distributions measured at  $R = 428R_c$  and  $770R_c$ , where the horizontal and the vertical axes are time and position respectively, color code represents velocity value. Black points appearing in the figures "zero" data caused by lack of reflection particle of

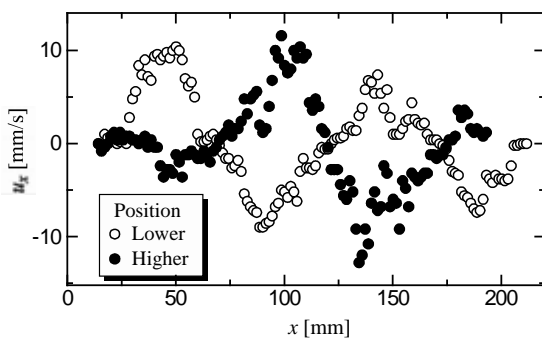


Figure 3: Temporally averaged velocity profile at a lower position or at a higher position, where  $u_x$  represents  $x$ -axial velocity component of the convective motion

ultrasonic burst. A vertical cross section of these figures represents an instantaneous velocity profile and thus we can see two pairs of rolls in these figures. These velocity distributions were measured at a lower position of the fluid layer.

At  $R = 428R_c$ , there are four convection rolls in the fluid layer (Figure 4 (a)), where counter clockwise rotation of a roll is represented by yellow and clockwise rotation by green. The rolls sway slowly as expressed by moving boundary between yellow and green. Small-scale velocity fluctuation, which is expressed as slight color variation in the figures, is superimposed on the large-scale fluctuation. But it is difficult to discuss such small-scale phenomenon because a degree of the small-scale fluctuation is only few times of a velocity resolution of the measurement,  $O(1 \text{ mm/s})$ , and is indistinguishable with noise. A band enclosed by broken line repeats expansion and contraction of the roll with keeping its position on  $x$  axis. This movement is very slow and its period is approximately 60 sec (it corresponds 0.017 Hz on frequency). At higher Rayleigh number,  $R = 770R_c$ , we can see a different type motion of a convection roll (Figure 4 (b)). There are also four rolls, which has the same size with that measured at lower Rayleigh numbers. But enclosed roll moves on the  $x$  axis periodically without changing its size in contrast to the convective motion shown in Figure 4 (a). Furthermore, a motion of neighbouring rolls of the focused roll corresponds to that at lower  $R$ . Convective motion becomes faster than in lower  $R$  and its frequency determined by Fourier analysis is 0.059 Hz. Simultaneous measurement of temperature fluctuation by using a thermistor shows the corresponding frequency on the fluctuation.

Convective motions shown in Figure 4 appear not always at each Rayleigh number, the number of roll and fluctuation pattern of roll are strongly depending

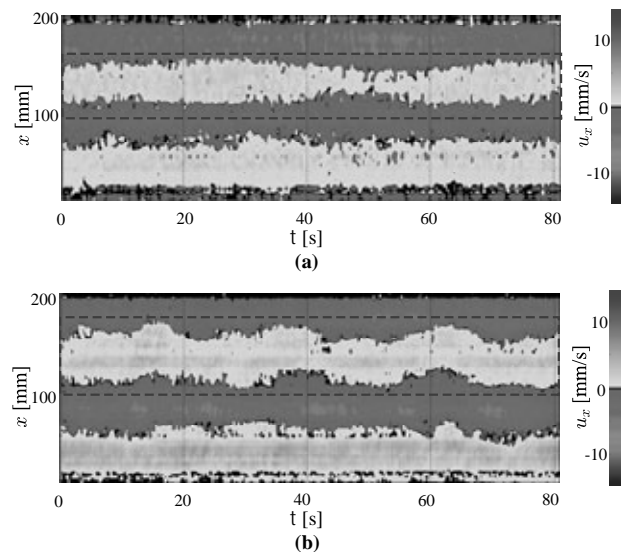


Figure 4: Spatio-temporal velocity profile; (a)  $R = 428R_c$  and (b)  $R = 770R_c$

on initial condition and boundary condition. We confirmed, however, that there are three states of the number of roll, which are 2, 3 and 4. Currently, it is difficult to control the number of rolls.

### 3.3 Axial motion of convection roll

We investigated spatio-temporal behavior of the convection roll on the rotating axis by simultaneous two-axes measurement of the instantaneous velocity profile. The measurement was realized by setting two transducers parallel at the same height of the fluid container. Figure 5 shows the results at  $R = 770R_c$ , where distance between the transducers is 32 mm and the location of each transducer on the  $y$  axis is 16 mm from the center. There are three rolls at the both measurement positions during measurement time and thus three rolls stably exist in the fluid layer. Motion of two rolls near the transducer is similar to the motion in Figure 4 (a), namely, the rolls repeat expansion and contraction with keeping its position on  $x$  axis. In comparison of the motion of the rolls between the figure 5 (a) and the figure 5 (b), there is a phase delay on the temporal variation of the boundary between the rolls and thus the motion of expansion and contraction has phase delay with around half period. Figure 6 shows the model of the motion of convection roll with phase delay.

Axial motion of convection roll in low  $Pr$  fluid was predicted by a stability analysis and figure 7 shows the sketch of the motion in which the bending of the rolls propagates along the roll axis in time. The motion expressed in figure 5 is not such a wavy motion but the propagation of the oscillation on the axial direction is similar to the motion predicted by stability analysis. The motion in this experiment may be strongly restricted by the fluid container that has small aspect ratio. Investigation about how the

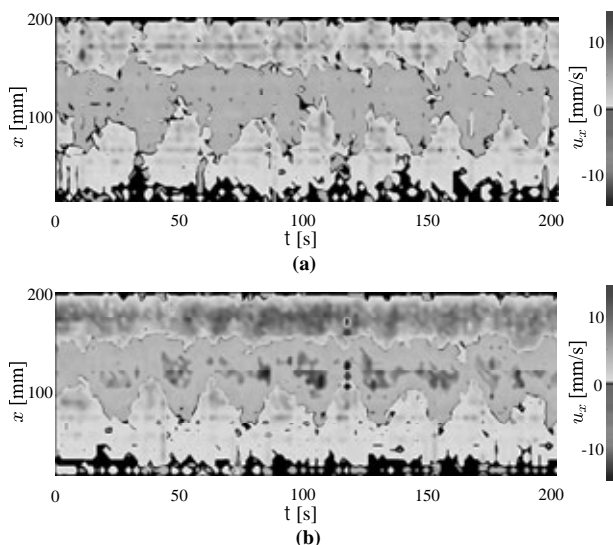


Figure 5: Simultaneous spatio-temporal velocity profiles measured at two different positions on the same horizontal plane

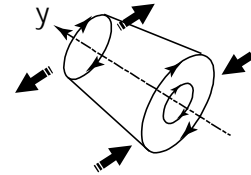


Figure 6: Schematic illustration of motion of a convection roll

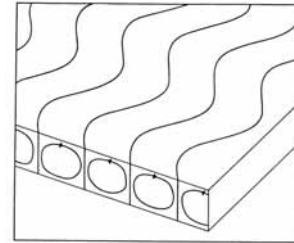


Figure 7: A qualitative sketch of oscillating convection rolls predicted by a stability analysis [6]. The bending of the rolls propagates along the roll axis in time.

convective motion changes in the container with a large aspect ratio is a future work.

## 4 SUMMARY

UVP was used for investigation of large-scale convective motion of low Prandtl number fluid. Liquid gallium container was designed and was constructed to solve wetting problem. Velocity profile measured at lower and higher position of the fluid layer showed convection rolls in the liquid gallium layer. Spatio-temporal velocity field measured by UVP expressed different motions of convection roll, which are repetition of expansion and contraction or periodically meandering motion. Such large-scale motion has been discussed on temperature variation at a point in the fluid layer [3], however, its spatio-temporal behavior has never been discussed on flow pattern until now and were first shown in this study. Simultaneous two-axes measurement of the instantaneous velocity profile clarified the phase delay of the temporal behavior on the roll axis.

## REFERENCES

- [1] Krishnamurti R: On the transition to turbulent convection. Part 2. The transition to time-dependent flow, *J. Fluid Mech.* 42 (1970) 309-320.
- [2] Rossby H.T.: A study of Benard convection with and without rotation, *J. Fluid Mech.* 36 (1969) 309-338.
- [3] Yamanaka Y, et al.: Rayleigh-Bénard oscillatory natural convection of liquid gallium heated from below, *Chemical Eng. J.* 71 (1998) 201-205.
- [4] Brito D, et al.: Experimental study of a geostrophic vortex of gallium in a transverse magnetic field, *Phys. Earth & Planet. Int.* 91 (1995) 77-98.
- [5] Aubert J, et al.: A systematic experimental study of rapidly rotating spherical convection in water and liquid gallium, *Phys. Earth & Planet. Int.* 128 (2001) 51-74.
- [6] Clever R.M., Busse F.H: Transition to time-dependent convection, *J. Fluid Mech.* 65 (1974) 625-645.

## Characteristics of echo signal of pulse ultrasound on boiling two-phase flow

Daisuke Ito, Hiroshige Kikura and Masanori Aritomi

Research Laboratory for Nuclear Reactors, Tokyo Institute of Technology, 2-12-1-N1-13 Ohokayama, Meguro-ku, Tokyo, 152-8550, Japan

Pulse ultrasound technique has been applied to measure the reflected echo signals from vapor bubbles in boiling two-phase flow. In this study, an ultrasonic transducer was developed for the ultrasonic measurement in boiling two-phase flow under the atmospheric pressure. Since the Curie point of piezoelements of the transducer is above 250 °C, it has an allowable temperature limit of 120 °C. The basic frequency of the ultrasonic transducer is 2 MHz and the ultrasonic beam diameter is 10 mm. The measured flow has rising vapor bubbles generated by the cartridge heater. The pulse ultrasound transmitted from an ultrasonic transducer travels into a vessel through the carbon steel wall of 1mm thickness. Echo signals are received by the same transducer. So the delay time and strength of a pulse echo are obtained from this measurement, and the distribution of vapor bubbles is obtained from reflected echo signals. Therefore the effect of boiling phenomena is estimated by the ultrasonic echo distribution.

**Keywords:** Pulse ultrasound, echo signal, boiling two-phase flow, ultrasonic transducer

### 1 INTRODUCTION

Boiling phenomena are observed in a lot of industrial plants such as nuclear plants and have been investigated by many researchers to clarify its flow structure. Conventionally boiling flow measurements have been done by using such techniques as pressure drop and electrical conductivity [1-4]. However many of these techniques are invasive and have a disadvantage of disturbing flow fields. So the non-invasive and more workable techniques for flow measurements and visualization are required. An Ultrasonic Velocity Profile (UVP) monitor [5,6] is an advanced measurement system on fluid flow, and has been successful in fluid flow measurements. The UVP monitor can obtain flow velocity profiles and visualize flow fields. The chief advantage of the UVP method is a non-invasive measurement. UVP measurement requires a sensor with high sensitivity, which can obtain the ultrasonic echo signals including flow velocity information. However the sensitivity of piezoelements of the sensor attenuates with increasing temperature. There are two approaches available to prevent the decrease in sensitivity of the sensor. One is to put a thermal buffer between a sensor and a high temperature fluid in order to keep the sensor temperature low. In addition, cooling the thermal buffer has a more positive effect. However sufficient knowledge on ultrasonic characteristics of a thermal buffer is essential. Eckert et al. [7] developed an integrated sensor which consists of a buffer rod and piezoelements, and measured velocity profiles of liquid metal flow over 200 °C by using the ultrasound Doppler method. Lynnworth et al. [8] have tried to apply the ultrasound to measuring the flow including gas or steam with the temperature up to 600 °C or

liquid with up to 500 °C by using the extensional bundle waveguide. The other is a development of a sensor which can be used at high temperature. It means that the piezoelements with the high Curie point are necessary. This method costs more than thermal buffer method. However it has found a wide range of applications.

The purpose of this study is to measure boiling two-phase flow by using the pulse ultrasound technique. For this purpose, an ultrasonic sensor is developed using the piezoelements with a Curie point above the saturation temperature under the atmospheric pressure. Then by using the sensor, the intensity distributions of the ultrasonic echo signals are obtained in the flow field including bubbles generated by the cartridge heater.

### 2 HIGH-TEMPERATURE SENSOR

To make the ultrasonic measurement of the high temperature fluid flow fields such as a boiling two-phase flow and a liquid metal flow, the Curie point of piezoelements of an ultrasonic sensor for transmitting and receiving ultrasound is significant. Generally the piezoelectric effect of the element may be destroyed if its temperature exceeds the Curie point. A normal sensor for use at room temperature has an operating temperature limit of about 60 °C. So it can not be used at high temperature flow field. As a result, an ultrasonic sensor should be developed for measuring boiling two-phase flow.

#### 2.1 Development of a sensor

Since the ultrasonic transducer developed in this study has an allowable temperature limit of 120 °C, so it can be used in boiling two-phase flow measurement under the atmospheric pressure. The

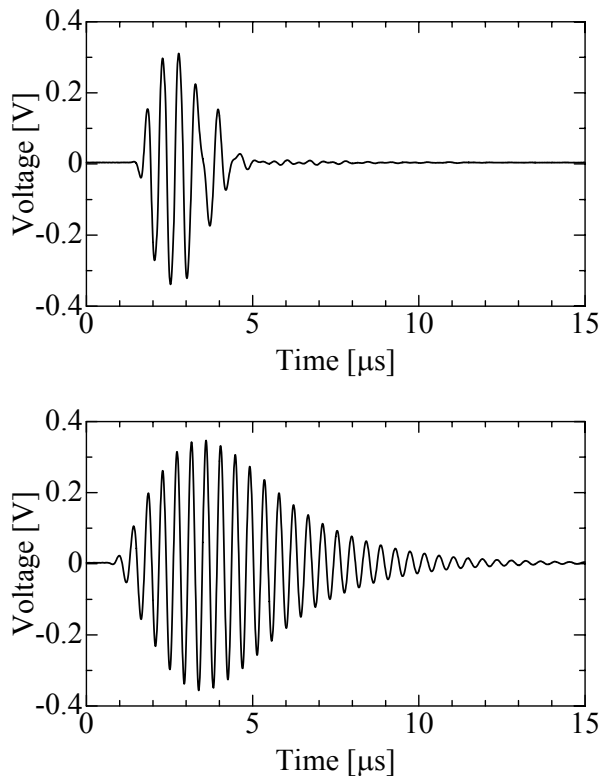


Figure 1: Typical echo signal reflected from a flat plate in water, Upper: Normal transducer, Lower: High-temperature transducer.

piezoelements are 1-3 composite vibrators. The Curie point of this element is above 250°C. The heat resistance of resin surrounding the piezoelement column is taken into consideration. Furthermore, this sensor is fabricated with the operating temperature limit of an adhesive in mind.

## 2.2 Comparison of sensors

The typical echo signals of normal and high temperature transducers are shown in Figure 1, respectively. The basic frequency and beam diameter of each transducer are 2 MHz and 10 mm, respectively. These signals are measured in water of 23 °C and reflected from a flat steel plate. An output pulse wave from a pulser has two bursts. In the signal of a normal transducer, a clear burst wave is obtained. Two reflected signals compared, the echo signal of a high temperature transducer is widely trailed and wave number increases as shown in Figure 1. This shows that there is a significant decrease in the sensor sensitivity.

## 3 EXPERIMENTAL SET-UP AND METHOD

### 3.1 Experimental set-up

Figure 2 shows a schematic diagram of the experimental set-up. A rectangular vessel has a size of 80×80×200 mm and made of carbon steel. Tap water is filled in the vessel, and a cylindrical cartridge heater, which is made of stainless steel, is inserted into the middle of the bottom. The heater has a diameter of 9.4 mm and a length of 100 mm.

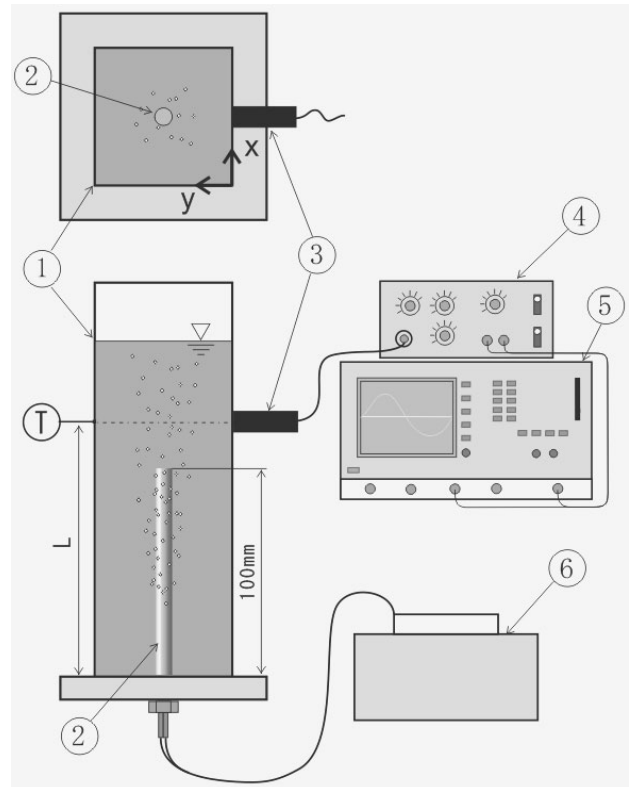


Figure 2: Schematic diagram of experimental set-up; 1. Vessel, 2. Heater, 3. Ultrasonic transducer, 4. Pulser/receiver, 5. Digital oscilloscope, 6. Slidax.

Table 1: Specifications of ultrasound and pulser/receiver.

Basic frequency	2 MHz
Beam diameter	10 mm
Pulse width	1.0 μs
Burst per pulse	2 burst
Input voltage	300 V
Pulse repetition frequency	2 kHz
Gain	32 dB
High pass filter	1 MHz
Low pass filter	2.25 MHz

The ultrasonic transducer is attached to the side surface of the vessel. The ultrasonic couplant (50A4084: Staveley Sensors Inc.) is filled between the transducer and the vessel wall surface for transferring the ultrasound into the vessel. This couplant, which is designed for high temperatures, provides the high coupling efficiency and can transmit an ultrasound at the temperature up to about 350 °C. The distance from the bottom to the central axis of the transducer is L [mm]. The coordinate system of the top surface of the vessel seen from above is represented by x [mm] and y [mm] as shown in Figure 2.

### 3.2 Experimental method

A pulse wave sent from a Pulser/receiver (TB-1000: Matec Inc.) is emitted by an ultrasonic transducer

into the vessel through the wall, which is made of 1 mm thick carbon steel plate. The echo signal of pulse ultrasound reflected from vapor bubbles or the vessel wall is received by the same transducer. The waveform of echo signals is loaded on the digital oscilloscope (C547AL: LeCroy Corp.). The specifications of the ultrasound and the pulser/receiver are shown in Table 1. The ultrasonic basic frequency of the high temperature transducer is 2 MHz, and the beam diameter is 10mm. The pulse repetition frequency is 2 kHz because it should be fast enough to understand the boiling phenomena. The sound velocity in water at 95 °C is about 1540 m/s.

The temperature of the vessel was measured by a thermocouple. During the ultrasonic measurement, the temperature of the outer surface of the vessel was about 92 °C, which can be thought to be the temperature of the transducer itself.

#### 4 RESULTS AND DISCUSSION

Figure 3 shows the ultrasonic echo signals reflected from the boiling flow field. The horizontal axis is the distance from the transducer,  $y$ , and the vertical axis is the detected voltage. The position of the transducer is  $L=120$  mm and  $x=40$  mm. The

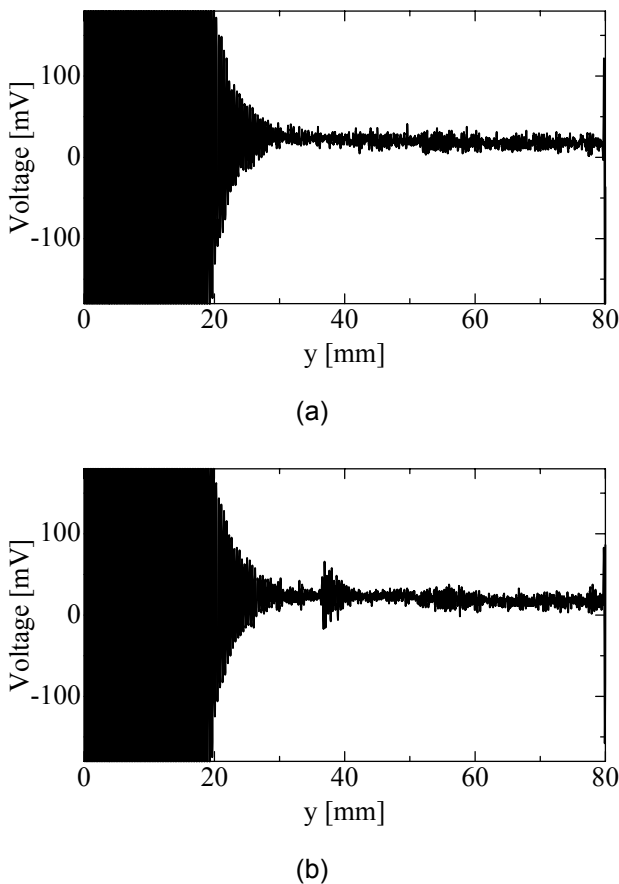


Figure 3: Typical echo signals from the boiling two-phase flow field at  $L=120$ mm,  $x=40$ mm, (a) Flow field has no bubbles inside ultrasonic beam, (b) Flow field has a bubble around  $y=40$ mm.

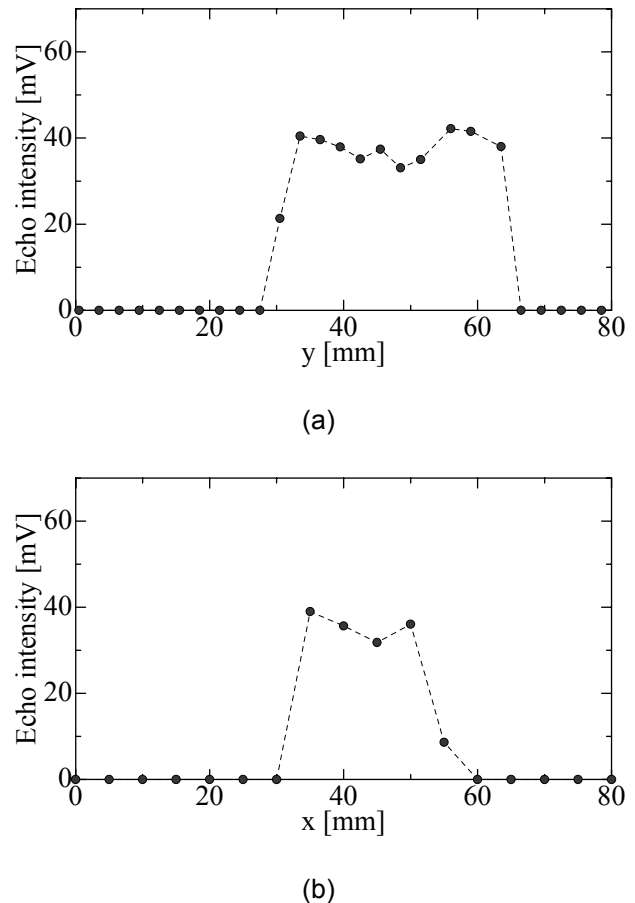


Figure 4: Averaged distribution of echo intensity from boiling flow field at  $L=120$ mm, (a) distribution on  $y$  axis,  $x=40$ , (b) distribution on  $x$  axis,  $y=40$ .

ultrasonic beam travels above the heater. Figure 3(a) and 3(b) show the echo signals which involve no bubbles and a bubble inside an ultrasonic beam, respectively. These figures indicate that the echo signals from bubbles cannot be obtained over 20 mm away from the transducer, because of the ringing of pulse waves inside the vessel wall. In Figure 3(a), there are no visible signals from bubbles. In Figure 3(b), however, it is found that the echo signal reflected from vapor bubbles appears around 40 mm.

Because the position estimated from the delay time of the echo signals from a bubble is equal to the position of the bubble, the strength of the echo signals and the bubble position can provide the distribution of bubbles passing through the ultrasonic beam. The strength is defined as an echo intensity which is a peak to peak value of detected voltage at a certain position. Figure 4 shows the distribution of the echo intensity from the boiling flow. These distributions were cleared off the standing wave and averaged by time series for about 3 seconds. The horizontal axis means the position of the reflection along the ultrasonic beam in Figure 4(a) or the position of the transducer in Figure 4(b) and the vertical axis means the average value of the

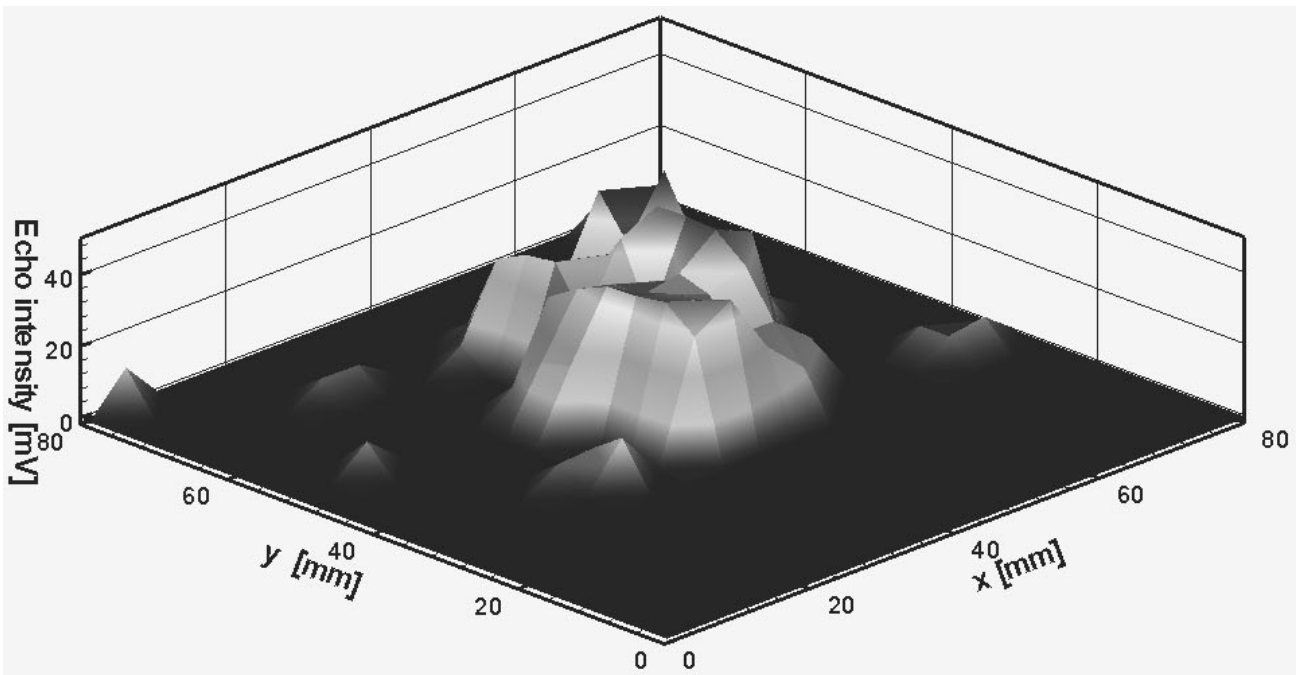


Figure 5: Cross-sectional distribution of echo intensity reflected from boiling flow field at  $L = 120$  mm.

echo intensities. Figure 4(a) shows an echo distribution along the ultrasonic beam direction at  $x=40$  mm. The echo intensity is stronger around the middle of the vessel. Thus the bubbles rise near the heater at  $L=120$ . The echo intensity distribution, which is measured by laterally traveled transducer on  $x$  axis, at  $y=40$  is shown in Figure 4(b). It is also shown that the echo is obtained in the middle region. The region where the bubbles exist can be given by distributions on the line.

It would appear that the structure of the flow field is easy to understand by using the echo distribution in a cut plane. Figure 5 shows the cross-sectional distribution of the echo intensity at  $L=120$ . The averaged echo intensity at each point is plotted and drawn by the color density. In Figure 5, the vapor bubbles exist only near the upper part of the heater, and the bubble distribution is available to understand the boiling flow structure.

From these results, the flow field of the boiling two-phase flow could be visualized by the reflected echo signal and the cross-sectional distribution of the echo intensities.

## 5 CONCLUSION

An ultrasonic transducer has been developed for the ultrasonic measurement of the boiling two-phase flow under the atmospheric pressure, and the distribution of the echo intensity of rising bubbles generated by a cartridge heater has been obtained. The present work shows that the boiling two-phase flow field has been visualized by using the pulse ultrasound technique.

## REFERENCES

- [1] Kockum H, Jernqvist A: Boiling vertical two-phase flow at sub-atmospheric pressures, *International Journal of Heat and Mass Transfer* 41 (1998) 2909-2924.
- [2] Wen DS, Kenning DBR: Two-phase pressure drop of water during flow boiling in a vertical narrow channel, *Experimental Thermal and Fluid Science* 28 (2004) 131-138.
- [3] Huo X, et al.: Flow boiling and flow regimes in small diameter tube, *Applied Thermal Engineering* 24 (2004) 1225-1239.
- [4] Mayinger F: Two-phase flow and boiling: Insights and understanding through modern noninvasive measuring technique, *Experimental Thermal and Fluid Science* 15 (1997) 141-153.
- [5] Takeda Y: Development of an ultrasound velocity profile monitor, *Nuclear Engineering and Design* 126 (1991) 277-284.
- [6] Takeda Y: Velocity profile measurement by ultrasonic Doppler method, *Experimental Thermal and Fluid Science* 10 (1995) 444-453.
- [7] Eckert S, et al.: Velocity measurements at high temperatures by ultrasound Doppler velocimetry using an acoustic wave guide, *Experiments in Fluids* 35 (2003) 381-388.
- [8] Lynnworth LC, et al.: Extensional bundle waveguide techniques for measuring flow of hot fluids, *IEEE Transactions on ultrasonics, ferroelectrics, and frequency control* 52 (2005) 538-544.

## Velocity Profile of Non-magnetic Fluid and Magnetic Fluid Sloshing

Shin-ichi Yoshida, Kenji Tomita, Andrea Benvenuti, Tatsuo Sawada  
and Masaaki Motozawa

Department of Mechanical Engineering, Keio University  
3-14-1 Hiyoshi, Kohoku-ku, Yokohama 223-8522, Japan

The dynamic behavior of a two-layered fluid in a laterally oscillated rectangular container under a vertical non-uniform magnetic field was studied experimentally and theoretically. The two-layered fluid was formed of water based magnetic fluid and silicone oil. In the experimental approach, the dynamic behavior was studied by measuring the velocity profile of the two-layered fluid using an ultrasound velocity profile measuring technique while varying the vertical magnetic field. In the theoretical approach, analytical results are obtained from nonlinear theory using perturbation method. The effect of the magnetic field on the sloshing of the two-layered fluid was considered.

Keywords: Magnetic Fluid, Sloshing, Ultrasonic Velocity Profile Method, Rectangular Container, Non-uniform Magnetic Field

### 1 INTRODUCTION

A magnetic fluid is a stable colloidal solution of many surfactant-coated ferromagnetic particles in a liquid carrier. When magnetic fluids are used as a work fluid of a fluid mechanical system, it is necessary to know the flow characteristics. However, we cannot measure internal velocity profiles using optical methods because magnetic fluid is opaque.

The Ultrasound Velocity Profile (UVP) method [1-2] is a method of measuring a velocity profile on a line with respect to the velocity component along the ultrasonic beam. This technique has a typical advantage in comparison with ordinary methods. It can be applied to an opaque fluid like a magnetic fluid [3-4].

Several studies have been performed to investigate liquid sloshing [5]. Sawada et al. [6] analyzed sloshing using a magnetic fluid in a rectangular container subject to non-uniform magnetic fields and measured inner velocity profiles using the UVP method. Although these theoretical and experimental studies have been carried out to better understand sloshing, the mechanisms involved in two-layered fluid sloshing with a magnetic fluid remain unclear and inner velocity profiles of such a system have not been measured as yet.

In the present paper, we experimentally measured the displacement of the free surface and the inner velocity profiles of a two-layered fluid sloshing under a non-uniform magnetic field. The test fluid included layers of a water-based magnetic fluid and a silicone oil. The influence of magnetic field on resonant frequency and inner velocity profiles are presented.

### 2 TEST FLUIDS

A water based magnetic fluid (W-40) and a silicone oil (KF-56) are used. W-40 has a 40 % weight concentration of fine magnetic particles and is produced by Taiho Industries Co., Ltd., Japan. Its

sound velocity[6], viscosity and density are  $c = 1440$  m/s,  $\mu = 25$  mPa·s and  $\rho = 1400$  kg/m<sup>3</sup> at 25 °C. A porous SiO<sub>2</sub> powder (MSF-10M, Liquidgas, Co., Ltd.) having grains with an average diameter of about 0.9  $\mu$ m is added to provide reflectors for the ultrasonic waves. KF-56 is produced by Shin-Etsu Chemical, Co., Ltd., Japan. Its sound velocity, viscosity and density are  $c = 1250$  m/s,  $\mu = 15$  mPa·s and  $\rho = 1400$  kg/m<sup>3</sup> at 25 °C. A nylon powder produced by Ono Science Co. Ltd. is added in order to provide reflectors for the ultrasonic waves for KF-56. The average diameter of grains is about 4  $\mu$ m.

### 3 EXPERIMENT

Figure 2 shows the experimental apparatus and Figure 3 shows the test rectangular container. The rectangular container measures 90 mm  $\times$  30 mm  $\times$  380 mm and is made of acrylic resin. The oscillator has a frequency range from 0.8 Hz to 3.5 Hz. The amplitude of oscillation is 1.0 mm for all experiments. Three permanent magnets are used. Their averaged magnetic flux densities are as follows: 16.9 mT, 24.3 mT and 34.6 mT. An ultrasonic transducer is fixed on the side wall of the container in order to measure

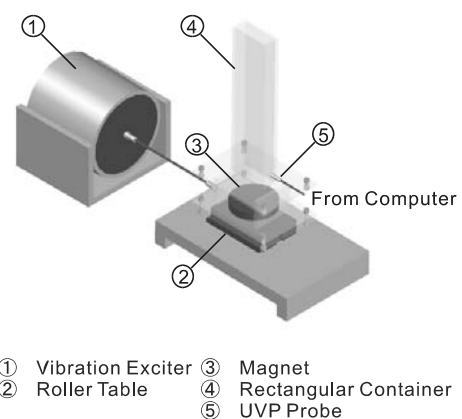


Figure 1: Experimental apparatus

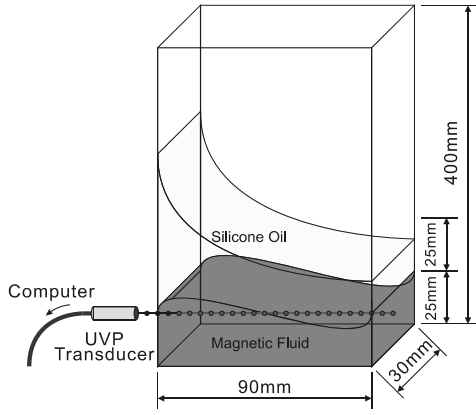


Figure 2: Test container

the horizontal velocity profile. The ultrasonic transducer has an active diameter of 5 mm and the measuring volume is a thin-disc shape element  $\phi 5 \text{ mm} \times 0.71 \text{ mm}$ . The basic frequency is 4 MHz. LabVIEW is used in order to transmit and to receive the ultrasonic pulse wave.

#### 4 THEORY

The flow behavior of sloshing is essentially nonlinear. In particular, forced oscillation clearly shows nonlinear characteristics in its resonance curves. Thus, a nonlinear approach is necessary to investigate velocity fields and high frequency responses of the free surface. Here we deal with an analytical solution for sloshing subject to non-uniform magnetic field using a perturbation method. An analytical model is shown in Figure 4. Here  $x$ -axis is horizontal while  $z$ -axis is measured vertically from the mean position of the free surface.  $L$  is the length of the container and  $\eta$  is the free surface elevation.  $X_0$  and  $\omega$  are the amplitude and forced angular frequency, respectively.

With the assumptions of irrotational flow and an incompressible fluid, a velocity potential  $\phi$  exists which should satisfy the continuity equation:

$$\frac{\partial^2 \phi}{\partial x^2} + \frac{\partial^2 \phi}{\partial z^2} = 0 \quad (1)$$

The unsteady Bernoulli equation is given by

$$\frac{\partial \phi}{\partial t} + \frac{1}{2} \left\{ \left( \frac{\partial \phi}{\partial x} \right)^2 + \left( \frac{\partial \phi}{\partial z} \right)^2 \right\} + \frac{p}{\rho} + gz - \frac{1}{2} \mu_0 \chi_m H^2 = X_0 \omega^2 x \sin \omega t \quad (2)$$

where  $p$ ,  $g$ ,  $\mu_0$ ,  $H$  and  $\chi_m$  are pressure, gravitational acceleration, magnetic permeability of vacuum, magnetic field and susceptibility of a magnetic fluid respectively. The magnetic field  $H$  is approximated by

$$H(z) = H_0 e^{-\alpha(z+h)} \quad (3)$$

where  $H_0$  is the magnetic field intensity at the bottom of the container ( $z = -h$ ) and  $\alpha$  is a constant which is determined by measurement of the

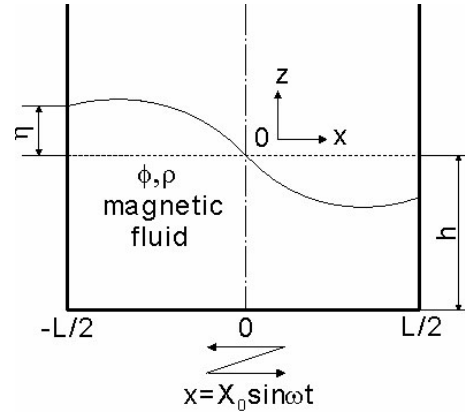


Figure 3: analytical model

magnetic field. The boundary conditions on the bottom and side walls, and the kinematical and dynamical free surface conditions are given by following equations:

$$\left( \frac{\partial \phi}{\partial x} \right)_{x=\pm L/2} = 0 \quad (4)$$

$$\left( \frac{\partial \phi}{\partial z} \right)_{z=-h} = 0 \quad (5)$$

$$\left( \frac{\partial \eta}{\partial t} + \frac{\partial \phi}{\partial x} \frac{\partial \eta}{\partial x} \right)_{z=\eta} = \left( \frac{\partial \phi}{\partial z} \right)_{z=\eta} \quad (6)$$

$$\left[ \frac{\partial^2 \phi}{\partial t^2} + 2 \left( \frac{\partial \phi}{\partial x} \frac{\partial^2 \phi}{\partial x \partial t} + \frac{\partial \phi}{\partial z} \frac{\partial^2 \phi}{\partial z \partial t} \right) + \left\{ \left( \frac{\partial \phi}{\partial x} \right)^2 \frac{\partial^2 \phi}{\partial x^2} + \left( \frac{\partial \phi}{\partial z} \right)^2 \frac{\partial^2 \phi}{\partial z^2} \right\} + 2 \frac{\partial \phi}{\partial x} \frac{\partial \phi}{\partial z} \frac{\partial^2 \phi}{\partial x \partial z} + g_m \frac{\partial \phi}{\partial z} - X_0 \omega^3 x \cos \omega t - X_0 \omega^3 \frac{\partial \phi}{\partial x} \sin \omega t \right]_{z=\eta} = 0 \quad (7)$$

where  $g_m$  is an effective gravity due to the magnetic force and is given by

$$g_m = g + \frac{\alpha \mu_0 \chi_m H_0^2 e^{-\alpha h}}{\rho} \quad (8)$$

Since Eqs. (6) and (7) for the free surface conditions are nonlinear, they are linearized by developing  $\phi$  and  $\eta$  into power series of small parameter  $\varepsilon = (X_0/L)^{1/3}$  up to the third order perturbation. These expressions are written in the following dimensionless forms:

$$\phi^* = \frac{\phi}{L^2 \omega_1} = \varepsilon \phi_1 + \varepsilon^2 \phi_2 + \varepsilon^3 \phi_3 + O(\varepsilon^4) \quad (9)$$

$$\eta^* = \frac{\eta}{L} = \varepsilon \eta_1 + \varepsilon^2 \eta_2 + \varepsilon^3 \eta_3 + O(\varepsilon^4) \quad (10)$$

Where  $\omega_1$  is the first resonant angular frequency obtained by linearized theory and where the function  $O$  represents other perturbation orders. The first resonant frequency  $\omega_1$  is given by

$$\omega_1 = \sqrt{\frac{\pi g_m \tanh \frac{\pi h}{L}}{L}} \quad (11)$$

Space and time variables are also defined in the following dimensionless forms:

$$x^* = \frac{x}{L}, \quad z^* = \frac{z}{L}, \quad t^* = \omega t \quad (12)$$

Since we are interested in the behavior at the vicinity of the resonant point, we write angular frequency  $\omega$  as follows:

$$\frac{\omega}{\omega_1} = 1 + \varepsilon \omega_1^* + \varepsilon^2 \omega_2^* + O(\varepsilon^3) \quad (13)$$

Using the mathematical preparations, Eqs. (6) and (7) are linearized and we obtain the following nonlinear solutions of  $\eta_1$ ,  $\eta_2$  and  $\eta_3$ :

$$\eta_1 = a \sin \pi x^* \sin t^* \quad (14)$$

$$\eta_2 = a^2 A_{22} \cos 2\pi x^* \cos 2t^* \quad (15)$$

$$\begin{aligned} \eta_3 = & a^3 A_{11} \sin \pi x^* \sin t^* - a^3 A_{31} \sin 3\pi x^* \sin t^* \\ & + a^3 A_{13} \sin \pi x^* \sin 3t^* + a^3 A_{33} \sin 3\pi x^* \sin 3t^* \\ & + \frac{2T_H}{\pi} \sin \pi x^* \sin t^* \\ & + \frac{4T_H}{\pi} \sum_{n=2}^{\infty} \frac{(-1)^{n+1} \sin(2n-1)\pi x^*}{(2n-1)^2 \{1 - (\omega_1/\omega_{2n+1})\}^2} \sin t^* \end{aligned} \quad (16)$$

where  $\varepsilon$  satisfies the following equation:

$$R\varepsilon^3 a^3 - \left( \frac{\omega}{\omega_1} - 1 \right) \varepsilon a - \frac{2T_H X_0}{\pi L} = 0 \quad (17)$$

and  $T_H$ ,  $R$  and  $A_{ij}$  are given by

$$T_H = \tanh\left(\frac{\pi h}{L}\right)$$

$$R = \frac{\pi^2}{64} (9T_H^{-4} - 14T_H^{-2} - 3)$$

$$A_{11} = \frac{\pi^2}{64} (3T_H^{-4} - 12T_H^{-2} - 1)$$

$$A_{12} = \frac{\pi^2}{256} (9T_H^{-4} + 54T_H^{-2} - 15)$$

$$A_{22} = \frac{\pi}{8} (3T_H^{-3} - 12T_H^{-1})$$

$$A_{31} = \frac{\pi^2}{256} (27T_H^{-4} + 51T_H^{-2} - 87 - 15T_H^{-2})$$

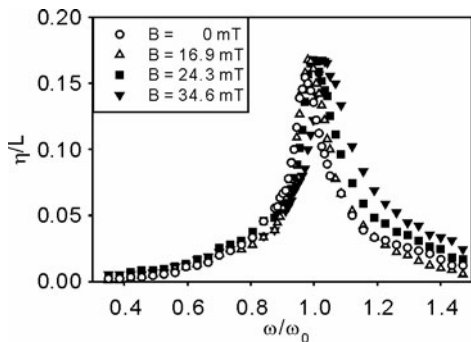


Figure 4: Frequency response of surface elevation of the magnetic fluid

$$A_{31} = \frac{\pi^2}{256} (81T_H^{-6} - 27T_H^{-4} - 27T_H^{-2} - 9)$$

## 5 RESULTS AND DISCUSSIONS

### 5.1 Magnetic Fluid Sloshing

The frequency response of the free surface of magnetic fluid sloshing is shown in Figure 4. The fluid height is 50 mm. Here  $B$  is the surface average magnetic flux density,  $\eta$  is the maximum free surface elevation at the side wall and  $\omega_0$  is the resonant angular frequency obtained experimentally for  $B = 0$  mT. This frequency is  $f = 2.775$  Hz. As the forcing frequency increases, the surface elevation also increases until the free surface is intensively shaken near the resonant frequency. After the resonant frequency, the surface shaking is suppressed. As the magnetic field intensity increases, the first resonant frequency shifts to a higher frequency. For  $B = 34.6$  mT, the first resonant frequency is 2.925 Hz.

In Figure 6 experimental results are compared with the linear and nonlinear theoretical results for  $B = 16.9$  mT. In the low frequency region, the nonlinear solution is larger than the experimental values because calculated amplitude does not become zero with decrease of the frequency. Experimental and nonlinear theoretical results have a good agreement, especially in the high frequency region. UVP measurements were carried out at the first resonant frequency. Figure 6 shows the magnetic field dependent velocity profiles. Here the start phase is the minimum surface elevation time and  $z$

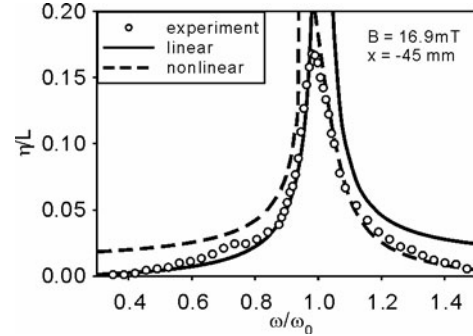


Figure 5: Comparison of theoretical and experimental results for frequency response of surface elevation

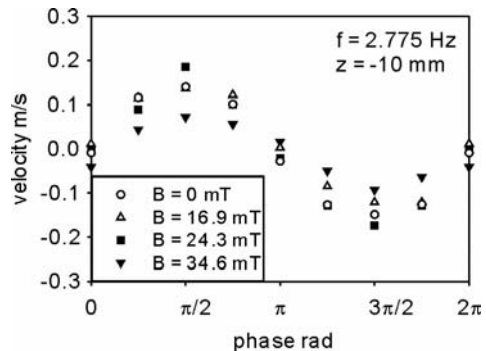


Figure 6: Time dependent velocity profiles of the magnetic fluid at the middle point

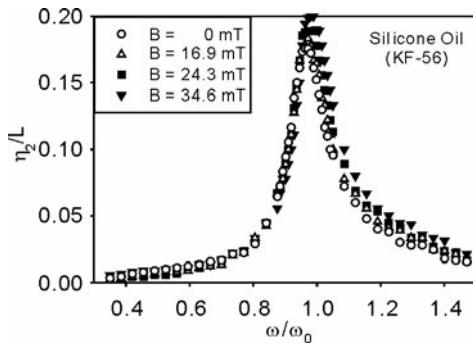


Figure 7: Frequency response of surface elevation for two-layered fluid sloshing

corresponds to the position of the UVP transducer from the static free surface of a magnetic fluid.

### 5.2 Two-layered Fluid Sloshing

The frequency response of the free surface of the two-layered fluid sloshing is shown in Figure 7. The fluid height of each fluid is 25 mm. Here  $\eta_2$  is the maximum free surface elevation of a silicon oil at the side wall. As the forcing frequency increases, the surface elevation also increases until the free surface is intensively shaken near the resonant frequency. This tendency is similar to the result for single magnetic fluid sloshing. After the resonant frequency, the surface shaking is reduced. Similar to the above, the first resonant frequency shifts to a higher frequency as the magnetic field intensity is increased. For  $B = 34.6$  mT, the first resonant frequency is 2.825 Hz. In this case, the rate of change of the resonant frequency and increasing rate of the surface elevation are smaller than those for single magnetic fluid sloshing because the magnetic force is relatively small.

Figure 8 shows the magnetic field dependent velocity profiles of two-layered fluid sloshing. Here  $z_2$  corresponds to the position of the UVP probe from the interface between the two layers. Comparing Figures 6 and 8, there do not appear to be significant differences. The rate of change of the velocity in the two-layered sloshing is slightly smaller. The expected reduction of the inner velocities according to the magnetic field does not occur. In the present experiment, we have used a constant fluid volume ratio, i.e. 1:1. In the future, it will be useful to perform more detailed experiments while changing the arrangement/combination of the two layers.

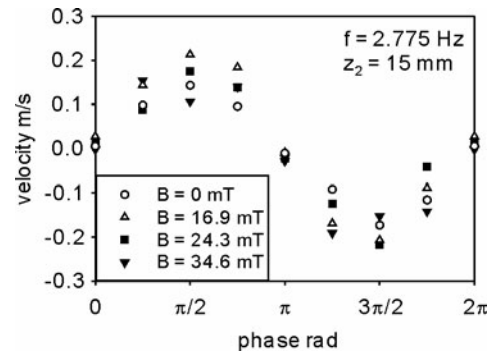


Figure 8: Time dependent velocity profiles for two-layered fluid sloshing

### SUMMARY

Lateral sloshing of a magnetic fluid and a two-layered fluid in a rectangular container in a vertically-applied non-uniform magnetic fields has been investigated. In magnetic fluid sloshing, frequency response of the free surface and the inner velocity profile can be controlled using a magnetic field. In two-layered fluid sloshing, frequency response of the free surface and the inner velocity profile are generally similar to those in a single magnetic fluid. However, there appears to be the possibility for reducing the disturbance of the upper fluid by using magnetic fluid for the lower layer and applying a magnetic field.

### REFERENCES

- [1] Takeda, Y., Velocity profile measurement by ultrasound Doppler shift method, *Int. J. Heat Fluid Flow*, 7 (1986), pp. 313-318.
- [2] Takeda, Y., Velocity profile measurement by ultrasonic Doppler method, *Exp. Therm. Fluid Sci.*, 10 (1995), pp. 444-453.
- [3] Kikura, H., Takeda, Y. and Durst, F., Velocity profile measurement of the Taylor vortex flow of a magnetic fluid using the ultrasonic Doppler method, *Expt. Fluids*, 26 (1999), pp. 208-214.
- [4] Sawada, T., Kikura, H. and Tanahashi, T., Kinematic characteristics of magnetic fluid sloshing in a rectangular container subject to non-uniform magnetic fields, *Expt. Fluids*, 26 (1999), pp. 215-221.
- [5] Handa, K. and Tajima, K., Sloshing of two superposed liquid layers in a rectangular tank, *Trans. Jpn. Soc. Mech. Eng.* 45, B (1979), pp. 1450-1457.
- [6] Motozawa, M., Matsumoto, Y. and Sawada, T., Effect of external magnetic field on ultrasonic propagation velocity in magnetic fluids, *JSME Int. J.*, B, 48, (2006), pp. 471-477.

# UVP Measurement of a Turbulent Channel Flow Containing Large Bubbles

Yuichi Murai, Hideki Fujii, Yuji Tasaka and Yasushi Takeda

Div. Energy & Env. System, School of Engineering, Hokkaido University, 060-8628, Sapporo, Japan

UVP has been applied to measurement of gas-liquid two-phase flow in a horizontal channel. The original data acquired by UVP is transformed by a filter that extracts interfaces of bubbles. The best filter is chosen among several candidates to accurately obtain liquid volume flow rate. Conditional averaging for liquid phase provides valid mean velocity profiles that have been altered significantly by presence of bubbles. The modified flow field by the bubbles involves accelerated region of liquid owing to reduction of skin friction through the bubbles. Whilst local turbulent intensity increases there monotonically with increment of both flow rates, it takes the highest value at the near-wall void fraction of around 2%.

**Keywords:** Multiphase Flow, turbulent flow, drag reduction, bubble dynamics, UVP, interfacial detection, air-film method, channel flow

## 1 INTRODUCTION

Ultrasound velocity profiler (UVP) is applied to measurements of water flow structure in a turbulent channel flow in which cm-order bubbles are mixed. The purpose of this study is originally planned to investigate the mechanism of frictional drag reduction provided by air bubbles. For the same purpose a number of experimental approaches were reported to date, such as by Hotwire, LDV [1], optical probe and PIV [2-3]. In our lab., UVP or ultrasound Doppler-base technique has been newly introduced to the elucidation of the flow structure altered through bubbles. Extension of UVP measurements to bubbly two-phase flow was first reported by Suzuki et al[4]. Their method was based on detection of the local maximum velocity in each instant profile to identify the bubble interface in a counter-current vertical two-phase flow. Eckert et al[5] developed an ultrasound transducer applicable for high temperature liquid metal containing rising bubbles in a bath. They detected velocity of bubbles smaller than the effective beam diameter, referring spatio-temporal diagram of liquid velocity profiles. Murakawa et al[6] reported the use of two ultrasound transducers with different frequencies for capturing the motion of size-dependent bubbles' in a pipe flow. An excellent application of UVP to a pipe flow containing a large buoyant bubble was recently reported by Minagawa et al[7] who obtained average velocity profiles using two ultrasound transducers to measure the average velocity vector field. This paper deals with a method for signal processing of UVP-output to detect the gas-liquid interface without using optical information. This work is positioned as an intermediate but indispensable step on a way to achieve an ultrasound sensing of drag reduction phenomena. Our future application is of a complete monitoring of bubbly two-phase boundary layer only using UVP but not introducing any other tool for the interface detection since this

technique is desired to be applied to ships and pipelines.

## 2 MEASUREMENT METHOD

### 2.1 Target of Flow Measurement

Fully developed turbulent two-phase flow in a horizontal rectangular channel is measured. The schematic is shown in Fig.1. The size of the channel is 40mm in height, 160mm in lateral width, and 6m in length. Tap water and room air are used as two phases. Bubbles are injected through several capillary tubes mounted on the upper surface of the channel. Size of the bubbles ranges from 10mm to 100mm, which is larger than the effective beam diameter of ultrasound. Mean flow velocity varies within  $0.3 < U < 1.5$  m/s, corresponding to Re number of  $1.2$  to  $6.0 \times 10^4$ . Measurement position of UVP is located at 920mm ( $x/H=23$ ) downstream of the bubble injection point. Tracer particles, with density and mean diameter of  $1020$  kg/m<sup>3</sup> and  $200$  μm, are seeded in the water as an ultrasound reflector. We tested the quality of velocity-acquisition, which depends on the number density of the particles and concluded that  $10^7$  per m<sup>3</sup> was sufficient.

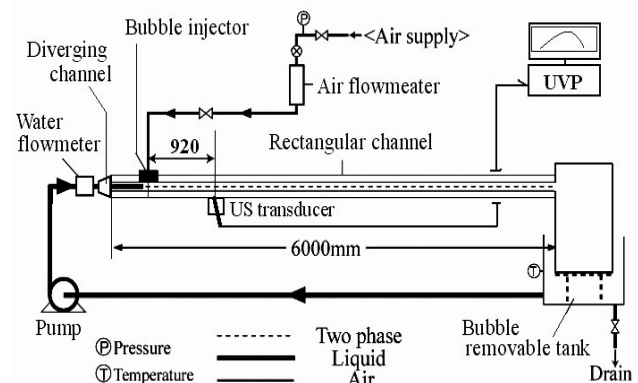


Figure 1: Experimental facility

## 2.2 UVP Specification

Head of an ultrasound transducer is fixed below the bottom channel wall with inclination angle of 5.0 degree. Measurement lines thus is oriented nearly upward to capture the velocity profile as function of the vertical coordinate while bubbles are mainly suspended near the upper wall. The head diameter of the transducer is 5mm. A commercial processor (MetFlow SA, UVP-DUO) is used to control the ultrasound wave and to process the echo signal for acquiring the velocity profile. The transducer emits a pulsed ultrasound with basic frequency of 4MHz and pulse-repetition frequency of 6.6kHz. The sampling rate is 30Hz, which means that the velocity data are output as ensemble averaging of pulse-by-pulse velocity information during 1/30 s, as around 128 shots of pulse.

## 2.3 Spatial Resolution Relative to Bubble Size

Fig.2 shows several samples of bubble images taken from the top of the channel at  $Re=2.8 \times 10^4$ . The picture size is 160mmx160mm. Symbol  $\alpha$  denotes the bulk average void fraction defined by volume flow rates of two phases:  $\alpha = Q_G / (Q_L + Q_G)$ . The bubbles migrate from left to right in the picture. The maximum Weber number;  $We = \rho U^2 d / \sigma$  ( $\rho$ : density of liquid,  $d$ : bubble diameter,  $\sigma$ : surface tension) is  $10^3$  and hence individual bubbles are considerably deformed with the inertia of liquid flow. The thickness of the lateral double lines in the figure stands for the effective beam thickness of UVP, which is estimated at around 7mm, being smaller than the bubble size.

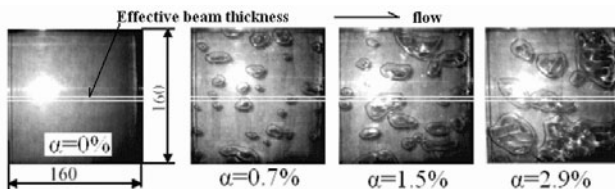


Figure 2: Beam streak and bubbles

## 2.4 Ultrasound Behavior about Interface

Ultrasound mostly reflects on the gas-liquid interface due to the large difference in acoustic impedance. The ultrasound phase is reversed during reflection because of the fixed pressure (here, a small closed interface such as microbubble is an exception because of the strong surface tension). Thus, local standing waves occur within a length of pulsed ultrasound from the interface. Fig.3 shows the wave behavior of pulsed ultrasound as it reflects on the interface, analyzed by a one-dimensional wave equation. The lateral coordinate is time evolution. In the case of a four-cycle pulse that is used in the present UVP, four layers of weak pressure regions come out due to the local standing waves. The particles existing inside these layers do not produce

significant echo that no longer involve regular Doppler information. The internal program of a commercial UVP processor outputs zero-velocity in such a region. The particles existing on peak region of the standing wave has two echoes produced by advancing and returning waves so that the composed wave has no Doppler shift frequency though the individual shift exists. Consequently UVP outputs nearly zero velocity inside the standing wave region regardless the real velocity. Therefore the interface can be detected by finding such a layer out of the data. The thickness of the standing wave in the normal direction to the interface is estimated by

$$\delta = \frac{1}{2} \lambda k \cos \theta \quad (1)$$

where  $\lambda$ ,  $k$ , and  $\theta$  are the wavelength of the ultrasound, the cycle number of single pulse, and the inclination angle of the measurement line. The estimated thickness is about 0.74mm in the case of 4-cycle-pulsed 4MHz-ultrasound.

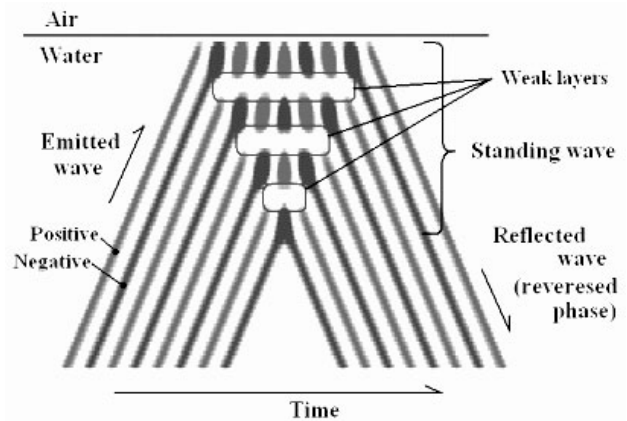


Figure 3: Reflection of pulsed ultrasound on interface

## 2.5 Interface Detection Algorithm

Fig.4 shows a sample of the procedure to detect bubble interfaces. Brightness of each map is a) original velocity measured by UVP, b) a filtered image, and c) resultant interfaces obtained. The filter employed eventually is Sobel filter, which smoothens temporal noise and takes vertical gradient in space simultaneously. The filter well captures the bottom interface of individual bubbles. We examined other types of filters including Laplacian filter, high-pass and band-pass filters to conclude that Sobel filter works the best. The resultant interface is verified by the flow rates measured by flow meters. For instance, the liquid flow rate estimated by integrating the mean velocity profile inside liquid phase matches the flow rate directly measured by a floating type flow meter within 5% error. Note that the applicability of the present method is limited to the case that bubbles have nearly flat bottom interface longer than the beam diameter. The method needs to be improved

when the flow contains small bubbles or high turbulent bubbles.

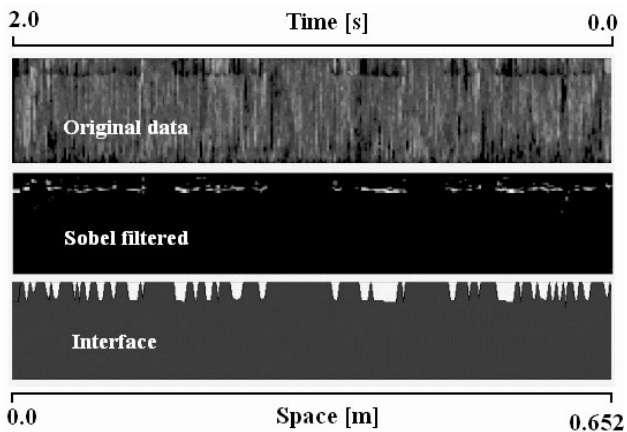


Figure 4: Bubble interfaces detected by Sobel filter

### 3 MEASUREMENT RESULTS

#### 3.1 Mean Profiles of Bubbly Channel

Fig.5 shows comparison of mean profiles, where  $u$ : mean liquid velocity,  $\alpha$ : mean void fraction, and  $q$ : turbulent intensity. The mean liquid velocity is calculated by conditional averaging of velocity inside the liquid, using the interface information. The void fraction is calculated by the ratio of liquid phase to the total sampling period. The bulk void fraction can be calculated by averaging all the profile in the vertical direction and it matched the one given by the two flow meters within 5%. Local void fraction just on the upper wall corresponds to the bubble-covering ratio, to which drag reduction generally works proportionally. The turbulent intensity  $q$  is here defined by the on-beam component fluctuation of velocity. Therefore  $q$  distributes asymmetrically even in the symmetrical single-phase channel flow because of inclined measurement line[8]. The data show that the liquid velocity increases inside the bubbly layer. This is caused by advection effect of bubbles that have finite deformation. The turbulent intensity increases in the border region between the bubbly layer and the outer region, or the high gradient-region of void fraction.

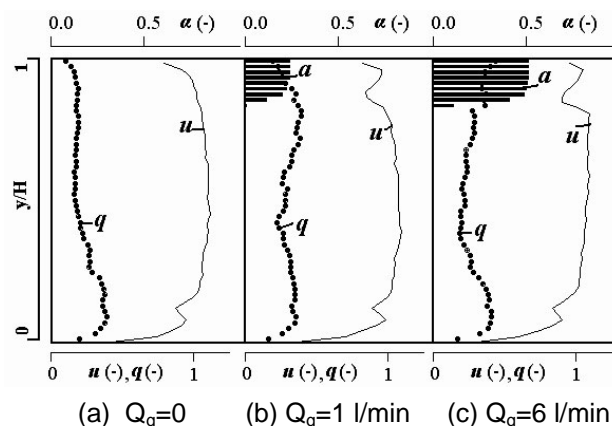


Figure 5: Mean profiles of bubbly channel at  $Re=1.2 \times 10^4$

#### 3.2 Velocity Field Modified by Bubbles

To clearly see the effect of bubbles on the liquid flow structure, the modified component of velocity is extracted by subtracting the mean velocity profile of single-phase turbulent flow. Fig.6 shows those in four different bulk void fractions. White region indicates high-speed parts relative to the mean value. In the single-phase flow ( $\alpha=0$ ), the high-speed parts emerge semi-periodically near the two walls. Such events correspond to momentum mixing in turbulent shear flows, and those distribute symmetrically in the vertical direction. After bubbles are injected, accelerated parts come out in the vicinity of the upper wall. This is caused by the interaction between the bubbles and the boundary layer, that is, the bubbles are driven in the flow direction by the liquid but simultaneously resist against the deformation owing to the surface tension. With this force balance, the bubbles that migrate with keeping their shape provide accelerated layer in the vicinity of the wall. This acceleration promotes the increment of local skin friction while the total skin friction tends to decrease with the bubble-occupying area on the wall. Another finding is also confirmed in the figures, which is propagation of high-speed region from the top to the bottom part. The propagation begins on the rear edge of individual bubbles and advances downward with around 45 degree in space. This implies that the drag reduction effect provided by individual single bubbles alters the flow within a certain spatial/temporal scale.

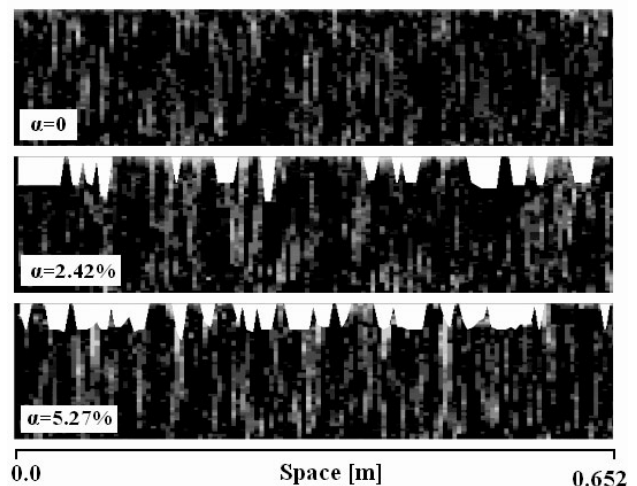


Figure 6: Modified component of velocity at  $Re=1.2 \times 10^4$

#### 3.3 Turbulent Intensity inside Bubbly Layer

Fig.7 shows the turbulent intensity  $q$ , which is averaged inside the bubbly layer. The sampling height of the bubbly layer is fixed at  $0.16H$  according to the void fraction profile. The graph tells us that the turbulence increases with mean velocity (or  $Re$  number) almost monotonically, and also that the mixing of bubbles enhances the turbulence. This

trend is generally inverse to the microbubble drag reduction. Microbubble drag reduction utilizes the suppression of the turbulence inside the boundary layer. The use of bubbles much larger than the turbulent eddy scale makes the turbulence event stronger.

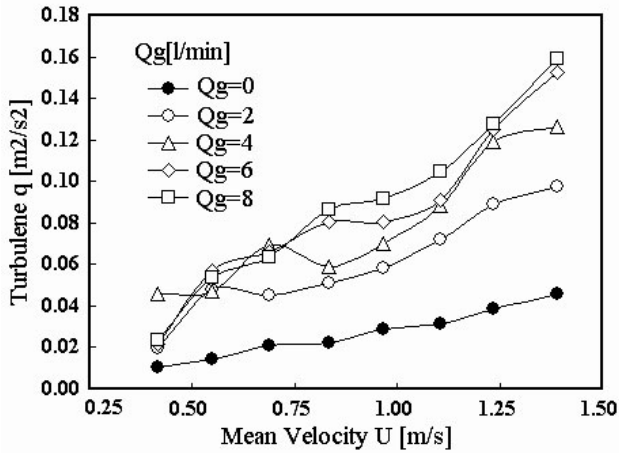


Figure 7: Turbulent intensity inside bubbly layer;  $y/H < 0.16$

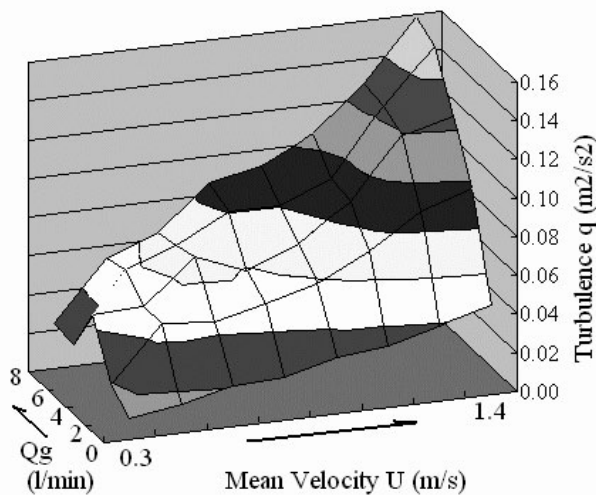


Figure 8: Turbulent intensity inside bubbly layer;  $y/H < 0.16$

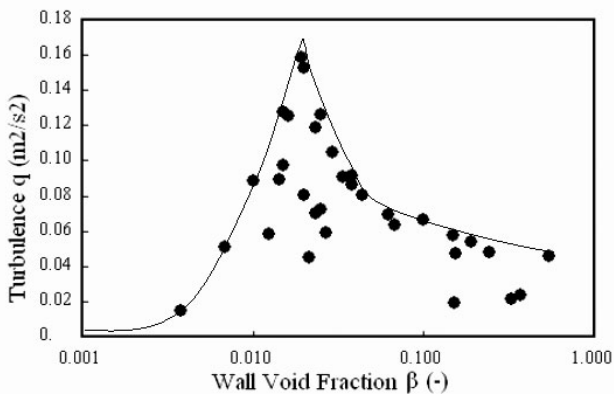


Figure 9: Turbulent intensity versus wall void fraction

Fig.8 shows the same data drawn as function of two flow rates. While the turbulence simply increases

with both flow rates, a new trend is found when it is plotted as a function of wall-void fraction  $\beta$ , as shown in Fig.9. Here  $\beta$  is defined by the local average void fraction inside the bubbly layer;  $y/H < 0.16$ , which is equivalent to the bubble-occupying area ratio on the wall. The plots say that the turbulence takes the highest value around  $\beta = 0.02$ , and decreases when larger area is provided.

#### 4 SUMMARY

UVP has been applied to the measurement of turbulent bubbly channel flows to assess the modification of flow through bubbles. Summarizing the obtained data, the following scenario is deduced on the drag reduction by large bubbles. 1) Bubble-occupation on the wall reduces the total skin friction, and this provides the acceleration of liquid in the vicinity of the wall. 2) Turbulence inside the boundary layer increases with the acceleration. This effect propagates downward to alter the original flow within a certain spatio/temporal scale. 3) With these balance, the turbulence inside the boundary layer gets maximum at around 2% in area-based void fraction on the wall.

#### REFERENCES

- [1] Gabillet C, Colin C, Fabre J: Experimental Study of Bubble Injection in a Turbulent Boundary Layer, *Int. J. Multiphase Flow.* 28 (2002) 553-578.
- [2] Kitagawa A, Hishida K, Kodama Y: Flow Structure of Microbubble-laden Turbulent Channel Flow Measured by PIV Combined with the Shadow Image Technique, *Exp. Fluids.* 38 (2005), 466-475.
- [3] Murai Y, Oishi Y, Takeda Y, Yamamoto F: Turbulent Shear Stress Profiles in a Bubbly Channel Flow Assessed by Particle Tracking Velocimetry, *Exp. Fluids.* *In press* (2006) DOI 10.1007/s00348-006-0142-9
- [4] Suzuki Y, Nakagawa M, Aritomi M, Murakawa H, Kikura H, Mori M: Microstructure of the Flow Field Around a Bubble in Counter-Current Bubbly Flow, *Exp. Thermal Fluids Sci.* 26 (2002) 221-227.
- [5] Eckert S, Gerbeth G, Melnikov VI: Velocity Measurements at High Temperatures by Ultrasound Doppler Velocimetry Using an Acoustic Wave Guide, *Exp. Fluids.* 35 (2005), 381-388.
- [6] Murakawa H, Kikura H, Aritomi M: Application of Ultrasonic Doppler Method for Bubbly Flow Measurement Using Two Ultrasonic Frequencies. *Exp. Thermal Fluids Sci.* 29 (2005) 843-850.
- [7] Minagawa H, Fukuzawa T, Nakazawa Y, Yamada S, Shiomi Y: Measurements of Averaged Liquid Velocity Field Around Large Bubbles Using UVP, *Trans. Japan Soc. Mech. Eng.* 72 (2006) 345-352 (in Japanese).
- [8] Taishi T, Kikura H, Aritomi M: Effect of the Measurement Volume in Turbulent Pipe Flow Measurement by the Ultrasonic Velocity Profile Method – Mean Velocity Profile and Reynolds Shear Stress Measurement, *Exp. Fluids.* 32 (2002) 188-196.

## ADV measurements in a flotation tank with bubble containing water

Lennart Jönsson

Dep of Water Resources Engineering, Univ of Lund, Sweden

Univ of Lund, P.O.Box 118, S-221 00 Lund, Sweden. Email: [Lennart.Jonsson@tvrl.lth.se](mailto:Lennart.Jonsson@tvrl.lth.se)

Dissolved Air Flotation (DAF) is a method for separating suspended, microscopic particles in water and wastewater treatment. The basic idea is to generate huge amounts of microscopic bubbles, which should attach to the particles whereby less dense aggregates are obtained, rising to the water surface. The flow structure in a flotation tank is important for the separation efficiency. ADV measurements have been performed in a DAF pilot plant for different hydraulic loads and dispersion flows. The bubbles (volumetric fraction  $< 3-4 \%$ ) constitute a difficult environment for the ADV. Tests were performed to evaluate the ADV application. Direct measurements showed that the acoustic wave velocity was not affected. Velocity directions seemed to be fairly accurate, whereas magnitudes were underestimated. The measurement point seemed to be located very close to the ADV transmitter. Multiscattering of the acoustic waves was important. Mapping of the flow structures showed that three states existed – a low dispersion flow ( $< 4 \%$ ) giving a large rotational flow in the tank, higher dispersion flow and limited hydraulic load ( $< \text{about } 16 \text{ m}^3/\text{h}$ ) caused a stratified flow situation beneficial for the separation and finally a large hydraulic load ( $> 15-20 \text{ m}^3/\text{h}$ ) caused the stratified structure to break down with detrimental effect on the separation.

**Keywords:** Dissolved air flotation, bubbles, flow structure, ADV

### 1 INTRODUCTION

Production of drinking water/process water in water works or the treatment of municipal wastewater involves a very important and central process concerning the separation of suspended, microscopic particles or flocs from the water, for instance generated through biological or chemical treatment but also existing naturally. These particles/flocs have to be separated before the use or the discharge of the water. Dissolved Air Flotation (DAF) is a potentially efficient method for the separation process with a number of advantages compared to the conventional sedimentation technique. The basic idea with DAF is to generate huge amounts of microscopic air bubbles (size of the order of  $50-100 \mu\text{m}$ ), which should attach to the suspended flocs/particles. In this way less dense bubble/floc aggregates are generated, which should rise to the water surface in the flotation tank, where a sludge layer is formed. DAF is a relatively complex process and in order to utilize the full potential of the process a profound knowledge is required of the process and the effect of different factors on the separation ability. Several important basic aspects on the DAF process have been studied by the author, such as the flow structure, appearance and rise velocities of aggregates, separation in relation to particle sizes, bubble characteristics. Thus, it has been shown that the introduction of bubbles to the process strongly affects the flow structure and that this in turn strongly affects the separation efficiency.

Detailed studies and measurements using a laboratory Nortek Acoustic Doppler Velocimeter (ADV) have been performed on a DAF pilot plant, Fig 1 in order to get insight into the detailed characteristics of the flow structure for different hydraulic loadings and different dispersion flow rates. The presence of bubbles (volumetric proportion  $2-4 \%$ ) constitutes a difficult environment for the ADV. Thus some tests were initially performed in order to assess the applicability of the ADV. The paper will discuss the following aspects on the ADV and on DAF

- ADV in bubbly water
- flow structure in the tank
  - \* without bubbles
  - \* with bubbles, internal waves
  - \* with bubbles, stratified conditions, medium hydraulic load and sufficient dispersion flow
  - \* with bubbles, high hydraulic load, breakdown of the stratification.

### 2 DAF PILOT PLANT

The pilot plant, Fig 1, was 1.2 m long, 0.7 m wide, 1.3 m high with a transparent side. The hydraulic load ( $0 - 17 \text{ m}^3/\text{h}$ ) was entered (no particles) to the bottom left into a riser shaft (contact zone) ending a few dm:s below the water surface. Huge amounts of micro bubbles were produced by depressurizing water saturated with air at 5 bar via valves into the

contact zone where the hydraulic load was entered. The dispersion flow rate was about 10 % of the hydraulic load. The hydraulic load together with the bubble flow then entered the separation zone (the main part of the tank), where different flow structures could be obtained. Fig 1 shows the case with a distinct stratified condition with an upper, less dense, bubble-containing layer and bottom layer with more or less clear water. Discharge of (clean) water took place at the bottom via two perforated pipes. The ADV was mounted on a moveable rig on the top of the tank.



Figure 1. The pilot plant with hydraulic load and dispersion flow (bubbles) entering the riser shaft to the left

## ADV PERFORMANCE

In normal circumstances (clean water with few scattering particles) the ADV works very well with the measurement point located 5 cm below the transducer. The ADV functioning is dependent on the behaviour of the acoustic waves (speed and attenuation) in the water. Thus, one might expect that the presence of microscopic air bubbles ( $\approx 50 \mu\text{m}$ , volumetric fraction  $\leq 4 - 5 \text{‰}$ ) would affect wave propagation significantly. A number of tests were performed in order to evaluate the ADV performance in such conditions. In the first place a 10 MHz acoustic receiver was placed 5 cm below the ADV transmitter in bubbly water. A digital oscilloscope was triggered each time an acoustic pulse was emitted and the received pulse could be visualized on the scope together with the time passed. Fig 2 shows an example of the transmitted and the received pulses respectively. The time difference between the two pulses was constant irrespective of the amount of bubbles ( $\leq$  about 4 – 5 ‰) corresponding to a wave velocity of 1470 m/s, i.e. the same as for pure water. Theory [1] confirms this finding using relevant data – number of bubbles/unit volume of water  $\approx 6.4 \cdot 10^{10}$ , bubble radius  $\approx 25 \cdot 10^{-6}$  m, acoustic frequency  $f = 10^7$  Hz.

The wave speed is thus obviously not affected by the bubbles.

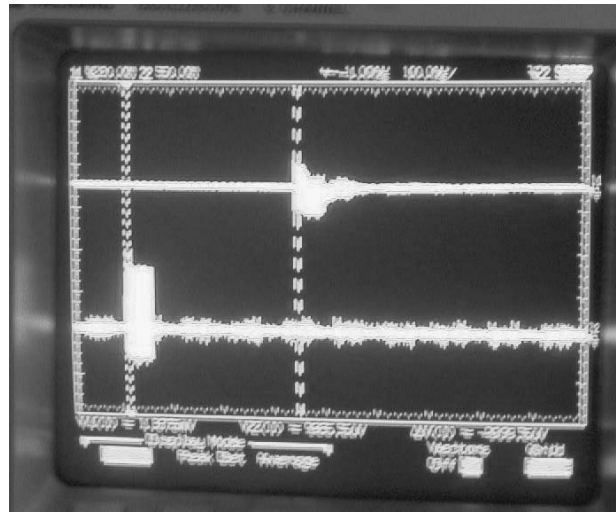


Figure 2. Direct measurement of the wave speed.

Another test was performed with the rig and the ADV moved horizontally about 30 cm at a fairly constant speed along the pilot plant with the ADV immersed into the bubbly water. The output from the ADV was recorded giving movement time and the ADV-recorded mean velocity. This latter velocity was corrected for the slow, horizontal water velocity and comparison could then be made with the rig velocity. A clear water test showed that there was almost no difference between the two velocities, for instance:  $A_{\text{rig}} = 10.86 \text{ cm/s}$ ,  $A_{\text{ADV}} = 10.42 \text{ cm/s}$ . Tests with bubbly water showed significant differences, for instance:  $A_{\text{rig}} = 9.51 \text{ cm/s}$ ,  $A_{\text{ADV}} = 6.17 \text{ cm/s}$ . A general result was that the ADV velocity was smaller than the rig velocity consistently, with less difference moving the rig upstream as compared to downstream movement.

A number of other tests with the ADV in bubbly water strongly indicated that the measurement point was dislocated to a point much closer to the transmitter. However, the operation of the ADV electronics - gating of the receivers to open only during the expected arrival of a pulse in normal conditions - meant that the acoustic waves could not propagate directly from the transmitter to the receiver horizontally ( $\approx 3 \text{ cm}$ ) but had to propagate about 10 cm. It was also found that the emitted pulses, although attenuated by the bubbles, were scattered in all directions in the neighbourhood of the transmitter. These facts strongly indicate that multiscattering on the bubbles takes place for the acoustic waves propagating from the transmitter to the receiver. Yet fairly good and reasonable velocity signals were obtained with SNS values 45 – 50 dB and correlation coefficients 90 – 98 %. A possible explanation is that the bubbles involved in the multiscattering process move in a very similar way

during the short time for a pulse to propagate from the transmitter to the receiver. This means that the detected Doppler shift is not affected by the multiscattering process, only the first and the last scattering matter. The general conclusion of the ADV performance, based on tests and mapping of the flow structure in the tank, was that the measurement point seemed to be very close to the transmitter and the horizontal velocities were underestimated but that velocity directions seemed to be more or less correct. As the real velocities were small one has to bear in mind that the ADV measured the movement of the bubbles, which were assumed to move with the water flow in the horizontal direction. Vertical ADV velocities were offset by the rise velocity of the bubbles ( $\approx 1$  mm/s).

### 3 FLOW STRUCTURE IN THE FLOTATION TANK

The existence of micro bubbles in the flotation tank has two implications – generation of aggregates and influence on the flow structure. The latter aspect is strongly related to the DAF separation efficiency. Detailed ADV measurements were performed in the pilot plant of the average horizontal ( $v_x$ ) and the vertical ( $v_z$ ) velocities for different hydraulic loads ( $Q_l$ ) and different dispersion flows ( $Q_d$ ) but without particles/flocs in order to study possible flow structures and their characteristics. Flow velocities were mainly in the interval 0 – 2 cm/s (ADV). Averaging time was at least 300 s. The measurements were performed in the longitudinal center plane only. Three significantly different flow structures were identified:

- S1: the case with no bubbles or a sufficiently small  $Q_d$  giving a large, clockwise rotating flow, Fig 3
- S2: the case with sufficiently high  $Q_d$  but sufficiently small  $Q_l$  giving a stratified flow situation, Fig 4
- S3: the case with sufficiently high  $Q_l$  where the stratified flow situation broke down, Fig 6.

Figures 3,4,6 have been produced using a software, which transforms the measurements into a vector plot on a regular x-z grid by means of the krieging technique.

#### 3.1 Flow structure S1

The flow structure in Fig 3 represents the case with  $Q_l = 12$  m<sup>3</sup>/h,  $Q_d = 0$  m<sup>3</sup>/h, i.e. no bubbles. Inflow takes place horizontally to the left at the top 16 cm. Outflow at the bottom. The flow structure could basically, as expected, be described as a large, clockwise eddy encompassing the whole flotation tank. Particles/flocs entering the tank will be transported horizontally to the downstream wall and

then vertically with fairly high velocities to the pipe outlet arrangement on the bottom, i.e. no good separation. The same flow situation will occur for

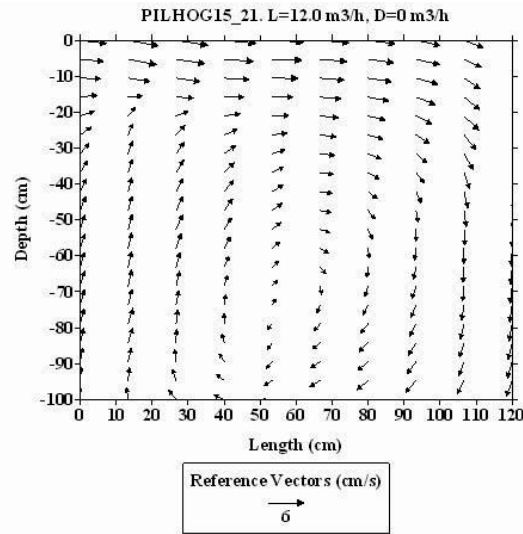


Figure 3. Case S1. ADV-determined flow structure in the pilot plant without any dispersion flow.

small  $Q_d$  (< about 4 % of  $Q_l$ ). A large amount of bubbles will thus also reach the bottom as the vertical downstream velocity is significantly larger than the bubble rise velocities.

#### 3.2 Flow structure S2

The flow structure in Fig 4 represents the case with  $Q_l = 10$  m<sup>3</sup>/h,  $Q_d = 0.98$  m<sup>3</sup>/h, i.e.  $Q_d \approx 10\%$  of  $Q_l$ . Inflow takes place horizontally to the left at the top 35 cm. Increasing  $Q_d$  from 0 to about 4 % of  $Q_l$ , maintaining  $Q_l$  constant, will abruptly change the flow structure from S1 to a stratified situation, S2, according to Fig 4, due to density differences given by different volumetric air contents, Fig 5. There is an upper, bubble-containing, less dense layer, where water moves horizontally towards the downstream wall. After that a horizontal return flow occurs, containing less amount of bubbles. Beneath, a downward, bubble-free, denser plug-like, homogeneous flow with low velocities arises towards the outlet. Such a stratified situation is beneficial for the separation efficiency. Aggregates, particles entering the tank will tend to stay in the upper layers as the vertical, downward velocities are small as compared to S1 where a concentrated, vertical high-velocity region existed. Increasing  $Q_l$  will tend to extend the upper layer downwards, thus causing aggregates, particles and bubbles to approach the outlet arrangement with possible deteriorating separation.

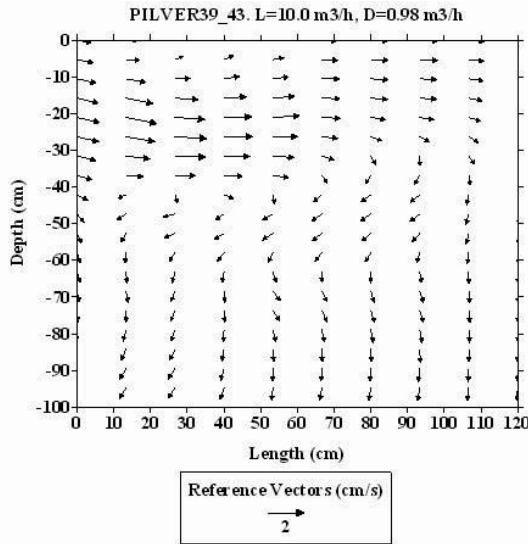


Figure 4. Case S2. ADV-determined flow structure in the pilot plant.  $Q_d \approx 10\%$  of  $Q_l$ ,  $Q_l = 10\text{ m}^3/\text{h}$

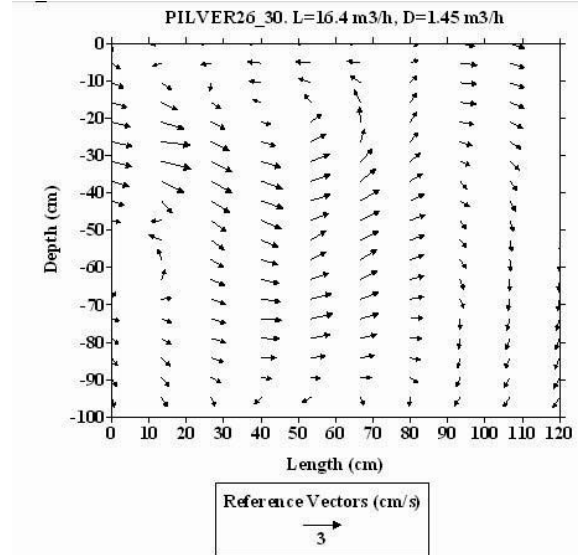


Figure 6. Case S3. ADV-determined flow structure in the pilot plant.  $Q_d \approx 9\%$  of  $Q_l$ ,  $Q_l = 16.4\text{ m}^3/\text{h}$

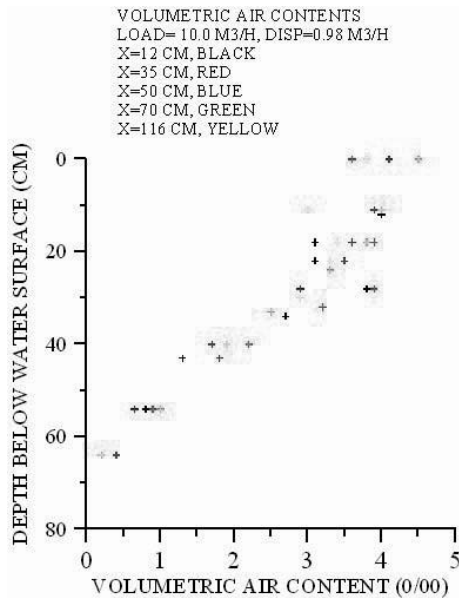


Figure 5. Case S2. Volumetric air contents in different verticals (x) from the riser shaft

### 3.3 Flow structure S3

The flow structure in Fig 6 represents the case with  $Q_l = 16.4\text{ m}^3/\text{h}$  and  $Q_d = 1.45\text{ m}^3/\text{h}$ , i.e.  $Q_d \approx 9\%$  of  $Q_l$ . It is obvious that the stratified structure has broken down and the flow with aggregates, particles and bubbles has a high probability of reaching the bottom outlet thus causing a deteriorating separation. The reason for the breakdown of the stratified structure is not known. It is, however, important to understand the mechanism, as possible measures for maintaining the stratified situation at higher hydraulic loads would be of practical interest.

### 4 SUMMARY

The ADV has been used in micro bubble containing water in a flotation tank, which potentially is a difficult environment for the instrument. However, reasonable velocity data were obtained, at least qualitatively. Direct measurements showed that the acoustic wave velocity was not affected by the bubbles, also confirmed by theory. A number of different tests indicated that velocity directions were fairly correct, whereas velocity magnitudes were underestimated. The measurement point seemed to be located very close to the transmitter. A possible explanation is hypothesized

Three different kinds of flow structures were identified depending on the hydraulic load and/or the dispersion flow. Beneficial stratified flow conditions occurred for hydraulic loads less than about  $16\text{ m}^3/\text{h}$  and dispersion flow rates larger than  $4\%$  of the hydraulic load.

### REFERENCES

[1] Urlick R: Principles of underwater sound. McGraw-Hill (1983), 3<sup>rd</sup> ed. ISBN 0-07-066087-5

# Determination of the flow structure in bubble-driven liquid metal flows using ultrasound Doppler method

Chaojie Zhang, Sven Eckert and Gunter Gerbeth  
MHD Department, Forschungszentrum Rossendorf, 01314 Dresden, Germany

The ultrasound Doppler velocimetry (UDV) was validated for its capability to measure both gas and liquid velocities in transparent as well as opaque two-phase flows. A special threshold method has been tested successfully for processing of UDV data acquired from bubble-driven flows. Our experimental work presented here is focused on the influence of a transverse static magnetic field on a bubble plume in a cylindrical vessel. The liquid flow field has been measured by means of the ultrasound Doppler velocimetry. Despite the well-known damping effect of a DC magnetic field, it was observed, that the application of a moderate magnetic field may also cause an intensification of the liquid recirculation. The global flow field was found to be dominated by quasi-two-dimensional large scale vortex structures, whose axes are parallel aligned with the magnetic field direction. Therefore, the time-averaged flow field shows a distinct anisotropy. Local recirculating zones are found in the meridional plane perpendicular to the magnetic field lines, while velocity distributions become more uniform in the other plane parallel to the magnetic field.

**Keywords:** bubble plume, liquid metal, magnetic field, ultrasound Doppler velocimetry.

## 1 INTRODUCTION

Magnetic fields are widely used to control the melt flow in metallurgical engineering, which directly governs the heat and mass transfer rate and hence the final product quality [1, 2]. Gas bubbles are injected into a bulk liquid metal to drive the liquid into motion, to homogenize the physical and chemical properties of the melt or to refine the melt. For such gas-liquid metal two-phase flows, external magnetic fields might provide a possibility to control the bubble motion in a contact-less way. Well-controlled laboratory experiments equipped with suitable measuring techniques can deliver us a deeper insight into the physical process encountered in real industrial application.

Owing to the induced electromagnetic force, static magnetic fields are known to be suitable for damping mean and turbulent flow in metallic melts. However, several investigations concerning thermal convection in liquid metals revealed to some extent an enhancement of convective heat transfer at moderate DC magnetic fields [3-5]. Measured temperature signals displayed periodical oscillations with large amplitudes indicating that the global flow field becomes time-dependent. Large scale vortex structures were assumed to occur, which are very efficient for the transport of heat. In this paper we present some experimental results obtained from a study of a bubble plume in a cylindrical vessel exposed to a transverse DC magnetic field

Recently, the ultrasound Doppler velocimetry became an attractive non-intrusive measuring technique especially for determining velocity profiles in opaque fluids such as liquid metals [6, 7]. Previous studies have demonstrated its capability in

MHD flow measurements, and especially, in two-phase flows [8 - 11].

## 2 EXPERIMENTAL SET-UP

Figure 1 shows a sketch of the experimental configuration. The eutectic alloy GaInSn was stored in an open cylindrical vessel made of Plexiglas with an inner diameter of 90 mm. The height of the liquid metal bulk is 220 mm leading to an aspect ratio of  $A = H/D = 2.44$ . Argon bubbles were injected through a single nozzle at the center of the container bottom and rise up in a region around the cylinder axis. A mass flow controller (MKS 1359C) was utilised to adjust the gas flow rate in a range between 0.3 and 7 cm<sup>3</sup>/s. Such low gas flow rates were selected to ensure the formation of a dispersed bubbly flow regime.

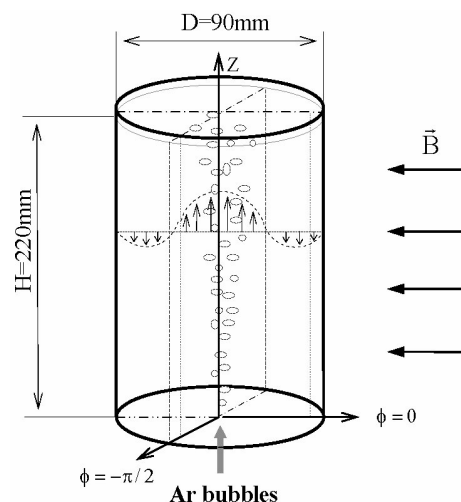


Figure 1: Sketch of the experimental set-up showing the bubble plume driven flow exposed to a transverse static magnetic field

A pair of water-cooled copper coils provides a static transverse magnetic field covering homogeneously the full volume of the liquid metal. The field strength scales with the non-dimensional Hartmann number, indicating the ratio between the electromagnetic force and the viscous force,

$$Ha = BR \sqrt{\frac{\sigma}{\rho\nu}}$$

where  $\sigma$ ,  $\rho$  and  $\nu$  denote the electrical conductivity, the density and the kinematic viscosity of the fluid.  $B$  is the magnetic field strength and  $R$  the radius of the fluid vessel.

The DOP2000 velocimetry (Model 2032, Signal-Processing, Lausanne, Switzerland) equipped with a standard 4 MHz (TR0405LS) has been used to perform the velocity measurements. Both the vertical and radial component of the liquid phase velocities were measured by coupling the transducer at the outer container wall. The transducer position was controlled by a traversing mechanism. The measurements at different spatial positions allowed for a flow mapping in the sense of time averaged velocity field. The scan rate of the consecutive velocity profiles was adjusted to 27.5 Hz by setting a 2370 Hz pulse repetition frequency and 60 bursts per profile. At each position, 6000 velocity profiles were recorded corresponding to a time period of 218 s, which was found to be sufficient for giving reliable time-averaged results. The measuring volume can be considered as a series of discs lined up concentrically along the ultrasound beam, due to the divergence of the beam, the lateral size of the measuring volumes is increasing with the distance from the transducer. In the present measurements, we achieved a spatial resolution of 0.69 mm in axial direction and 10.5 mm in lateral direction at the distance of 100 mm ahead of the transducer. The ultrasound Doppler method has shown its capability to measure simultaneously both liquid and bubble velocities in bubbly flows at low gas flow rates [9]. It is possible to clearly distinguish between the bubble and the liquid velocities in the region of low gas flow rates. In the case of single bubbles the method enables a detailed analysis of the bubble wake structure [10]. Isolated artifacts occur in the velocity signal if the gas flow rate is increased until attaining a bubble chain driven flow. For such flow structure an iterative threshold method was developed to obtain correct profiles of the liquid velocity. A comparison regarding time averaged velocity profiles of the liquid phase delivered by UDV and measurements performed with LDA showed an excellent agreement. A detailed description can be found in [9].

### 3 RESULTS AND DISCUSSION

Since the impact of the DC magnetic field is

anisotropic with respect to the field direction we focus on the flow field in two orthogonal mid-planes being parallel and perpendicular to the magnetic field lines, respectively. The time-averaged flow pattern obtained at a gas flow rate of  $0.33 \text{ cm}^3/\text{s}$  are shown in figure 2 (a) and (b) for the ordinary and the MHD case at  $Ha = 271$ , respectively. The velocity distributions of an ordinary bubble plume are quite analogous in both orthogonal planes. The liquid is driven upward in the central region due to the rising bubbles, whereas a global recirculation with poloidal structures is generated close to the container wall. The flow field becomes anisotropic if the bubble plume is exposed to the magnetic field. Strong vertical structures with axes parallel to the magnetic field lines appear in the plane perpendicular to  $B$ .

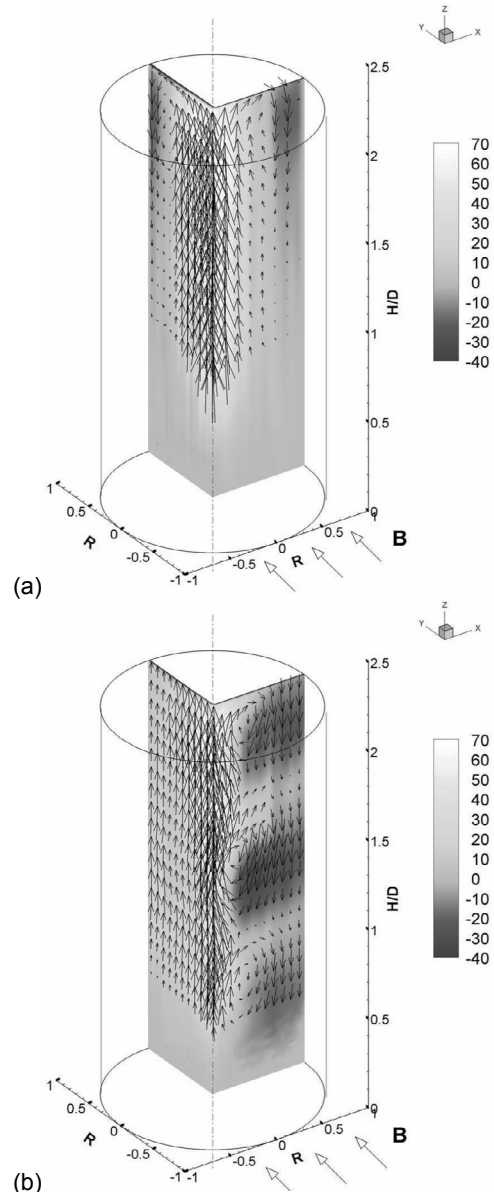
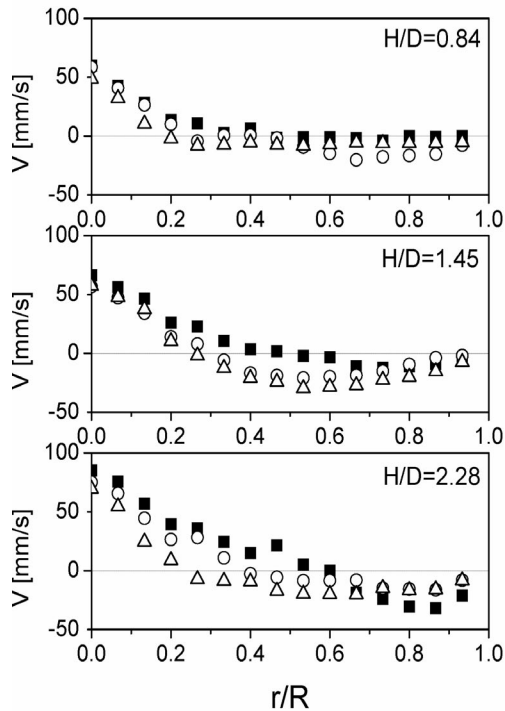


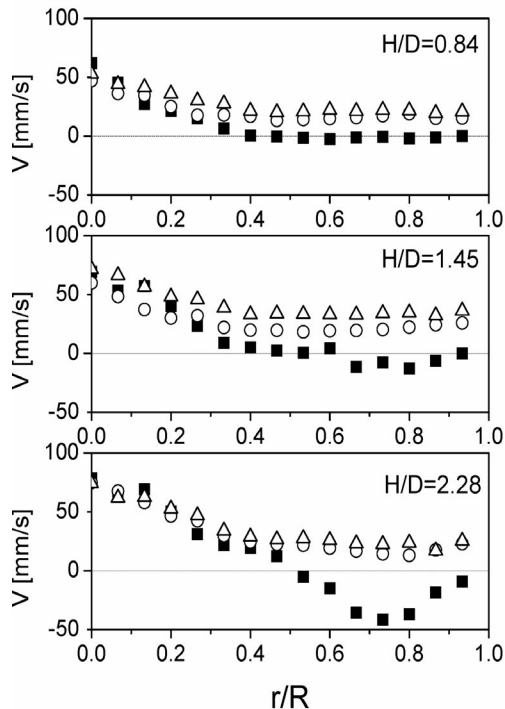
Figure 2: Contour and vector plots showing the vertical velocity and the 2D flow field ( $r$ - $z$ -plane), respectively.

(a)  $B = 0$ ; (b)  $B = 0.16 \text{ T}$ . Positive values correspond to upward flow, and negative values to downward flow. The velocities are in unit of mm/s. ( $Q_g = 0.33 \text{ mm}^3/\text{s}$ )

Generally, the recirculation in the perpendicular plane is amplified and extended over the entire height of the cylinder. In the plane parallel to the magnetic field a suppression of descending and promotion of ascending flow can be observed.



(a)



(b)

Figure 3: Radial distributions of the liquid velocity at different heights and Hartmann numbers, (a) in the plane perpendicular to  $B$ ; (b) in the plane parallel to  $B$ . For both figures (a) and (b) the symbols denote  $_{-}Ha = 0$ ;  $_{-}Ha = 271$ ;  $_{-}Ha = 484$ . ( $Q_g = 0.83 \text{ mm}^3/\text{s}$ )  
Equivalent velocity measurements at higher gas

flow rates revealed qualitatively analogue flow pattern. Figure 3 displays radial distributions of the vertical velocity obtained at several vertical positions. The liquid flow in the ordinary bubble plume can be considered as almost axisymmetric. The rising bubbles generate an ascending flow around the container axis, while the maximum of recirculation occurs at larger radial positions close to the wall closely beneath the free surface. Especially in the lower region of the vessel, an intensification of the descending flow in the perpendicular plane appears with applied magnetic field. In the plane parallel to  $B$  the liquid is solely flowing upwards resulting in a plug-like uniform velocity distribution.

The modification of the flow structures described above is consistent with the theoretical predictions as discussed by Davidson [12] for the case of an axisymmetric jet flow under the influence of a transverse magnetic field. The evolution of the flow structures is governed by the minimization of the Joule dissipation. This is the explanation for the observation, that the cross-sectional area of the jet has been stretched along the field lines direction. The velocity distribution tends to become independent of the coordinate parallel to the magnetic field direction, since the existence of considerable velocity gradients in the field line direction is the reason for the induced current. Finally, the velocity field becomes quasi-two-dimensional.

The redistribution of momentum by the electromagnetic force as described above is responsible for a distinct modification of the transient flow behaviour, too. To illustrate this, the spatial-temporal distribution of the vertical velocity component is displayed in figure 4.

In figure 4, the  $z$ -coordinate is normalized with the total height of the container  $H$  to represent the spatial position, which is plotted along the ordinate. The abscissa of the figure corresponds to the time scale. Each figure is composed of a consecutive series of velocity profiles acquired in a period of two minutes. Compared to the ordinary flow shown in figure 4 (a), the relatively weak magnetic field gives rise to a state of oscillating flow in a large part of the container. The oscillating structure shows a periodicity of about 25 s. In the plane perpendicular to the magnetic field, wave-like flow structures are formed at the free surface. A spot with a strong, i.e. downwards directed, velocity is quasi-periodically moving from the free surface downwards. Reaching approximately the middle of the container it returns abruptly to the surface region. In the lower part of the cylinder between  $z/H = 0$  and 0.2, there appears a layer of enhanced descending flow compared to that of the ordinary case without magnetic field. Qualitatively similar, but inversed flow structures can be found in the plane parallel to  $B$ . Further measurements at various gas flow rates and

magnetic field intensities inclusive detailed description and discussion can be found in [11].

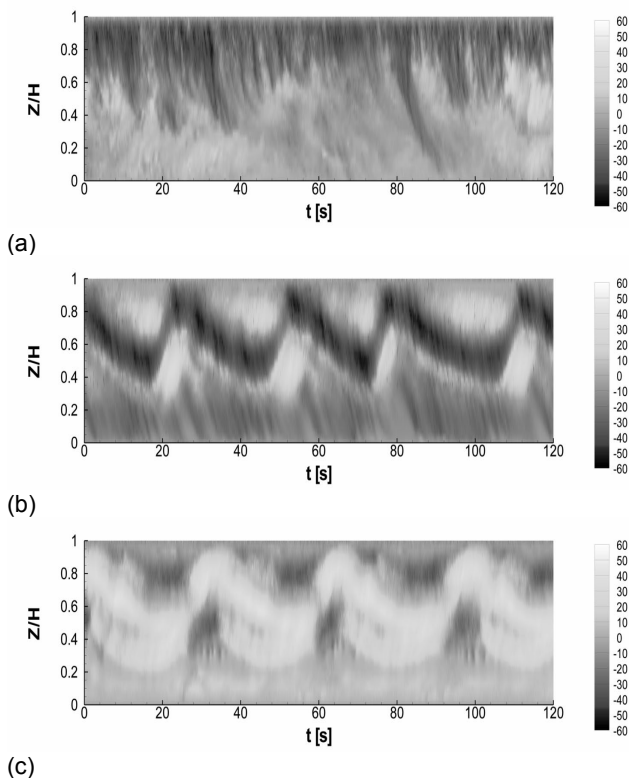


Figure 4: Spatial-temporal distributions of the vertical component of liquid velocity measured at the radial position of  $r/R = 0.87$ , (a)  $Ha = 0$ ; (b)  $Ha = 271$ , in the plane perpendicular to  $B$ ; (c)  $Ha = 271$ , in the plane parallel to  $B$ . For all the figures, the dark colour represents downward flows, bright colour represents upward flows. The velocity values are given in mm/s.

#### 4 SUMMARY

The paper presents an experimental study of the bubble-driven liquid metal flow exposed to a transverse magnetic field. The characterization of the flow field inside the melt was carried out using the ultrasound Doppler technique.

The experimental results reveal the main impact of the magnetic field in a modification of the flow pattern to become anisotropic with respect to the magnetic field direction. The cross section of the bubble-driven jet being circular in the case of an ordinary bubble plume is elongated along the magnetic field direction. This leads to an intensification of descending fluid flow in the plane perpendicular to  $B$  and correspondingly an intensification of ascending flow in the plane parallel to  $B$ . The plug-like velocity profile found in the planes parallel to the field lines are similar compared to the phenomenon of the Hartmann profile occurring in MHD channel flows.

The fluid motion was found to be dominated by large scale structures elongated along the magnetic field direction over the entire chord lengths of the circular

cross section. For moderate Hartmann numbers the vertical position of these vertical structures oscillates. Particularly, even counter-rotating vortices appear. The occurrence of such vertical structures is supposed to explain the intensification of the convective heat transfer as observed in MHD thermal convection [3-5]. At higher Hartmann numbers the motion of the vertical structures will be suppressed, obviously associated with a reduction of the transfer properties.

The two-fold influence of a static magnetic field needs to be taken into account for electromagnetic flow control by DC magnetic fields in industrial processes, for instance the use of an electromagnetic brake for the continuous casting of steel.

#### ACKNOWLEDGEMENT

This work was financially supported by Deutsche Forschungsgemeinschaft in form of the collaborative research centre SFB 609 "Electromagnetic Flow Control in Metallurgy, Crystal Growth and Electrochemistry".

#### REFERENCES

- [1] Szekeley J: Fluid flow Phenomena in Metals Processing, Academic Press, New York (1979).
- [2] Davidson PA: An introduction to magnetohydrodynamics, Cambridge Univ. Press, Cambridge (2001).
- [3] Tagawa T, Ozoe H: Enhanced heat transfer rate measured for natural convection in liquid gallium in a cubical enclosure under a static magnetic field, J. Heat Transfer. 120 (1998) 1027-1032.
- [4] Burr U, Mueller U: Rayleigh-Benard convection in liquid metal layers under the influence of a horizontal magnetic field, J. Fluid Mech. 453 (2002) 345-369.
- [5] Burr U, Barleon P, Jochmann P, Tsinober A: Magnetohydrodynamic convection in a vertical slot with horizontal magnetic field, J. Fluid Mech. 475 (2003) 21-40
- [6] Takeda Y: Measurement of velocity profile of mercury flow by ultrasound Doppler shift method, Nucl Technol. 79 (1987) 120-124.
- [7] Brito D, Nataf H-C, Cardin P, Aubert J, Masson JP: Ultrasonic Doppler velocimetry in liquid gallium, Exp. Fluids 31 (2001), 653-663.
- [8] Eckert S, Gerbeth G: Velocity measurements in liquid sodium by means of ultrasound Doppler velocimetry, Exp Fluids. 32 (2002) 542-546.
- [9] Zhang C, Eckert S, Gerbeth G: Gas and liquid velocity measurements in bubble chain driven two-phase flow by means of UDV and LDA, Proc. 5<sup>th</sup> Intl. Conf. Multiphase Flow, Yokohama, ICMF04-260.
- [10] Zhang C, Eckert S, Gerbeth G: Experimental study of single bubble motion in a liquid metal column exposed to a DC magnetic field, Int. J. Multiphase Flow 31 (2005), 824-842
- [11] Zhang C, Eckert S, Gerbeth G: The flow structure of a bubble-driven liquid metal jet in a horizontal magnetic field, paper submitted to J. Fluid Mech. (2006)
- [12] Davidson P A: Magnetic damping of jets and vortices. J. Fluid Mech. 299 (1995), 153-186

# Velocity Measurement around a Large Bubble Rising in Stagnant Water in a Round Pipe Using the UVP (2nd Report: The Effect of Bubble Length and Pipe Diameter)

Hisato Minagawa, Tsuyoshi Fukazawa, Yoshiyuki Nakazawa, Satoshi Yamada  
Department of Mechanical Systems Engineering, The University of Shiga Prefecture, 2500 Hassaka,  
Hikone, 522-8533 Shiga, Japan

Yoichi Shiomi  
Department of Mechanical Systems Engineering, Ryukoku University, 1-5 Yokotani, Seta Ooe-cho,  
Otsu, 520-2194 Shiga, Japan

The averaged liquid velocity fields around a large bubble rising in stagnant liquid in a vertical round pipe were measured using Ultrasonic Velocity Profile monitor (UVP) in order to obtain fundamental information of the gas-liquid two-phase slug flows. Two ultrasonic transducers were set at different directions to get velocity vectors. In this report, the effects of bubble length and the pipe inner diameter on the velocity field are investigated and discussed. In the liquid film near the bubble nose, the liquid downward flow is almost the free-fall with negative of bubble rising velocity as initial velocity even if bubble length and pipe diameter change. The velocity profiles in the liquid phase above and below the large bubble (wake) are also discussed.

**Keywords:** Ultrasonic Measurements, Large Bubble, Average Velocity Field, Velocity Distribution, Wake

## 1 INTRODUCTION

Gas-liquid two-phase slug flows in vertical pipes are frequently encountered in industrial pipelines, chemical and nuclear reactors and other fluid machineries. The averaged velocity field around a large bubble rising in a stagnant liquid, which is one of the simplified forms of large bubbles in slug flows in vertical pipes, is first required to know the velocity field around the large bubbles in the slug flow, and to establish a more reasonable model of the flow. The authors have proposed a measuring method using an Ultrasonic Velocity Profile monitor (UVP) to clarify the averaged velocity field around a large bubble, and succeeded to present the velocity field for a vertical pipe of 54mm diameter [1].

As for the existing studies on the measurement of the velocity field around a large bubble rising in a stagnant liquid, we can enumerate the measurement using photochromic dye activation method by Kawaji et al.[2], and those using PIV by Nogueira et al.[3], by van Hout et al.[4], and by Bugg and Saad[5]. Tomiyama et al.[6] also performed the measurements using LDV especially to clarify the flow field in the wakes behind the large bubbles. But, no systematic data including the effect of bubble length and of pipe diameter is available. So we still need a systematic and precise data base on the velocity field, especially on the effect of large bubble length and pipe diameter on the velocity field.

## 2 EXPERIMENTAL FACILITIES

### 2.1 Experimental Apparatus and Procedure

A schematic of the experimental apparatus is shown

in Figure1. The precise of the apparatus should be referenced the previous report [1].

The test section was consisted of a transparent acrylic round pipe set vertically. To clarify the effect of pipe diameter on the velocity field, we carried out experiments using four different pipes of 26, 32, 42 and 54mm inner diameter. They are denoted by 25A, 32A, 40A and 50A, respectively, in this paper. Two ultrasonic transducers of UVP (frequency: 4MHz) were set at the outside of the test section: one +20 degree and the other -20 degree inclined from the horizontal line.

Velocity field of about 20 large bubbles were measured for one bubble length in each diameter pipe. Four groups of bubble length ( $L_B = 1.5D, 2D, 3D$  and  $4D$ ) are adopted to investigate the effect of large bubble length on the velocity field.

### 2.2 Shape of Large Bubble

The shapes of large bubbles were obtained by measuring the film thickness around large bubbles using images from a digital video recorder. As a result, the shapes of the large bubbles in this study are estimated with average relative error of 6.9% by the bubble shape function proposed by Nakahara et al.[8]. Hence the large bubble shape is estimated by this function in this study.

### 2.3 Equation of Continuity

In order to confirm the uncertainty in measurement, the continuity relation was applied to the measured velocity field. Figure 2 is an example of the results for the case of  $D = 50A$  (54mm) and  $L_B = 2D$ . Because the flow system in this study is essentially a static system, the flow rate  $Q$  should be zero

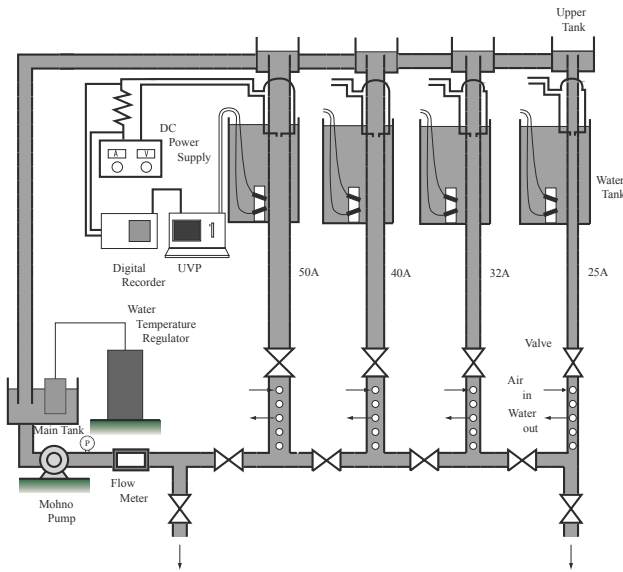


Figure 1: Schematic of Experimental Apparatus

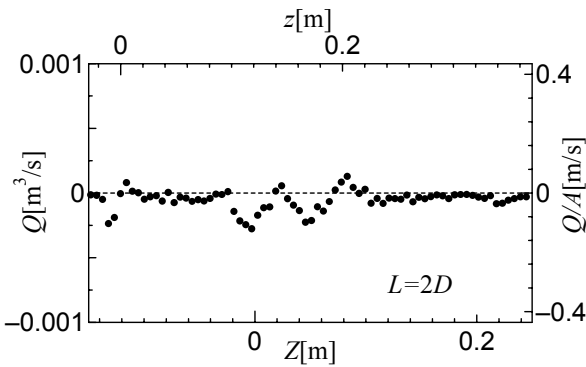


Figure 2: Continuity Relation

ideally. Although the data depart from zero line in some degree around large bubble tail ( $Z = 0$ ;  $Z$  denotes the downward distance from the tail of the large bubble and  $z$  from the nose.), the average absolute value of velocity ( $Q/A$ ) is not so large ( $= 0.0291m/s$ ) compared with the large bubble rising velocity,  $u_B$  ( $= 0.269m/s$ ). It can be confirmed that the UVP measurement system in this study can measure the velocity field by such accuracy.

### 3 EXPERIMENTAL RESULTS AND DISCUSSION

#### 3.1 Outline of Velocity Field [1]

An example of the obtained result of the velocity field is presented in Figure 3 for a whole slug unit for the case  $L_B = 1.5D$  and  $D = 50A$ . It is recognized that the very small velocities are measured in the liquid phase in front of the large bubble. On the other hand, very large velocities are found in the liquid phase in the liquid film around the bubble and behind the large bubble. We can observe a downward accelerating flow in the liquid film, which penetrates into the liquid bulk behind the large bubble near the wall, and attenuates soon. In the center of pipe just below the large bubble, we can

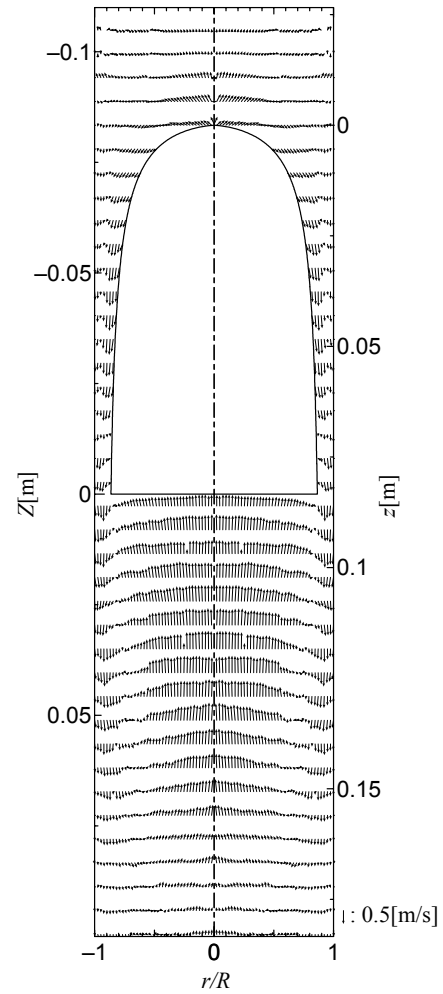


Figure 3: Velocity Field for  $L_B = 1.5D$ ,  $D = 50A$

see large upward velocities, which form a large ring vortex with the wall-side downward flow.

From now, the precise characteristics in each part are exhibited and discussed with considering the effect of large bubble length  $L_B$  and pipe inner diameter  $D$ .

#### 3.2 Liquid Velocity above Large Bubble

In order to make the flow field clear, we enlarged the velocity vector display in this region as shown in Figure 4 because in the liquid phase in front of the large bubble, only very small velocities are recognized. The liquid near the pipe axis is lifted owing to the rising bubble nose, whereas near the pipe wall, the downward flow is recognized, which will flow into the liquid film around the large bubble. There is another downward flow near the pipe wall from  $z \approx 0$ . These two downward flows join together in the film to make a complex flow pattern.

The effect of bubble length is essentially negligible for the velocity field in this area; even if the bubble length changed from  $1.5D$  to  $4D$ , the velocity field is identical. It is quite natural because the bubble rising velocity and bubble nose shape are identical for different bubble lengths, and this area connects the

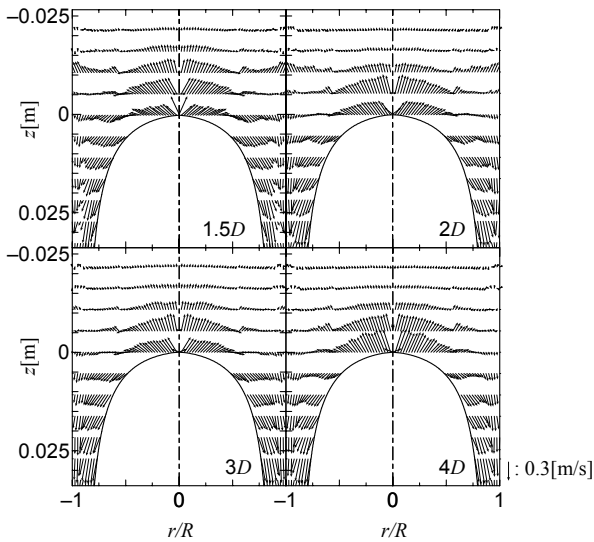


Figure 4: Liquid Velocity in Front of Large Bubble

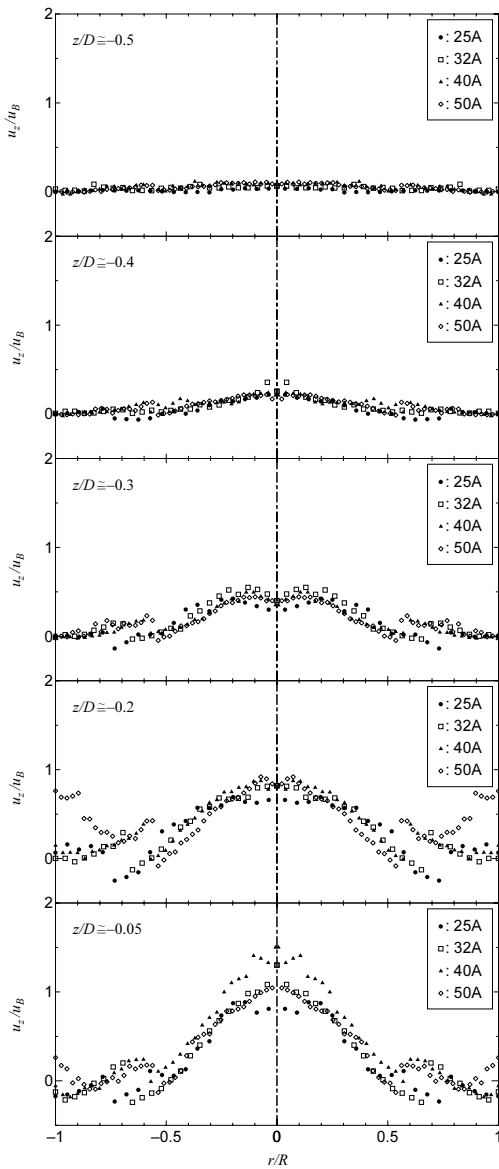


Figure 5: Velocity Profile above Large Bubble ( $L_B = 1.5D$ )

area where the effect of pipe diameter is obvious as will be described later (wake part) only through the thin liquid film.

Figure 5 shows the normalized velocity profile or the flow direction velocity component in this region divided by large bubble rising velocity  $u_B$  with the pipe diameter as parameter. Agreement of profiles for different pipe diameter is so good even if the positions from the bubble nose,  $z/D$ , change. Thus, we can conclude that the effect of pipe diameter on the liquid velocity in front of large bubble is explained clearly only by the difference of  $u_B$ .

### 3.3 Liquid Film around Large Bubble

Figure 6 shows the velocity fields in the liquid film for different bubble lengths in 50A pipe. We can observe a downward accelerating flow in the liquid film, which will penetrate the liquid bulk called the wake part behind the large bubble near the wall. Therefore, the velocity of the downward flow when it penetrates the wake depends on the large bubble length; the longer, the faster.

In Figure 7, the maximum downward velocities at each position  $z$  in the liquid film,  $u_{zmax}$ , minus large bubble rising velocity,  $u_B$ , are plotted against  $z$ . If we suppose the liquid downward velocity is the result of the free-fall from  $-u_B$  as the initial velocity, the downward velocity data should agree with the curves of free falling in the figure. Near the bubble nose, they agree well, especially  $z$  is smaller than about 0.05m. The data deviate downward as  $z$  becomes larger, probably because of the wall friction. Both the bubble length and the pipe diameter do not effect on the feature.

### 3.4 Wake Part below Large Bubble

The velocity fields in the wake part just below the large bubble are shown in Figure 8 for each large bubble length. As mentioned above, a downward accelerating flow in the liquid film around the large

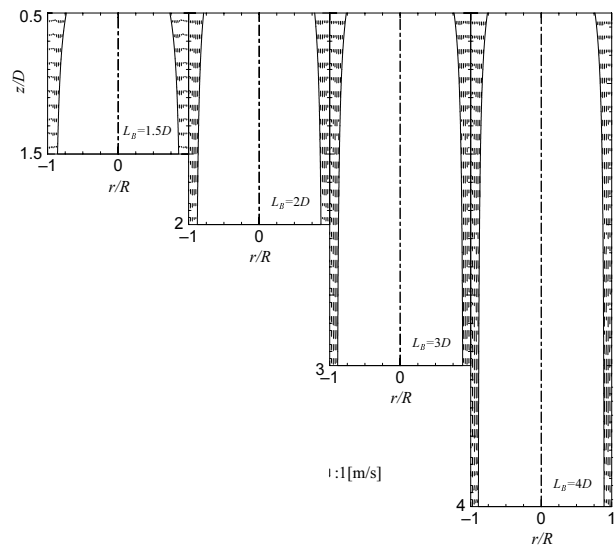


Figure 6: Liquid Velocity Field in Film ( $D = 50A$ )

bubble penetrates it, which causes a downward flow near the pipe wall. Around the pipe axis, on the other hand, an upward flow appears following the large bubble. These two flows form a large ring vortex as shown in Figure 8.

In Figure 9, normalized vertical velocity profiles are plotted. The vertical components of the velocity are again divided by large bubble rising velocity. Then, the profiles at the same position from the large bubble tail  $Z$  normalized by  $D$  agree very well in four different pipe diameters.

**4 SUMMARY**

In this report, the effects of bubble length and the pipe inner diameter on the velocity field are investigated and discussed. In the liquid film near the bubble nose, the liquid downward flow is almost the free-fall with negative of bubble rising velocity as initial velocity even if bubble length and pipe diameter change. The velocity profiles in the liquid phase above and below the large bubble (wake) are also discussed. It is concluded the normalization by bubble rising velocity and pipe diameter match the both profiles very well.

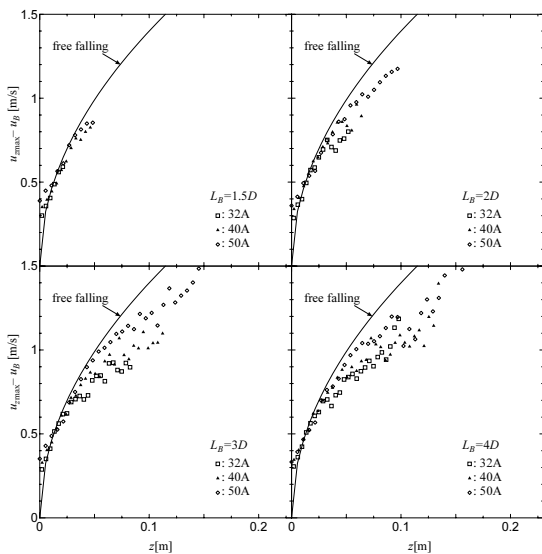


Figure 7: Liquid Downward Velocity in the Film

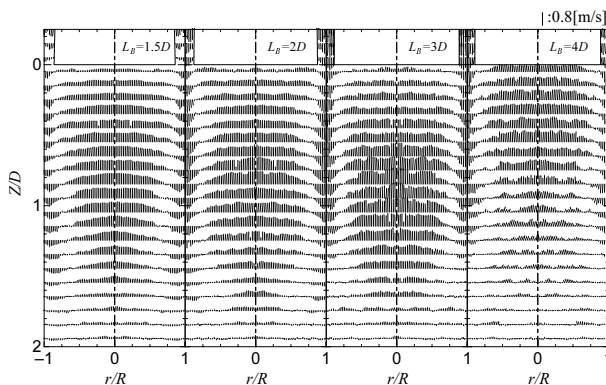


Figure 8: Velocity Fields in Wake ( $D = 50A$ )

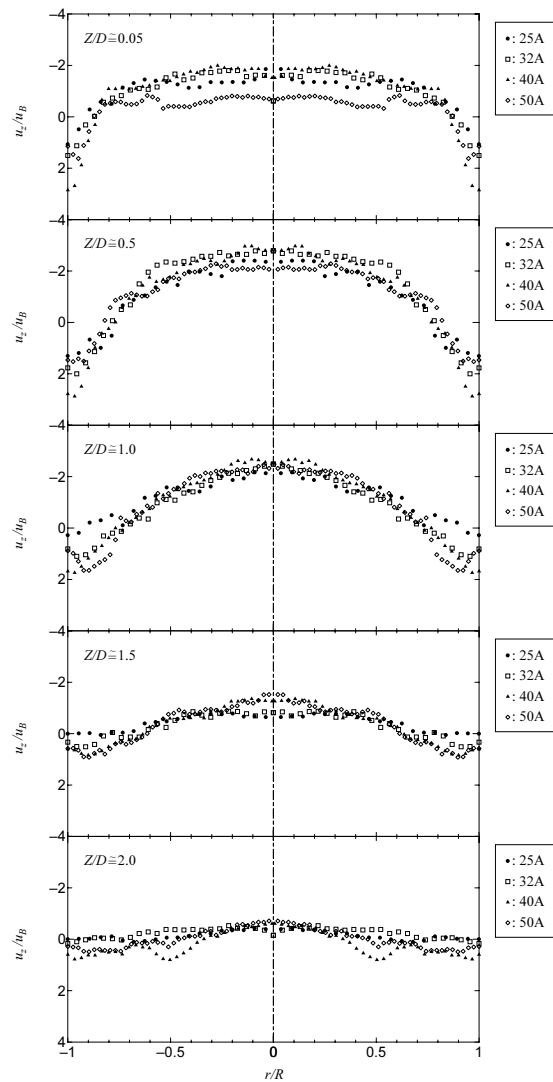


Figure 9: Velocity Profiles in Wake ( $L_B = 1.5D$ )

**REFERENCES**

- [1] Minagawa, H., Ibuki, M., Yamada, S., and Shiomi, Y., Velocity Measurement around a Large Bubble Rising in Stagnant Water in a Round Pipe Using the UVP, proc. 4th Int. Symp. Ultrasonic Doppler Method for Fluid Mechanics and Fluid Engineering, Sapporo(2004), pp.133-138.
- [2] Kawaji, M., Dejesus, J.M., and Tudose, G.: Investigation of flow structures in vertical slug flow, Nuclear Engineering and Design, Vol.175(1997), pp.37-48.
- [3] Nogueira, S., et al.: Flow Patterns in the Wake of Taylor Bubbles Rising in Stagnant Liquid, proc. 4th Int. Conf. on Multiphase Flow, (2001), in CD-Rom.
- [4] van Hout, R., et al.: Experimental investigation of the velocity field induced by a Taylor bubble rising in stagnant water, Int. J. Multiphase Flow, Vol.28(2002), pp.579-596.
- [5] Bugg, J.D. and Saad, G.A.: The Velocity Field around a Taylor Bubble Rising in a Stagnant Viscous Fluid: Numerical and Experimental Results, Int. J. Multiphase Flow, Vol.28(2002), pp.791-803.
- [6] Tomiyama, A., Tamai, H., and Hosokawa, S.: Velocity and Pressure Distributions around Large Bubbles rising through a Vertical Pipe, proc. 4th Int. Conf. Multiphase Flow, (2001), in CD-Rom.

# Spatial-temporal Variation of Turbulence Characteristics in Sewer Flow

Vojtěch Bareš, Jakub Jiráč, Jaroslav Pollert

Department of Sanitary and Ecological Engineering, CTU Prague, Thákurova 7, 166 29, Prague 6, Czech Republic, email: bares@fsv.cvut.cz; jakub.jirak@fsv.cvut.cz; pollert@fsv.cvut.cz

Presented study deals with theoretical and experimental investigation of the steady uniform and transient flows with a free surface in channels with a circular cross section with smooth walls as well as with rough sediment deposits. The aim of the study is to define the relationship between the flow unsteadiness and selected flow/turbulence characteristics in circular tube running partially full. Furthermore, the influence of the sediment bed on spatial distribution on given characteristics is studied. The results show strong influence of the cross section geometry on the local values of friction velocity above the sediment bed and, interestingly, decreasing its relative value with increasing relative flow depth. The temporal/spatial turbulence intensities and Reynolds stress distribution in the mid-vertical of the pipe were identified. Generally, the values of turbulent characteristics are larger in the rising branch of the hydrograph. Finally, the individual terms of the bottom shear stress were identified. The omission of any flow property leads to clear misinterpretation of the calculated bottom shear stress.

**Keywords:** circular tube, Reynolds stress, sewer, sediment deposits, unsteady flow, velocity profile,

## 1 INTRODUCTION

Both combined and storm sewer flows are characterized by a strong unsteadiness coming from rain events as well as from artificial factors. Field and laboratory studies have shown that during the passage of the flood hydrographs, the bed-load movement, suspended-load distribution, as well as sewer flow processes are different from those in the steady flow. In order to parameterize the above-mentioned processes, a knowledge of unsteady sewer flow and turbulence characteristics is needed.

In the past decade there have been published numerous field studies describing transport and transformation processes in transient sewer flows. These works often neglected a detailed analysis of the hydraulic and turbulence characteristics which leads to clear misinterpretation of their results. Beside that, the omitting of the hydrodynamic processes in unsteady sewer flow by engineering society can lead to cost-ineffective design.

Several previous laboratory experiments have dealt with unsteady open-channel flow over rough bed, in rectangular flumes. Tu and Graf (1993) estimated friction velocity as well as shear stress distribution using the kinematic wave theory and flow measurements using micro-propeller current meters. A two-dimensional velocity and turbulence analysis using Acoustic Doppler Velocity Profiler (ADVP) or Laser Doppler Anemometer (LDA), respectively was presented by Song and Graf (1996) and Nezu et al. (1997). Unsteady open-channel flows in a semicircular cross section flume were studied by De Sutter (2001) who used generally the same approach as Tu and Graf (1993). However, that investigation [4] was mainly concerned with the unsteady sediment transport phenomena.

Therefore, the properties of unsteady open-channel turbulent flow were investigated in a channel with a circular cross section with smooth walls as well as with rough fixed sediment deposits. The aim of the study is to define the relationship between the flow unsteadiness and selected flow/turbulence characteristics in circular tube running partially full. Furthermore, the influence of the sediment bed on spatial distribution on given characteristics is studied. The information obtained should help to better understand unsteady flow transport and transformation processes in urban drainage systems.

## 2 METHODS

### 2.1 Experimental setup

An experimental flume of plexiglass pipe (inner diameter  $D = 0.29$  m) was constructed with a constant bottom slope  $S_0 = 0.1\%$  to investigate different uniform flow conditions and triangular-shaped hydrographs (Fig. 1). The sediment bed consisted of gravel material with nearly uniform grain size  $d_s = 12$  mm. An electromagnetic flowmeter was installed for continuous discharge measurements  $Q_{MD}(t)$  in the supply conduit of the plexiglass flume. Three ultrasonic (US) water level transducers with extended temperature probes were installed on the top of the conduit at distances  $X$  [m] = 5.10, 6.94, 9.31. Measured quantities (flow depth  $h(x,t)$ , discharge  $Q(t)$ , temperature  $T$ ) were digitized and recorded through a data acquisition system and synchronized with the velocity measurements.

Total of 72 reference steady flow experiments and 36 unsteady flow experiments were performed in flows over smooth pipe as well as rough sediment deposits.

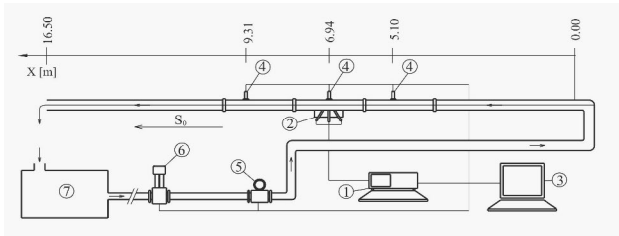


Figure 1: Experimental setup (1. UVP unit; 2. ultrasonic transducers; 3. data acquisition system; 4. ultrasonic water level gauges; 5. MID flowmeter; 6. electronically controlled valve; 7. recirculation tank).

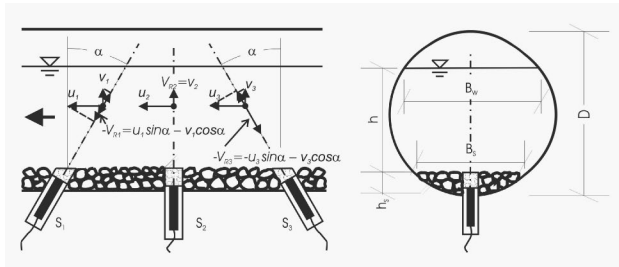


Figure 2: Geometry of UVP transducers and velocity components decomposition.

### Velocity and turbulence measurements

The instantaneous information regarding velocity and turbulence distribution was obtained using two independent UVP units (Met-Flow, S.A.) connected to the couple of US velocity transducers; either  $S_1, S_2$  or  $S_1, S_3$  (Figure 1). The UVP Monitor operates on the principle of the Doppler shift and the details of this method have been presented by Takeda (1999). Mentioned setup allows receiving the time-averaged information about the vertical distribution of longitudinal  $\bar{u}(y)$  and vertical  $\bar{v}(y)$  velocity, longitudinal  $\sqrt{u'^2}(y)$  and vertical  $\sqrt{v'^2}(y)$  turbulence intensity and Reynolds stress  $-\overline{u'v'}$  [6], making it possible to minimize the error originating from the repeatability of hydrographs. US velocity transducers were placed in closed movable boxes under the channel bottom to prevent a disturbance of the flow (Fig. 2) and to move out the near field of the US signal [7].

### Data treatment

An accurate definition of temporal mean values from measured quantities is one of the most difficult aspects of unsteady flow experiments. Therefore, the Butterworth infinite impulse response filter of the 6<sup>th</sup> order was applied in both time series directions [8]. This approach was found to be preferable to the fast Fourier transform (FFT) used by the others [2-4], particularly in outlying sections of the filtered signal. However, our results showed that the application of FFT on mirrored coupled array can provide comparable results.

## 3 RESULTS

### Steady uniform flow

In flows over the rough sediment bed the turbulence intensities and the Reynolds stress distribution was analyzed (Fig. 3 - 5). It was found that the vertical distribution of turbulence intensities can be described by theoretical equations proposed in literature [9-10]. It was confirmed as well that the Reynolds stress distribution takes a linear distribution under steady uniform flow conditions. However, it is clearly seen, that the data dispersion in case of horizontal turbulence intensity (Fig. 3) and Reynolds stress (Fig. 5) is significantly higher. It can be explained by two factors: *i*) both characteristics are analyzed at least by two US transducer. *ii*) both characteristics are more sensitive to propagation of the error coming from wrong setting of flow uniformity. Also, the mixing length distribution was found to be in good agreement with Prandtl's hypothesis.

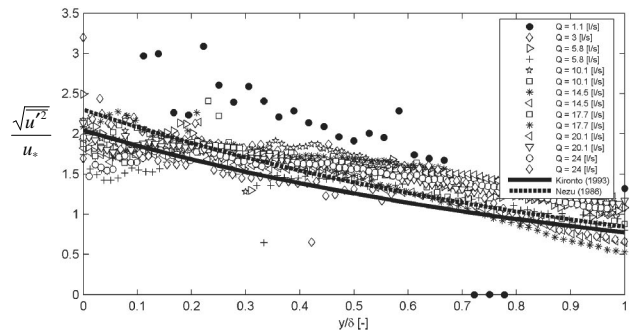


Figure 3: Dimensionless distribution of horizontal turbulence intensity  $\sqrt{u'^2}/u_*(y)$  for different flow conditions.

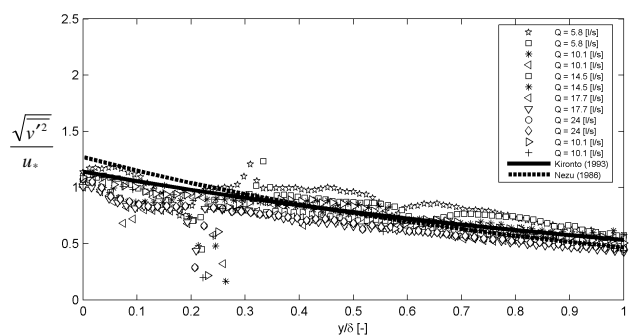


Figure 4: Dimensionless distribution of horizontal turbulence intensity  $\sqrt{v'^2}/u_*(y)$  for different flow conditions.

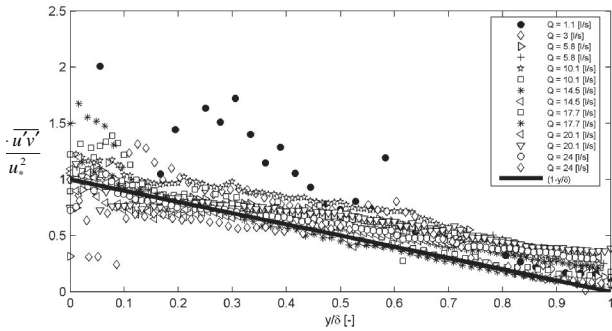


Figure 5: Dimensionless distribution of Reynolds stress  $-\overline{u'v'}/u_*^2(y)$  for different flow conditions.

The influence of the cross section geometry and relative flow depth  $(h+h_s)/D$  on local values of the friction velocity  $u_*$  was studied as well. The local values of  $u_*$  were independently experimentally analyzed by the Clauser method (applying the log-law for measured velocity distribution in inner region of boundary layer) given as:

$$\bar{u} = \frac{u_*}{k} \ln\left(\frac{y'}{k_s}\right) + B_R \cdot u_* \quad (1)$$

where  $k_s$  is the sediment roughness and  $B_R$  is the constant of integration. Further, direct measurement of Reynolds stress was used as:

$$u_*^2 = \frac{t_0}{r} = -\overline{u'v'}(y \rightarrow 0) \quad (2)$$

where  $t_0$  is the bottom shear stress. In literature, the method of Clauser is often criticized because of its instability especially in flows over rough bed. However, our results proposed a close correlation between both methods.

Further, values of  $u_*$  related to the wetted perimeter  $P$  were calculated using a simplified Saint Venant equations. The results show strong influence of the cross section geometry on the local values of  $u_*$  above the sediment bed (factor 1.2 ÷ 1.5) (Fig. 6). Those values are significantly higher than other researchers pronounced [11-12].

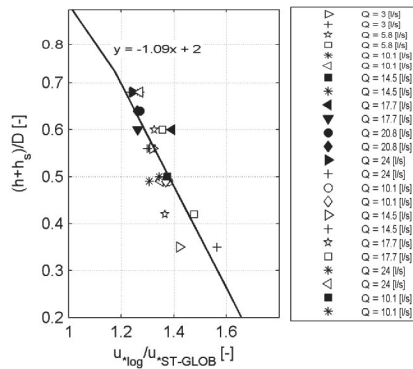


Figure 6: Relation between ratio of local ( $u_{*log}$ ) and global ( $u_{*ST-GLOB}$ ) values of friction velocity and relative pipe filling  $(h+h_s)/D$ .

It can be explained by higher ratio between roughness of the bed and walls in our study. Interestingly, the relative values of  $u_*$  decreased with increasing  $(h+h_s)/D$ . On the other side, in flows without the sediment bed (i.e. over smooth wall) was averaged value of the ratio defined by 1.04. However, the slight decreasing tendency of normalized local value of friction velocity with relative flow depth  $h/D$  was observed as well.

#### 4 Unsteady flows

36 unsteady flow experiments have been carried out in flows over rough sediment bed. Triangular hydrographs with different degrees of the unsteadiness were generated in the experimental flume. One of the hydrograph was repeated 14 times to prove the experimental repeatability and to evaluate the resulting error in the estimated friction velocity  $u_*$ .

The hydrograph analysis revealed a dynamic wave behaviour, where the time lags of friction velocity  $u_*(t)$ , mean cross section velocity  $V(t)$ , discharge  $Q(t)$  and flow depth  $h(t)$  were all evident. In agreement with the theoretical assumptions for a complete dynamic wave, the friction velocity  $u_*$  reached the maximum value first, followed in chronological order by the mean cross section velocity  $V$ , the discharge  $Q$  and the flow depth  $h$ .

The temporal/spatial turbulence intensities and Reynolds stress distribution (Fig. 7) in the mid-vertical of the pipe were identified. Generally, the values of turbulent characteristics are larger in the rising branch of the hydrograph. With regard to the vertical distribution, theoretical equations proposed in literature [2-3] were found to be adequate.

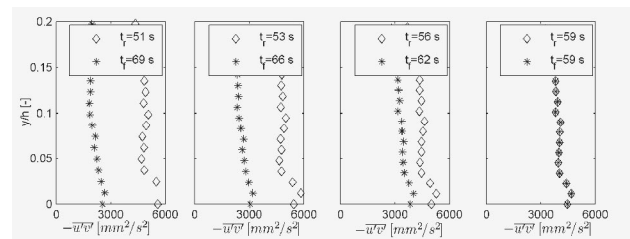


Figure 7: Measured Reynolds stress distribution for the equal flow depths  $h$  in the rising ( $t_r$  [sec]) and in the falling ( $t_f$  [sec]) branch of the hydrograph HYDR\_13.

Above mentioned experimental methods (eq. (1-2)) were used to estimate the friction velocity  $u_*$ . The Clauser method and the direct measurements of the Reynolds stress propose quantitatively similar results of local values of  $u_*$  in the centre of sediment bed. However, the standard deviation of estimated  $u_*$  is significantly smaller for the method of Clauser. It was found that the relative standard deviation of  $u_*$  is approximately 5.0 % when the Clauser method is applied (Fig. 8).

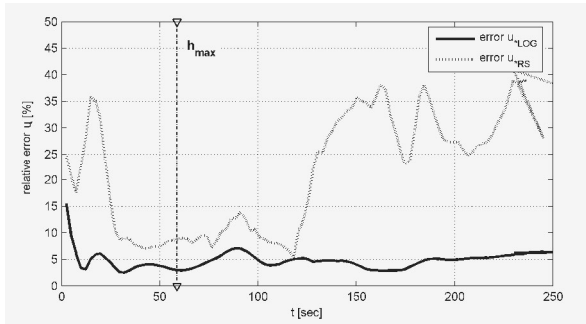


Figure 8: Relative error along the hydrograph HYDR\_1 of friction velocity  $u$ -estimated by the Clauser method  $u_{LOG}$  and by direct measurement of the Reynolds stress  $u_{RS}$

With respect to broadly used 1-D flow modeling approach, the applicability of the Saint Venant equation of motion given as:

$$\frac{\partial h}{\partial x} - S_0 + \frac{1}{g} \frac{\partial U}{\partial t} + \frac{U}{g} \frac{\partial U}{\partial x} + \frac{1}{h} \frac{t_0}{rg} = 0 \quad (3)$$

where  $S_0$  is a bottom slope, was analyzed. All terms of eq. (3) were individually calculated from the instantaneous measured variables  $U(t)$ ,  $h(x,t)$  using both the dynamic and the kinematical flow principle (Fig. 9). The spatial variation of the flow depth  $\partial h/\partial x$  is the most significant term for the correct determination of the friction characteristics. At the time instant of the minimal value of  $\partial h/\partial x$  ( $t \approx 80 \div 90$  sec), the flow is most accelerating and kinematical approach is inadequate (Fig. 9).

Further, the individual terms of the bottom shear stress were identified. The contribution of *i*) the bottom slope  $\tau_{01}$ , *ii*) non-uniformity  $\tau_{02}$ , *iii*) unsteadiness  $\tau_{03}$  and *iv*) cross section geometry  $\tau_{04}$  was evaluated (Fig. 10).

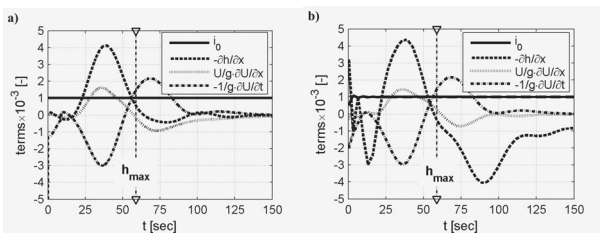


Figure 9: Time variation of individual terms of the Saint Venant equation of motion: a) the dynamic flow principle; b) the kinematic flow principle.

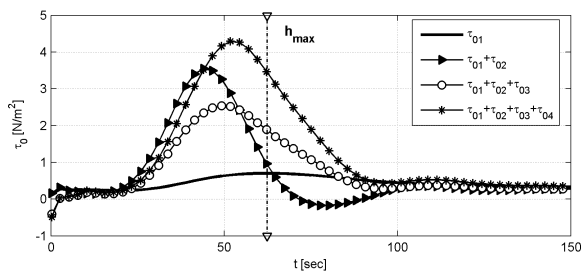


Figure 10: Contribution of the bottom slope  $\tau_{01}$ , non-uniformity  $\tau_{02}$ , unsteadiness  $\tau_{03}$  and cross section geometry  $\tau_{04}$  on the behavior of the bottom shear stress.

The omittance of any flow property leads to clear misinterpretation of the calculated bottom shear stress. This leads to the important conclusion that the bottom shear stress in unsteady sewer flow cannot be simplified by the steady flow approach. Those modeling approaches for sediment transport which are based on bottom shear stress, must consider therefore the specific attributes of the flow.

## SUMMARY

The influence of unsteady sewer flow characteristics on various flow variables has been clearly demonstrated in the study. The methodology described allows studying highly dynamic processes in mentioned regime of flow without any intrusions of the observed flow. With regard to sewer applications, the generalized results support various tasks related to the description of dynamic sewer transport and transformation processes.

## ACKNOWLEDGEMENT

This work was supported by the Czech Science Foundation; project No.103/04/1350, by the project of Czech Ministry of Education, Youth and Sport No. MSM6840770002.

## REFERENCES

- [1] Tu HZ and Graf WH: Friction in Unsteady Open-Channel Flow over Gravel Beds, Journal of Hydraulic Research, 31(1) (1993) 99-110.
- [2] Song T and Graf WH: Velocity and turbulence distribution in unsteady open-channel flows, Journal of Hydraulic Engineering-Asce, 122(3) (1996) 141-154.
- [3] Nezu I, Kadota A, and Nakagawa H: Turbulent structure in unsteady depth-varying open-channel flows, Journal of Hydraulic Engineering-ASCE, 123(9) (1997) 752-763.
- [4] De Sutter R: Erosion & Transport of Cohesive Sediment Mixtures in Unsteady Flow, PhD thesis, Universiteit Gent, (2001).
- [5] Takeda Y: Ultrasonic Doppler method for velocity profile measurement in fluid dynamics and fluid engineering, Experiments in Fluids, 26(3) (1999) 177-178.
- [6] Lemmin U and Rolland T: Acoustic velocity profiler for laboratory and field studies, Journal of Hydraulic Engineering-Asce, 123(12) (1997) 1089-1098.
- [7] Povey MJW: Ultrasonic Techniques for Fluids Characterization, Academic Press (1997).
- [8] Qu Z: Unsteady open-channel flow over a mobile bed, PhD thesis, No. 2688, École Polytechnique Fédérale de Lausanne, (2002).
- [9] Kironoto BA and Graf WH: Turbulence Characteristics in Rough Uniform Open-Channel Flow, Proceedings of the Institution of Civil Engineers-Water Maritime and Energy, 106(4) (1994) 333-344.
- [10] Nezu I and Rodi W: (1986). Open-Channel Flow Measurement with a Laser Doppler Anemometr. Journal of Hydraulic Engineering-Asce, 112(5), 335 -355.
- [11] Berlamont JE, Trouw K and Luyckx G: Shear stress distribution in partially filled pipes, Journal of Hydraulic Engineering-ASCE, 129(9) (2003) 697-705.
- [12] Knight DW and Sterling M: Boundary shear in circular pipes running partially full, Journal of Hydraulic Engineering-ASCE, 126(4) (2000) 263-275.

# Simultaneous UVP and PIV measurements related to bed dunes dynamics and turbulence structures in circular pipes

A. H. Rabenjafimanantsoa, Rune W. Time

Department of Petroleum Engineering, University of Stavanger, N-4036, Ullandhaug, Norway

Arild Saasen

Statoil ASA

N-4035 Stavanger, Norway

An Ultrasound Velocity Profile (UVP) monitoring instrument is used for measurement of shear, turbulence and friction for particles transport and bed dunes dynamics in circular pipes. In order to complement and verify the measurements from the UVP a Particle Imaging Velocimetry (PIV) was used. Simultaneous 2D velocity vector maps above the dunes was obtained by PIV to detect the spatial flow structures while the instantaneous 1D velocity profiles as well as the turbulence structures over the dunes sheared by water flow was measured by the UVP instrument. The flow field of water and glass sphere particles (200 micron range) involves complex turbulence patterns. Different dunes flow regimes or geometrical patterns form depending on the actual flow rate. Of particular interest are dune regimes, where bed and overlaying fluid changes dynamics. In particular this involves bed roughness and particle lift, which are related to the particle transport rates, generation of macroturbulence and frictional pressure drop.

**Keywords:** PIV, UVP, liquid particle flow, particle beds, macroturbulence

## 1 INTRODUCTION

Moving particle beds occur as part of natural flow phenomena like in rivers and turbidites, as well as in engineering applications, like hydraulic conveying of coal and cuttings transport during oil well drilling. Trains of dunes are normally observed in long pipes [1]. It is important to measure flow profile and turbulence characteristics of the liquid and particle flow fields in order to determine the dynamics of such largely self-organized systems. In this work we combined two of the most promising techniques for measurement of liquid particle flows; ultrasonic based velocity profiling (UVP) and laser based particle imaging velocimetry (PIV). It is important to perform cross check and consistency analysis of the techniques, as well as to reveal strong and weak aspects of each technique for analysis of particle laden flows. A small flow cell was made to reveal flow structures of only a few dunes. It is complementary to a larger flow loop at our laboratory for study of long trains of dunes. The flow in this smaller cell reproduces most of the characteristics of the flow patterns in the larger pipe, while also easily allowing easier adaptation for the UVP and PIV measurements. The dynamics of dunes has been investigated extensively using numerical simulation [2-4]. Also experimental studies, e.g. of turbidites and river flows using both PIV and UVP have been carried out. Bennett and Best [5] made detailed measurement of flow velocity and turbulent fluctuations using LDA. They found that the dune-related macroturbulence emerges from the shear layer instabilities. Best [6] also traced the evolution of such macroturbulent events over

dune-covered bed using PIV. Special attention was paid at the lee and stoss sides of the dunes. The results provided a mechanism that may explain the entrainment of sediment into both suspended and bed load transport.

However, no published reports have so far been found on the simultaneous use of UVP and PIV as done in this work. We have applied both techniques successfully in previous experiments. This made it simpler to perform the combination and determine the validity of the results.

## 2 EXPERIMENTAL SETUP

### 2.1 Flow rig – pipes and pump system

The flow rig is shown in Figure 1. A single glass pipe segment of 1 meter long and 4 cm inner diameter is placed inside a water filled optical cell 90x20x30 cm. Small glass particles form beds during flow inside the pipe. Water flow is supplied from two small pumps. The particles are initially fed through a hole in the rear flange via a rubber hose to form an initial bed. A self-organized bed shape will form readily during the flow. The particles will eventually reach the pipe outlet and are then trapped by a large pipe at the bottom to prevent them from circulating into the pumps. For these experiments the pump flow rate was approximately 0.2 l/s, equivalent to 0.18 m/s in the 4 cm glass pipe.

### 2.2 Ultrasonic measurements - UVP system

A UVP system (Met-Flow) allows instantaneous flow profiles to be recorded through the pipe wall from virtually any position above the bed, as shown in Figure 1.

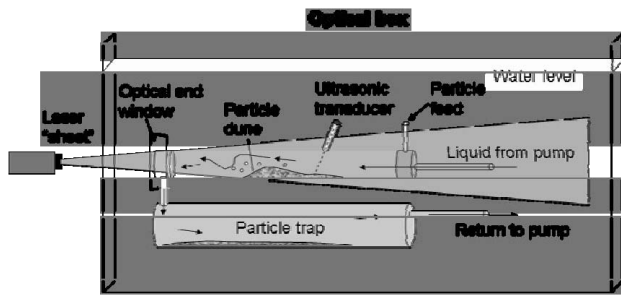


Figure 1: Flow rig with water filled optical box, transparent pipe and laser sheet setup.

Water in the optical cell works as contact fluid. A thorough description of the physical principle of UVP may be found in [7]. Three different frequencies are used in our arrangement; 1, 2 and 4 MHz. In essence the instrument measures the speed component along the ultrasonic beam axis, based on the backscattered signal from particles passing through the beam. We used the 4 MHz probe for these tests, requiring a particle diameter of approximately 93 microns.

**2.3 Laser based velocity profiles based on PIV**

A PIV system (Dantec dynamics) supplies a 1mm thick lasersheet (Solo ND:YAG laser 106 mJ, New Wave Research) acting as a fast repetition flash into the flow. It is synchronized with a computer controlled high speed camera (HiSense, 1024x1280 pixels) to record multiple instant pictures. The processing unit (Flowmap 1500) performs picture analysis to determine particle speed based on a two-dimensional cross correlation technique. The whole unit is controlled from PC using the program Flowmanager 4.1. The UVP system is triggered to start simultaneously with the PIV system, thus enabling timing synchronization and comparison of the one-dimensional flow profiles with calculated velocity along the UVP line in the PIV pictures.

**2.4 Bed and “seeding” particles**

The particles added to the flow serves two main purposes; creation of sedimentary beds, and acting as seeding particles for flow visualization and ultrasonic beam reflectors. A combination of two different particle sizes is used; 10 micron Spherical® Hollow glass spheres (Potters Industries Inc.) as PIV seeding particles, and 200 micron glass particles for bed formation. Electron microscopy images of the particles are shown in figure 3.

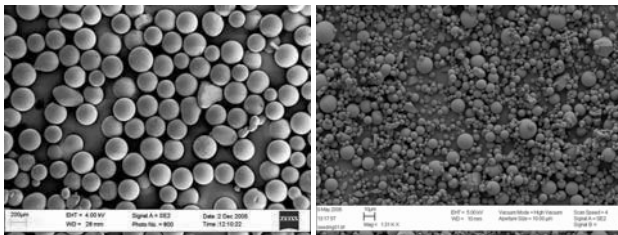


Figure 3: SEM pictures of bed particles (left) and seeding particles (right).

**3 TESTS**

Three different PIV planes were used for the tests. For each test plane UVP was also applied for comparison of results. Each PIV test consisted of a series (10 pairs) of pictures.

**3.1 Axial velocity profiles**

The experiments show that a shear layer develops from the dune crest. The shear layer delimits the recirculation zone below and the main flow above, as shown in Figure 4.

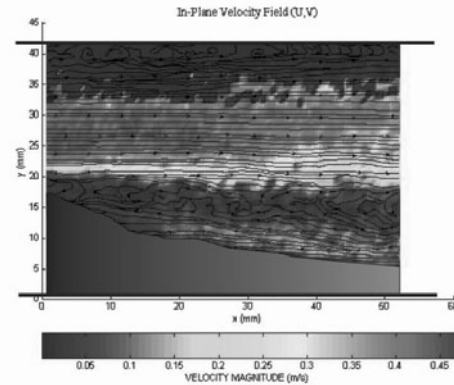


Figure 4: Development of shear layer between the main flow and the recirculation zone. The direction of the flow is from left to right. Flow rate is 0.2 l/s.

In Figure 4 the velocities on top of the main stream appear to be almost zero. This artifact, also appearing in Figures 6 and 7, is caused by particles attaching to the inner pipe wall at the top.

The results using UVP for the same flow as in Figure 4 are depicted in Figure 5. Zero velocities observed here (approximately between channels 2 and 8), are associated with the pipe wall. The plot is based on 1000 profiles in time, each with 128 channels representing depth. The time between successive profiles is 132 ms, and channel 128 is at depth 99.7 mm

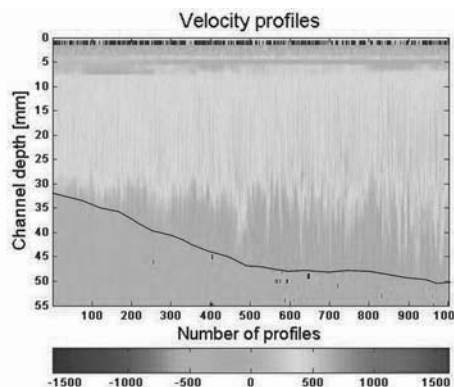


Figure 5: UVP velocity profiles above the dune. The UVP transducer is placed streamwise on top of the pipe at 12° from horizontal. The flow direction is from left to right. Mean flow velocity U = 0.18 m/s. Colorbar in mm/s.

The velocity profile of primary interest for transport

purposes is the axial profile, since most of the kinetic energy, shear and lift are in the axial  $z$ -direction. However flows involving particle beds do not have radial symmetric flow profiles as in single-phase pipe flow. Thus there are two other interesting profile planes; the transverse profile and profiles parallel to the bed surface. From flow over plane walls it is well known that rolling hairpin vortices develop in the plane parallel to the wall. The rollup sequence depends on local wall geometry and particles will modify the process.

The PIV velocity profile derived from the same image underlying Figure 4 is shown in Figure 6 below. Both the shear layer development, represented by the zero velocities sandwiched between the main stream and the bottom flow reversal can be seen from Figure 6.

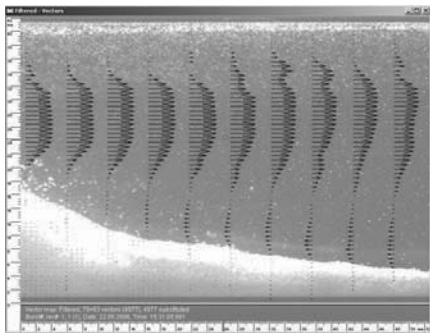


Figure 6: A close-up of an example of the axial velocity profile superimposed on the picture of the sand dune. The flow direction is from left to right. The image grayscale is inverted for clarity.  $U = 0.18$  m/s.

Particles attached on top of the pipe wall as previously mentioned can also be observed. By increasing the mean flow, the velocity profiles became more flat as shown by PIV in Figure 7.

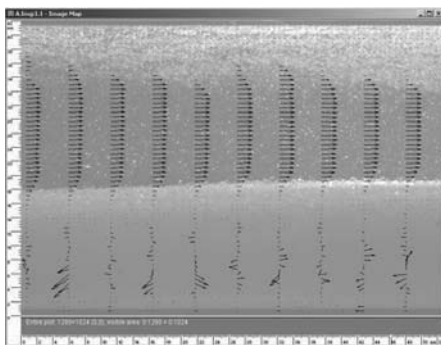


Figure 7: PIV velocity profiles above the dune stoss. The flow direction is from left to right. The image grayscale is inverted for clarity.  $U = 0.22$  m/s.

### 3.2 Transverse cross sectional velocity profile

The transverse profile typically contains numerous large and small vortices. The PIV reveals such structures as shown in Figure 8. In contrast the UVP works along a line heading from the pipe surface. It can be difficult to adjust the UVP properly since

direct wall reflections may survive several back and forth reflection and thus interfere with the pulse sequence. In many cases it is necessary to reduce the pulse repetition rate, thus limiting the use to only low speed flows. In general however, the transverse velocities are normally also quite small, and the limitation of measurement range is not so crucial. Letting the reflected beam hit the bed for dampening is often a useful method to avoid multiple passes of the beam.

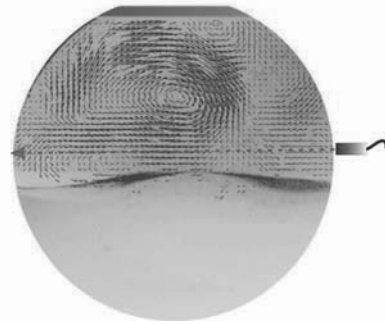


Figure 8: Velocity profile in cross section transverse to the pipe axis. The position of the UVP probe is indicated at the right. The image grayscale is inverted for clarity.

### 3.3 Velocity profile parallel to the bed surface

Regarding flow details and shear layer generation, planes parallel and close to the crest is of interest.

An example is shown in Figure 9. The UVP transducer line was in the same position and direction as shown in Figure 8. In Figure 9 the velocity profile plane is taken approximately 5 mm above the bed surface. However, it is difficult to screen the laser sheet completely from secondary stray light hitting the bed surface.

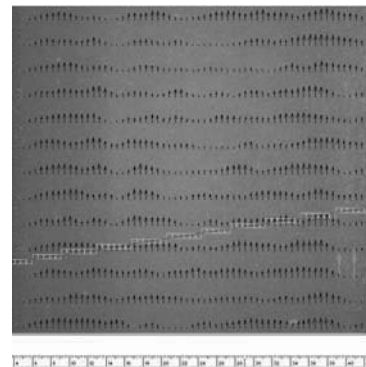


Figure 9: Time-averaged velocity profile in a plane 5 mm above and parallel with the bed surface. The transducer path line (red line) is also shown. The flow direction is from bottom to top. The image grayscale is inverted for clarity.

## 4 DISCUSSION

Based on the PIV recordings even very weak transverse rolls can be determined in the plane perpendicular to the pipe axis, as shown in Figure 8. The UVP instrument has only limited value for

measurement lines parallel to the bed surface, due to the one-dimensional nature of the measurements. However, also another line direction lies in this plane; shooting from the top of the pipe onto the bed surface. This direction is also in accordance with the PIV plane along the pipe in the vertical direction. Note that the UVP method yields only the velocity component along the beam. Thus different particles having the same absolute speed crossing the beam at the same azimuthal angle will give identical speed. This is illustrated in Figure 10.

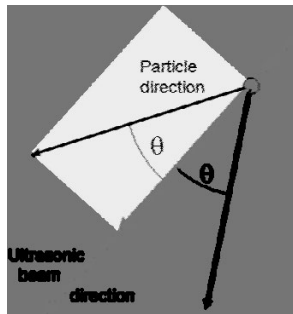


Figure 10: The axial symmetric nature of the UVP measurements may cause different particle directions to yield the same velocity component.

The validity of interpretation is very important. The UVP velocities may be interpreted both as the component in axial ( $z$ ) direction related to Figure 5, but also as the velocity in the transverse cross section (Figure 8) if the transducer is pointing slightly in the  $z$ -direction.

In addition to particles attaching to the pipe wall (as in Figures 4,6 and 7), a difficult aspect with PIV arises in connection with velocity profiles parallel to the bed surface in Figure 9. Although the recorded PIV picture has only a limited focal sharpness, it may pick up some details from the stationary bed surface just 5 mm below. Thus stationary structures can become superimposed the moving particles and thus cause a bias in the PIV estimate.

A direct comparison of the measurements from UVP and PIV is in principle possible, since the test involved simultaneously triggered recordings. The UVP measurements apply to the velocity component along the ultrasonic beam. For direct comparison with PIV, the analysis program (Flowmanager 4.1) must calculate the corresponding vector along the same beam direction. It is not advisable to compare e.g. the  $u$  (horizontal) or  $v$  (vertical) components in the PIV picture with the corresponding decomposed values of the UVP profile. The comparison may be based both on instantaneous recordings with single profile versus pairs of single frames, and on time (ensemble) averages. The instantaneous method was found to have a fairly large amount of scatter, most likely due to the fast changing character of the ultrasonic signal. The PIV frames and the UVP profiles are not synchronized on individual basis,

only the start of the recordings is simultaneous. On a time averaged basis there is a much better agreement between the two techniques. An example is shown in Figure 11. The analysis is based on average of 10 picture pairs and average of

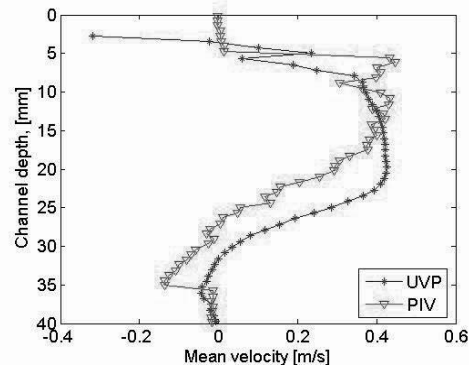


Figure 11: Direct comparison of UVP and PIV estimate, calculating the PIV component along the ultrasonic beam.

all UVP profiles during the corresponding time interval. Inflection point and flow reversal zone at the bottom can be seen from 30 mm and down. Flow rate is 0.2 l/s.

## 5 CONCLUSION

Both UVP and PIV measurements provide very useful measurements of particle laden flows. Clearly PIV is superior in optically perfect systems. UVP has an advantage in opaque systems where PIV cannot be used. However, single beam UVP is a one-dimensional technique and proper care must be done not to draw invalid conclusions in three-dimensional flows. PIV on the other hand is limited to transparent systems and care must be taken to avoid "contamination" of the images from particles on the walls or from flow structures illuminated outside the laser sheet.

## 6 SUMMARY

A comprehensive study was carried out to investigate liquid-particle flow with dunes formation in pipe flow, using combined UVP and PIV techniques. However both methods have traps and limitations that must be accounted for. The methods are complementary in use, but give consistent results if correct interpretation is made.

## REFERENCES

- [1] M. Simkhis, D. Barnea and Taitel: Dunes in solid-liquid flow in pipes. 14<sup>th</sup> International Conference on Slurry Handling and Pipeline, BHR Group. Conference series; publication no. 36 (1999).
- [2] C. Marcioli: Mechanisms for transfer, segregation and deposition of heavy particle in turbulent boundary layers, Tesi di Dottorato, Universita degli studi di Udine (2003), Italy.
- [3] R. Street, N-S. Cheng. Large-eddy simulation of sediment entrainment over dunes, Singapore-Stanford partnership proposal

[http://www.ntu.edu.sg/CEE/ssp/forms/SSP\\_PhD\\_Topics\\_Mar\\_2004.pdf](http://www.ntu.edu.sg/CEE/ssp/forms/SSP_PhD_Topics_Mar_2004.pdf)

[4] A.H. Rabenjafimanantsoa, R.W. Time, M. Hana and A. Saasen: Dunes dynamics and turbulence structures over particle beds – Experimental studies and numerical simulations. Annual Transaction of the Nordic Rheology Society, Vol. 13, (2005) pp. 171-176

[5] S.J. Bennett and J.L. Best: Mean flow and turbulence structure over fixed, two dimensional dunes: implications for sediment transport and bedform stability. *Sedimentology* (1995), 42, 491-513

[6] Jim Best: Kinematics, topology and significance of dune-related macroturbulence: some observations from laboratory and field. *Spec. Publs Int. Ass. Sediment.* (2005), 35, 41-60

[7] Metflow (2000). UVP Monitor – Model UVP-XW, Users guide, Metflow SA, Lausanne, Switzerland



# PIV and UDM measurement of axial and circumferential flow modes between rotating disks

Masato Furue, Jiro Funaki and Katsuya Hirata  
Dept. Mech. Eng., Doshisha Univ., Kyoto, 610-321, Japan

In the present study, we experimentally investigate the flow between co-rotating disks in a stationary cylindrical enclosure. This flow is often non-axisymmetrical and complicated. This flow sometimes causes magnetic-head oscillations in disks storage devices of PCs. We carry out the measurements of radial velocities by UDM (Ultrasonic Doppler Method) analyses, as well as flow visualizations using a high-speed camera and PIV (Particle Image Velocimetry) analyses. Tested cases are two, that is, A ( $Re=1.22 \times 10^4$  and  $\delta=0.12$ ) and B ( $Re=2.44 \times 10^4$  and  $\delta=0.20$ ). Here,  $Re$  is the rotating Reynolds number, and  $\delta$  is a non-dimensional gap between disks. Case A is in the axial mode and Case B is in the axial mode. Here, the axial modes are related with the symmetry of a pair of toroidal-vortical structures. As a result, in case A, non-dimensional dominant frequency is about 20 from radial velocity, while half of 20 from axial velocity. In case B, non-dimensional dominant frequency is much lower than near 20, which is considered to be related with the circumferential mode.

**Keywords:** Co-rotating disks, Flow visualization, PIV, UDM

## 1 INTRODUCTION

Our present interest is the flow between two disks. Namely, we consider a pair of the same radius in a stationary cylindrical enclosure. The gap between disks is much narrower than the disk's radius. The disks are connected with a common shaft and co-rotate. Such a flow is often seen in hard-disk drives, the most popular storage devices in modern PCs. This flow is often complicated and non-axisymmetrical, consisting of two regions, that is, the core region in solid-body rotation and the outer turbulent region. The flow causes pressure and velocity fluctuations, and yields read/write errors of hard-disk drives due to magnetic-head oscillation. Therefore, for the accurate positioning operation of read/write magnetic heads in high-speed and high-capacity hard-disk drives, we are required to understand the flow.<sup>[1]</sup>

Until now, various researches have been carried out in order to know the flow. Lennemann (1974) observed some non-axisymmetric circumferential modes.<sup>[2]</sup> We can usually observe that two flow regions, namely, the core region in solid body rotation near the centre shaft, and the outer turbulent region. There is almost rigid-body-rotational flow in the core region, and much larger velocity fluctuation in outer turbulent region. The core region has a polygonally-shaped boundary, and the polygonal shape rotates slower than disks. Lenneman defined the circumferential mode with the number of core apices. In the outer turbulent region, flow is not completely turbulent, but has a larger structures described below. Later, Herrero et al. (1999) performed three-dimensional numerical simulations for the flow between co-rotating disks, and classified the flow into three axial modes, and .<sup>[3]</sup> We can usually observe a pair of toroidal-

vortical structures near the stationary cylindrical enclosure in the outer turbulent region. In the axial mode, the vortical structures are steady and keep symmetry with respect to the interdisk midplane. In the axial mode, the symmetry is broken with a periodic fluctuation. In the axial mode, the symmetry is broken in a random manner without periodicity. For a need to comprehend the flow field between co-rotating disks from three-dimensional point of view, we (2005) have conducted an experimental study using quasi-three-dimensional PIV (Particle Image Velocimetry) analysis technique based on time-successive real-time analysis.<sup>[1]</sup>

In the present study, we conduct radial velocity measurements based on UDM (Ultrasonic Doppler Method) technique. As well, we carry out flow visualizations by high-speed camera and time-successive three-dimensional PIV analyses. Our purpose is to get accurate and precise information in order to reveal the complicated flow with both axial and circumferential modes. More concretely, we study two cases with the axial modes and .

## 2 EXPERIMENTAL METHOD

### 2.1 Apparatus and governing parameters

Fig.1 shows a schematic diagram of our experimental apparatus. The experimental apparatus is a geometrically-simplified model of hard-disk drives. Two disks with the same radius are connected with a common shaft. Variable-speed motor makes the shaft rotate. The working fluid is water with which we fill the stationary cylindrical enclosure including two disks. The gap between disks is controlled by inserting acrylic pipes between disks as a spacer. Pipes are painted black in order to prevent the reflection of a YAG laser.

The present coordinate system is cylindrical ( $r, \theta$ ,

z). Important geometrical parameters are as follows (see Fig.1). Disk radius  $R_d$  ( $=153$ [mm]), acrylic-pipe radius  $R_s$  ( $=34$ [mm]) and stationary-cylindrical enclosure radius  $R_w$  ( $=155$ [mm]) is fixed to be constant. The gap between disks is  $G$ .

Rotating Reynolds number based on the disk radius is

$$Re = \frac{\omega R_d^2}{\nu} \tag{1}$$

Here,  $\nu$  is the coefficient of kinematic viscosity.  $\omega$  is disk-rotation speed, and is fixed to  $5$ [rpm] or  $10$ [rpm]. Corresponding  $Re$  is  $1.22 \times 10^4$  and  $2.44 \times 10^4$ .

The aspect ratio of disk gap to disk radius is

$$\delta = \frac{G}{R_d} \tag{2}$$

$\delta$  is equal to  $0.12$  or  $0.20$ . Non-dimensional radius of the stationary cylindrical enclosure is

$$\lambda = \frac{R_w}{R_d} \tag{3}$$

As the gap between a disk tip and a stationary cylindrical enclosure is sufficiently narrow ( $0.013R_d$ ),  $\lambda$  is approximately  $1.0$ .

Tab.1 shows the details of our experimental parameters. We performed experiments for two cases; namely, Case A and Case B, which are in the axial mode, and in the axial mode, respectively. The velocity scale is the disk tip velocity  $V_d$  and the scale time is one period of the disk rotation  $t_d$ .

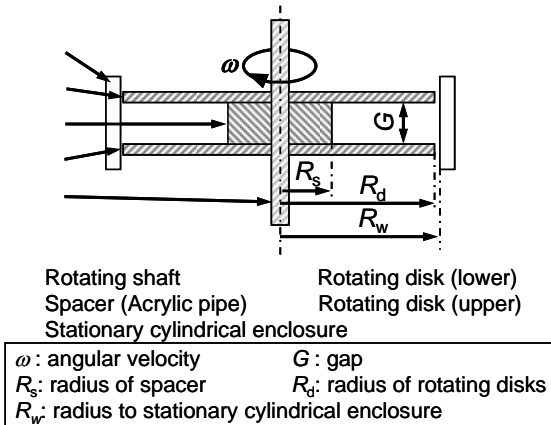


Fig.1 : Schematic diagram of model.

Tab.1 : Experimental parameters.

Case	A	B
Axial modes		
Circumferncial modes	more than 6	
$Re$	$1.22 \times 10^4$	$2.44 \times 10^4$
$\delta$	$0.12$	$0.20$
$\lambda$	$1.0$	$1.0$

## 2.2 Classification of axial modes and circumferncial modes

### 2.2.1 Axial modes

We can usually observe a pair of toroidal-vortical structures near the stationary cylindrical enclosure in the outer turbulent region (see later). On the basis of the vortical structure's stability, Herrero et al.<sup>[3]</sup> classified the flow into three, namely, axial modes, and. In the mode, the vortical structures are steady and keep symmetry with respect to the interdisk midplane. In the mode, the symmetry is broken with a periodic fluctuation. In the mode, the symmetry is broken in random manner without periodicity.

### 2.2.2 Circumferncial modes

When we observe the flow on the  $r-\theta$  plane, we can usually observe that there are two flow regions; namely, the core region in solid-body rotation near the centre shaft, and the outer turbulent region. These regions are well characterized by radial profiles of circumferncial velocity<sup>[4]</sup>. We can confirm almost rigid-body-rotation flow with very small velocity fluctuation in the core region, and non-rigid-body-rotation flow with much larger velocity fluctuation in outer turbulent region.

The core region has a polygonally-shaped boundary, and the polygonal shape rotates a little bit slower than disks. Lenneman<sup>[2]</sup> defined the circumferncial mode with the number of core apices. For example, in the circumferncial mode 3, we see a triangle of the solid-body rotation core region. In addition, in the outer turbulent region, flow is not completely turbulent, but has large vortical structures in the circumferncial plane as well as the axial plane.

## 2.3 UDM Measurement

We conduct to measurements of radial velocity  $v_r$ . The tracer particle is chemically-briged polyethylene-resion particles coated with fluorescent paint and less than  $100$ [ $\mu\text{m}$ ] of diameter. Ultrasonic inflects by the stationary cylindrical enclosure. In order to remove the inflection, we cut a part of cylindrical enclosure to make flat plane in the outside of cylindrical enclosure.

## 2.4 Flow visualization and PIV analysis

We also conduct both flow visualization and PIV analyses. The flow visualizations are performed using the same particles as the UDM measurements. For the PIV analyses, we use two consecutive photos, and carry out cross-correlation analyses. A laser sheet from a YAG laser lightens up the  $r-z$  plane or the  $r-\theta$  plane between two of disks. The flow visualization is recorded by a high-speed camera. Light inflection through the stationary cylindrical enclosure induces the distortion of images. In order to remove the distortion, we put a square-prism container surrounding the cylindrical enclosure, and fill up water between the cylindrical

enclosure and the square-prism container.

### 3 RESULTS AND DISCUSSION

#### 3.1 Case A (axial mode)

Fig.2 shows PIV analyses on the  $r$ - $z$  plane. Five successive figures (a)-(e) are taken with a regular interval of the same non-dimensional time  $t/t_d$  of 0.100/4. We can see a pair of toroidal-vortical structures near the cylindrical enclosure. The structures fluctuate periodically in the  $z$  direction. Then we can classify the flow into the mode . Note that the core boundary is at  $r/R_d = 0.65$ , and that the fluctuation of  $v_r$  is much smaller than  $v_z$  far from the core boundary.

Fig.3 (a) shows the time history of radial velocity  $v_r$  by PIV, and Fig.3 (b) shows one by UDM. The vertical axis is non-dimensionalised as  $v_r/V_d$  and horizontal axis is non-dimensionalised as  $t/t_d$ . The measuring point is non-dimensional radius  $r/R_d=0.93$  and on the interdisk midplane. Fig.4 shows the spectral analyses of the fluctuating component of Fig.3, respectively. There is one dominant spectral peak at non-dimensional frequency ( $f \cdot t_d$ ) of 20.8 by PIV, and at ( $f \cdot t_d$ ) of 20.7 by UDM. Therefore, we can confirm a good agreement between PIV and UDM, and the accuracy of PIV.

Fig.5 (a) shows the time history of axial velocity  $v_z$  by PIV, and Fig.5 (b) shows spectral analysis of it. In Fig.5, the measuring point is same as Fig.3. We can confirm the one dominant peak in Fig.5 (b). However, the peak is about 9.97, which is half of Fig.4 because of the singularity of the interdisk midplane.

#### 3.2 Case B (axial mode)

Fig.6 shows PIV analyses on the  $r$ - $z$  plane. Five successive figures (a)-(e) are taken with a regular interval of the same non-dimensional time  $t/t_d$  of 0.333/4. We can see a pair of toroidal-vortical structures near the cylindrical enclosure. The structures are not symmetry and fluctuate non-periodically in the  $z$  direction. Then we can classify the flow into mode .

Fig.7 (a) shows the time history of  $v_r$  by PIV, and Fig.7 (b) shows one by UDM. The measuring point is same as Fig.3. Fig.8 shows the spectral analyses of Fig.7, respectively. There is one dominant spectral peak at ( $f \cdot t_d$ ) of 1.99 by PIV, and at ( $f \cdot t_d$ ) of 2.00 by UDM. Again, we can confirm a good agreement between PIV and UDM, and the accuracy of PIV.

Fig.9 (a) shows the time history of  $v_z$  by PIV, and Fig.9 (b) shows the spectral analysis of it. Also, the measuring point is the same as Fig.7. We can confirm one dominant spectral at ( $f \cdot t_d$ ) of 2.99, no dominant peaks at ( $f \cdot t_d$ ) 20. Hence, the dominant peaks are considered to corresponding to the circumferential mode 2 or 3.

### 4 CONCLUSIONS

In order to reveal the flow modes between co-rotating disks, we have conducted both PIV and UDM measurements for two cases A and B. The following conclusions are obtained.

1. We have confirmed the axial modes (Case A) and (Case B), using UDM measurement technology, as well as PIV analysis. Both results by UDM and PIV show good agreements, by which we can confirm the accuracy of PIV.
2. In the axial mode (Case A), radial velocity shows dominant non-dimensional frequency of 21. In particular, axial velocity on the interdisk midplane shows half of this frequency.
3. In axial mode , both radial and axial velocities show no dominant spectrum peak at non-dimensional frequency of about 20, but show a dominant peak at much lower frequency. The peak is considered to correspond to the circumferential mode 2 or 3.

### REFERENCES

- [1] Hirata K, Furue M, Sugawara N, Funaki J: An experimental study of three-dimensional vortical structures between co-rotating disks, IOP Journal of Physics Conference Series, Vol.14 (2005), 213-219.
- [2] Lennemann E: Aerodynamic aspects of disk files, IBM J. Res. Dev., Vol.15, No.16 (1974) 480-488.
- [3] Herrero J, Giralt F, Humphery J A C: Influence of the geometry on the structure of the flow between a pair of corotating disks, Physics of Fluids, Vol.11, No.1 (1999) 88-96.
- [4] Funaki J, Takizawa K, Hirata K, Yano H: Flow modes in gap between coaxial rotating disks, Trans.JSME, Vol.61, No.588 (1995) 160-165 (in Japanese).

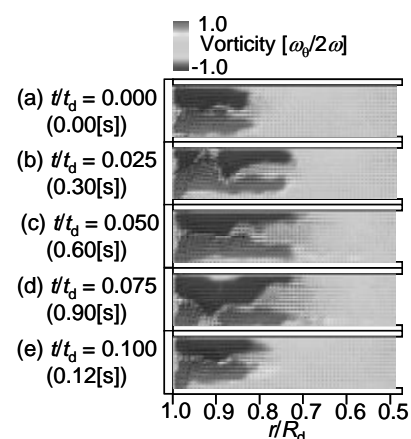


Fig.2 : Velocity vectors and vorticity  $\omega_b$  on the  $r$ - $z$  plane (for Case A).

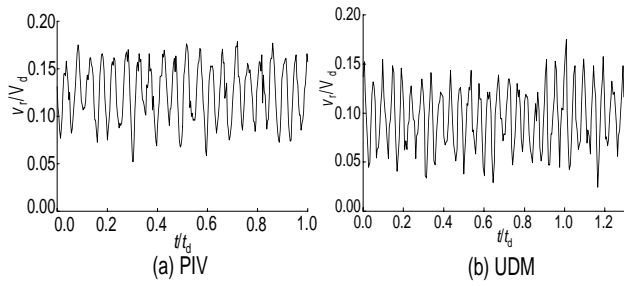


Fig.3 : Radial velocity  $v_r$  at  $r/R_d=0.93$  and on the interdisk midplane (for Case A).

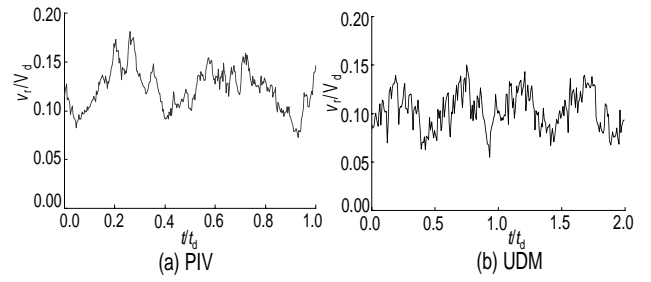


Fig.7 : Radial velocity  $v_r$  at  $r/R_d=0.93$  and on the interdisk midplane (for Case B).

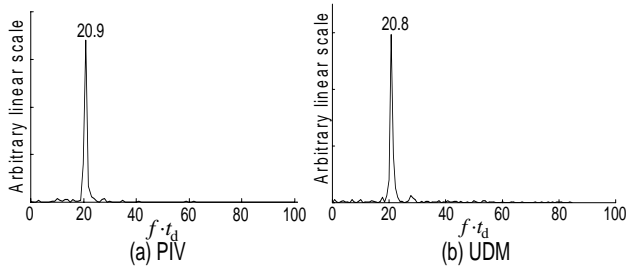


Fig.4 : Spectra of radial velocity  $v_r$  at  $r/R_d=0.93$  and on the interdisk midplane (for Case A).

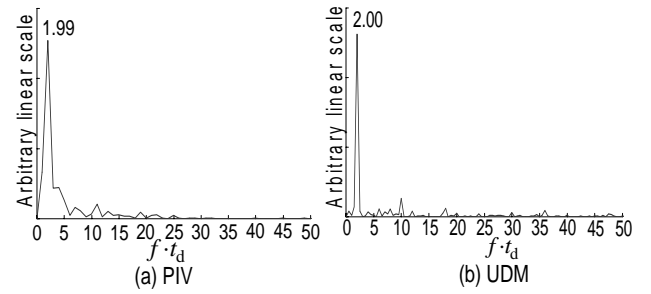


Fig.8 : Spectra of radial velocity  $v_r$  at  $r/R_d=0.93$  and on the interdisk midplane (for Case B).

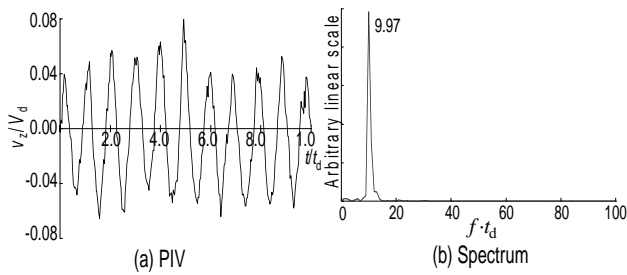


Fig.5 : Axial velocity  $v_z$  (by PIV) at  $r/R_d=0.93$  on the interdisk midplane, and its spectrum (for Case A).

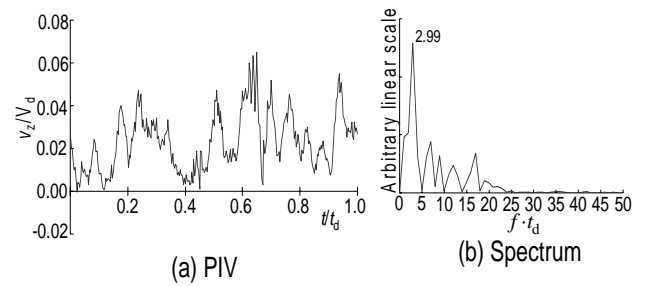


Fig.9 : Axial velocity  $v_z$  (by PIV) at  $r/R_d=0.93$  on the interdisk midplane, and its spectrum (for Case B).

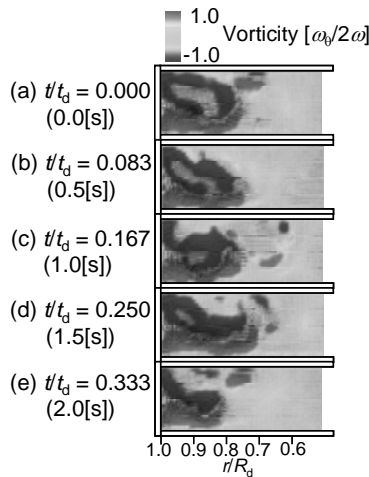


Fig.6 : Velocity vectors and vorticity  $\alpha_\theta$  at  $r/R_d=0.93$  and on the interdisk midplane (for Case B).

## Flow Visualisation inside a Flip-Flop using UVP

Jiro FUNAKI, Katsuya HIRATA, Tatsuya INOUE and Hiroyuki MATSUDA  
Dept. Mech. Engng., Doshisha Univ., Kyoto 610-0321, Japan

Hirochika TANIGAWA  
Dept. Mech. Engng., Maizuru Tech., Maizuru 625-8511, Japan

This research deals with the switching mechanism of a flip-flop jet nozzle with a connecting tube, which is based on the measurements of pressure in two chambers, velocity in the connecting tube and velocity distribution between two inside walls of the nozzle, *i.e.*, reattachment walls. The authors particularly focus on the details of switching flow field inside the nozzle, using a Ultrasound-Velocity-Profile monitor (UVP monitor). As a result, two re-circulating flows, *viz.*, two vortical structures, are shown on both side walls inside the nozzle. By means of the simultaneous observation of chamber pressures and connecting-tube velocity with UVP results, we show a coherent scenario of this jet-oscillation phenomenon.

**Keywords:** Flowmeter, Fluid Logic, Fluidics, UVP, UDM, Flow Induced Vibration

### 1 INTRODUCTION

The flip-flop jet nozzle (hereafter, referred to as FFJN) is one of the oscillator elements of the fluid logic, which uses the Coanda effect where a jet reattaches to a side wall. (for example, see[1]). The FFJN has control ports on both side walls near a primary nozzle. Two chambers connected to the control port are linked by a connecting tube, to cause jet's oscillation. From the practical points of view, we can use the FFJN as a flow meters, because its oscillation frequency increases with flow rate. In addition, the FFJN is useful for shear-layer control and mixing enhancement with secondary flow. For example, Morris et al.[2] have considered the application to gas-solid two phase flow, and showed the mixing enhancement as fuel-spray nozzles. In general, as the FFJN has no mechanically moving parts, it keeps good features such as low production cost, high reliability and robustness against temperature variation density variation and so on.

References [2]-[6] are best studies about the FFJN. Raman et al.[5] has conducted experiments on the nozzle with various geometries, and shown the relation of the oscillation frequency with the connecting-tube length, with the connecting-tube volume and with the nozzle-pressure ratio. Funaki et al.[6] have shown that the jet's switching occurs when the time-integral of inflow momentum from the control port into the lower side attains a certain value. However, we have no knowledge about the detail of the flow inside the FFJN.

In the present study, in order to reveal the flow field inside the FFJN, we carry out the measurements on flow velocity distributions inside the FFJN, on pressures in the chambers and on velocity in the connecting tube. Because flow inside the FFJN is turbulent, we conduct a conditional sampling by ultrasound-velocity-profile monitor (hereafter,

referred to as UVP), using a connecting tube velocity as a reference.

### NOMENCLATURE

$b$	: breadth of an primary-nozzle exit [m]
$d$	: inner diameter of a connecting tube [m]
$f$	: frequency of a oscillating jet [Hz]
$L$	: length of a connecting tube [m]
$P_A$	: pressure in Chamber A [Pa]
$P_B$	: pressure in Chamber B [Pa]
$Q$	: total flow rate [m <sup>3</sup> /s]
$Q_A$	: half section flow rate of the side A [m <sup>3</sup> /s]
$t$	: time [s]
$T$	: period of a oscillation jet [1/s]
$U_{PN}$	: velocity at a primary-nozzle exit [m/s]
$U_{CT}$	: velocity at a connecting-tube section [m/s]
$R_A$	: reattachment length on the side A [m]
$R_B$	: reattachment length on the side B [m]
$\zeta$	: vorticity [s <sup>-1</sup> ]
*	: non-dimensional

### 2 EXPERIMENTAL METHOD

Fig.1 shows a schematic diagram of the tested FFJN. We decide its basic geometrical dimensions according to Viet's[3]. (For the details, see Tab.1.) Here we take the breadth  $b$  of an primary-nozzle exit as a length scale, and the mean flow velocity at the primary-nozzle exit as a velocity scale. Tested Reynolds number is fixed to  $1.83 \times 10^4$ .

Fig.2 shows a schematic diagram of the present experimental apparatus. A turbo pump ① drives the flow of water from a large water tank. Through a flow meter ② and a long straight pipe ③ as a flow conditioner, water flows into a FFJN ④. As the

FFJN is sunk in the large water tank, water can circulates.

We measure velocities inside the FFJN and a connecting tube ⑤ using a UVP monitor system ⑥ and ⑦. we measure pressures in two chambers are using pressure transducer ⑧ with a strain amplifier ⑨. Data from the UVP monitor and the pressure transducers are simultaneously recorded by a PC ⑩ with a A/D-converter board.

Fig.3 shows the position of a ultrasound transducer for the inside FFJN measurement with the present coordinate system. We traverse the transducer in the  $y$  direction (cross-streamwise) with a spatial resolution of  $0.15s$ , or in the  $x$  direction (streamwise) with a spatial resolution of  $0.22s$ .

The transducer's oscillation frequency is  $4$ [MHz]. UVP measurement volume is a disc with a diameter of  $5$ [mm] and with a thickness of  $0.75$ [mm].

The transfer particles are made of polyethylene with a mean diameter of  $1.2 \times 10^{-4}$ [m]. As the Specific gravity of the tracer particles is  $0.918$ , we coat them with detergent in order to avoid them, floating on water surfaces.

Fig.4 (a) shows a sample raw of the velocities inside the FFJN. In general, the flow inside the FFJN is periodical, but it include strong turbulent components. For simultaneous, the number of available UVP transducers is limited. Therefore, it is necessary to conduct a conditional sampling to only periodic components. Here, we take the pressure difference  $\Delta P$  between two chambers, as a reference signal. Specifically speaking, as shown in Fig.4 (b), we divide one period  $T$  into eight, equivalently. Then, at the times of these eight points, we assembly average raw velocities over 50 periods.

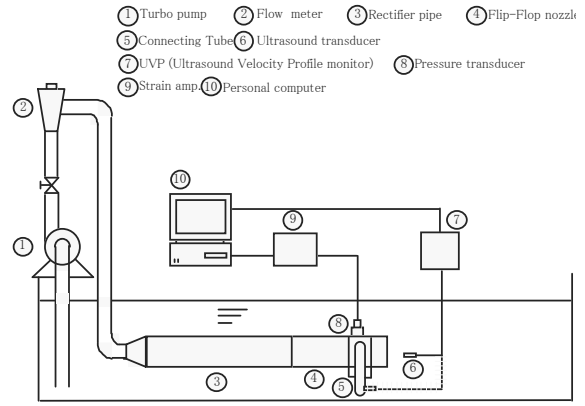


Fig. 2: Schematic of experimental apparatus.

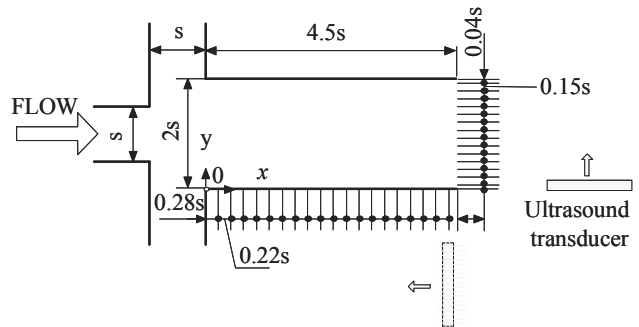


Fig. 3: Position of Ultrasound transducer and coordinate system.

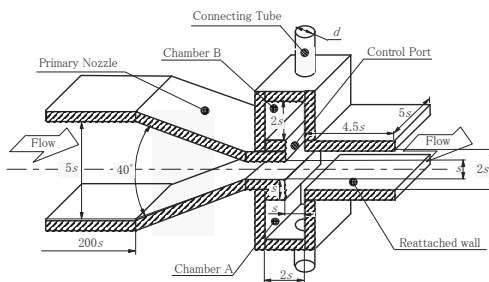
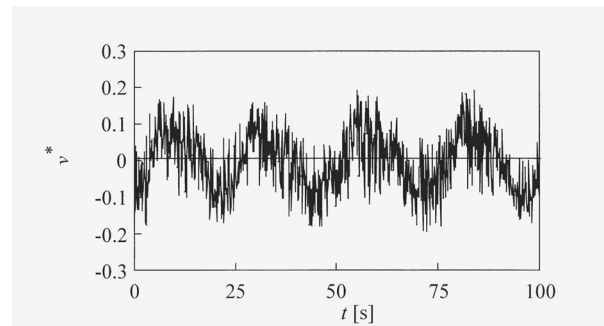


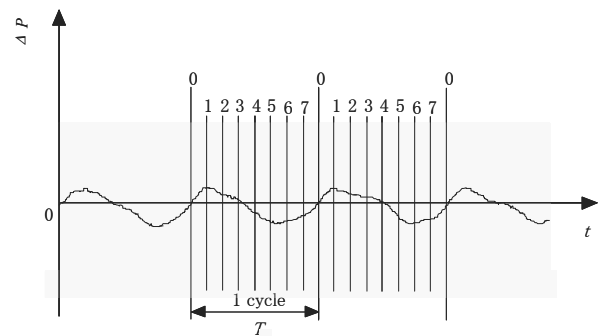
Fig. 1: Schematic of flip-flop jet nozzle.

Tab. 1: Experimental parameters.

$s$ [m]	0.04
$h$ [m]	0.2
$AR (=h/s)$	5
$d$ [m]	0.052
$d/s$	1.3
$L$ [m]	1.6
$L/s$	40
$Re$	$1.83 \times 10^4$



(a)  $v^*$  ( $x/s=3.83, y/s=1.00$ )



(b)  $\Delta P$  and sampling-point definition

Fig. 4: Sampling raw data.

### 3 RESULTS AND DISCUSSION

#### 3.1 Velocity vectors and vorticity contours inside the FFJN

Fig.5 shows velocity vectors and vorticity contours inside the FFJN with no oscillation. Here, to cease flow oscillation, we close the control parts. The jet from the side A, which is the lower side in the figure, usually, the primary-nozzle jet keeps to deflect toward either the side A or the side B. And we can make the jet deflect toward the side B by means of appropriate initial disturbances.

We compare the no-oscillation jet in Fig.5, with the most deflected jet in Fig.6 (g) and Fig.7 (g). At first, we focus on re-circulating flow on the upper side B. The re-circulating flow in Fig.5 (a) is slightly longer than that in Fig.6 (g). While it is difficult to read the magnitude of the reverse-flow velocity from the figures, the magnitude in Fig.5 (a) tends to be much longer than Fig.6 (g). The magnitudes of vorticity in the reverse-flow in Fig.5 (b) are almost same as Fig.7 (g). But, the maximum-magnitude location, which is approximated to be the re-circulating-flow centre, in Fig.5 (b) is closer to the side wall B than Fig.7 (g).

Next, we show the jet in ordinary oscillation. Fig.6 and 7 show timely-successive velocity vectors and vorticity contours in one period, respectively. We can confirm exactly periodic oscillator flow in both figures. We can also confirm the close correspondence between Fig.6 and 7.

When we watch near side-wall areas, we can observe reverse flows on the both side walls at any time. Namely, a re-circulating flow always exists on each side wall.

Next, we focus on a re-circulating flow on the lower side A. There is no reverse flow, in Fig.5, while there is small but strong reverse flow in Fig.6 (g) and 7 (g). In Fig.5, a re-circulating-flow region becomes small enough to go out of the present visualized range.

In summary, the flow in ordinary oscillation jet is far from the corresponding non-oscillation flow.

#### 3.2 Relation of inside FFJN flow with connecting-tube flow

Fig.8 show assembly-averaged time histories of the connecting-tube flow parameters and the inside-FFJN flow parameters. Specifically speaking, as the former, we show the pressures  $P_A$  and  $P_B$  in the chamber A and B, the difference  $\Delta P$  between  $P_A$  and  $P_B$ , and the non-dimensional velocity  $U_{CT}^*$  at a connecting-tube cross section. As the latter, we show the non-dimensional reattachment lengths  $R_A$  and  $R_B$  on the side A and B, the non-dimensional vorticities  $\zeta_A^*$  and  $\zeta_B^*$  at upstream points on the side A and B at  $(x/s, y/s) = (0.50, 0.67)$  and  $(0.50, 1.67)$ , and the non-dimensional half-section flow rate  $Q_A/Q$  on the side A. Here,  $U_{TU}^*$  is positive, when the flow

in the connecting tube goes from the side A to the side B, and vice versa. We can confirm almost synchronized relations among  $P_A, P_B, \Delta P, R_A^*, R_B^*, \zeta_A^*$  and  $\zeta_B^*$ , but there are a slight phase lag in  $Q_A/Q$  and large phase lag in  $U_{TU}^*$  in comparison with those.

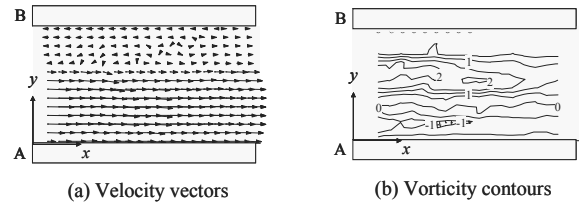


Fig. 5: Flow of non-oscillating jet.

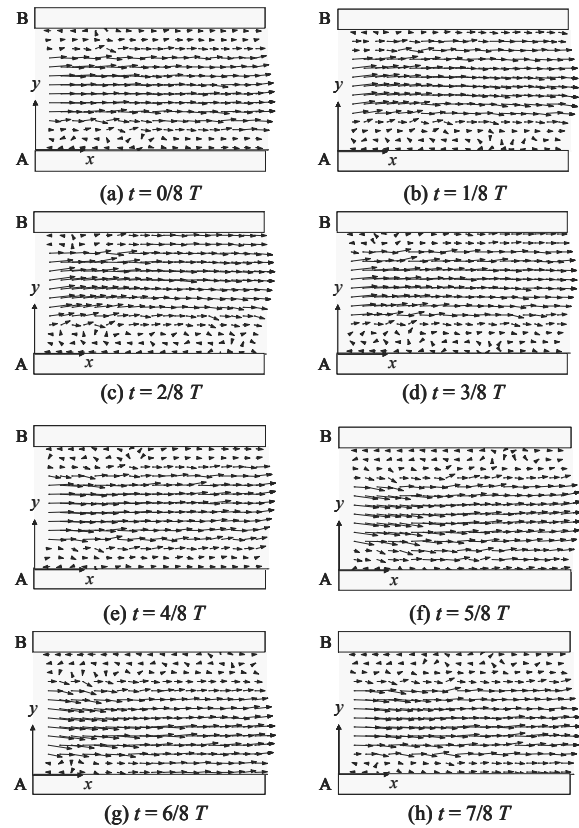


Fig. 6: A sequence of velocity vectors in a period.

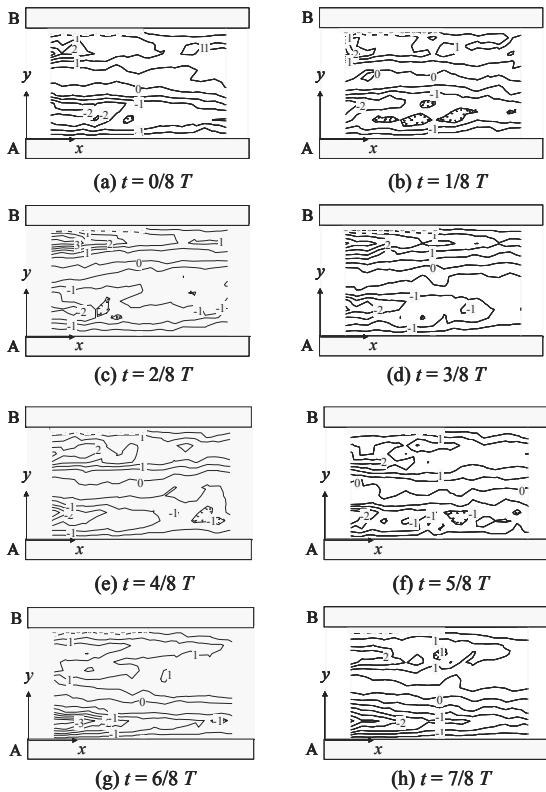


Fig. 7: A sequence of vorticity contours in a period.

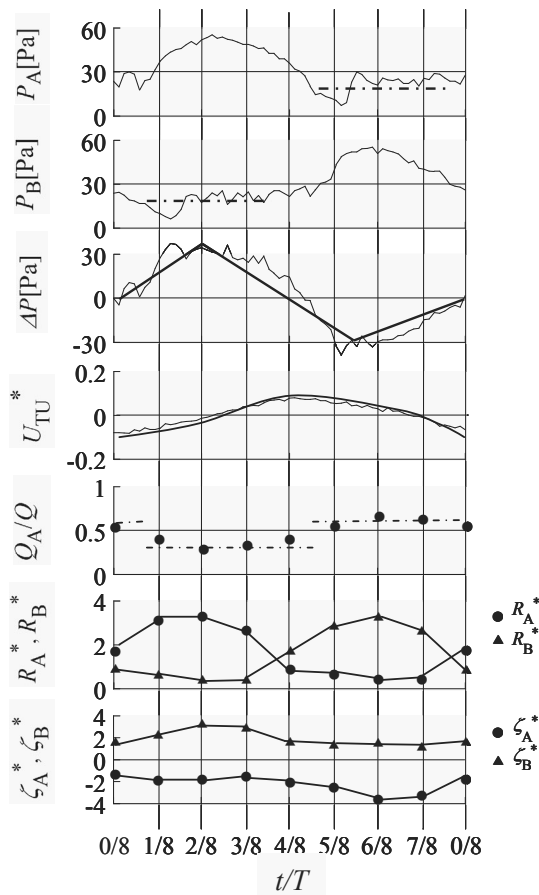


Fig. 8: Time history of  $P_A$ ,  $P_B$ ,  $\Delta P$ ,  $U_{TU}$ , and  $Q_A/Q$  in a period.

### ACKNOWLEDGEMENTS

This study was partly supported by the Academic Frontier Research Project on “Next Generation Zero-emission Energy Conversion System” of Ministry of Education, Culture, Sports, Science and Technology.

### 4 CONCLUSIONS

In order to reveal the oscillation phenomenon in the FFJN, we have conducted UVP measurements using a conditional sampling technique. Non-oscillating flow is far from the flow in ordinary oscillation. At any time, there is a re-circulating flow, which is accompanied with a flow re-attachment and with reverse flow. We have shown timely-consecutive velocity vectors and vorticity contours in one period. In addition, by means of simultaneous measurements for a connecting tube, we have shown the relation between the inside flow and the connecting tube flow.

### REFERENCES

- [1] Ozaki, S. and Hara, Y., Introduction to Fluid Logic, Nikkan-Kyoto-Shinbunsha, Tokyo, 1963.
- [2] Morris, G.J., Jurewicz, J.T. and Palmer, G.M., “Gas-Solid Flow in a Fluidically Oscillating Jet,” *Trans. ASME Journal of Fluids Engineering*, Vol.114, 1992, pp. 362-366.
- [3] Viets, H., “Flip-Flop Jet Nozzle,” *AIAA Journal*, Vol.13, No.10, 1975, pp. 1375-1379.
- [4] Raman, G., Hailye, M. and Rice, E. J., “Flip-Flop Jet Nozzle Extended to Supersonic Flows,” *AIAA Journal*, Vol.31, No.6, 1993, pp. 1028-1035.
- [5] Raman, G., Rice, E. J., Cornelius, D. M., “Evaluation of Flip-Flop Jet Nozzle for Use as Practical Excitation Devices,” *Trans. ASME*, Vol.116, 1994, pp.508-515.
- [6] Funaki, J., Mizuno, Go., Kondo, M. and Hirata K., “Oscillation Mechanism of a Flip-Flop Jet Nozzle Based on the Flow which Flows through a Connecting Tube,” *Trans. JSME(Series B)*, Vol.65, No.631, 1999, pp. 928-933 (in Japanese).
- [7] Rockwell, D. and Naudascher, E., “self-Sustained Oscillations of Impinging Free Shear Layers,” *Ann. Rev. Fluid Mech.*, Vol.11, 1979, pp. 67-94.

# An Investigation in Using UVP for assisting in Rheological characterisation of Mineral Suspensions

Rainer Haldenwang, Reinhardt Kotzé, Paul Slatter and \*Olivier Mariette

Flow Process Research Institute, Cape Peninsula University of Technology, PO Box 652 Cape Town 8000, South Africa. \*Met-Flow, Av. Mon-Repos 14 - 1005 Lausanne, Switzerland.

The rheological characterisation of mineral suspensions for the prediction of flow in pipes and open channels is of considerable practical importance. Most predictive models depend on accurate rheological parameters. Mineral suspensions including mining tailings are mostly non-Newtonian suspensions with many exhibiting an apparent yield stress. These models are empirical in nature and require extensive laboratory testing to determine their characteristics. The Flow Process Research Centre at the Cape Peninsula University of Technology has for a number of years been investigating the behaviour of such suspensions. Rheological parameters have been mainly obtained from tube viscometry. This means measuring pressure drop and flow rate in two or more tubes of different diameter to produce flow curves. For comparison, rotary viscometry has also been used. Mineral suspensions are opaque and laser technology cannot be used. To progress to a more fundamental understanding of the flow behaviour of these fluids in pipes, fittings and flumes it is essential to measure velocity profiles. The principal problem here is that the acoustic behaviour and measurement techniques for these fluids using UVP techniques is as yet unproven. This objective of this paper is to show that these techniques are viable, and show some promising initial results in both the tube and flume geometries with two different mineral suspensions.

**Keywords:** Mineral suspensions, rheology, velocity profiles, tube viscometry, ultrasound.

## 1 INTRODUCTION

As chemical, mechanical and mining engineers all over the world have had to deal with stricter environmental restrictions and use less water, the concentrations of the mining tailings have had to increase, in order to comply with superior disposal techniques. With this increase in concentration the tailings have become progressively non-Newtonian in character, and therefore more and more difficult to transport in pipelines and flumes. A proper understanding of the rheological behaviour and in-line control of rheology has become critical. These tailings are complex suspensions and are opaque. With the development and adaptation of the UVP system for measuring velocity profiles and using this for in-line rheological characterisation [1-6] this has given engineers and scientists in the mining engineering field a new tool to investigate the industrial flow process behaviour of these fluids.

## 2 LITERATURE

The objective of this paper is not to give a detailed overview of the literature available in this field but only to provide the relevant material related to the test work.

### 2.1 Rheological characterisation

The two fluids tested can be classified as follows: The Bentonite is a typical Bingham fluid and the kaolin suspension a Herschel-Bulkley or yield-pseudoplastic fluid. The general rheological equation for a Herschel-Bulkley fluid is:

$$\tau_0 = \tau_y + K(\dot{\gamma}_0)^n, \quad (1)$$

where  $\tau_0$  is the wall shear stress,  $\dot{\gamma}_0$  true shear rate at the wall, K the consistency index and n the power law index [7].

### 2.2 Tube viscometry

A tube viscometer is in essence a small diameter pipeline and therefore geometrically similar to a pipe. The test fluid flows at a measured flow rate through the tube and the pressure drop  $\Delta p$  is measured between two fixed points L m apart in the pipe. The relationship between the wall shear stress  $\tau_0$  and the volumetric flow rate Q and the shear stress  $\tau$  is as follows [8]:

$$\frac{Q}{\pi R^3} = \frac{8V}{D} \frac{1}{\tau_0^3} \int_0^{\tau_0} \tau^2 f(\tau) d\tau \quad (2)$$

Where  $\tau_0 = \frac{R}{2} \left( -\frac{\Delta p}{L} \right)$  and  $\left( -\frac{\Delta p}{L} \right)$  is equal to the pressure drop per unit length of tube. The shear stress at any radius r is:

$$\tau = \frac{r}{2} \left( -\frac{\Delta p}{L} \right). \quad (3)$$

A plot of  $8V/D$  vs  $\tau_0$  will give a unique line for a given material for all values of R and  $\left( -\frac{\Delta p}{L} \right)$  in laminar flow, [9]. This also provides confirmation of the assumption that the time dependent properties

of the fluids tested are not significant (ibid).

The problem with tube viscometry is that  $8V/D$  is not true shear rate but the wall shear rate for a Newtonian fluid, therefore this “pseudo” shear rate has to be transformed to the true shear rate at the wall,  $(\dot{\gamma}_0)$ .

For a flow curve where the form is unknown Equation 1, after some manipulation, will yield the following according to (ibid).

$$\left(-\frac{du}{dr}\right)_0 = \frac{8V}{D} \left(\frac{3}{4} + \frac{1}{4} \frac{d \log(8V/D)}{d \log \tau_0}\right). \quad (5)$$

Various forms of this equation exist, one being the Rabinowitsch-Mooney Equation:

$$\dot{\gamma}_0 = \left(-\frac{du}{dr}\right)_0 = \frac{8V}{D} \left(\frac{3n'+1}{4n'}\right) \quad (6)$$

where

$$n' = \frac{d(\log \tau_0)}{d(\log(8V/D))}. \quad (7)$$

If one plots a log-log pseudo shear diagram with  $\tau_0$  versus  $8V/D$  for the laminar flow region, then  $n'$  is the slope of the tangent of the graph. The slope will only be approximately constant if the fluid is a power-law fluid (ibid).

## 2.2 Velocity Profiles

Equation (1) can be integrated to yield the velocity profile in a pipe [10]. In the case when  $\tau = \frac{r\Delta p}{2L} \leq \tau_y$ , the fluid does not shear and adjacent laminae are stationary relative to one another. This occurs for values of  $r \leq r_{\text{plug}}$  where

$$r_{\text{plug}} = \frac{R\tau_y}{\tau_0}. \quad (8)$$

For  $R > r > r_{\text{plug}}$  the fluid shears and Eq. (1) can be integrated to yield

$$u = \frac{\left(\frac{1}{K}\right)^{\frac{1}{n}}}{\left(\frac{\Delta p}{2L}\right)^{\frac{n}{n+1}}} \left[ \left(\tau_0 - \tau_y\right)^{\frac{n+1}{n}} - \left(\tau - \tau_y\right)^{\frac{n+1}{n}} \right]. \quad (9)$$

When  $0 < r < r_{\text{plug}}$  the fluid moves as a plug at a uniform plug velocity  $u_{\text{plug}}$ .

## 3 EQUIPMENT USED

The tests were all conducted in the Flow Process Research Centre laboratory of the Cape Peninsula University of Technology.

### 3.1 Flow Profile Measurements

For measuring the velocity profiles the Metflow-SA UVP was used with a 4 MHz transducer mounted at

an angle of 20 degrees with the vertical. The measurements in the pipe were made through the Perspex wall. A small adaptor was fitted onto the pipe and US gel was used to transmit the echo from the transducer to the pipe wall. In the flume the transducer was suspended into the fluid from a small unit housing the transducer.

### 3.2 Tube viscometer

The pipe used was a 50 mm diameter plexi-glass tube which forms part of a fittings rig. The flow in the tube is measured with a mass flow meter and the point pressure with Fuji pressure sensors. The pressure transducers are mounted 2 m apart. Flow is produced by a progressive cavity positive displacement pump fitted with a variable speed drive. The pressure drop and flow measurement signals are relayed via a data logger to a PC.



Figure 1: Layout of fittings rig.

The transducer position is displayed in Figure 2.

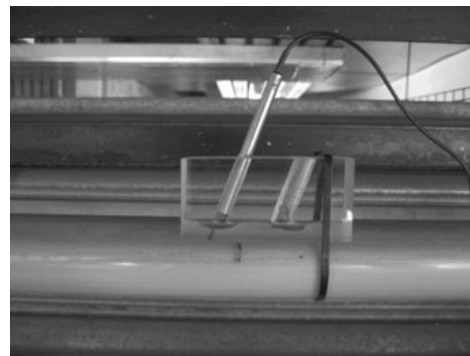


Figure 2: The 4 MHz probe fitted to the 40 mm pipe.

### 3.3 Tilting Flume

The flume used for the test work is a 75 mm wide by 5 m long tilting flume. The flume is linked to an in-line tube viscometer fitted with three diameter pipes from 13 mm to 80 mm in diameter. Each tube is fitted with a magnetic flow meter and pressure tappings connected to a differential pressure sensor. Flow depth in the flume is measured with electronic

depth gauges. For purposes of these preliminary tests a simple device was built to lower the ultrasound transducer at a fixed angle into the fluid flowing in the flume. A picture of the flow setup depicting the position of the probe in the flume is shown in Figure 3.

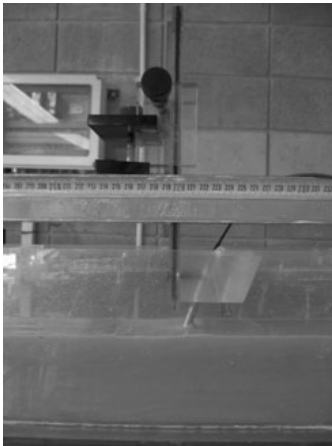


Figure 3: The 4 MHz probe fitted to the flume.

### 3.4 Rotary Viscometer

The rheological parameters were also obtained from flow curves measured with a Paar Physica MC-1 rheometer fitted with a cup and roughened bob.

### 3.5 Materials tested

Two mineral suspensions were tested namely kaolin and Bentonite.

**Kaolin:** Dry kaolin powder was used to prepare kaolin:water suspensions. The  $d_{85}$  was about 8 micron. The concentration tested was 8,25% c/v with an RD of 1,136.

**Bentonite:** The concentration tested was 5,66% c/w with an RD of 1,035.

## 4 RESULTS AND DISCUSSION

### 5.1 Rheology

From the rotary viscometer a flow curve for the kaolin and Bentonite was obtained and the rheological parameters determined. The results are summarised in Table 1.

Table 1: Rheological parameters of fluids tested

Material	$\tau_y$ (Pa)	K (Pa.s)	n
Kaolin 8.25%	5	0.92	0.59
Bentonite 5.66%	21.95	0.043	1

### 5.2 UVP settings

The setting used for the velocity measurements are summarised in Table 2.

Table 2: UVP settings

Kaolin 8.25%	2,8 l/s	1.9 l/s	1.3 l/s
Sound speed (m/s)	1601	1601	1601
PRF (kHz)	12.87	8.75	5.26
Angle probe	$20^0$	$20^0$	$20^0$
Frequency (MHz)	4	4	4
Cycles	4	4	4
US Voltage (V)	150	150	150
Bentonite 8.25%	2.26 l/s		
Sound speed (m/s)	1628		
PRF (kHz)	4.75		
Angle probe	$20^0$		
Frequency (MHz)	4		
Cycles	2		
US Voltage (V)	60		

### 5.3 Velocity profiles in pipe

The following velocity profiles in Figures 4-6 were obtained for the kaolin suspension at flow rates of 2.8, 1.9 and 1.3 l/s respectively.

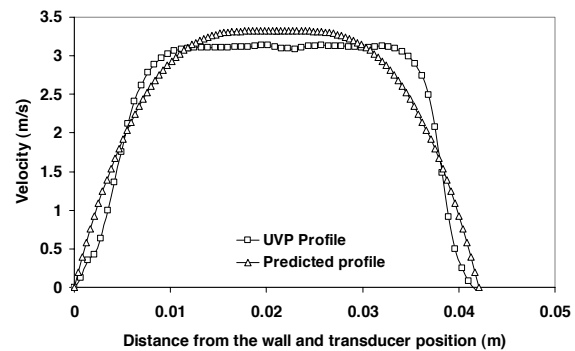


Figure 4: Velocity profile in 42 mm pipe for kaolin at flow rate of 2.8 l/s.

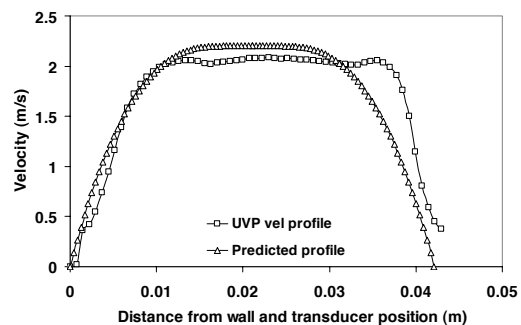


Figure 5: Velocity profile in 42 mm pipe for kaolin at flow rate of 1.9 l/s.

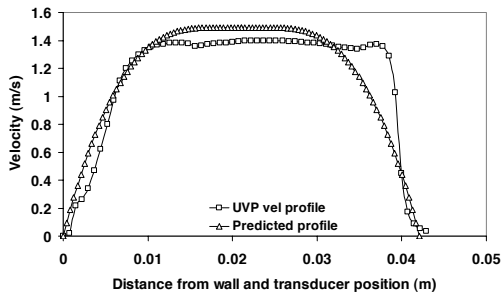


Figure 6: Velocity profile in 42 mm pipe for kaolin at flow rate of 1.3 l/s.

From the above profiles it can be seen that if the instrument is set up properly the ultrasound signal is able to penetrate the fluids at least to just about the end of the plug. The kaolin attenuates the signal more than the Bentonite. With higher concentrations and larger pipe diameters this could present a problem. This could however be overcome if two transducers were used.

#### 5.4 Velocity profile in Flume

The tests in the flume were more of an exploratory nature and the intention was to determine how well the UVP profile would function in the Bentonite suspension. The setup was somewhat crude and the following profile will show that the attenuation in the Bentonite is minimal and the whole flow depth was easily penetrated.

In Figure 7 the velocity profile for the Bentonite suspension is presented.

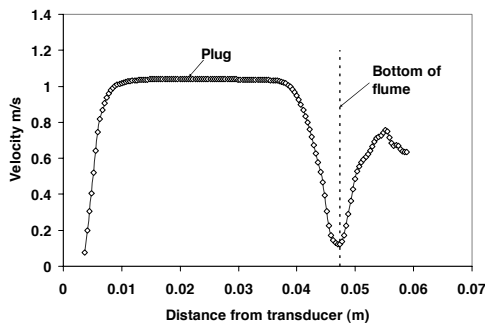


Figure 7: Velocity profile in 75 mm wide flume for Bentonite at flow rate of 2.26 l/s.

## 6 CONCLUSION AND RECOMMENDATIONS

The initial results obtained have been very encouraging and we are confident that the instrument will assist us in obtaining velocity profiles of complex non-Newtonian mineral suspensions. This opens a number of new avenues of research to us. Some of these are in-line measurement of rheology which has already been shown to be feasible by Ouriev and Windhab and Wiklund *et al.* [3-6]. Flow velocity profiles through various

geometries now also becomes a possibility as well as establishing accurate flow profiles in different flume cross-sections.

What will be essential is to test the attenuation of the ultrasound signal in different concentrations of the suspensions so as to better understand the limitations of the instrument.

The initial tests have however given us a window of opportunity to examine the flow of viscous mineral suspensions in different flow configurations.

## 7 ACKNOWLEDGEMENTS

The authors would like to acknowledge the following:

Mr Gerard Gogniat of Met-Flow SA of Lausanne for sponsoring Olivier Mariette's visit to South Africa to assist in the testing programme.

The National Research Foundation of South Africa (NRF) and the Cape Peninsula University of Technology for funding.

## REFERENCES

- [1] Takeda Y. 1995. Velocity Profile Measurement by Ultrasonic Doppler Method. *Exp Thermal and Fluid Sci.* 10:444-453.
- [2] Takeda Y. 1999. Ultrasonic Doppler Method for Velocity Profile Measurement in Fluid Dynamics and Fluid Engineering. *Experiments in Fluids.* 26:177-178.
- [3] Ouriev B. 2000. Ultrasonic Doppler Based In-Line Rheometry of Highly Concentrated Suspensions. ETH dissertation No. 13523, ISBN 3-905609-11-8. Zurich, Switzerland.
- [4] Ouriev B. & Windhab E.J. 2002. Rheological study of concentrated suspensions in pressure-driven shear flow using a novel in-line ultrasound Doppler method. *Experiments in fluids.* 32:204-211.
- [5] Wiklund J., Johansson M., Shaik J., Fischer P., Stading M. & Hermansson A. 2001. In-Line rheological measurements of complex model fluids using an ultrasound UVP-PD based method. *Trans Nord Rheol Soc.* V8-9:128-130.
- [6] Wiklund J., Johansson M., Shaik J., Fischer P., Windhab E., Stading M. & Hermansson A. 2002. In-line ultrasound based rheometry of industrial and model suspensions flowing through pipes. *International Symposium on Ultrasonic Doppler Methods for Fluid Mech and Fluid Eng.* 3:69-76.
- [7] Steffe, F.J. 1996. *Rheological processes in food process engineering.* Freeman Press, Michigan, USA.
- [8] Abulnaga, B.E., 2002. *Slurry Systems Handbook.* McGraw Hill, New York.
- [9] Chhabra, R.P., Richardson, J.F. 1999. *Non-Newtonian Flow in the Process Industry.* Oxford: Butterworth-Heinemann.
- [10] Govier, G.W. & Aziz, K. 1972. *The flow of Complex mixtures in pipes.* Van Nostrand Reinhold Co. Florida USA.

# Flow Measurement of Lead Bismuth Eutectic in Spallation Target Model Loop

Hironari Obayashi and Kenji Kikuchi

Nuclear Transmutation Technology Group, Japan Atomic Energy Agency,

2-4, Shirane, Shirakata, Tokai-mura, Ibaraki-ken, 319-1195 JAPAN

E-mail: obayashi.hironari@jaea.go.jp

Yasushi Takeda

Laboratory for Flow Control, Division of Energy and Environmental System,

School of Engineering, Hokkaido University,

N13 W8, Kita-ku, Sapporo, 060-8628 Japan

E-mail: yft@eng.hokudai.ac.jp

Measurement of Lead Bismuth Eutectic (LBE) flow velocity profile was successfully realized in the spallation target model loop of Accelerator Driven System (ADS) by the Ultrasonic Velocity Profiler (UVP) technique. UVP is a powerful tool to measure an instantaneous space-time velocity profile especially on a velocity measurement of an opaque liquid flow, such as liquid metal. However, it has not yet been done well because both of its poor wetting property with stainless steel and of the difficulty in manufacturing probe at high temperature. At lower temperature, wetting of LBE to stainless steel that is a material of target loop is too poor. Therefore, the surface of the test section was treated by polishing, flattening and finally coating with nickel and solder. And we performed velocity measurement along the centerline of the loop and confirmed basic performance of the loop. It was found that there were periodical releases of eddy from the re-circulation region formed near the wall surface of the inner cylinder. We made then a measurement for non-parallel directions with the centerline and observed 3-dimensional structure of LBE flow configuration.

**Keywords:** Liquid Metal, LBE, high temperature, Ultrasonic Velocity Profiler, space-time velocity profile

## 1 INTRODUCTION

### 1.1 Liquid metals as a flowing medium

In the industrial processes, metals are treated and processed in liquid state and they are mostly flowing. For instance, in the steel making, a flow of liquid iron plays an important role in determining its operational efficiency of manufacturing processes and also for designing the molten pot and process channels, especially from the thermal insulation point of view. It is also observed for molten metals to play an important role in welding processes. Flow velocity in such situation becomes unexpectedly large due to a high surface tension and low viscosity of liquid metals.

On the other hand, in active examples of industrial applications, various liquid metals are used as a flow medium for coolant or reacting materials. Typical one is Sodium for fast breeding nuclear reactor (FBR). Other liquid metals are also used in various situations in industry. Among these liquid metals, mercury was convenient since it is in liquid state under room temperature but it is not any more usable due to its toxicity. Sodium is also convenient but as it is reactive with water; its handling requires very careful preventive measures against fire. Gallium is also low melting temperature metal, and it reacts with oxygen in air very radically and a price is too high to use it in a large quantity.

Lead-Bismuth Eutectic (LBE) has advantage to use because its melting temperature is not very high and its chemical state is relatively stable comparative with sodium.

### 1.2 Measurement method of liquid metal flow

It is of utmost importance to investigate flow structure and behavior of liquid metals when it is used in an active manner not only in heat transportation but also a flowing medium, as is the case for any kinds of situations of fluid flow is involved, and as such, fluid mechanics is applied.

It is obvious that any optical method of flow measurement cannot be applied since all the liquid metals are opaque. This meant that non-invasive flow measurement was not possible until the ultrasonic measurement has been established. A single way is to use radiation such as X-ray [1] [2] or neutron [3-6] to visualize the flow. These methods, however, have no sufficient resolution in space and time for making qualitative evaluation of the flow behavior. Furthermore, apparatus for them are inconveniently large, expensive and difficult to use so that they were used only under some special conditions and configurations. Hot-wire/film [7] anemometer, thermal sensor [8] [9] and magnetic probe [9] [10] are all invasive and point wise measurement methods. This is especially disadvantageous for liquid metal flow measurement because high  $Pr$  number and low viscosity causes a

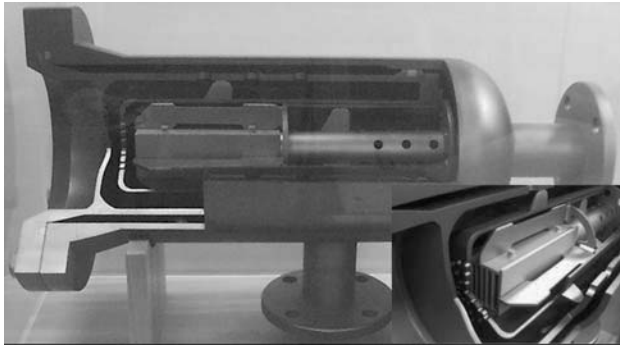


Fig.1: Photograph of LBE spallation target model

very different behavior of momentum and thermal boundary layer around the probe compared with conventional non-metal liquids such a water flow.

#### 1.4 ADS target model loop

Accelerator Driven System (ADS) has been developing in Japan Atomic Energy Agency (JAEA). In the present investigation, a given flow configuration is related to a LBE flow in an ADS target loop mock-up which is described below in some detail. Fig.1 is a photograph of the LBE spallation target model. LBE is enclosed as a neutron source and a coolant in this loop. It is impossible to confirm the cooling performance of the target model loop without knowing of the LBE flow. Furthermore, the flow structure and erosion of the materials of the loop are closely related. Therefore, it is most important work to measure actual LBE flow. Thus, the objectives of this study are to measure LBE flow in this loop, and to investigate the flow structure and the cooling performance. However, as shown in Tab.1, lead bismuth alloy has a high melting point, about 125 degrees centigrade. Because flow temperature of LBE is very high, the measurement is more difficult than other liquid metals flow at room temperature. Therefore, we made a trial measurement and probe the flow structure near a target window sphere.

## 2 EXPERIMENTAL APPARATUS AND CONFIGURATION

### 2.1 JAEA Lead Bismuth loop-2 (JLBL-2)

JAEA Lead Bismuth Loop-2 (JLBL-2) is a model of the spallation target. It is a closed-loop driven by an electro-magnetic pump. Flow rate of the working fluid driven by this pump is constant and it is observed by an electro-magnetic flow meter. This model loop has coaxially arranged annular and tube channels. The radius of the outer cylinder tube is 63 mm and inner cylinder is 35.5mm. The gaps between the two coaxial cylinders are 3 mm. And the total length of the loop is 1504.5 mm. In operating ADS, the temperature of the LBE is expected to reach 500 degrees centigrade. In consideration

Table 1: Physical properties of liquid metals

Physical properties*	Symbol	Unit	Sodium	LBE	Mercury
Melting point	$T_m$	°C	97.8	125	-38.9
Density	$\rho$	kg/m <sup>3</sup>	860.2	10236	13.53
Thermal conductivity	$k$	W/mK	72.3	11.86	8.34
Specific heat capacity	$C_p$	kJ/kgK	1.30	0.147	0.14
Temperature diffusivity	$\alpha \times 10^5$	m <sup>2</sup> s	6.48	0.790	0.60
Prandtl number	$Pr$	-	0.0051	0.189	0.015

\*Sodium and LBE: measured at 371 °C

Mercury: measured at 25 °C

of the durability and heat-resistant temperatures of high temperature transducers, we set the temperature of LBE to 150 degrees centigrade. Because the surface tension of LBE is very high in the temperature range in the neighborhood of the melting point, the wetting conditions with the stainless steel pipe wall surface and LBE are very poor. This insufficient wetting condition does not erode the solid surface, but some problems occur in UVP measurement [11]. Therefore, the inner surface of the measurement section was treated by polishing, flattening and finally coating with nickel and solder. As a result, wetting condition is improved markedly.

### 2.2 Experimental set-up

The temperature of the loop and the LBE are monitored by a plural thermocouple, and kept uniformly at 150 degrees centigrade. The LBE flow passes the gap between the two cylinders, turns over and then forms the reverse direction flow in the inner cylinder. UVP Monitor model-Duo (Met-Flow) was used for the velocity measurement. A high temperature transducer (Japan probe) undertakes the emission and the reception of the ultrasonic burst signals. We used argon gas bubbles rolled up at the free surface in the LBE tank as reflectors for the ultrasonic burst signal to be able to trace the LBE flow. The velocity measurement was performed at the edge of the loop end of the window sphere where a proton beam was incident to the target. This window sphere has a spherical shape and is 3.5 mm thick. Fig.2 (b) is a front view of the measurement window. As shown in the figure, the measurement position is located at the center of the window sphere, and eight points on an arc have this point as their center. The radius of this arc is 14mm, and measurement positions are located at every 45 degrees. As well, the ultrasonic transducer is installed perpendicular to the surface of the window

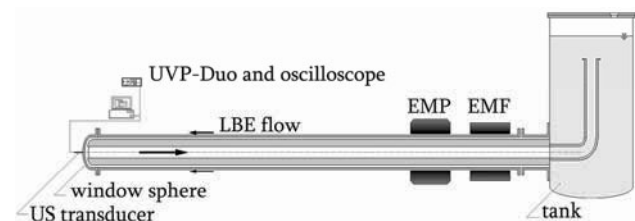


Fig.1: Experimental set-up and schematic illustration of JLBL-2.

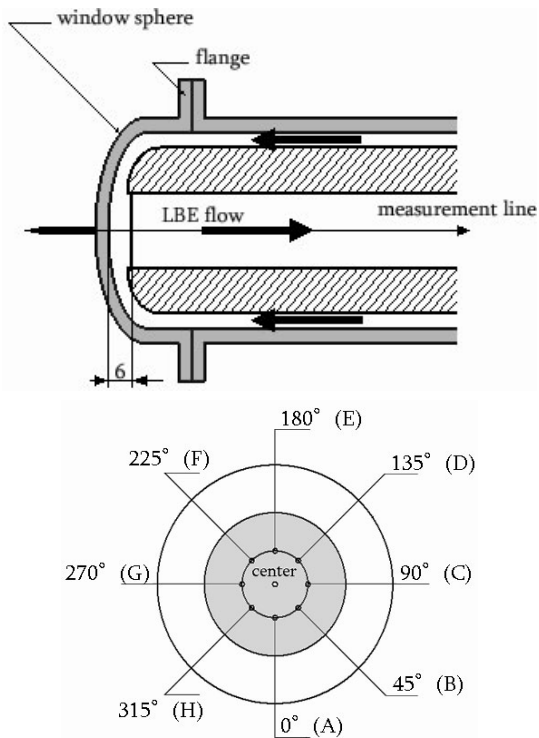


Fig.2: Experimental configuration of the measurement line on the window sphere

- (a) Side view of the test section with measurement line  
 (b) Window sphere and installing position of an ultrasonic transducer

sphere as a countermeasure to prevent the refraction phenomenon of an ultrasonic pulse beam that is caused at the wall surface of the window sphere.

### 3 EXPERIMENTAL RESULTS

#### 3.1 Velocity profiles along the centerline

We changed the flow rates flowing through the loop and measured the velocity profile at the centerline of the inner cylinder. Experimental results are shown in Fig.3, which presents the velocity profiles of each flow rate at the centerline of the inner cylinder of the loop. In this figure, the horizontal axis represents the measured position and corresponds to the distance on the centerline assuming the edge of the loop as the origin. The vertical axis represents averaged velocity data; that is, the number of averaged velocity profiles is 512. In this experiment, the averaged velocity ( $U$ ) in the annular region of the loop was changed, and then measured with an electro-magnetic flow meter installed in the upstream side of the loop. The velocity conditions were set to four phases ( $U = 0.25, 0.50, 0.75,$  and  $1.00$  m/s). Under all velocity conditions, in the averaged velocity profiles provided by this experiment the velocity data shows zero data from the starting position of the measurement to a neighborhood distance of 15 mm. At the inner wall

surface of the target window sphere, the LBE flows coming from annular channels collide with each other. Therefore, a local dead region is formed for the LBE flow near the center of the edge of the loop. It is thought that this result represents a dead region of the LBE flow that extends to the neighborhood a distance of 15 mm from the inner wall surface at the center of the loop. Even if the LBE flow rate of in JLBL-2 increases, the formation of this dead region cannot be avoided. When a proton beam is incident in the JLBL-2, countermeasures apart from increasing the LBE flow rate are necessary; further, it is thought that this dead region interferes with the cooling of the target model loop.

In the side downstream from the dead region, the velocity profiles are at a maximum in the vicinity of a distance 30 mm, and after having suddenly increased, they gently decrease thereafter. By increasing the velocity conditions, the maximum velocity profiles show a proportional relationship; however, there is no proportional relation in the tendency for a decrease in the velocity after the maximum data is obtained. A re-circulation region of the LBE flow is formed on the cylinder pipe wall near the edge of the inner cylinder of the loop. A shrinking flow occurs for the flow in the main direction at any position in this re-circulation region.

A color density plot of the data set on the space-time domain, as given in Fig.4. In this figure, velocity condition is  $U_1$ . Horizontal axis represents the time, and vertical axis represents the distance on the centerline. Color represents the velocity. In this figure, almost velocity data is positive. It is observed that there occurs a space-temporal oscillation in the measured area. In this figure, velocity data shows oblique line and appears periodically in time. These lines show the motion of a fluid volume moving on the measurement line. A moving velocity of this volume that calculated by the inclination of the velocity stripes is about 2.3 mm/s. It is thought that this flow structure is eddies that discharged from the re-circulation region which moved along the centerline.

#### 3.2 Angular velocity profiles

Fig.5 shows the experimental results of the averaged

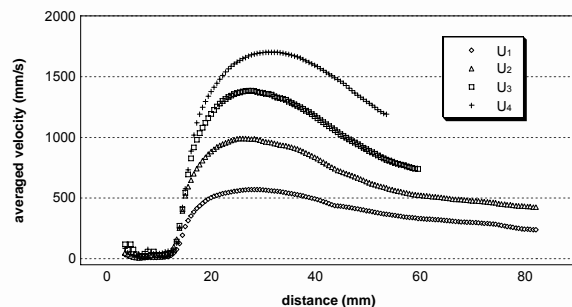


Fig.3: Averaged velocity profile at the centerline of JLBL-2, where velocity conditions are  $U_1, U_2, U_3, U_4 = 0.25, 0.50, 0.75, 1.00$  m/sec

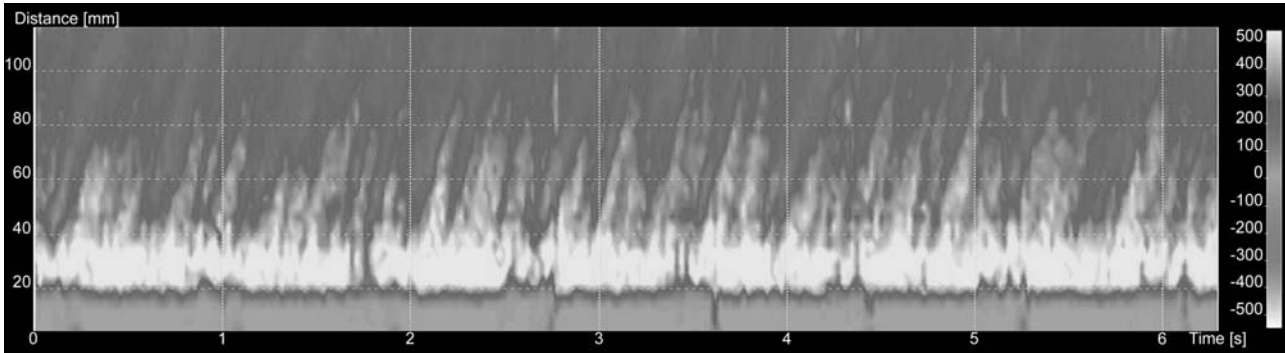


Fig.4: Space-time representation of the time dependent 1D velocity profile, where velocity condition is  $U_1$ .

velocity profiles. Each velocity profile (A) to (H) shows a result measured counterclockwise from positions at intervals of 45 degrees. A velocity condition is  $U_1$ . This figure represents that the LBE flow is approximately symmetric. In the position near the window sphere, it was observed that the flow of the upper side was fast and the lower side was slow. Furthermore, the velocity profiles of the lower side (A, B, H) changes from negative velocity to positive velocity continually. This shows the possibility that an eddy caused by the characteristic of the equipments is formed in the lower side.

#### 4 SUMMARIES

The measurement of LBE flow in JLBL-2 by using UVP, we can obtain following results.

\*There is a space-temporal oscillation that shows the motion of a fluid volume moving on the measurement line near the target window sphere. It is the small eddies that discharged from the recirculation region which moved along and crossed the centerline.

\*LBE flow near the target window sphere is approximately symmetric. However, a standing eddy could be formed in the lower side.

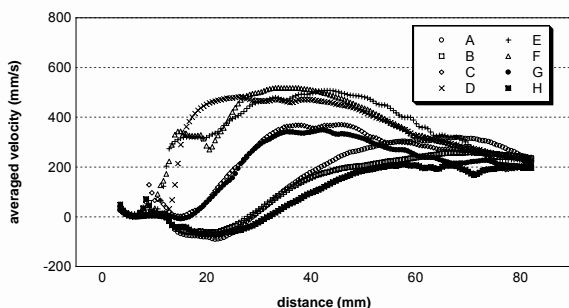


Fig.5: Averaged velocity profiles measured around the centerline of the measurement window at even intervals of angle, where measurement position labeled with A to G are expressed in Fig.2 (b) and velocity condition is  $U_1$ .

#### REFERENCES

- [1]H.Sherif, Abdulla, L.Xin, H.Mark, Anderson, B,Riccardo, L.Michael, Corradini, C.Dae: Liquid-Metal/Water Direct Contact Heat Exchange: Flow Visualization, Flow Stability, and Heat Transfer Using Real-Time X-Ray Imaging, . Nucl. Sci. Eng.Vol.150-2 (2005) 182-220.
- [2]D.Wildenschild, J.W.Hopmans, M.L.Rivers and A.J.R.Kent: Quantitative Analysis of Flow Processes in a Sand Using Synchrotron-Based X-ray Microtomography, Vadose Zone Journal 4 (2005) 112-126.
- [3]Sito, et al.: Visualization and Measurements of Liquid Phase Velocity and Void Fraction of Gas-Liquid Metal Two-Phase Flow by Using Neutron Radiography, Proc. 9<sup>th</sup> International Symposium on Flow Visualization (2000)
- [4]N.Takenaka, et al.: Visualization of Streak Lines in Liquid Metal by Neutron Radiography, Neutron Radiography Vol.4, Gordon and Breach (1993) 355-362.
- [5] N.Takenaka, et al.: Liquid metal flow measurement by neutron radiography, Nucl. Instrum. Methods. Phys. Res. A. Vol.377 (1996) 156-160.
- [6]H.Umekawa, et al.: Visualization of bed material movement in a simulated fluidized bed heat exchange by neutron radiography, Nucl. Instrum. Methods. Phys. Res. A. Vol.424 (1999) 77-83.
- [7]M.Sadjben: Hot-wire anemometry in liquid mercury, Rev. Sci. Instrum. 36 (1965) 945-953.
- [8]H.Ji, W.Fox, D.Pace: Study of small amplitude magneto hydrodynamic surface waves on liquid metal, Phys. Plasmas (2005) 012102\_1-13.
- [9]A.Cramer, S.Eckert, V.Galindo, G.Gerbeth, B.Willers, W.Witke: Liquid metal model experiments on casting and solidification processes, J. Materials Sci. 39 (2004) 7285-7294.
- [10]S.Men, C.Resagk, M.Ziolkowski, M.Kuilekov and H.Brauer: Measurement of magnetic flux density on a rotating distorted electrolyte-metal interface, Meas. Sci. Technol. 15 (2004) 1323-1326.
- [11]H.Obayashi, Y.Tasaka, M.Morinaga, Y.Takeda and K.Kikuchi: Measurement of Liquid Metal Flow using Ultrasonic Velocity Profiler (1st Report, Flow Measurement of LBE Target), Journal of JSME, 72 (2006) 642-628.
- [12]Y.Takeda: Measurement of velocity profile of mercury flow by ultrasound Doppler shift method, Nucl. Tech. Vol 79, (1987)120-124.
- [13]H.Kikura and Y.Takeda: Flow mapping using ultrasonic Doppler method, ASME Fluid Eng. Division Summer Meeting FED-Vol.245 FEDSM98-5084 (1987).

## **Flow velocity measurements in a large amplitude meandering flume using an acoustic doppler velocity profiler**

Donatella Termini and Mafalda Piraino

Università di Palermo, Viale delle Scienze, 90128 Palermo, Italy, E-mail: dony@idra.unipa.it

A natural meandering stream represents one of the most complex flow situations for its irregular topography and its changing plane shape. The modifications of its planform geometry can induce undesirable consequences and can disturb the ecological equilibrium of the areas neighboring the channel. The analysis of the morphodynamic evolution of the channel is strongly related to the kinematic characteristics of flow. Along the curved reaches of the channel, characterized by changing curvature in longitudinal direction, many interrelated factors occur and the definition of forecasting methodologies is complex. In this work, the results of an experimental investigation of flow conducted in a large meandering laboratory channel are shown. The experiments have been carried out over a deformed bed. During the experiments the flow velocity components have been measured by using an Ultrasonic Doppler Profiler (DOP2000), that allows to measure instantaneous flow velocity profiles. The analysis of the collected data confirm that when the aspect ratio is small ( $<10$ ) the cross-circulation assumes a great importance. Furthermore, it seems that, in accordance with previous findings (Blanckaert and Graf, 2001), a second counter rotating secondary flow cell appears along the bend near the outer bank. Blanckaert K. & Graf W.H. (2001). Mean Flow and Turbulence in Open-channel Bend. *Journal of Hydraulic Engineering*, vol. 127, n. 10, pp 835-847.



## **From fundamental investigations towards industrial application of ultrasound based in-line rheometry**

Boris Ouriev and Klaus-Jochen Lisner

Bühler AG, Uzwil, Switzerland, E-mail: boris.ouriev@mail.ru

Erich Windhab

Institute of Food Science and Nutrition, Laboratory of Food Process Engineering, ETH Zurich, Switzerland, E-mail: erich.windhab@ilw.agrl.ethz.ch

The characterization of flow effects and their correlation with the flow properties of multiphase fluid systems is essential to understanding the development of the flow process. How can flow effects be generated and used profitably? This is a key question in our research with the goal of accelerating, optimizing and controlling structure formation in flow. There is a wide range of industrial fluid treatment technologies available that often contain a variety of hidden flow effects. Such flow effects can be named as: slip-stick, memory effect, shear heating, dynamic sedimentation, separation and forced aggregation, fracture and etc. Most of mentioned effects are uncontrollable and as consequence can strongly influence the overall energy consumption of the fluid treatment and, most importantly, they contribute adversely to the characteristic quality parameters of the fluid. Therefore application of non invasive on-line methodology as UVP-PD helps to understand structure-processing relationships and also steer flow effects without interruption of process line. This work gives a number of examples where such methodology can be applied for understanding of flow effects. This know how can be applied for process optimisation and steering of commercial processing. The observations revealed in this abstract provide a solid basis for further fundamental investigations of structure formation regularities and their interaction with processing of any highly concentrated system.



# A study of ultrasonic propagation for flow rate measurement using ultrasonic flowmeter

Yuto Inoue, Hiroshige Kikura, Masanori Aritomi

Research Laboratory for Nuclear Reactors, Tokyo Institute of Technology, 2-12-1 Ohokayama, Meguro-ku, Tokyo, 152-8550 Japan

Michitsugu Mori

Tokyo Electric Power Company, 4-1 Egasaki-cho, Tsurumi-ku, Yokohama, 230-8510 Japan

The purpose of this study is to measure flow rates with high accuracy by using ultrasound. Experimental study has been conducted on ultrasonic properties which are necessary for the measurement. An automatic measurement system which can measure three-dimensional sound field has been developed. With this system, ultrasonic sound pressure distributions and refraction angles in the water have been measured. According to Snell's principle the ultrasonic transmission property can be obtained on the basis of incidence angle, acoustic impedance, basic frequency of ultrasound, and material and thickness of metallic plate. However this principle can't be applied to certain cases where an ultrasonic incident wave passes through a metallic plate and turns into a longitudinal wave, a shear wave and a Rayleigh wave. Consequently the ultrasonic propagation paths have been investigated experimentally at various angles of incidence. The most suitable incidence angle has been determined from the result of measurements, and flow rates are measured.

**Keywords:** flow rate measurement, ultrasonic flowmeter, ultrasonic propagation, incidence angle, refraction of ultrasound

## 1 INTRODUCTION

At present differential pressure type flow meters such as Orifice, Nozzle and Venturi have been used for industrial piping flow rate measurements from the view point of low cost and global standard. However these methods have a problem of measurement errors which are caused by changes in flow conditions under aging phenomena, for example, surface wear, corrosion and metal deposition inside pipes. To cope with these concerns, time-of-flight (TOF) and Cross-Flow type ultrasonic flow meters, which are strapped onto the outside of a pipe, are being introduced to nuclear power plants in the United States. These methods are easier to install. However, these methods, which require flow profile factors (PFs) determining the theoretical velocity profile, strongly depend on the real flow profiles. Since real velocity profiles in plants are affected by turbulent flow and inner surface wear in the pipe under aging phenomena, PFs can't be determined easily.

On the other hand, as a new flow metering system in a circular pipe, an ultrasonic velocity profile (UVP) method has been developed [1][2]. This method can measure instantaneous velocity profiles in a pipe over a diameter directly, so flow rate is calculated using the integration of the averaging velocity profile [3][4]. In order to establish the technique and investigate its absolute accuracy, experimental results have been compared with flow standard at NIST [5]. These results showed that the difference between the averaged Ultrasonic Doppler Method values and NIST gravimetric measurement is about

0.18%. In addition, even if a bigger turbulent flow is developed, the error is 0.38%. In this case two more ultrasonic measurement lines are used to achieve higher accuracy [4].

In the case of clamp-on type ultrasonic flow meters, acoustic parameters such as ultrasonic pressure and incidence angle have a huge effect on flow metering accuracy [6][7]. According to Snell's principle the ultrasonic transmission property can be obtained on the basis of incidence angle, acoustic impedance, basic frequency of ultrasound, and material and thickness of metallic plate. However this principle can't be applied to certain cases where an ultrasonic incident wave propagated through a metallic plate turns into a longitudinal wave, a shear wave and a Rayleigh wave.

Experimental study was conducted on ultrasonic properties which are necessary to measure flow rates with accuracy. The automatic measurement system which can measure three-dimensional sound field has been developed. By using this system, ultrasonic sound pressure distributions and refraction angle in the water were measured.

Consequently the ultrasonic propagation paths were investigated experimentally at various angles of incidence. The most suitable incidence angle was determined from the result of measurements, and flow rates were measured.

## 2 ULTRASONIC PROPAGATION PROPERTY

UVP method processes reflected signals from particles in working fluids to measure velocity profiles. In addition ultrasonic refraction angle in pipe

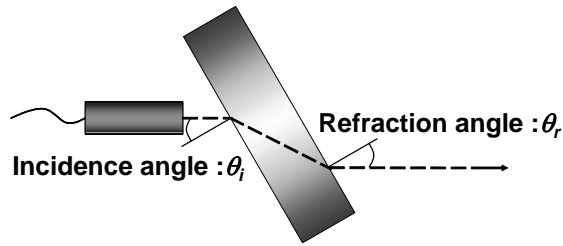


Figure 1: Incidence angle  $\theta_i$  and refraction angle  $\theta_r$

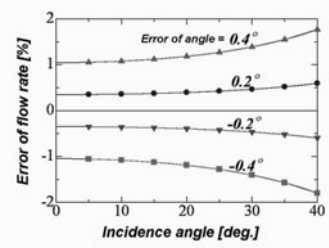


Figure 2: Theoretical error of ultrasonic flow meter when incidence and refraction angles change

is used to calculate axial velocities. There are some concerns about the measurement using UVP. One is signal degradation from particles because of a bigger impedance difference between metallic pipes and working fluids. Another is that errors of ultrasonic incidence angle and refraction angle shown as Figure 1 have a significant effect on flow measurement accuracy. In theory, flow rates calculated from velocity profiles is derived from the followings:

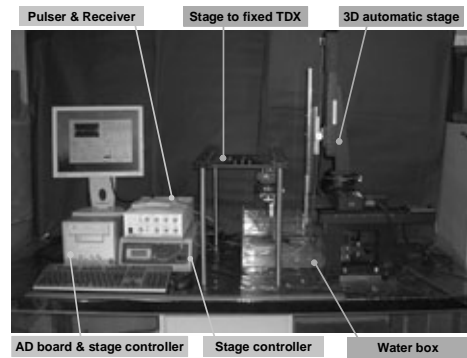
$$Q(t) = \iint V_x(r, \theta_r, t) r dr d\theta \quad (1)$$

$\theta_r$  : refraction angle ,  $V_x$  : axial direction velocity  
 $r$  : pipe radius,  $t$  : time

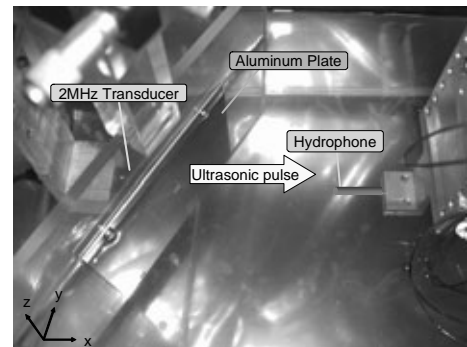
Figure 2 shows the flow measurement errors caused by the errors of incidence and refraction angle. In the results, ultrasonic propagation properties through metallic piping need investigations.

**2.1 Experimental-setup and method**

The schematic diagram of the system for measuring 3D ultrasonic distributions is shown in Figure 3-(a). This system consists of an ultrasonic transmitting and receiving system, and an oscilloscope and a 3D-automatic stage with PC. And the schematic diagram of the measuring area is shown in Figure 3-(b), consisting of a fixed transducer (2MHz,  $\phi 10$ ), a hydrophone ( $\square 1\text{mm}$ ) and aluminum plate (thickness = 1.5mm). A hydrophone is movable freely by using the automatic XYZ axis stage, as shown Figure 3-(b). The aluminum plate can rotate horizontally to change incidence angles in a water box (400mm x 200mm x 200mm; Plexiglas). This test area is filled with filtrate 23degree-water. Ultrasonic pulse, which is emitted from a pulser (Matec; TB-1000, Pulse



(a) Overall view



(b) Measurement tools

Figure 3: Experimental system for measuring ultrasonic pressure distribution

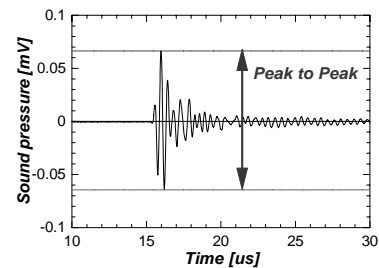


Figure 4: A typical example of sound signal

Width = 1us), penetrates the aluminum plate and is received by the hydrophone. This averaging signal is stored in a computer using AD converter (National Instruments; NI5112, 8bit, 100MHz Sampling).

The test sections are the square of having size of 21mmx21mm, so both x and y axes measuring division is 0.5mm. And the squares locate at 30mm, 70mm 120mm along z axis. Sound pressure is defined as Peak to Peak shown by Figure 4 and sound pressure is calculated from averaging signals.

**2.2 Results and discussion**

Figure 5 shows the ultrasonic sound pressure distribution through an aluminum plate at 29deg. Incidence angle.

Figure 6 shows the ultrasonic intensity, *Peak to Peak*, calculated from received signals. In the case of using

a thick plate, *Peak to Peak* attenuates near longitudinal and shear critical angles, 13.3degrees and 29.1degrees respectively. But the values of sound pressure are the largest near the critical angle of shear wave in the case that plate thickness is thick plate. This phenomenon is attributed to leaky wave.

Figure 7 shows the differences between  $\theta_r$  and  $\theta_i$ . Larger differences can be seen at the critical angle of longitudinal wave and above the critical angle of shear wave. When the incidence angle is nearly equal to 29degrees, the differences are smaller than the other incidence angles in the case of a thin plate (thickness = 1.5mm).

It can be concluded that the best incidence angle is 29degrees in the case of thin plates to measure flow rates using UVP with high accuracy.

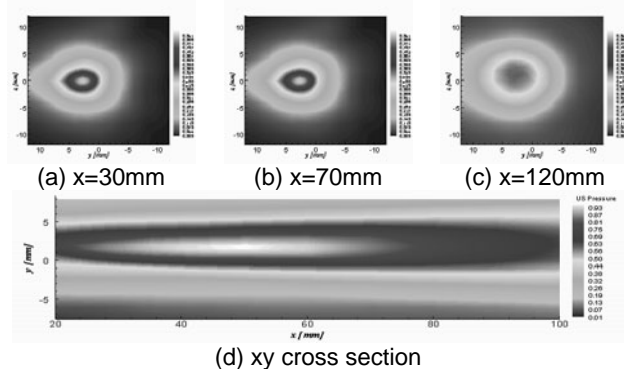


Figure 5: Sound pressure distributions ( $\theta=29$ deg. TDX:2MHz, Aluminum plate thickness: 1.5mm)

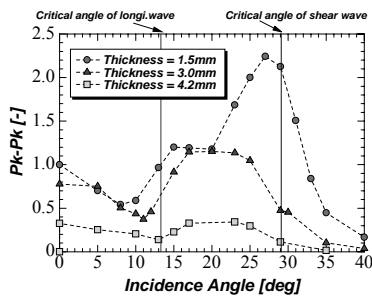


Figure 6: Maximum of transmission coefficients at each incidence angle through a aluminum plate (TDX:2MHz)

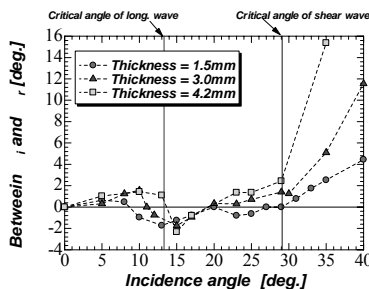


Figure 7: Distances between incidence angle  $\theta_i$  and refraction angle  $\theta_r$ . (TDX:2MHz)

### 3 FLOW RATE USING VELOCITY PROFILES

#### 3.1 Experimental-setup and method

Considering the results described above, velocity profiles and flow rates have been measured using UVP. The experimental apparatus consists of a water circulation system, a test section and a measurement system. Figure 8 is the schematic diagram of this apparatus, which is designed and built to emphasize the formation of fully developed turbulent pipe flow in both downward and upward directions. In this study, single-phase turbulent pipe flow in the upward direction was investigated. Water is circulated by a centrifugal pump from the storage tank into the pipe. The vertical pipe is made of Plexiglas, of which the total length, inner diameter and wall thickness were 2.5m, 50mm and 5mm respectively. Reynolds number is 20000 regulated by the needle valve and monitored by an electro magnetic flowmeter located upstream of the test section. And upstream which arrives at the overflow tank is drained off to the storage tank. Working water is monitored to keep  $20\pm 0.5$ degC by a mercury thermometer. The measuring point is located at 12D from the line entry at the bottom. The material of the test section is aluminum and the wall thickness is 1.5mm. Velocity profiles were collected using UVP (Met-Flow; UVP-X3) at each incidence angle. The basic frequency, beam diameter and distance between to the adjacent measurement points are 2MHz, 10mm, and 0.74mm respectively. Considering acoustic impedance, water used as coupling between a transducer and an aluminum pipe. Nylon particles (WS200P) whose averaging diameter and relative density is  $80\mu\text{m}$  and 1.02 are used as ultrasonic reflectors because its density is nearly equal to density of working water.

Flow rate measurements using UVP require a

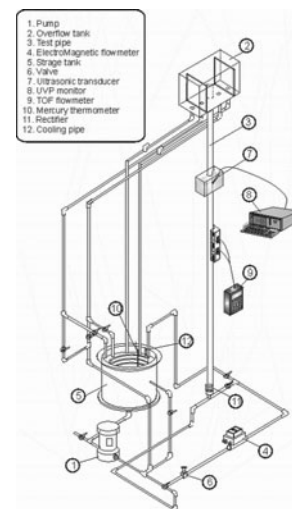


Figure 8: Experiment apparatus for measuring velocity profiles and flow rates (test section: Aluminum; D=50mm, thickness=5.0mm, height  $\approx$  45D)

velocity profile inside a pipe in the case of axial symmetric flow. And flow rates are calculated by integrating a velocity profile around a pipe axis. This calculation formula is shown as Equation(2). In addition, linear interpolation is applied to distances between each measurement point.

$$Q(t) = \frac{\pi}{3} \left\{ \frac{R_0^3 - R_1^3}{R_0 - R_1} v_0 + \sum_{i=0}^{n-2} \frac{R_{i+1}^3 - R_{i+2}^3}{R_{i+1} - R_{i+2}} (v_{i+1} - v_i) + R_n^2 v_n \right\} \quad (2)$$

where  $R_i$  is the distance from the center of the pipe to the measuring point, and  $v_i$  is the velocity of the point.

**3.2 Results and discussion**

Figure 9 shows mean velocity profiles in aluminum pipe at 4 incidence angles (thickness = 1.5mm) on each incidence angle. These profiles were ensemble averaged using 1024 instantaneous velocity profiles. Noise from metallic wall disturbs velocity profiles near the transducer side. However, this problem is solved when incidence angle is 29degree, which is the best angle as described above. It is observed that velocities of the pipe center vary with each incidence angle as Figure 9. But it is been able to read out the changing pipe center velocity when

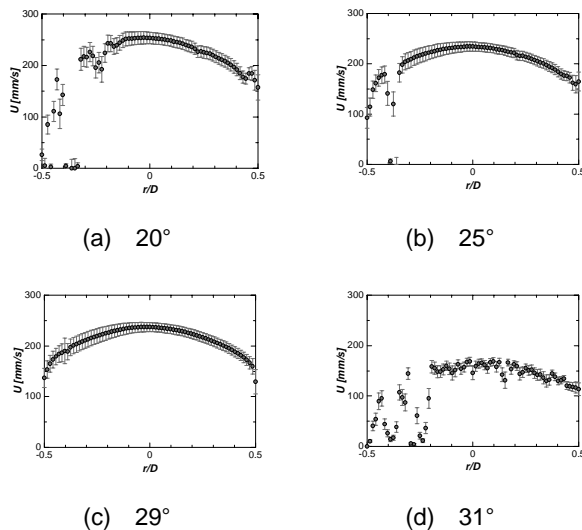


Figure 9: Mean velocity profiles in Aluminum pipes at 4 incidence angles (Pipe Thickness = 1.5 mm, h=12D)

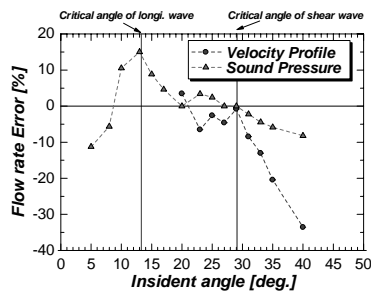


Figure 10: Error of flow rate at each incidence angle

incidence angle is changed. The result indicates changes of refraction angle. So Figure 10 shows the results of flow rate measurement using velocity profiles of the other side from the transducer and flow rate using the measurement of sound pressure.

Considering the results described above, ultrasonic flow metering using UVP is high accuracy measurement method, if a better incidence angle is chosen.

**4 SUMMARY**

Experimental study was conducted on ultrasonic properties which are necessary to measure flow rates with accuracy. The automatic measurement system which can measure three-dimensional sound field has been developed. By using this system, ultrasonic sound pressure distributions and refraction angles in the water were measured. According to Snell's principle the ultrasonic transmission property can be obtained on the basis of incidence angle, acoustic impedance, basic frequency of ultrasound, and material and thickness of metallic plate. However this principle can't be applied to certain cases where an ultrasonic incident wave propagated through a metallic plate turns into a longitudinal wave, a shear wave and a Rayleigh wave. Consequently the ultrasonic propagation paths were investigated experimentally at various angles of incidence. The most suitable incidence angle was determined from the result of measurements, and flow rates were successfully measured with high accuracy.

**REFERENCES**

[1] Y. Takeda: Measurement of velocity profile of mercury flow by ultrasound Doppler shift method, Nucl. Technol., 79, (1987) 120-124.  
 [2] Y. Takeda, 1995, Velocity profile measurement by ultrasonic Doppler method, Experimental Thermal Fluid Science, 10, pp.444-453.  
 [3] M. Mori, Y. Takeda, T. Taishi, N. Furuichi, M. Aritomi, H. Kikura, 2002, Development of a novel flow metering system using ultrasonic velocity profile measurement, Exp. Fluids, 32, pp.153-160.  
 [4] S. Wada, H. Kikura, Y. Koike, M. Aritomi, M. Mori and Y. Takeda: Development of pulse ultrasonic Doppler methods for flow rate measurement in power plant, Journal of Nuclear Science and Tech., 41 (2004) 339-346.  
 [5] M. Mori, Y. Takeda, T. Taishi, N. Furuichi, M. Aritomi, H. Kikura: Development of a novel flow metering system using ultrasonic velocity profile measurement, Exp. Fluids, 32, (2002) 153-160.  
 [6] S. Wada, H. Kikura, M. Aritomi, and M. Mori: Characteristics of sound pressure distribution on ultrasonic Doppler method, 4th International Symposium on Ultrasonic Doppler Methods for Fluid Mechanics and Fluid Engineering, (2004) 37-40.  
 [7] R. Motegi, S. Takeuchi: T. Sato, "WIDEBEAM ULTRASONIC FLOWMETER", ULTRASONIC SYMPOSIUM, (1990) 331-336.

## Stability of Anomalous Modes on Taylor-Couette vortex flow in Magnetic Fluid

Toshikazu Kotaka\*, Daisuke Ito\*\*, Hiroshige Kikura\*\*, Masanori Aritomi\*\* and Shuichiro Hirai\*

\* Research Center for Carbon Recycling & Energy, Tokyo Institute of Technology, 2-12-1 Ohokayama, Meguro-Ku, Tokyo, 152-8550, Japan.

\*\* Research Laboratory for Nuclear Reactors, Tokyo Institute of Technology, 2-12-1 Ohokayama, Meguro-Ku, Tokyo, Japan.

With the advance of technologies in bio-industrial field, development of a more practical device using Taylor-Couette vortex flow has been longed for. To bring this technology into active use, it needs to be downsized. And at the same time, it is necessary to secure sufficient volume for the reaction. This means that the Ekman effect will increase relatively. The Ekman effect generates various modes of Taylor-Couette vortex flow with a small aspect ratio. In the case of a practical device using this flow, fluid control is essential for controlling the reaction caused inside. Thus this study is focused on controlling Taylor-Couette vortex flow in a magnetic fluid. The Taylor-Couette vessel used in this study has a rotating inner cylinder and a stationary outer cylinder. It has an aspect ratio,  $\Gamma=3$  and a radius ratio,  $\eta=0.6$ . The axial velocity distributions are measured by a UVP model X-3 PSI. The Ultrasonic transducer has 3mm beam diameter and 8MHz basic frequency. The control of the mode transition by applying the magnetic fields has been investigated. As a result, three Anomalous modes were obtained. And their stabilities are being discussed.

**Keywords:** UVP, Taylor-Couette vortex flow, magnetic fluid, flow control, bioreactor

### 1 INTRODUCTION

Recently research and development of a bioreactor using animal and plant cells has been longed for. With the advance of technologies in medical and bio-industrial fields, it was revealed that animal and plant cells have a wide range of applications. However, animal and plant cells are adversely affected by shear stress. That is why the efficient bioreactor using Taylor-Couette vortex flow attracted a lot of attention. It is said that Taylor-Couette vortex flow has high mixing and reaction performance with little influence upon animal and plant cells. Ameer et al. [1] researched and developed a postdialyzer using Taylor-Couette vortex flow. And Haut et al. [2] examined the ability of a bioreactor using Taylor-Couette vortex flow to culture animal cells. However, when Taylor-Couette vortex flow was used for various reactions, variations in reaction efficiency appeared although bioreactors were operated at the same Reynolds numbers. Because many studies on bioreactors using Taylor-Couette vortex flow were not made from a fluid dynamical viewpoint but from a chemical and biological one, the fluid dynamical characteristics of Taylor-Couette vortex flow cannot be understood.

Taylor-Couette vortex flow is a flow between a rotating cylinder and a stationary cylinder. Many studies on Taylor-Couette vortex flow have already been done, and the following sequence of flow regimes has been observed. At very low Reynolds numbers Couette flow, which is simple shear flow, appears. On increasing the Reynolds numbers

Couette flow changes into Taylor-Couette vortex flow. Taylor-Couette vortex flow has some stable toroidal vortices. On increasing the Reynolds number further, the vortices oscillate. This flow mode is called Wavy vortex mode. On increasing the Reynolds number further and further, an additional wavy mode which modulates wavy vortex mode appears: this flow is called modulated wavy vortex mode. To bring a bioreactor using Taylor-Couette vortex flow into active use, it needs to be downsized. And at the same time, it is necessary to secure the enough volume for reactions. This means that the aspect ratio will be small and that the Ekman effect will increase relatively.

Taylor-Couette vortex flow with a small aspect ratio is an interesting physical phenomenon, typical of non-linear dynamics. Many researchers, for example Benjamin [3] and so on, have carried out the investigations on the mode bifurcation and the flow pattern [4]. Taylor-Couette vortex flow with a small aspect ratio bifurcates into the primary mode and the secondary mode. This bifurcation stems from the difference in initial acceleration of an inner cylinder. The primary mode will occur if an inner cylinder is accelerated gradually, and the secondary mode will occur by sudden acceleration. And these two modes bifurcate into the normal mode and the anomalous mode. The normal mode has an inward flow on both end-walls, and the anomalous mode has an outward flow at least on either end-wall or both. In the case of the aspect ratio 3, focused in this study, there are four flow modes: the normal 2cell mode (N-2cell mode), the normal 4cell mode

(N-4cell mode), the anomalous 3cell mode (A-3cell mode) and the anomalous 4cell mode (A-4cell mode).

If there is a perfect flow mode for a reaction caused in a bioreactor using Taylor-Couette vortex flow with a small aspect ratio, it is possible to improve the efficiency of reaction dramatically by maintaining the flow mode. Thus, the objective of this study is to control Taylor-Couette vortex flow in a magnetic fluid by applying the magnetic field using a permanent magnet and to analyze the stability of the anomalous modes.

## 2 EXPERIMENTAL SETUP

The schematic diagram of the experimental setup is shown in Fig.1. And our Taylor-Couette vessel is shown in Fig.2. The Taylor-Couette vessel consists of two concentric cylinders and two end-walls, which are made of Plexiglas. The length of the cylinders is  $H = 48 \text{ mm}$ , the outer radius of the inner cylinder is  $R_1 = 24 \text{ mm}$  and the inner radius of the outer cylinder is  $R_2 = 40 \text{ mm}$ . So our Taylor-Couette system has a radius ratio  $\eta = R_1/R_2 = 0.6$  and an aspect ratio  $\Gamma = H/d = 3$  ( $d = R_2 - R_1$ ). They are positioned vertically adjacent. Only the inner cylinder is rotated by the motor. The Reynolds number  $Re$  is defined as  $Re = \Omega R_1 d / \nu$  ( $\Omega$  is the frequency of rotation of the inner cylinder,  $\nu$  is the kinematic viscosity).

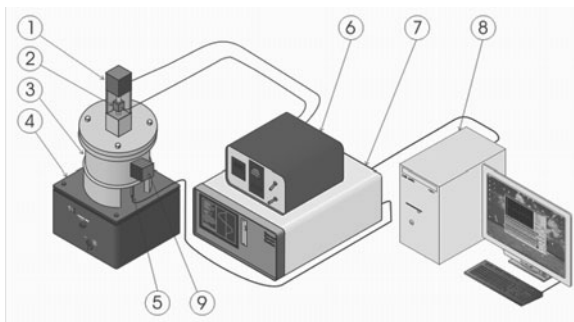


Figure 1: Experimental setup ① motor, ② encoder, ③ Taylor-Couette Vessel, ④ isolator, ⑤ US transducer, ⑥ controller, ⑦ UVP monitor, ⑧ PC, ⑨ magnet

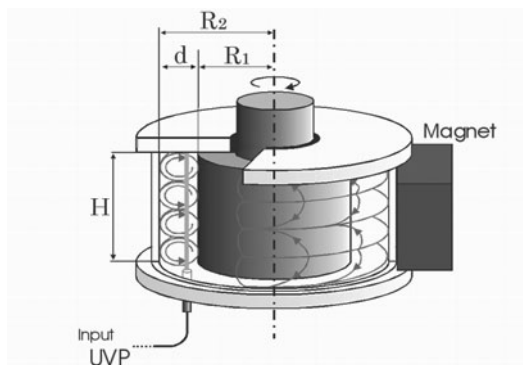


Figure 2: The Taylor-Couette vessel

The gap between the two cylinders is filled with a magnetic fluid. In this study, we used the water-based magnetic fluid of the weight concentration of 23.34wt%. The physical property of the magnetic fluid used in this study is shown in Tab.1.

The measurements were carried out with an ultrasonic velocity profiler (UVP), which can obtain a time series of instantaneous velocity profiles. Additionally UVP can obtain the velocity profiles of nebulous liquids such as a magnetic fluid. The UVP used in this work is the model X-3 PSi. The ultrasonic transducer was affixed to the outer surface of the stationary lower end-wall to measure the axial velocity distribution, as shown in Fig.2. The parameters of UVP measurement are shown in Tab.2. The ultrasound transducer was operated with a basic frequency of 8MHz and a beam diameter of 3mm. The channel distance, which is the distance between two adjacent measurement volumes, was 0.73mm. The non-uniform magnetic field was applied by attaching three permanent magnets, shown in Fig. 3, outside the stationary cylinder. The locations of the ultrasonic transducer for measurements and the permanent magnet for applying magnetic field are shown in Fig.4.

Table 1: Physical property of the water-based magnetic fluid of the weight concentration of 23.34wt% at 22°C

Kinematic viscosity	2.6 mm <sup>2</sup> /s
Density	1.2 g/cm <sup>3</sup>
Sound velocity	1450 m/s

Table 2: Specifications of UVP measurement

Basic frequency of ultrasound	8 MHz
Ultrasonic beam diameter	3 mm
Channel distance	0.73 mm
Number of measurement points	128
Number of profiles	1024

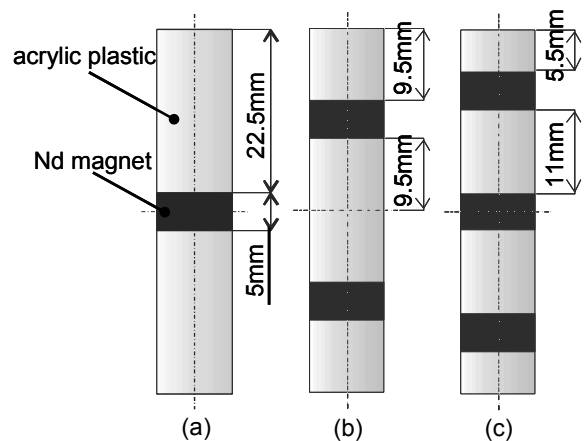


Figure 3: The permanent magnets

### 3 EXPERIMENTAL RESULTS

#### 3.1 Magnetic control of flow field

Figs.5-7 show the temporal-spatial velocity distributions transient change measured by a UVP when a magnetic field was applied. In these figures, the horizontal axis is time from 0 to 182 seconds and the vertical axis is the distance from the transducer and the velocity is represented by the color contour. Fig.5 (a), (b), and Fig.6 show the mode bifurcation control by applying the magnetic field from N-2cell mode to A-3cell mode, from N-2cell mode to N-4cell mode and from N-2cell mode to A-3cell mode, respectively. These mode bifurcations don't occur by changing  $Re$ . From here onwards, it is possible to control the mode bifurcation of Taylor-Couette vortex flow in a magnetic fluid by applying the magnetic field. In Fig.7, it appears as if the Anomalous vortex on the upper stationary end-wall had exchanged positions with the normal vortex on the lower stationary end-

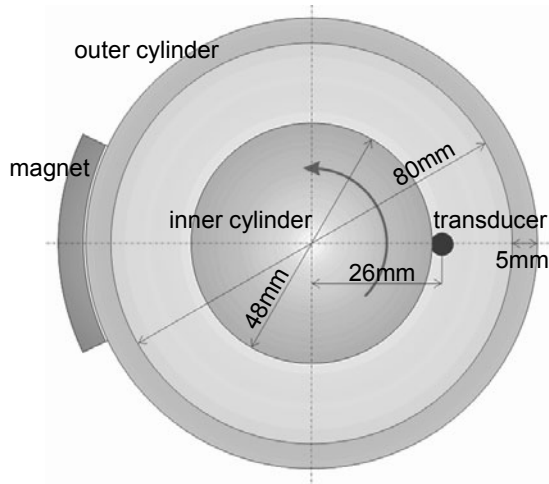


Figure 4: Top view of measuring position and applying a magnetic field position

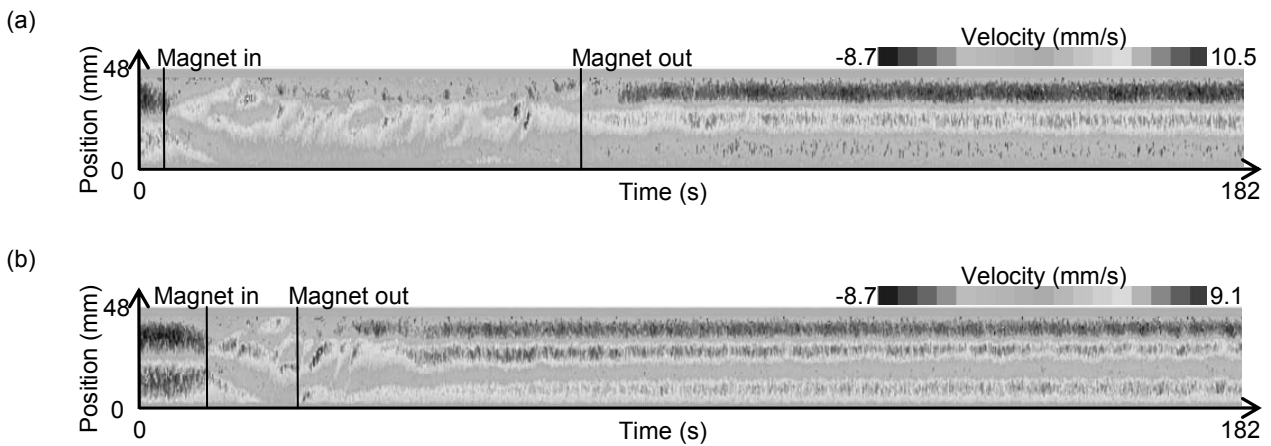


Figure 5: The temporal-spatial velocity distributions of transition by applying magnetic field with the magnet A ( $Re=420$ ); (a) transition from N-2cell mode to A-3cell mode (b) transition from N-2cell mode to N-4cell mode

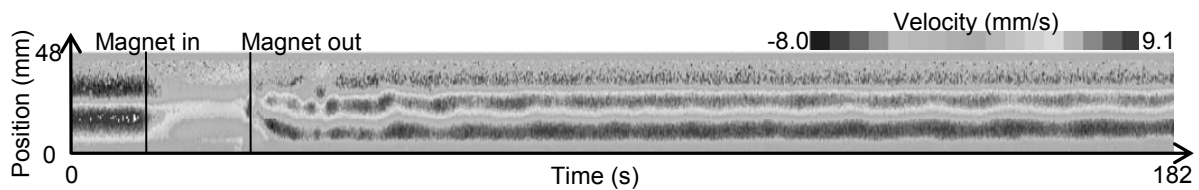


Figure 6: The temporal-spatial velocity distributions of transition from N-2cell mode to A-3cell mode by applying magnetic field with the magnet B ( $Re=420$ )

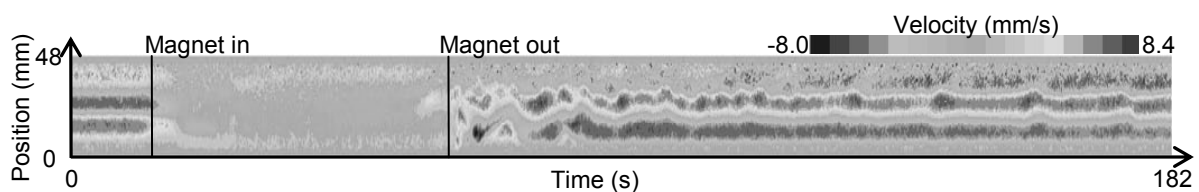


Figure 7: The temporal-spatial velocity distributions of transition from A-3cell U mode to A-3cell L mode by applying magnetic field with the magnet C ( $Re=420$ )

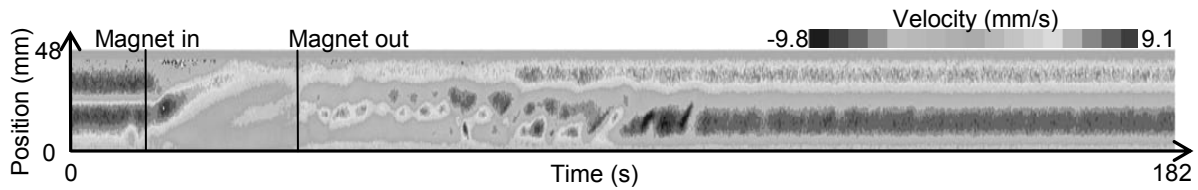


Figure 8: The temporal-spatial velocity distributions of transition from A-3cell U mode to A-3cell L mode by applying magnetic field with the magnet C ( $Re=420$ )

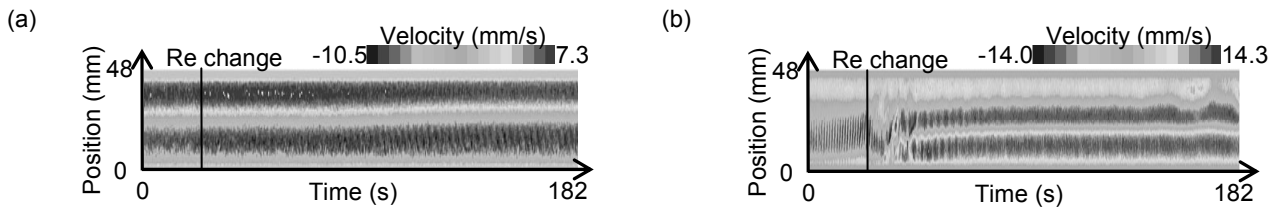


Figure 9: The temporal-spatial velocity distributions of transition on A-2cell mode by accelerating inner cylinder; (a) from A-2cell Taylor-Couette vortex flow to A-2cell Wavy vortex flow ( $Re=440 \rightarrow 460$ ) (b) from A-2cell Wavy vortex flow to A-3cell Taylor-Couette vortex flow ( $Re=670 \rightarrow 700$ )

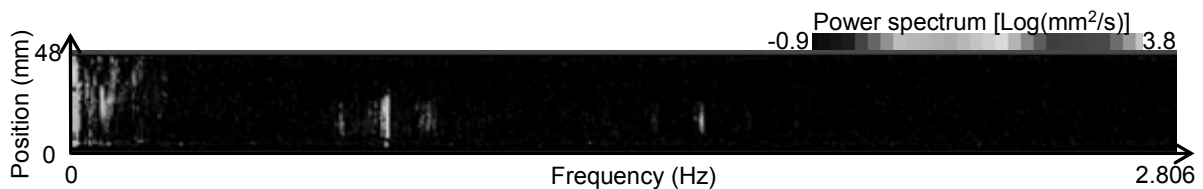


Figure 10: The result of the fast Fourier spectrum for the same data as for Fig.9 (a)

wall. Furthermore in Fig.8, Normal 2cell mode bifurcates to the opposite flow, because the color plot is inverted before and after applying the magnetic field. It shows that the cell mode has two anomalous cells, so it can be called Anomalous 2cell mode.

### 3.2 Anomalous 2cell mode

A-2cell mode consists of two vortices whose sizes are not the same. In this study, we refer to the larger vortex as main vortex and the smaller as sub. Fig.9 (a) and (b) show the temporal-spatial velocity distributions of the transition on A-2cell mode by changing  $Re$  from 440 to 460 and from 670 to 700, respectively. It can be observed that only the main vortex on the lower end-wall oscillated as shown in Fig.9 (a). And Fig.10 shows the result of the fast Fourier spectrum for the same data as those for Fig.9 (a). In these figures, the horizontal axis is frequency from 0 to 2.806 Hz and the vertical axis is a distance from the transducer and the power spectrum is represented by the color contour. From this result, a strong spectrum can be seen only at a lower position at nearly 0.71 Hz. This means that only the main vortex oscillated on A-2cell mode. On increasing  $Re$  further, the main vortex broke up to two vortices. Finally, the flow field settled to A-3cell mode.

## 4 CONCLUDING REMARKS

The controlling of Taylor-Couette vortex flow in a magnetic fluid by applying a magnetic field has been investigated using UVP. From the experimental result of applying magnetic fluid on Taylor-Couette vortex flow in a magnetic field, we found the practicability of mode bifurcation control and discovered a new cell mode, A-2cell mode. And the stability of A-2cell mode has been analyzed. Analyzing the stability of the bifurcation of A-2cell mode by changing  $Re$  is revealed.

## REFERENCES

- [1] Ameer G.A. et al.: Regional Heparinization Via Simultaneous Separation and Reaction in a Novel Taylor-Couette Flow Device, *Biotechnology and Bioengineering* 63-5 (1999) 618-624.
- [2] Haut B. et al.: Hydrodynamics and mass transfer in a Couette-Taylor bioreactor for the culture of animal cells, *Chemical Engineering Science* 58 (2003) 777-784.
- [3] Benjamin T. B.: Bifurcation phenomena in steady flows of a viscous fluid II. Experiments, *Proc. R. Soc. London A*-359 (1979) 27-43.
- [4] Nakamura I. et al.: An Experiment on a Taylor Vortex Flow in a Gap with a Small Aspect Ratio (2nd Report, Instability of Taylor Vortex Flows) (in Japanese), *Transactions of the Japan Society of Mechanical Engineers Series B* 54-505 (1988) 2425-2432.

# Improving Acoustic Doppler velocimetry in steady and unsteady flow by means of seeding with hydrogen bubbles

Tobias Meile, Giovanni De Cesare, Koen Blanckaert, Anton J. Schleiss

Laboratory of Hydraulic Constructions, Ecole Polytechnique fédérale de Lausanne, CH-1015 Lausanne

Velocimetry is used in various fields of research. In hydraulics, Ultrasonic Velocimetry based on the Doppler Shift effect can accurately resolve the mean flow and the turbulence if the acoustic scattering level is sufficiently high. But Ultrasonic Velocity instruments are known to perform poorly in clear water with low acoustic scattering level, such as often found in laboratory applications.

Artificial seeding of the flow can be used to increase the acoustic scattering level. This paper reports how seeding of the flow with micro-bubbles generated by means of electrolysis improves the quality of velocity profile measurements under unsteady flow conditions.

**Keywords:** water, hydrogen bubbles, velocity measurement, steady flow, unsteady flow

## 1 INTRODUCTION

Velocimetry is used in various fields of research. In hydraulics, different velocimetry methods exist (spinner, Pitot tube, electromagnetic methods, Laser Doppler methods (LDA), Particle Imaging Velocimetry (PIV), Ultrasonic Doppler methods, etc). Ultrasonic velocimetry based on the Doppler effect can accurately resolve the mean and turbulent flow fields if the acoustic scattering level is sufficiently high (Takeda, 2002; Blanckaert and Lemmin, 2006).

Due to the inherent constraints of classical velocimetry, especially the intrusive character of measurement devices such as micro-propellers or Pitot-tubes and the point wise and non-directional measurement, there has been a clear need to develop and dispose of a non-intrusive measurement technique also for the hydraulic engineer. Thanks to the UVP Method one can obtain velocity fields in space and time.

This technique with its advantages compared to more classical measuring methods is now being widely exploited in the Laboratory of Hydraulic Constructions (LCH) of the Ecole Polytechnique Fédérale de Lausanne (EPFL). Among the first performed studies at the LCH was the flow mapping of turbidity currents in a laboratory flume (De Cesare and Schleiss, 1999), where the suspended sediments gave very good ultrasound echo. Other studies also used either steady state measurement allowing a long acquisition time or were performed in rather dirty water (De Cesare, 1999). Nevertheless, as Ultrasonic Doppler instruments are known to perform poorly in clear water, such as often found in laboratory applications, artificial seeding of the flow can be used to increase the acoustic scattering level.

This paper applies the simple, low-cost and non polluting seeding technique proposed by Blanckaert and Lemmin (2006), which consists of generating

micro hydrogen bubbles in the flow by means of electrolysis. When a direct electric current is passed through water a chemical reaction takes place that produces two different gases at the cathodic and anodic electrodes. Elemental hydrogen ( $H_2$ ) is formed at the cathode and elemental oxygen ( $O_2$ ) at the anode. The size of the micro hydrogen bubbles is comparable to that of the cathodic electrode. The ideal size of acoustic tracers is about half of the wavelength of the acoustic signal.

This paper describes the set-up generating hydrogen bubbles and subsequently presents some results of velocity profile measurements under

- 1) Steady flow conditions with and without seeding
- 2) Highly unsteady flow conditions with seeding.

## 2 HYDROGEN BUBBLE GENERATION SETUP

### 2.1 Setup characteristics

The setup used for the hydrogen bubble generation and the data-acquisition are shown in Figure 1 and Figure 2.

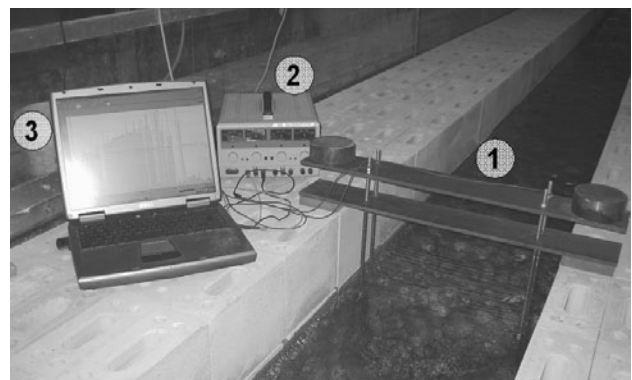


Figure 1: Setup for hydrogen bubble generation (1), electric direct current producer (2) and data-acquisition notebook (3).

The setup for the hydrogen bubble generation (1) is formed by two arrays of horizontal stainless steel wires (diameter  $100\ \mu\text{m}$ ). The anode is placed upstream and the cathode downstream. The distance between anode and cathode is 5 cm. The average vertical spacing between the stainless steel wires is 0.8 cm with increased density in the lower part of the arrays. The distance between the two insulating stems of the anode respectively the cathode is 38 cm. The stems are insulated by a waterproof painting layer. Insulation is important to guarantee the production of the hydrogen bubbles on the stainless steel wires and not on the stems. The stems are held by two PVC-plates with a vertical spacing of 8 cm. The setup has a total height of about 50 cm.

The setup for the hydrogen bubble generation must be placed sufficiently far upstream of the measuring volume to prevent flow disturbance.

## 2.2 Setup manufacturing

The setup manufacturing can be divided in three steps:

1. Preparation and assembling of the two PVC-plates and the four stems (Figure 2).
2. Winding of the stainless steel wires around the cathodic and anodic stems.
3. Insulation of the stems by a thick layer of waterproof painting.

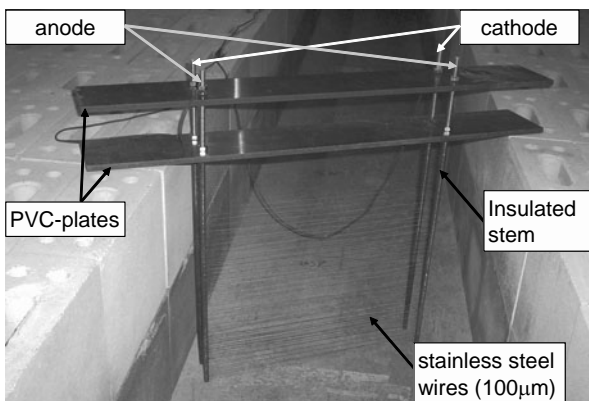


Figure 2: Hydrogen bubble generation set-up.

## 2.3 Power supply

An electric direct current producer (Instek GPC-3030 DC Power Supply 30-60V/3-6A) has been used with the following characteristics:

1. Constant tension of about 5 to 30 V, depending on flow depths (percentage of submerged wires).
2. Current from 0 to 3 A, also depending on flow depths.

The bubble generation is not efficient when the stainless steel wires are still clean. Only after few minutes of operation in water, a surface reaction is produced on the wires and the bubble generation becomes efficient.

## 2.4 Installation of the Ultrasonic (US) transducer

The experimental setup for the flow velocity measurements is schematically presented in Figure 3. The velocity was measured on the axis of a straight laboratory flume (width: 0.5 m; slope: 0.0014; length: 40 m) at a distance of 24.3 m from the entry.

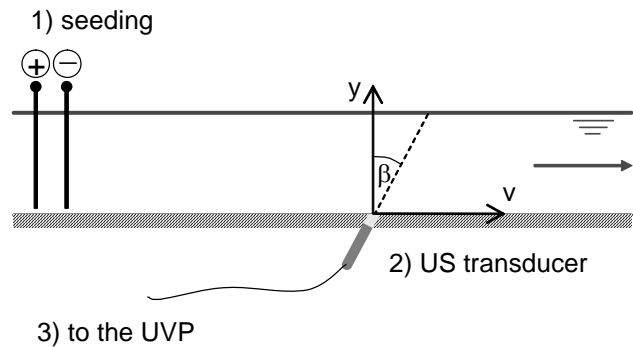


Figure 3: Velocimetry set up: (1) Setup for hydrogen bubble generation, (2) ultrasonic transducer.

The ultrasonic transducer (emitting frequency is 2 MHz) is installed in the bottom of the channel looking downstream with an angle  $\beta=30^\circ$ . The flow is not significantly disturbed by the transducer which is installed about 10 mm under the bottom-level of the channel. The free space between the transducer and the bottom level is filled with a contact gel covered by a self-adhesive tape. Data acquisition has been done by the means of the UVP-DUO velocity profiler instrument from Met-Flow SA, Lausanne (Met-Flow SA, 2002) using the following main measurement parameters (Table 1):

Table 1: Utilized measurement parameters of UVP-DUO

Parameter	Value
Number of channels	80 to 280
Number of profiles	256
Sampling period (maximum speed)	163 to 205 ms
Window start	3.7 mm
Window end	120 to 420 mm
Channel-distance / -width	1.48 mm / 1.48 mm
Frequency	2 MHz
Cycles / Repetitions / Noise level	4 / 246 / 4

## 3 APPLICATION

The setup described above has been used to increase the quality of the velocity measurements in a flume of rectangular cross-section with macro-roughness at the side walls (Meile et al., 2006, Fig. 1) by means of an Ultrasonic Doppler instrument. Experiments in this flume aimed at investigating the influence of macro-roughness (or form roughness) at the side walls on steady and unsteady flows.

### 3.1 Steady flow

Steady flow tests have been performed for two different discharges and three different distances (0.75 m, 2 m, 4 m) between the ultrasonic probe and the location of seeding. Velocity profiles were measured with and without seeding. Hydraulic test parameters are summarized in Table 2.

Table 2: Hydraulic conditions

Q (l/s)	h (m)	$U_{cal}=Q/(Bh)$ (m/s)	$U_{UVP}$ (m/s)	Re (-)	Fr (-)
8	0.043	0.38	$0.37 \pm 0.02$	14'000	0.60
60	0.175	0.71	$0.71 \pm 0.07$	72'000	0.56

The results of the velocity measurements are presented for the two tested discharges in Figures 4 and 5.

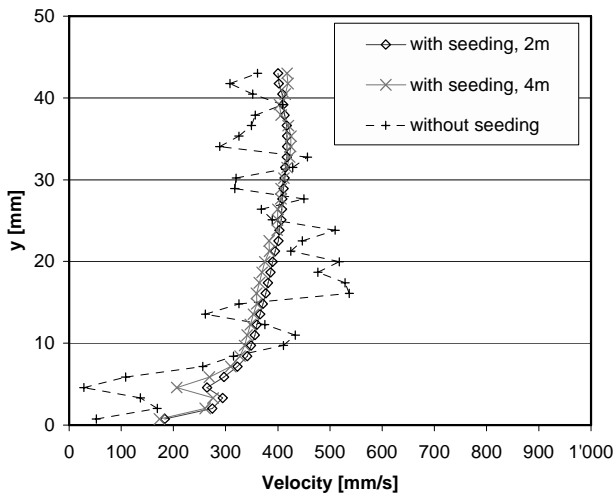


Figure 4: Velocity profiles (averaged over 10 s) with and without seeding for a discharge of 8 l/s.

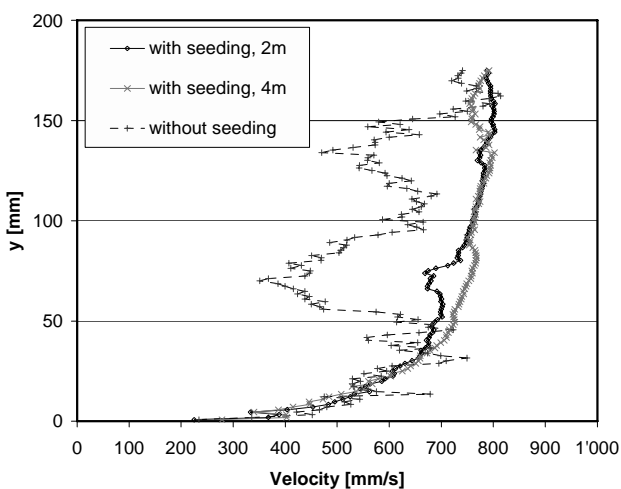


Figure 5: Velocity profiles (averaged over 10 s) with and without seeding for a discharge of 60 l/s.

Without seeding, velocity profiles are erroneous in both experiments, whereas they are rather well resolved with seeding. Remaining irregularities in the profiles may be attributed to the short sampling time (10sec).

The quality of the velocity profile remains more or less constant when the location of seeding moves upstream.

The effect of seeding is also well observable on a color plot (Figure 6). Seeding has been turned off during the measurements after 55 s. The period without seeding and therefore low acoustic scattering level is characterized by less homogeneous velocity measurements.

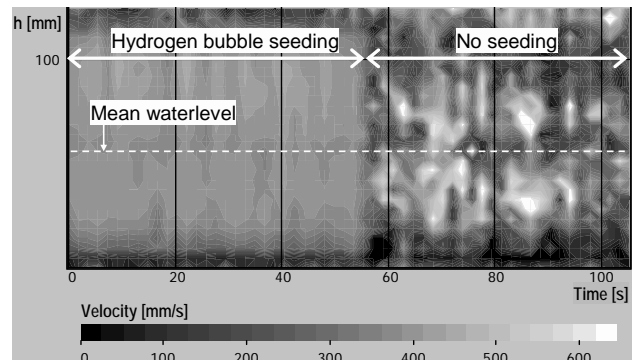


Figure 6: Time – flow depth - velocity plot for periods with seeding (left side) and without seeding (right side) of hydrogen bubbles. Steady flow test with 8 l/s.

### 3.2 Unsteady flow

Velocity measurement with seeding have been carried out under different unsteady flow conditions, schematically illustrated in Figure 7.

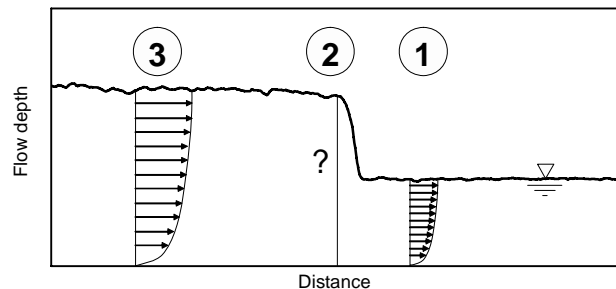


Figure 7: Velocity measurements before, during and after a positive surge wave.

Three different positive surge waves of 17.5 l/s, 30.6 l/s and 53.5 l/s have been added to a constant base flow of about 5.6 l/s (Figures 8 to 10).

For the smallest surge of 17.5 l/s, the time resolution of the measurements didn't allow to measure a velocity profile during the wave passing (Figure 8). For the second and third surge wave of 30.6 l/s and 53.5 l/s, respectively (Figures 9 and 10), non-logarithmic velocity profiles have been detected during a short period corresponding to the passage of a positive surge waves. In the lower part of the

velocity profile, the velocities during the passage of the positive surge waves are always in between the velocities before and after the wave passing. In the upper part of the velocity profile the velocities are temporarily increased during the passage of the wave. This indicates a separation of the flow into a higher, faster part moving on a lower, slower part.

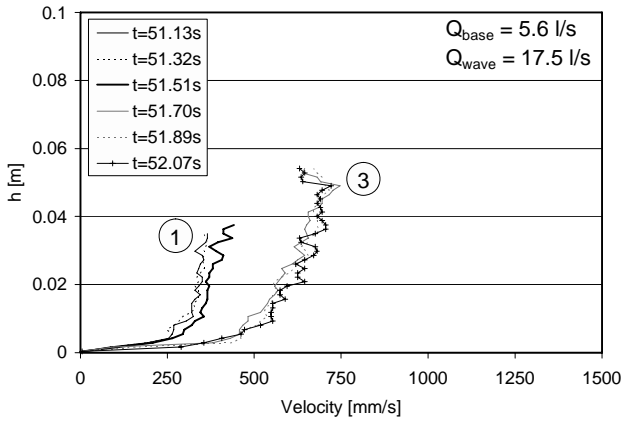


Figure 8: Velocity profiles for different times. Positive surge wave passes between  $t=51.32s$  and  $t=51.51s$ .

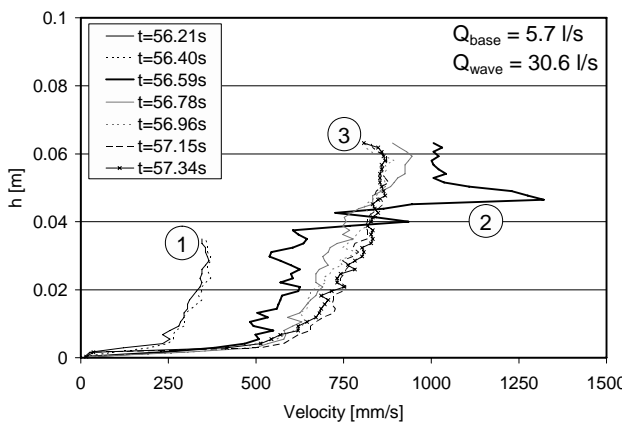


Figure 9: Velocity profiles for different times. Positive surge wave passes at about  $t=56.59s$ .

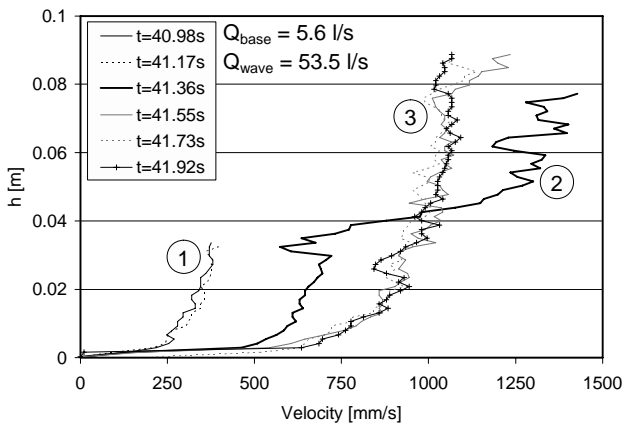


Figure 10: Velocity profiles for different times. Positive surge wave passes at about  $t=41.36s$ .

Nevertheless, it is interesting to note how fast the logarithmic velocity profile is re-established on the entire flow depth. Additional test would be interesting in order to see the influence of 1) absence of seeding 2) other base flows 3) breaking or non breaking waves on velocity profile measurements.

### 5 CONCLUSIONS AND SUGGESTIONS

Seeding of hydrogen bubbles allows significantly increasing the quality of flow velocity measurements.

The distance of the seeding from the ultrasonic transducer is not of paramount importance. Nevertheless, if the setup that generates hydrogen bubbles (seeding) is too close, the flow could be disturbed and if the seeding is introduced too far from the transducer, efficiency decreases.

Seeding allows to get good velocity measurements in highly unsteady flow conditions. Measurements of three different positive surge waves indicate non logarithmic velocity profiles during the wave passage. After a short moment, the distribution becomes logarithmic again.

Further developments should be related to a smaller setup having less influence on the flow and to a setup independent of the flow direction. Consequently it would be possible to place the setup closer to the measurement location and to increase the quality of velocity measurements for more applications (such as recirculation zones, ...).

### REFERENCES

[1] Blanckaert K. and Lemmin U: Means of noise reduction in acoustic turbulence measurements, *J. Hydr. Res. IAHR*, Vol. 44(1), 3-17, 2006.  
 [2] De Cesare G.: Use of UVP monitor in applied hydraulics, Proc. XVI. Symposium on Anemometry, Brno, Czech Republic, 12-13 Octobre 1999  
 [3] De Cesare, G., Schleiss, A.: Turbidity current monitoring in a physical model flume using ultrasonic Doppler method, Proc. 2nd International Symposium on Ultrasonic Doppler Methods for Fluid Mechanics and Fluid Engineering, Villigen PSI, Switzerland, 22 September 1999, pp. 61-64  
 [4] Meile T., Schleiss A., Boillat J.-L., Dubois J.: Experimental study on steady flow in a channel with macro-roughness at the side walls, *International Conference on Fluvial Hydraulics, River Flow 2006*, Lisbon, Portugal (accepted for publication in the proceedings).  
 [5] Met-Flow SA: UVP-DUO Monitor for flexible velocity profiling, [www.met-flow.com](http://www.met-flow.com), Lausanne, Switzerland, 2002.  
 [6] Takeda, Y.: Ultrasonic Doppler Method for Flow Measurement, Mini-symposium on Advanced Fluid Information Tokyo, Japan, 2002.

# Calibration Tests of Pulse-Doppler Flow Meter at National Standard Loop

Michitsugu Mori, Kenichi Tezuka, Takeshi Suzuki  
Tokyo Electric Power Co., Inc., Yokohama, Japan

Yasushi Takeda  
Hokkaido University, Sapporo, Japan

Calibration tests of UdFlow, ultrasonic pulse-Doppler flowmeter, were conducted at the national standard loop in Mexico, CENAM (The Centro Nacional de Metrologia) in order to evaluate the accuracy of the flowmeter. Four ultrasonic transducers are mounted on the surface of stainless steel piping circumferentially with the diameters of 100mm and 200mm to measure four velocity profiles. Figure 1 shows pipe arrangements at CENAM. Flow rates can be obtained by integrating each measuring line and taking the average of them. Air was injected at the upstream of measuring point for ultrasonic reflectors. Tests were conducted at five different flow rates with the Reynolds numbers between 200,000 and 1,200,000. Tests were repeated six times at each flow rate to evaluate repeatability. In addition, the put-off and put-back test was carried out at 100mm piping with the flowrate of 3000 L/m to evaluate reproducibly. The values of the CENAM loop are based on the average of weighing time while those of the ultrasonic-Doppler flow velocity-profile flowmeter are based on the time average of instantaneous values. The calibration tests found a deviation better than 0.3% between the two devices in terms of the average of the values recorded by six rounds of each measurement. From the results of measurement conducted with Reynolds number varied, it was found that the overall average deviation between the two devices was better than 0.3%.

**Keywords:** ultrasonic-Doppler, velocity profile, flowmeter, industrial application, calibration

## 1 INTRODUCTION

The feedwater (FW) systems of a power plant are generally exposed to high temperature and/or pressure conditions within large pipes. Therefore, determining a profile factor (PF) under the same flow conditions and configurations as large pipe diameters and curve bends is impractical and results in certain errors in measurement. In fact, it is impossible at the present time to determine a PF by a high-precision calibration loop using a weighing method under such high temperature and pressure conditions as in the FW system. Consequently, the PF has to be determined with a Reynolds number (Re) within one order of magnitude of the actual plant. The conventional ultrasonic flowmeters as described below round off all indeterminate errors by a PF as described in Figure 1(1). To remove these errors, efforts are needed to eliminate the PF by determining flow rates based on the calculation of true flow profiles in the piping (2, 3). In order to achieve a highly accurate flow measurement, the measurement of a flow profile is required to eliminate the PF (4). We have conducted field tests using UDF, the flow-metering system by ultrasonic pulse-Doppler profile-velocimetry (5) where instantaneous flow profiles and flow rates were widely measured in CW systems and steel penstock of hydro-turbines, etc(3). The application for the nuclear FW measurement requires further high accuracy within 0.5% to monitor the thermal power and to utilize the measurement uncertainty for a power uprate. Integration of instantaneously-determined flow velocity profiles, obtained by performing continuous line-measurements over

piping, will provide an accurate flow rate measurement system as an advanced flowmeter, superior to the conventional flowmeter using a PF. The conventional flowmeters based on the time-of-flight (TOF/transit time) method depend largely on the accuracy of a PF as it finally determines the flow rate of a fluid by multiplying it. This is also true of a one-point ultrasonic-Doppler flowmeter. Accordingly, these conventional methods are limited in the scope of application as they are effective only in measuring flows with steady-state developed flow. In other words, the methods have to use an approximation that is applicable only in a narrow flow range.(6)

Calibration tests were performed at the national standard loops in four countries. The UDF is based on the measurement of line velocity profiles, thereby eliminating PFs, resulting in a more accurate determination of flow rates.

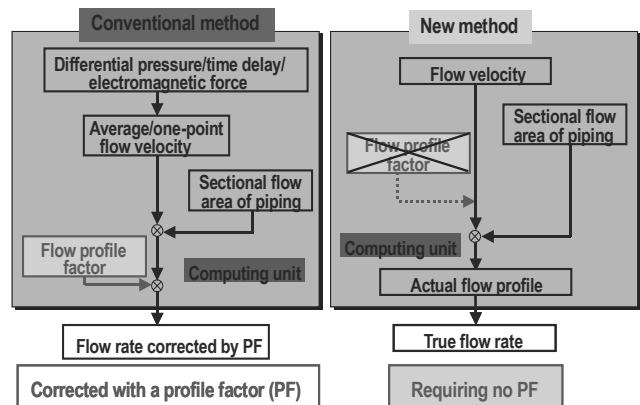


Figure 1. Conceptual comparison between conventional flowmeters and the flow-metering system by ultrasonic Pulse-Doppler profile-velocimetry.

## 2 CALIBRATION TESTS AT NIST, NMIJ, AND NMI

### 2.1 Tests at NIST

The flow rate of water per unit length of time can be determined by accumulating fluid flowing down the measuring test section into the weighing tank in a given period of time and dividing the volume of the fluid thus accumulated by the time elapsed. The nominal measurement error of the test loop at NIST is 0.12%. In these tests, the flow of water was measured at the point where it reached the stage of full development. The UDF was found to meet the approved values of the standard loop with sufficient accuracy. Table 1 compares the approved values of the NIST standard loop and the corresponding data on the UDF at  $Re = 400,000$ . The values of the NIST loop were based on the average of weighing time while those of the UDF were based on the time average of instantaneous values. As indicated in the table, the measuring test found a deviation of 0.03% between the two devices in terms of the average values recorded by five rounds of measurement. From the results of measurement conducted with varied  $Re$  numbers, it was found that the overall average deviation between the two devices was determined to be no more than 0.2% (7).

Table 1. Comparison of the approved values of the NIST standard loop.

Run No.	UdFlow	NIST	Deviation	
			L/s	%
#1	69.760	69.600	-0.161	-0.23%
#2	69.670	69.613	-0.057	-0.08%
#3	69.725	69.612	-0.113	-0.16%
#4	69.444	69.622	0.178	0.26%
#5	69.569	69.609	0.040	0.06%
<b>Average</b>	<b>69.634</b>	<b>69.611</b>	<b>-0.022</b>	<b>-0.03%</b>

### 2.2 Tests at NMIJ and NMI

Further calibration tests were conducted on the UDF by a liquid flowmeter calibration facility, a verification loop, at NMIJ in Japan and NMI in the Netherlands.

The calibration tests on the UDF were carried out for water with a measuring instrument attached to the 400A piping section of the loop at NMIJ. At NMI, the calibration tests were carried out for water and kerosene with the 150A piping section of the loop. Both calibration facilities (made to the national standard loop) have the standard uncertainty set at 0.02% of the reference flow rate. The results of the test at NMIJ and NMI are summarized in Table 2 and Table 3, respectively.

Table 2. Comparison of the approved values of the NMIJ standard loop.

Reference Flowrate $Q_1$ (m <sup>3</sup> /h)	Output of Flowmeter under Test $Q_m$ (m <sup>3</sup> /h)	Ratio of Flowrate and Uncertainty	
		Ratio $Q_m/Q_1$	Expanded Uncertainty (k = 2)
2000.5	2008.9	1.004	0.4%
1512.7	1508.2	0.997	0.1%
986.1	984.6	0.999	0.3%

The test findings indicate the uncertainty of the flowmeter examined in terms of the average of the results recorded in 10 rounds of measurement at NMIJ and three rounds at NMI, comparing with the reference flow rate set as a target. The reference meter of NMIJ was based on a weighing method, and that of NMI was a turbine flowmeter. Based on these measuring tests, the UDF was given a calibration certificate showing uncertainty ranges within 0.4% at NMIJ and 0.59% at NMI for water.

### 2.3 CALIBRATION TESTS at CENAM

Following improvements to the UDF System, calibration tests were carried out at CENAM, using ultrasonic transducers clamped on the surface of stainless steel piping having diameters of 100 mm and 200 mm.

Table 3. Comparison of the flow rates measured by UDF with the approved values of the NMI standard loop for water (left) and kerosene (right).

#### NMI - Nederlands Meetinstituut

Reference Flow-rate [l/min]	Reference Velocity [m/s]	Indicated Flow-rate [l/min]	Indicated Velocity [m/s]	Deviation [%]
1276.7	1.2041	1273.1	1.2007	-0.28
1276.6	1.2040	1280.7	1.2079	+0.32
1276.8	1.2042	1271.7	1.1994	-0.40
953.76	0.8995	959.4	0.9048	+0.59
953.41	0.8992	952.8	0.8986	-0.07
953.74	0.8995	949.1	0.8951	-0.49
632.02	0.5961	633.9	0.5979	+0.30
631.82	0.5959	628.5	0.5928	-0.52
632.04	0.5961	630.1	0.5943	-0.30

Reference Flow-rate [l/min]	Reference Velocity [m/s]	Indicated Flow-rate [l/min]	Indicated Velocity [m/s]	Deviation [%]
1276.6	1.2040	1279.5	1.2067	+0.22
1276.4	1.2038	1281.3	1.2084	+0.38
1276.5	1.2039	1281.5	1.2086	+0.39
956.19	0.9018	949.3	0.8953	-0.72
956.54	0.9022	959.1	0.9046	+0.27
955.92	0.9016	955.4	0.9011	-0.06
639.51	0.6032	641.1	0.6046	+0.23
639.49	0.6031	643.6	0.6070	+0.65
639.30	0.6029	643.90	0.6073	+0.73

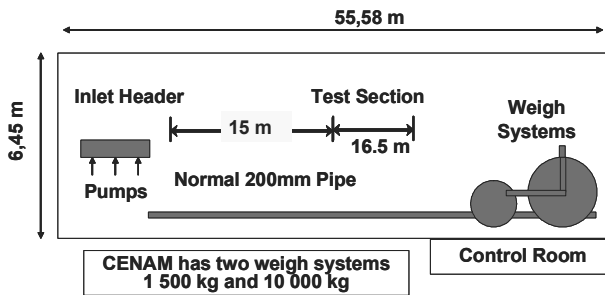


Figure 2. CENAM Water Flow Lab Layout-Normal 200mm Diameter Test

Figure 2 shows the pipe arrangement at CENAM. The CENAM loop contains a straight pipe long enough to produce the developed flow condition, an inlet header and pumps, and weigh systems. CENAM has two weigh systems of 1,500 kg and 10,000 kg.

Air was injected upstream of the measuring point up to ~400 ppm (0.04% as a volumetric fraction.). We confirmed that there was a negligible effect of air injection on the flow rates measured by the weigh systems of CENAM, comparing the flow rate measured without air injection with one using air injection.

Tests were conducted at five different flow rates with the Reynolds numbers between 200,000 and 1,330,000. Tests were repeated six times at each flow rate to evaluate repeatability. In addition, the take-off and put-back test was carried out on the 100 mm piping with the flow rate of 3000 L/m to evaluate reproducibility. The values of the CENAM loop are based on the average of weighing time while those of the UDF were based on the time average of instantaneous values. The references 8, 9, and 10 provide the following definitions of each Individual Value :

### 2.3.1 Relative Errors

The relative error between  $qv$  from the reference and  $qv$  from the meter is defined by:

$$e = \left( \left[ \frac{qv_{meter}}{qv_{primary\ standard}} \right] - 1 \right) 100 \quad (\%)$$

### 2.3.2 Meter Factor

The Meter Factor (MF),  $MF_i(q_j)$ , for a single measurement  $i$  at flow  $q_j$ :

$$MF_i(q_j) = \frac{qv_{j\ primary\ standard}}{qv_{j\ meter}}$$

where, :

$qv_{primary\ standard}$  – volumetric flow-rate determined by the primary standard at line conditions (L/min).

$qv_{meter}$  – time-averaged volumetric flow rate measured for the meter, at line conditions, over the calibration interval (L/min).

The MF arithmetic mean value for a series of measurements at the flow rate  $q_j$  :

$$\overline{MF}_j(q_j) = \overline{MF}_j = \frac{1}{n} \sum_{i=1}^n MF_i(q_j)$$

### 2.3.3 Meter Factor Uncertainties

The experimental variance of  $MF_i(q_j) = s^2(MF_j)$ , from repeated measurements at flow rate  $q_j$ :

$$s^2(MF_j) = \frac{1}{n-1} \sum_{i=1}^n \left( MF_i(q_j) - \overline{MF}_j(q_j) \right)^2$$

The experimental standard deviation of the mean of the Meter Factor,  $s_{dm}(\overline{MF}_j)$  at each flow, is given by:

$$s_{dm}(\overline{MF}_j) = \frac{1}{\sqrt{n}} s(MF_j)$$

where  $n$  is the number of the replicated tests at flow  $j$ . The meter Repeatability, i.e., the short term stability can be quantified as the experimental standard deviation of the mean at each test flow; the largest Repeatability is quoted as a bound for the meter for all of the flows tested.

### 2.3.4 Expanded Uncertainty

The Expanded Uncertainty,  $U$  is:

$$U(\overline{MF}_j) = kU_c(\overline{MF}_j)$$

The expanded uncertainty  $U$  can also be expressed using a coverage factor  $k$  based on t-distribution for  $v_{eff}$  degrees of freedom with a level of confidence of approximately 95 %. This uncertainty was evaluated according to Reference 9.

### 2.3.5 Reproducibility

For specific sets of tests done for the UDF, Reproducibility is defined in terms of the standard deviation of the mean of the multiple sets of runs taken at essentially the same flow condition after specific, typical changes in test conditions are made to assess the meter's performance in these conditions. The specific changes made need to be described. Typical changes needed by most meter users are turning the flow off and then turning it back on, and then repeating the tests; this effect can be quantified by the TOTO (turn-off-turn-on) Reproducibility. For clamp-on type meters, another typical change is quantified by TOPB (take-off-put-back) Reproducibility. The conditions changed in these tests include, for a single flow, both TOTO and TOPB and the Reproducibility, i.e., longer term meter stability obtained is quantified by the experimental standard deviation of the mean for these tests:

Table 4 Summary data of the tests on the 100 mm pipe diameter and on the 200 mm pipe diameter in fully-developed flow conditions. The table below lists the mean values of MF -meter factor - and standard deviation calculated from 6 values, the Reproducibility (for a single flow) and the expanded uncertainty of the meter factor.

Primary Standard				UdFlow	Test Result	
Reynolds Number	Average Flow Velocity $v$ (m/s)	Primary Standard Flow Rate $qv$ (L/min)	Relative Standard Deviation $s$ (%)	Meter Flowrate $Q_{vm}$ (L/min)	Meter Factor MF	Deviation $e$ (%)
200 mm pipe diameter						
$4.46 \cdot 10^5$	2.1	4 000.73	$1.59 \cdot 10^{-2}$	4 010.06	0.997 68	0.23
$6.59 \cdot 10^5$	3.1	6 006.78	$1.64 \cdot 10^{-2}$	6 012.02	0.999 13	0.09
$8.93 \cdot 10^5$	4.1	8 005.22	$1.46 \cdot 10^{-2}$	7 998.56	1.000 83	- 0.08
$1.11 \cdot 10^6$	5.2	9 998.64	$1.36 \cdot 10^{-2}$	9 980.48	1.001 82	- 0.18
$1.33 \cdot 10^6$	6.2	12 002.10	$5.22 \cdot 10^{-3}$	12 011.41	0.999 23	0.08
$4.46 \cdot 10^5$	2.1	4 000.73	$1.59 \cdot 10^{-2}$	4 010.06	0.997 68	0.23
$6.59 \cdot 10^5$	3.1	6 006.78	$1.64 \cdot 10^{-2}$	6 012.02	0.999 13	0.09

$$R = sdm \left[ \overline{MF}_j \right] = \sqrt{\frac{1}{m(m-1)} \sum_{i=1}^m \left[ MF_i(q_j) - \overline{MF}_j \right]^2}$$

where “j” is the flow for which the “changed conditions” tests were done again and “m” is the total number of repetitions of data points taken at essentially the same test flow. Table 4 summarizes the test data on the 100 mm and 200 mm pipe diameters in fully-developed flow conditions. The average flow velocities varied from ~2m/s to ~6m/s for both pipes. The Reynolds numbers were set up to 1,330,000 for the case of the pipe diameter of 200 mm, and 641,000 for 100 mm. From the results of measurement conducted with varied Reynolds numbers, it was found that the overall average deviation between the two devices was better than 0.3%. The table lists the mean values of meter factor and standard deviation calculated from 6 values, the Reproducibility (for a single flow) and the expanded uncertainty of the meter factor.

### 3 CONCLUDING REMARKS

The calibration tests of UDF were conducted at four national standard loops: NIST in the United States, NMIJ in Japan, NMI in the Netherlands, and CENAM in Mexico, in order to evaluate the accuracy of this new type flow-metering system. The test results at NIST, NMIJ, and NMI for the velocity profile measurements exhibited the deviations within ~0.5%. Following improvements to the UDF System, the maximum spreads in individual MF test results in the mean values for the UDF are from -0.17% to +0.14 % for the 100 mm diameter pipe and from -0.18% to +0.23 % for the 200 mm diameter pipe over the range of Reynolds numbers tested at CENAM. At CENAM the short term stability (Repeatability) and longer term stability (Reproducibility) are both considered good, i.e., better than 0.03 % in these test conditions. Further

testing needs to be done to better quantify Reproducibility characteristics.

The expanded uncertainty for the UDF Meter Factor in these tests at CENAM is bounded by  $\pm 0.21$  % for Test 1 (100 mm pipe) and by  $\pm 0.16$  % for Test 2 (200 mm pipe); these values are computed for 95% confidence levels. A negligible effect on the CENAM primary standard measurements was found for the air bubble injection used for these tests.

### REFERENCES

- [1] Mori, M., et. al., “Industrial Application Experiences of New Type Flow-metering System based on Ultrasonic-Doppler Flow Velocity-Profile Measurement,” Third International Symposium on Ultrasonic Doppler Methods for Fluid Mechanics and Fluid Engineering, EPFL, Lausanne, Switzerland, September 9 - 11, 2002
- [2] Takeda, Y., et. al., “Development of flow rate measurement using ultrasonic Doppler method [1]Theoretical background,” 1998 Fall Meeting of AESJ, [1998] F16, p.343
- [3] Mori, M., et. al., “Development of ultrasonic-Doppler velocity profile method for flow rate measurements of power plant,” [1999] ICONE-7, FP7429
- [4] Mori, M., et. al., “EFFECTS OF INNER SURFACE ROUGHNESS AND ASYMMETRIC PIPE FLOW ON ACCURACY OF PROFILE FACTOR FOR ULTRASONIC FLOW METER,” ICONE-14 89729, Proceedings of ICONE 14, July 17-20, 2006, Miami, Florida USA.
- [5] Mori, M., et. al., “Development of a novel flow metering system using ultrasonic velocity profile measurement,” Experiments in Fluids, 32 [2002] pp.153-160.
- [6] Takeda, Y., “Measurement of velocity profile of mercury flow by ultrasound Doppler shift method,” Nuclear Technology, 79 [1987]. pp 120-124.
- [7] Takeda, Y., et. al., “Development of a new flow metering system using UVP, Preliminary performance assessments using NIST flow standards,” Proceedings of ASME FEDSM'00, ASME 2000 Fluids Engineering Division Summer Meeting, June 11-15, Boston, Massachusetts.
- [8] ASME/ANSI MFC-9M-1988, Measurement of Liquid Flow in Closed Conduits by the Weighing Method, Amer. Soc. of Mech. Engrs., NY, NY.
- [9] ISO/IEC/BIPM/OIML - Guide to the Expression of Uncertainty in Measurement – 1995
- [10] International Vocabulary of Basic and General Terms in Metrology – Published by ISO 1999

# Application of Ultrasonic Pulse-Doppler Flow meter for Hydraulic Power Plant

Kenichi Tezuka, Michitsugu Mori, Takeshi Suzuki  
Tokyo Electric Power Co., Inc. , Yokohama, Japan

Toshimasa Kanamine  
Tokyo Electric Power Co., Inc. , Tokyo, Japan

At hydraulic power stations, Pitot tubes were commonly used to measure flow rates in steel penstocks for the performance tests of hydraulic turbines. Due to the difficulties of installations and measurements, time-of-flight (TOF) ultrasonic flow meters are being popular for the flow rate measurement. However, the accuracies of TOF ultrasonic flow meters are extremely sensitive for the flow profiles which are dependents of Reynolds numbers and surface roughness. In those situations, clamp-on type ultrasonic pulse Doppler flow meters (UdFlow) are considered to be suitable for the measurements of flowrates in large steel penstock because UdFlow can measure the flow profiles directly. This paper presents measurement results of velocity-profiles using ultrasonic pulse Doppler flowmeter applied for a steel penstock in an actual hydraulic power plant. The piping is more than one meter in diameter, and Reynolds number is more than five million. As a result, with certain amount of bubbles, ultrasonic pulse Doppler flowmeter can measure the flow profiles for the large steel penstock. Figure 1 shows the measurement result of field tests using an ultrasonic pulse-Doppler flowmetering system for the steel penstock for the case of a pipe diameter of 1.3m. Two ultrasonic transducers were placed on both side of the outer surface of the pipe. Each transducer catches the velocity profile from the pipe centerline to the corresponding far wall. The measurements were conducted simultaneously. Red line and blue line represent velocity profiles on each beam path. The time-averaged flow profile of large pipe with 1.3m in diameter well predicted the parabolic flow profile. Integrating the flow velocity-profile over the pipe section provides the flow rate. Figure 2 shows the steel penstock in hydraulic power plant.

**Keywords:** ultrasonic-Doppler, velocity profile, flowmeter, industrial application, calibration

## 1 INTRODUCTION

The field tests were carried out to extend the applicability of the ultrasonic-Doppler flow velocity-profile flowmeter. Table 1 shows the field application experiences of Ultrasonic-Doppler flow velocity-profile flowmeter. The flow rates of the condenser cooling water circulation system (CW) in thermal power plant were successfully measured for the pipe sizes of 1.5m and 1.7m, where the sufficient ultrasonic reflectors existed in the flow of the pipes to measure the velocity profiles because of low system pressure. Due to the pipe size, it is difficult with conventional flow meters to measure the flowrate accurately in steel penstock at hydraulic power plant.

Table 1: Field applications of Ultrasonic-Doppler flow velocity-profile flowmeter in electric power stations

System	Pipe Size	Fluid Type	Flow Rate
Hydraulic Turbine	1-4m	River water	1-40m <sup>3</sup> /s
Condenser Cooling water	1-2m	Sea water	20m <sup>3</sup> /s
Nuclear Reactor Feed water	0.5m	Pure water (high temperature and high pressure)	1m <sup>3</sup> /s

## 2 MEASURING THE FLOW RATE AT A HYDRAULIC POWER STATION

Pitot tubes were widely used to measure the flow rate in the steel penstock for the field efficiency test of hydraulic turbine at a hydraulic power station. At present, the time-of-flight ultrasonic flowmeters are mainly used for this purpose. Installation of Pitot tubes requires the steel penstock to be drained of the water, taking a very long time. In addition, Pitot tubes are likely to become clogged with dust or sand contained in water. With the time-of-flight ultrasonic flowmeters, the K factor, a coefficient of flow velocity used to derive the flow rate from the flow velocity measured, is influenced heavily by the velocity profile in the pipe cross section. As a result, the measured value may differ significantly from the actual flow rate if the flow remains undeveloped or if the inner surface the pipe is very rough. On the other hand, ultrasonic Doppler flow velocity profile measurement method (Ref. 1 – Ref. 3), which measures the velocity profile of the fluid using a transducer installed on the outer surface of a pipe, does not require a correction coefficient in flow rate calculations to measure the flow rate. This method allows highly accurate measurements and does not affect process systems. In addition, costs of installing equipment are reasonable. It is therefore an attractive and practical measuring method.

### 3 THE COMPOSITION OF UDFLOW MEASURING INSTRUMENTS

The ultrasonic pulsed Doppler flow measuring system consists of the followings;

(1) Measuring unit:

Flow rate measuring instruments (ultrasonic transducer, signal processing unit, and client personal computer)

(2)Bubble injection unit:

Injection pump, air compressor, nozzle

The ultrasonic transducers are installed on the surface of the steel penstock with plexi edge at the inclined angle of  $\theta$  (Fig. 1 and Fig.2) and the velocity profiles inside the steel penstock are measured along the ultrasonic beam path.

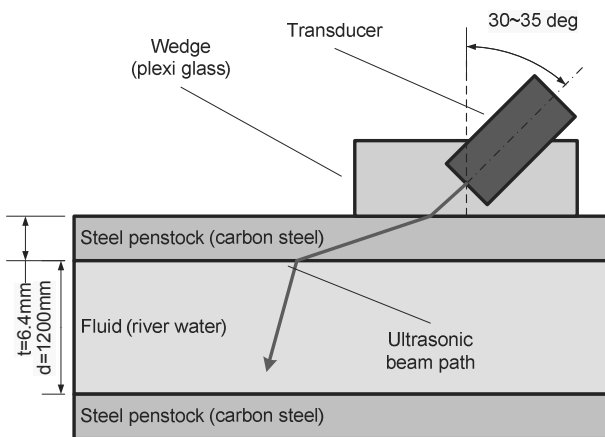


Figure 1: Schematic diagram of installation of ultrasonic transducer clamped on pipe surface



Figure 2: Ultrasonic transducer and wedge installed on the surface of steel penstock at hydraulic power plant

In order to secure reflectors, the bubble injector (Fig. 3 and 4) is installed at the inlet of the steel penstock and miniaturized bubbles are generated into the pipe inlet. Mixture of water and air goes into the nozzle and bubbles can be miniaturized at the outlet of nozzle throat. Those tiny bubbles are suitable for

the measurement by Ultrasonic Doppler flow meter.

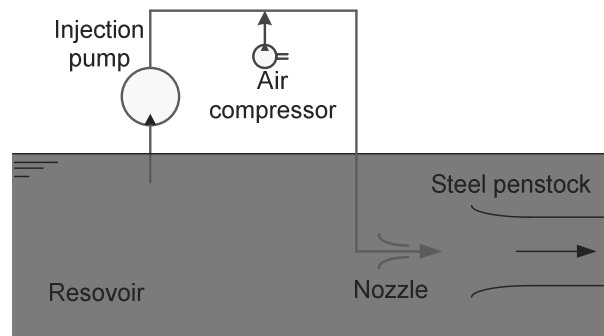


Figure 3: Configuration of bubble injection system to supply miniaturized bubbles as ultrasonic reflectors into steel penstock



Figure 4: Water jet from injection nozzle to supply miniaturized air bubbles

### 4 RESULTS OF FLOW RATE MEASUREMENTS AT DIFFERENT POWER OUTPUT LEVELS

Measurement tests were carried out at Nakazato hydraulic power station of the Tokyo Electric Generation Company. This power station generates electricity with a horizontal shaft Francis turbine, and has the maximum capacity of 700 kW, the effective head of 36 m and the maximum flow rate of approximately 3 m<sup>3</sup>/s. The steel penstock is a riveted pipe that is approximately 1,200 mm in inside diameter. Figure.5 shows the results of velocity profile measurements at horizontal diameter position of approximately 9D (D: The diameter of the pipe) from the inlet of the steel penstock and at power levels of approximately 280 kW, 450 kW and 580 KW. Although the flow was in developing region, the velocity profile in the region from the center of the pipe to the opposite wall of the pipe to calculate flow rate was successfully measured at different power output levels.

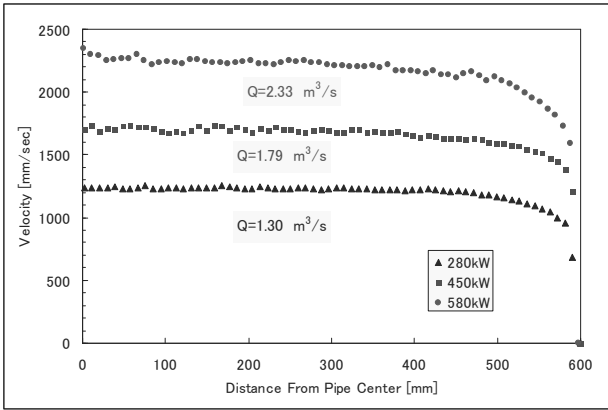


Figure 5: Velocity profiles for the different power outputs at the horizontal diameter position of 9D

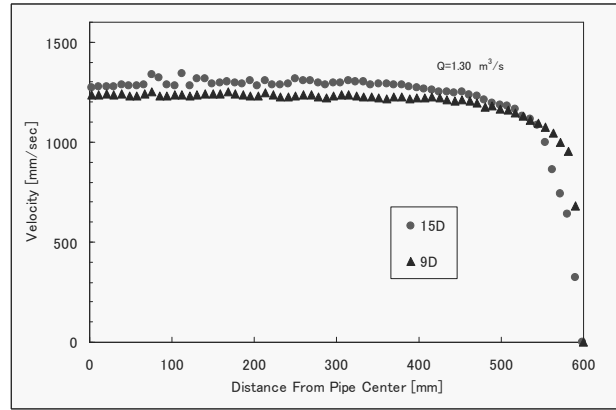


Figure 7: Velocity profiles for 280kW at the horizontal diameter positions of 9D and 15D

In addition to 9D, flow rates were also measured at the 15D and 30D points. Pitot tube flow rate measurements were formerly conducted at 15D position. A comparison of the velocity profiles measured by the Pitot tube and by the UdFlow is shown in Fig. 6. Pitot tube flow rate measurements were conducted radially at five different points. This Pitot tube measurement was carried out about 30 years ago and consequently the conditions of the hydraulic turbine were not the same as they are now. As a result, there was a little difference in the flow rate, but the trends in the velocity profile measured with the Pitot tube agree with those identified by the UdFlow measurements.

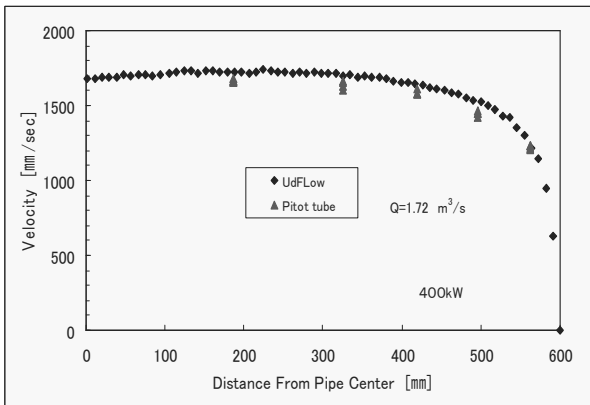


Figure 6: Comparison of velocity profile for 400kW between Pitot tube and UdFlow

A comparison of the velocity profiles at about 280 kW at the horizontal diameter positions of 9D and 15D is shown in Fig. 7. Compared with 9D, the flow velocity profile at the 15D point is faster in the center region and slower adjacent to the pipe wall. This indicates that the UdFlow has confirmed that the flow is almost developed.

The relationship between the flow rates measured by the UdFlow and power levels is shown in Fig. 8. A dashed line denotes the flow rates measured by the Pitot tube and compared with these values, the results of the flow rate measurements by the UdFlow show good agreement.

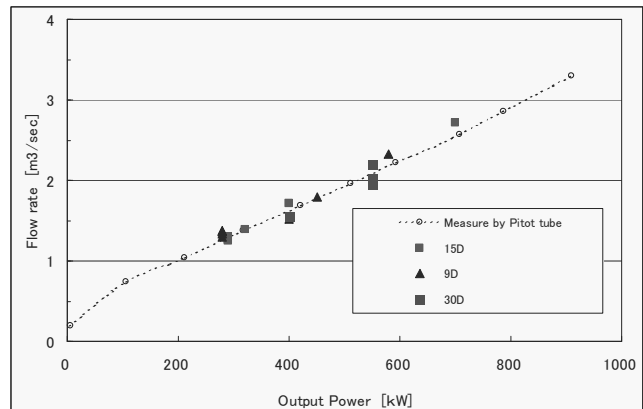


Figure 8: Comparison of flow rate vs. power output between Pitot tube and UdFlow at different horizontal diameter positions

## 5 MULTILINE VELOCITY PROFILE MEASUREMENTS

Steel penstock configuration, geographical conditions of upstream rivers and water reservoir are different in different power stations. Velocity profile is not always axisymmetric at measurement positions. In that case, multiline measurements that measure the flow rate with two or more transducers installed at different phases on the pipe are necessary. In the measurement, transducers were installed at the radially symmetric positions of the pipe and multiline, simultaneous measurements were carried out. Measurements were conducted at Okuragawa Power Station (Fig.9) of the Tokyo Electric Generation Company which has the penstock that is a welded pipe, with the maximum capacity of 1,900 kW, the flow rate of approximately

2.4 m<sup>3</sup>/s, and the penstock inside diameter of 1,250 mm. The electric power level during measurements was 1,100 kW.



Figure 9: Measuring point of ultrasonic flowmeter at horizontal diameter position of 19D from the inlet of steel penstock at Okuragawa hydraulic power station

Fig.10 shows an example of the velocity profile measurement. A red dot denotes the velocity measured by Transducer A and a blue dot indicates the velocity measured by Transducer B. It should be noted that the velocity profile is asymmetrical around the pipe center. The flow rate value is the time averaged obtained from the instantaneous velocity profiles during measurement.

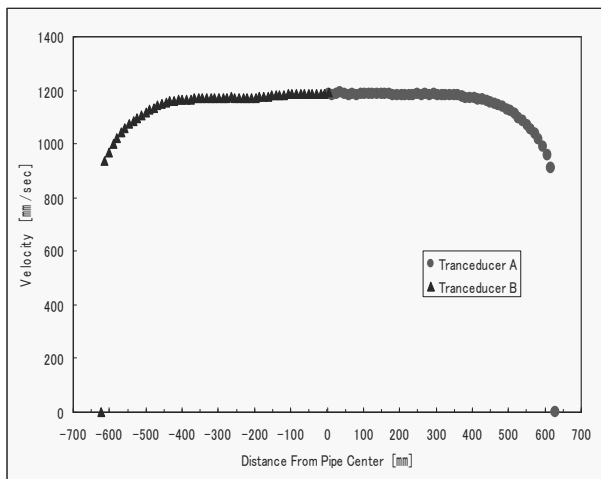


Figure 10: Velocity profiles obtained by multiline measurement method with two transducers placed at opposed circumferential positions on steel penstock

Flow rate measurements were conducted eleven times and the results of the measurements are shown in Table 2. This table shows the average flow rate in each measuring line, the standard deviation and the average flow rate in two measuring lines. The value measured by the time-of-flight ultrasonic flowmeter during efficiency tests is also shown. Even if the flow is asymmetrical, this method is expected to measure flow rate with greater accuracy

than single-line measurements.

Table 2: Comparison of flow rate measurements between UdFlow and Time-of-flight ultrasonic flow meter at 1100kW of Okuragawa hydraulic power station

	UdFlow		time-of-flight ultrasonic flowmeters
	Line A	Line B	
Average [m <sup>3</sup> /s]	1.39	1.33	1.38
Standard deviation[%]	1.07	1.55	
Total average [m <sup>3</sup> /s]	1.36		

## 6 CONCLUSIONS

The velocity profile and flow rates in the steel penstock were measured by the ultrasonic-Doppler flow velocity profile flowmeter at a hydraulic power station. Data on the velocity profile at different power output levels were obtained. A comparison has confirmed that the trends in the velocity profile measured by the Pitot tube agree with those measured by the UdFlow measurements. Moreover, two-line measurements were conducted and satisfactory results were obtained. The application of this method in measuring flow rates at power stations is expected to provide highly accurate flow measurements.

## REFERENCES

- [1] Takeda Y. et. al., "Development of a new flow metering system using UVP, Preliminary performance assessments using NIST flow standards," Proceedings of ASME FEDSM'00, ASME 2000 Fluids Engineering Division Summer Meeting, June 11-15 2000, Boston, Massachusetts
- [2] Mori M. et. al., "Development of a novel flow metering system using ultrasonic velocity profile measurements," Experiments in Fluids, 32, pp. 153-160, 2002
- [3] Mori M. et. al., "Industrial Application Experiences of New Type Flow-metering System based on Ultrasonic-Doppler Flow Velocity-Profile Measurement, 3<sup>rd</sup> ISUD, 2002

# Theoretical and Experimental Investigation of Effects of Flow Fluctuations on UDV Signals

Volkan Köseli, Yusuf Uludag

Department of Chemical Engineering, 06531 Ankara, Turkey

Effects of oscillating flows on the frequency spectrum of back-sampled pulsed ultrasound signals (PUS) are investigated both experimentally and theoretically. Simulation results revealed that while coherent component of velocity is encoded in the phase of the PUS, oscillating component is observed in terms of the amplitude and variance of the signal. The attenuation and variance increase on PUS spectrum in turbulent flow regime was also observed experimentally in measurements on a pipe flow system by means of DOP2125. Obtained PUS spectrums were closely related to the probability density function (pdf) of velocity at measurement point. The results indicate that ultrasound Doppler method can also be employed to determine turbulent flow characteristics such as time-averaged velocity, turbulence intensity and kinetic energy distributions in a pipe flow.

**Keywords:** Ultrasound Doppler Velocimetry(UDV), Discrete Fourier Transformation (DFT), Signal Attenuation, Pipe Turbulent Flow

## 1 INTRODUCTION

Pulsed Ultrasound Doppler Velocimetry (UDV) measurement technique is widely used in medical field for fluid flow measurements[1]. This technique is based on the velocity measurement using the phase of the successively recorded sound echo from a point through the spectral analysis of the signals. Here the main assumption is that velocity remains constant at least within the measurement time scales. Therefore UDV has mainly been applied for cases involving laminar flows[2]. In many applications, on the other hand, there are always small or large flow fluctuations[3]. These fluctuations can be expected to deteriorate the velocity measurement quality in ordinary UDV applications. Eliminating those negative effects and investigating the nature of the fluctuations themselves, such as turbulence, can be possible by understanding the impact of the flow fluctuations on the UDV signals quantitatively. A recent study about the intensity fluctuations of ultrasonic scattering in highly turbulent channel flow shows the potential of Doppler Ultrasound techniques for the investigation of turbulence[4].

Flow fluctuations that occur within the time scales of UDV measurement, i.e. from milliseconds to seconds, interfere with the regular build up of the signal phase. Typical time scales of the turbulence eddies in pipes also fall into this time interval. Therefore UDV can be potentially used as turbulence characterization probe in pipe flows. There are some studies in literature involving effects of the random

motions on another technique, nuclear magnetic resonance imaging (NMRI). Signal attenuation due to random molecular motion[5-6-7] and effects of oscillating flow components on velocity profiles obtained by NMRI[8] have been reported.

The aim of the present study is to investigate the effects of the flow fluctuations on the UDV signal both theoretically and experimentally. The results obtain through analytical derivations and computer simulations are compared with those of the experimental measurements. In the following sections, the followed methodology and some of the obtained results are presented

## 2 SIMULATIONS

A computer code was written to obtain the spectrum and velocity values for several points by fast Fourier transformation of back-sampled PUS from particles in a pipe flow. Motion of particles was incorporated by tracking their position in the flow. The particles are assumed to have a velocity which was composed of a constant local value superimposed by an oscillating component with a specified amplitude and frequency (Eq. 1).

$$V(r) = U(r) + A_f \sin(w_f t) \quad (1)$$

For a measurement gate of distance of  $d_0$  from probe tip, the signal from measurement point having velocity without an oscillating part can be represented by;

$$S_n = A_o \sin(2\pi f_o t_n) \quad (2)$$

where A is amplitude of PUS,  $f_o$  is emitting frequency and  $t_n$  is sampling time for  $n^{\text{th}}$  pulse. Discrete Fourier transform of these back sampled ultrasound signals will be;

$$S[k] = \frac{A_o}{2} j(e^{j(a_1 + a_2 + a_3)} N \delta[k - \frac{a_3 N}{2\pi}] - e^{j(a_1 + a_2 - a_3)} N \delta[k + \frac{a_3 N}{2\pi}]) \quad (3)$$

where  $a_1 = 4\pi \frac{f_o}{c} d_o$

$$a_2 = 4\pi \frac{f_o}{c} \frac{d_o}{c} U_{|R_{\text{cd}}|} \cos\theta$$

$$a_3 = 4\pi \frac{f_o}{c} U_{|R_{\text{cd}}|} \cos\theta T_{\text{pr}}$$

N is total sampling number,  $\theta$  is angle between pipe and probe

R is pipe radius.

and when  $k = \frac{a_3 N}{2\pi}$  (at Doppler frequency point)

amplitude of spectrum is;

$$\left| S\left[\frac{a_3 N}{2\pi}\right] \right| = \frac{A_o N}{2} \quad (4)$$

and phase of spectrum is;

$$\text{Arg}\left[S\left[\frac{a_3 N}{2\pi}\right]\right] = 4\pi \frac{f_o}{c} \left(d_o + U_{|R_{\text{cd}}|} \cos\theta (1 - T_{\text{pr}})\right) + \pi/2 \quad (5)$$

This shows that constant or coherent velocity only affects the phase of spectrum of PUS and has no effect on the amplitude. But random or oscillating velocity also affects the amplitude of spectrum as seen in simulation results. Spectrum taken from constant velocity flow point (Figure 1) and oscillating flow points with two different frequencies are presented (Figure 2 and 3) below. Simulations revealed the amplitude attenuation of PUS spectrums for oscillating type flow compared to laminar type constant velocity flow. This attenuation effect increases with increasing flow oscillation frequency and becomes less and less when flow oscillation period becomes much smaller than data acquisition period. However increasing amplitude of fluctuations always leads to a broadening and spectral energy spreading on spectrum.

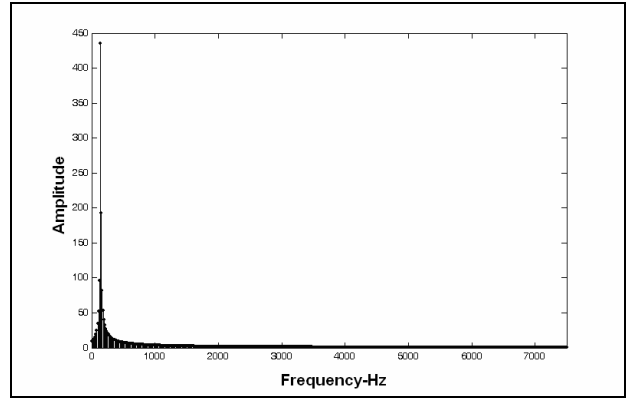


Figure 1: Spectrum of PUS received from center of pipe (ID=50mm) for velocity component in probe direction. Sampling frequency is 14346 Hz and sampling number is 1024. Local velocity is 78 mm/s without any fluctuation.

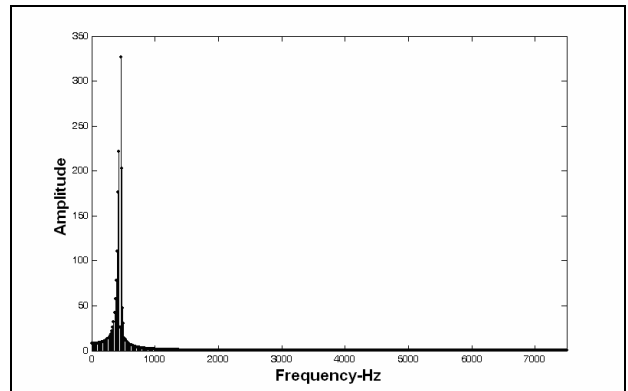


Figure 2: Spectrum of PUS received from center of pipe (ID=50mm) for velocity component in probe direction. Sampling frequency is 14346 Hz and sampling number is 1024. Local average velocity is 234 mm/s and it has an oscillating part with frequency 10Hz and amplitude 10% of the average.

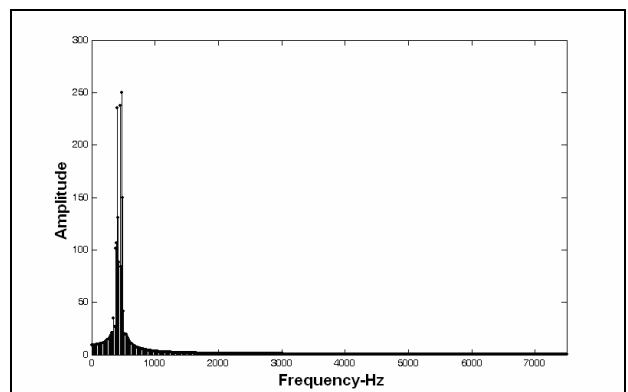


Figure 3: Spectrum of PUS received from center of pipe (ID=50mm) for velocity component in probe direction. Sampling frequency is 14346 Hz and sampling number is 1024. Local average velocity is 234 mm/s and it has an oscillating part with frequency 20Hz and amplitude 10% of the average.

In Figure 4, it is clear that there is a complex relation between PUS amplitude and flow fluctuation. However one can observe a decreasing in PUS amplitude at high flow oscillation frequencies. But this behavior is not smooth. Amplitude of oscillating velocity component determines the period and frequency dependency (decreasing behavior) of this PUS amplitude attenuation. Flow oscillations distribute the total phase-shift information (caused by velocity) over a frequency interval in spectrum. This shows itself as an energy attenuation at frequency corresponding to average velocity value. If the flow oscillation period is shorter than total sampling period, signal attenuation becomes more pronounced.

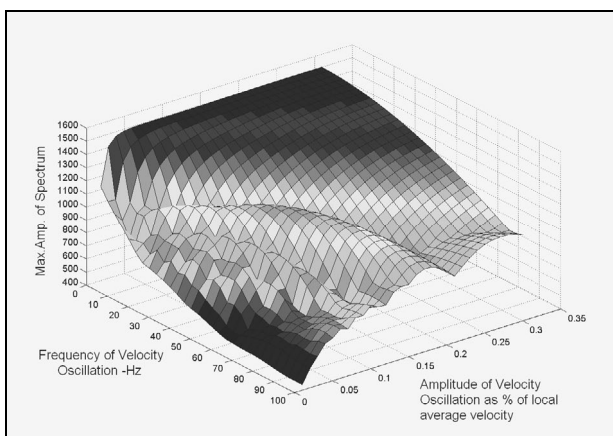


Figure 4: Change of maximum spectral amplitude P.U.S. with oscillating velocity components. Simulation parameters are: local average velocity is 0.234 m/s, , for the center of pipe with ID=50mm, Tpc (one profile measurement time)=0.2855 s (3.5 Hz).

### 3 EXPERIMENTAL MEASUREMENTS

Experimental measurements of velocity and spectrum were performed by means of a circulating flow system and DOP2125 Ultrasonic Doppler Velocimeter (Signal Processing, Switzerland). Measured values were taken for a gate of 25.9 mm away from pipe wall (pipe ID=46mm) and water flow for different Reynolds numbers. Tabulated velocities are velocity components of the flow which are parallel to the probe. Probe-pipe angle is 66°. Results tabulated in Tab. 1

Standard deviation of spectrum increases with the Reynolds number. This is an expected result due to broadened probability density function (pdf) of velocity associated with the higher turbulence. Maximum amplitudes in spectrums were normalized

by area under spectrum in order to eliminate the internal scaling of DOP2125. An exponential decreasing of this normalized maximum amplitude value with increasing turbulence effects is seen in accordance with simulation results (Figure 4).

### 4 SUMMARY

Effects of flow fluctuations on the UDV signals are investigated by means of both experimentally and computationally. According to the experimental results signal amplitude attenuation is the main effect on spectrum caused by oscillations. According to simulation results there is a complex relation between spectral amplitude and flow oscillation frequency. Experimental measurements confirmed the exponential type spectral attenuation caused by increasing oscillation frequencies which were obtained by increased Reynolds numbers. Also a broadening on spectrum of PUS was observed in experimental results. These broadening effects are closely related with probability density function of velocity for a real turbulent flow point. The results show that ultrasound Doppler velocimetry is a promising technique to study the turbulent flows.

### REFERENCES

- [1] J.A. Jensen: Algorithms for estimating blood velocities using ultrasound, *Ultrasonics* 38 (2000) 358-362.
- [2] Y. Takeda: Development of an ultrasound velocity profile monitor, *Nuclear Engineering and Design* 126 (1991) 277-284.
- [3] M. Teufel et al.: Determination of velocity profiles in oscillating pipe flows by using laser Doppler velocimetry and ultrasonic measuring devices, *Flow measurement and Instrumentation* 3 (1992) 95-101.
- [4] C. Sen and U. Lemmin: Intensity fluctuations of ultrasonic scattering in a highly turbulent flow, *Ultrasonics* 37 (2000) 603-613.
- [5] P. T. Callaghan and J. Stepisnik: Frequency-Domain analysis of spin motion using modulated gradient NMR, *Journal of Magnetic Resonance, series A*. 117 (1995) 118-122.
- [6] J. Stepisnik and P.T. Callaghan, Low frequency velocity correlation spectrum of fluid in a porous media by modulated gradient spin echo, *Magnetic Resonance Imaging*. 19 (2001) 469-472.
- [7] J. Stepisnik et al.: Diffusion and flow in a porous structure by the gradient spin echo spectral analysis, *Physica B*. 307 (2001) 158-168.
- [8] Y. Uludag et al: Effects of periodic flow fluctuations on magnetic resonance flow images, *AIChE Journal*. 50, 8 (2004) 1662-1671.

Table 1: Measurement results for flow point which is 25.9 mm away from pipe wall

NRe	$V_{\text{mean}}$ (mm/s)	Area under spectrum	Standard deviation of P.U.S. spectrum	Maximum amplitude in P.U.S spectrum	Normalized Maximum amplitude by area under P.U.S. spectrum
1022	12.70	1.2860	0.0046	102.60	79.78
1227	14.20	1.1646	0.0051	95.98	82.41
1449	17.90	1.1401	0.0045	94.84	83.18
1508	23.30	1.8503	0.0071	118.80	64.20
1878	27.10	1.7660	0.0073	109.00	61.72
2022	31.20	1.7320	0.0061	119.60	69.05
2438	33.70	1.7306	0.0057	110.50	63.85
2487	36.40	1.5276	0.0065	95.97	62.82
4331	44.60	2.6314	0.0137	105.00	39.90
7832	75.40	3.0949	0.0168	88.74	28.67
10518	98.05	4.2960	0.0224	94.97	22.10
12694	118.90	4.7100	0.0254	93.88	19.93
14159	133.47	5.4701	0.0281	93.60	17.11
17530	178.50	7.2060	0.0381	94.68	13.14
20452	200.60	11.3400	0.0463	114.30	10.08
24542	244.99	10.3900	0.0495	98.92	9.52

# Flow velocity measurements using Ultrasound Doppler Velocity Method - 10 years experience in hydraulic modeling -

Giovanni De Cesare and Jean-Louis Boillat

Ecole Polytechnique Fédérale de Lausanne (EPFL), Laboratory of Hydraulic Constructions (LCH), CH - 1015 Lausanne, Switzerland

The Ultrasound Doppler Velocity Profile method (UVP method) has been developed for fluid mechanical measurements in physics and engineering. The principle of the method is straightforward; Ultrasound echography and Doppler effect. This method was originally applied in medical engineering to measure blood flow. The developers of the instrument subsequently extended this method to non-medical flow measurements and implemented specific application systems. The method itself was found to be quite useful to flow measurements in general. Through years of use it has gradually become accepted as a tool to study the behavior of fluid flow. The present paper will not focus on the measurement method itself, but some applications at the Laboratory of Hydraulic Constructions (LCH) of the Ecole Polytechnique Fédérale de Lausanne (EPFL) will be reviewed. After a short introduction to the missions and equipment of LCH, an insight look at some results of past and ongoing research projects will be presented. The subjects cover a very large range of applications and configurations in hydraulic engineering. The Ultrasound Doppler method for velocity profile measurement has now become established at the LCH as a user-friendly research and monitoring tool.

**Keywords:** Ultrasound Doppler Velocity Profile, UVP, physical modeling, hydraulic engineering, flow measurement

## 1 INTRODUCTION

The first Ultrasound Doppler Velocity (UVP) Profile measuring instrument has been purchased by the Laboratory of Hydraulic Constructions (LCH) of the Ecole Polytechnique Fédérale de Lausanne (EPFL) in 1995. Its first application was to monitor the unsteady flow field of turbidity currents reproduced in a laboratory flume.

The LCH activities comprise education, research and services in the fields of hydraulic structures and schemes. Aspects of hydraulic structures related to flood control, hydropower plants, water supply, dams, etc. are studied. These investigations are mainly carried out using physical scale models and numerical simulations or a combination of both (hybrid modeling).

Research carried out at the LCH concentrates on the interactions of hydraulic structures and schemes with their environment, in particular with water, sediments, air and underground. The ongoing projects at the LCH focus on the following themes:

- Natural hazard, extreme floods, debris flow, sediment transport and erosion in catchment areas and rivers
- Dynamic water solicitation due to plunging jets, pressure propagation in rock fissures, scouring in fissured media
- Reservoir management, influence of reservoir geometry on sedimentation
- Development strategy for new multi-purpose hydropower schemes, reduction of hydropeaking effects by river training works

- Hydro-informatics, numerical simulation of water flow in complex hydraulic systems
- Fluvial hydraulics, flow in river bends, overflow dams and fuse plugs at river banks, bioengineering in river training works
- Shore erosion protection measures, oil spill retention systems

Teaching at the LCH includes university level courses at graduate and master levels, taking into account environmental and socio-economic aspects. Master of advanced studies (MAS) in water resources management and engineering, with special focus on hydraulic schemes are also offered.

Services such as consulting and commissioned studies are offered to the public and private sectors in the field of applied hydraulics, transferring LCH know-how acquired through research projects.

The UVP instrument has been used in research, education and services as well. In the presented paper, the measurement method itself will not be described, but some representative applications at the LCH will be reviewed.

## 2 FLOW VELOCITY MEASUREMENTS IN RESEARCH

All major research activities at the LCH comprise physical modeling. Since 1995, out of 16 PhD theses accomplished or ongoing at the LCH, 8 used or are using ultrasound Doppler velocimetry in their experimental research. The following illustrated list shows all PhD studies where flow measurement using ultrasound techniques is concerned.

1995-1998: G. De Cesare - 1 and 2D Turbidity current monitoring in a physical model flume [1]. The overall objective of the study is to evaluate reservoir sedimentation due to turbidity currents, Fig 1.

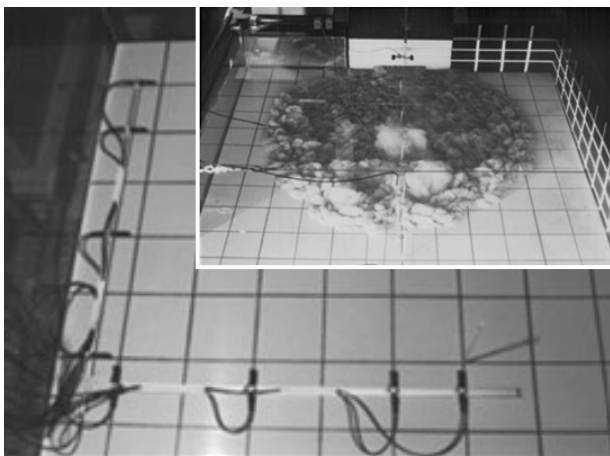


Figure 1: Layout of UVP probes on a fixed 4x4 frame to assess the 2D velocity distribution inside a turbidity current. Small picture: Spreading current with frontal arrangement of UVP probes to monitor the advancing front

1999-2003: D. Hersberger - 3D flow monitoring to assess wall roughness effects on flow and scouring in curved channels with gravel bed [2]. The wall roughness is created by vertical ripples on the outer side of the river bend, Fig. 2.

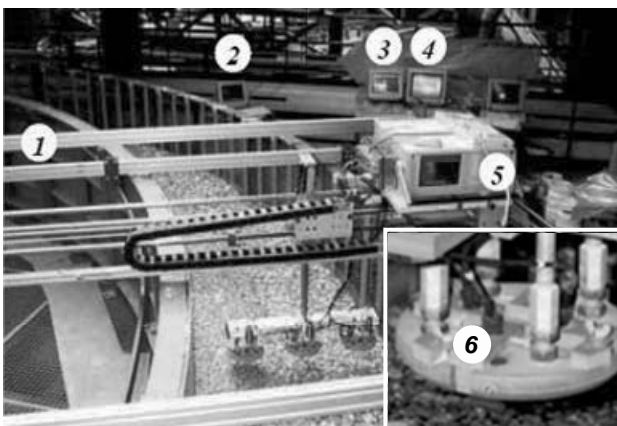


Figure 2: Arrangement and configuration of 9 UVP probes on a 3D traversing system to measure flow circulation in a 90° river bend, 1) Measurement frame, 2) Discharge controller, 3) Frame controller, 4) Level acquisition 5) Velocity acquisition, 6) UVP probes and support

2000-2003: Ch. Oehy - 2D flow monitoring to determine the effects of obstacles and jets on sedimentation due to turbidity currents in a flume [3]. In its final application, this research work gives valuable information on how to design obstacles in reservoir to reduce sedimentation induced by turbidity currents in the lowest part of the basin, Fig. 3.

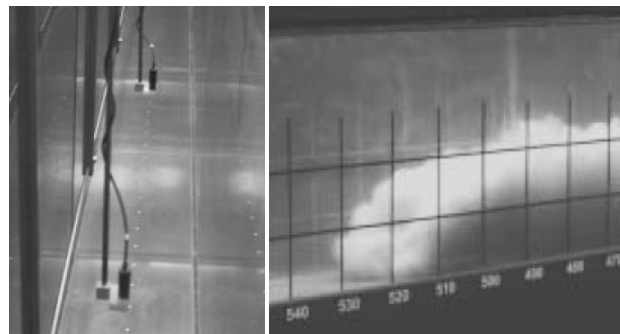


Figure 3: Layout of UVP probes (left) to assess velocity profiles inside a turbidity current (right) in a flume

2000-2006: B. Rosier - 2D flow monitoring to investigate the influence of lateral overflow on mobile bed [4]. As a result, the design principles for lateral overflow spillways have to be reconsidered taking into account the evolution of the mobile bed in rivers, Fig. 4.

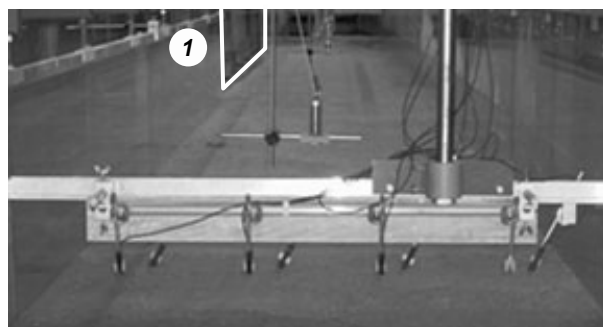


Figure 4: Layout and configuration of the 8 UVP probes on a measuring frame to monitor the flow in a flume with a side wear 1)

2003-2006: T. Meile - 1D velocity profile measurement of rapid wave propagation in a flume. This project is part of the research work related to hydropeaking effects in natural rivers.

2004-2007: A. Amini - 2D UVP measurements of the flow around a floating barrier for confinement and recuperation of oil slicks.

2005-2007: S. Kantoush - 3D circulation measurement in a shallow reservoir to study its influence on sedimentation.

The tree above cited ongoing research project and their relation with UVP are object of three papers in the 5<sup>th</sup> ISUD.

2006-2008: A. Duarte - 3D flow measurement to investigate main flow, secondary flow and turbulence in open-channel bends and their interaction with outer-bank geometry.

PhD research studies always require the best and most accurate instrumentation available. UVP is such an efficient and valuable monitoring tool that convinces researchers in all major scientific fields in hydraulic engineering.

### 3 FLOW VELOCITY MEASUREMENTS IN COMMISSIONED EXPERIMENTAL STUDIES

Consulting and commissioned studies are offered to the public and private sectors in the field of applied hydraulics, dealing with river engineering, flood protection, hydropower exploitation and reservoir operation.

Among the first ones in 1996 was the study of the flow circulation in the Essert compensation basin, part of the hydropower scheme of Emosson in the Canton Valais. The model was built in a 1/30 geometrical scale in order to study the sedimentation processes pattern as a function of inflow and outflow conditions, Fig. 5.

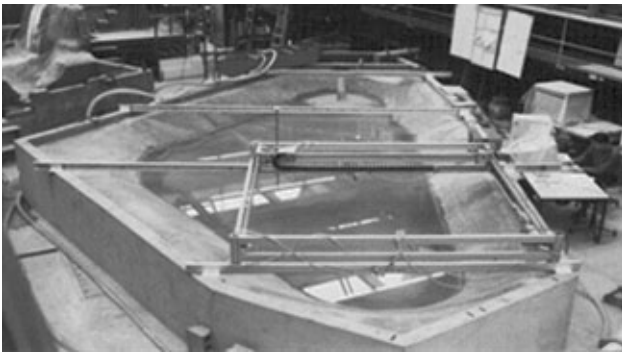


Figure 5: The physical scale model of the Essert compensation basin, UVP probes fixed on a 3D traversing frame

In 1997 the behavior of muddy debris flow through the Pissot discharge control structure located on the Highway A9 south of Montreux was investigated [5].

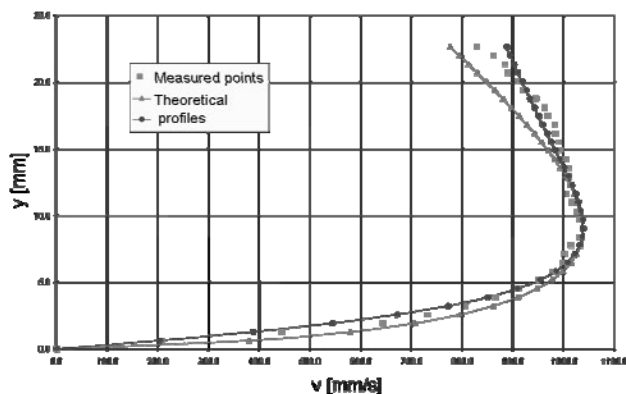


Figure 6: Results of the calibration of the theoretical velocity profiles based on the measured profile for mud flow

The required hydraulic capacity of the canal has been tested with fluids of different volumetric concentrations and therefore different rheological behaviors. UVP measurements of the mud flow allowed to assess the flow velocity distribution inside the fluid, Fig. 6. The transducers were fixed on the flume bottom looking upwards.

In 1998, a physical model was built to assess the

efficiency of measures to reduce the silting up of a waste loading station at the junction of the Rhone and Arve Rivers in Geneva, Fig. 7. Flow direction and velocities inside the lock could be measured to compare the various alternatives investigated to reduce sediment deposits at this place. The UVP transducers were fixed outside the PVC side walls of the model.

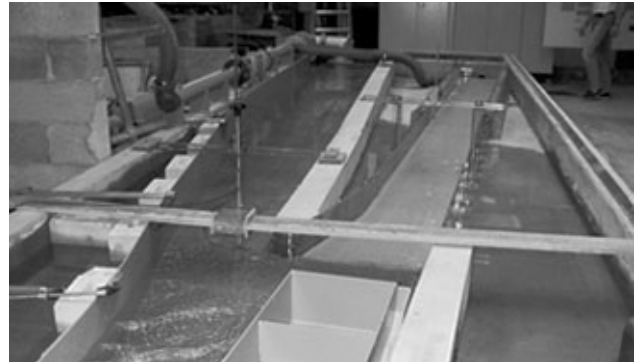


Figure 7: Physical model of the waste loading station facility at the junction of the Rhone and Arve Rivers in Geneva

The same year, in relation with the rehabilitation of the Maigrage hydropower plant in Fribourg, built in 1870, the approach flow condition upstream of the new water intake have been evaluated using UVP. The physical model was built at a 1/50 scale.

In 2004, as part of the project of the third correction of the Rhone River in Canton Valais, the effect of a gravel mining pit situated in the riverbed close to Rarogne was studied [6], Fig. 8.

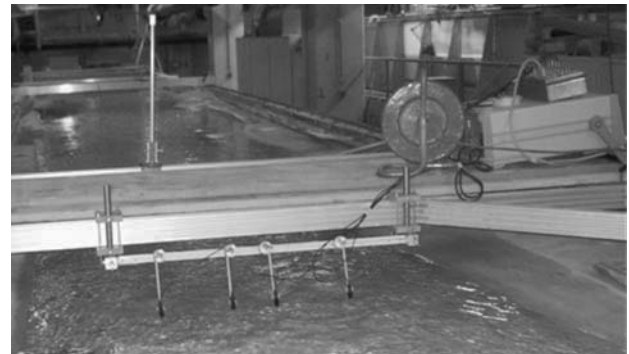


Figure 8: UVP transducers mounted on the measurement platform over the gravel pit in the physical model

A 1/45 scale physical model with mobile bed was constructed and a series of experimental tests were conducted in order to investigate the pit migration. Velocity profiles were measured in different locations using UVP probes. The time evolution of the bed geometry and development of the mining pit could be instantly determined during the test by analyzing the US echo and velocity profiles.

The use of UVP in commissioned studies has become a general rule and is offered nowadays as a standard monitoring tool for flow velocity.

#### 4 FLOW VELOCITY MEASUREMENTS IN EDUCATION AND TEACHING

The LCH offers teaching at Bachelor, Master and Master of Advances Studies (MAS) level. Access to the laboratory facilities for student work is normally granted only for at least Master level within the frame of a diploma thesis. Physical model test for students are in most cases in close relation with a commissioned study, thus allowing the LCH to have an installation ready for students. The first time UVP have been used by students was in 1996 in the Essert compensation basin model (see previous paragraph).

Later in 1998, Lavelli [7] assessed the surface roughness by analyzing the velocity profiles of the flow close to the bottom. Measurements were performed in a 0.30 m wide and 8 m long laboratory flume with UVP. The aim of this study was to determine the equivalent sand roughness  $k_s$  for several bottom surfaces such as smooth concrete, negative roughness plates and garden flagstones.

Use of UVP by students has been very convincing and will be offered for existing projects. Since 1998 many students could familiarize with UVP techniques through semester projects related to ongoing research and commissioned projects.

#### 5 CONCLUSIONS

An Ultrasound Doppler Velocity Profiler has been purchased by the Laboratory of Hydraulic Constructions in 1995 to monitor the time depended flow field of turbidity currents reproduced in a laboratory flume. Already during this earliest study, research engineers of the LCH became aware of the great potential of this monitoring technique, finally available in a user-friendly, portable and reliable measuring device. This method is now integral part of the standard techniques normally used in a hydraulic laboratory such as micro-propellers, Pitot tubes, hot wire and laser Doppler anemometers (not available at the LCH) and several types of visual flow tracking methods. Each one has its advantages and disadvantages and limited applicability.

The working principle of the UVP method is straightforward using pulsed ultrasonic Doppler effect together with the echography relationship. An ultrasound pulse is emitted from a transducer into the liquid, and in the case of the UVP instrument the same transducer receives the echoes. Its great advantage resides in the facts that:

1. It obtains a spatio-temporal flow information
2. It is applicable to opaque liquids
3. It is non intrusive
4. It is a line measurement
5. Flow mapping is practicable with multiple transducers

Through UVP technique, each of these advantages is now being exploited in the presented past or ongoing studies. Spatio-temporal flow information is essential in hydraulic engineering studies, where rapidly varying, unstationary phenomena can occur.

Despite the fact that numerous and important improvements have been realized with the original measurement device, further developments are desired, particularly in the following perspectives:

- Detection of moving interfaces (liquid-liquid, solid-liquid, liquid-air)
- 2D and 3D measurements in a stationary flow field with one fixed and one mobile transducer to increase number of intersection points
- Increase of instrument velocity range and distance

Even if most of the engineering studies are undertaken in stationary flowing environments, this non-invasive measuring technique allows monitoring from outside of the control domain, thus not disturbing the flow field.

As shown, the use of UVP covers a very large range of applications and configurations in hydraulic engineering. This measurement method has become established at the LCH as a user-friendly, cost and time effective research and monitoring tool. The rapid availability of flow information is a non negligible advantage of the hydraulic laboratory.

#### REFERENCES

- [1] De Cesare G. and Schleiss A.: Turbidity current monitoring in a physical model flume using ultrasonic Doppler method, Proc. 2<sup>nd</sup> ISUD, Villigen PSI, Switzerland, 22 September 1999, pp. 61-64 (1999)
- [2] Hersberger D. S.: Measurement of 3d flow field in a 90° bend with ultrasonic Doppler velocity profiler, Proc. 3<sup>th</sup> ISUD, EPFL, Lausanne, Switzerland, September 9 - 11, 2002, pp. 59-66 (2002)
- [3] Oehy Ch.: Effects of obstacles and jets on reservoir sedimentation due to turbidity currents, EPFL PhD Thesis No 2684 and Communication of the LCH No 15 (2003)
- [4] Rosier B., Jordan F., De Cesare G., Boillat J.-L. and Schleiss A.: Determination of velocity profiles and bed morphology using UVP transducers to investigate the influence of lateral overflow on mobile bed, Proc. 4<sup>th</sup> ISUD, Hokkaido University, Sapporo, Japan, 6.-8. September 2004, pp. 47-50 (2004)
- [5] Boillat J.-L. and Bollaert E.: Modelling and measurement of muddy debris-flows, Proc. 2<sup>nd</sup> ISUD, Villigen PSI, Switzerland, 22 September 1999, pp. 65-68 (1999)
- [6] Nilipour N., De Cesare G. and Boillat J.-L.: Application of UVP transducers to measure bed geometry and velocity profiles in a hydraulic scale model with gravel pit, Proc. 4<sup>th</sup> ISUD, Hokkaido University, Sapporo, Japan, 6.-8. September 2004, pp. 41-46 (2004)
- [7] Boillat J.-L. and Lavelli A.: Surface roughness determination based on velocity profile measurements, Proc. 2<sup>nd</sup> ISUD, Villigen PSI, Switzerland, 22 September 1999, pp. 57-60 (1999)

## UVP Measurement for Flows Accompanying Free Surface

Shinya KOJIMA, Yuji TASAKA, Yuichi MURAI, Yasushi TAKEDA

Division of Energy & Environmental System, School of Engineering, Hokkaido University,

North-13 West-8 Kitaku Sapporo, Japan.

For environmental conservation, we attempted to develop a measurement system with high efficiency and high accuracy for fluid flow with interface; namely, fixed river bed with irregular surface and moving free surface. The detection method of the bottom position on a measurement line of UVP by using the probability density for zero velocity was established and confirmed by the laboratory experiment using an open channel. We measured velocity distribution in cross-section of an actual river by UVP, and the bottom of the river was determined by the established method. Discharge of the river was obtained by integrating the velocity distribution, and compared with a reference discharge determined by weir. We confirmed that this discharge measurement has high accuracy and high efficiency in comparison with the conventional techniques. On the other hands, we also attempted to establish the method to determine position of the moving free surface by analyzing Ultrasonic (US) echo signal. UVP measurement was synchronized with US displacement meter to confirm the method.

**Keywords:** Environmental flow, Ultrasonic technique, Velocity Profile, Free surface, Interface detection

### 1 INTRODUCTION

For environmental conservation, it is important to measure a discharge of environmental flow with high accuracy and high efficiency. The discharge is currently determined by applying an empirical equation estimated in an ideal system. Actual environmental flow in large scale, however, has many uncertain factors and thus the estimated discharge has large uncertainties and errors, which may be an order of several tens to one hundred percent. Therefore such an estimation method of discharge is not suitable, for instance, for a precise control of the volume of water kept in storage. On the other hand, the current measurement technique requires measuring the depth of water by a scale at several points to determine a shape of a cross-section of flow field in order to estimate the discharge. Such a measurement takes long time and reduces efficiency of the measurement.

Until now, we have studied environmental flow measurement by using ultrasonic velocity profiler (UVP) [1] to realize more accurate measurement of the discharge in two typical configurations; an open channel flow [2] and an overflow [3]. Cross-sectional velocity distribution in the both configurations was measured by UVP. Discharge, which is calculated by integrating the velocity distribution, was compared with discharge determined from the empirical equation, and it was confirmed that the obtained discharge has high accuracy for the both configurations.

In the measurement of the open channel flow, an ultrasonic (US) transducer was mounted at the top of the channel and the measurement line of UVP was set toward to the bottom. In this case, cross section of the channel has a certain form and thus it is not necessary to measure the depth of water. However, in an actual river, measuring the bottom position is required. On the other hand, in the

measurement of overflow, an US transducer was mounted under the weir and the velocity profile was measured on the vertical direction upward. To reduce error in the measurement of the discharge, we must acquire the position of the free surface on the measurement line. But the detection of moving free surface has further difficulties than the detection of the bottom position in the open channel flow since it is time dependent. In the both cases, if detection of the interfaces becomes available without using another tool such as a scale, the efficiency of environmental flow measurement using UVP might increase significantly.

In this study, we established the detection method of bottom position on measurement line in the open channel. The method was confirmed in the laboratory open channel and was later applied to measurement of an actual small river. We also attempted to establish a method to detect moving free surface by analyzing ultrasonic echo signal, which is used for obtaining instantaneous velocity profile in UVP measurement.

### 2 MEASUREMENT OF RIVER

#### 2.1 Detection of Bottom Position

Figure 1(a) shows a temporally averaged velocity profile measured in the open channel. The horizontal axis,  $z$ , represents the distance from US transducer, and the vertical axis is the mean velocity. Error bar represents standard deviation of the velocity fluctuation. In this measurement, distance from the transducer to the bottom is 175 mm. Near the bottom, the mean velocity decreases to around zero and standard deviation also has small value. Viscous fluid has a no-slip condition at a rigid boundary and thus the profiles show such a behavior. Profile beyond the bottom position shows a velocity measured by reflected US beam at the bottom and it is difficult to determine which velocity

was measured. In the ideal situation, a position at which the velocity becomes zero corresponds to the bottom. In UVP measurement, however, each measurement point has non-negligible measurement volume and velocity becomes not always zero even at the bottom.

Figure 1(b) shows the probability density distribution for zero velocity  $Pd_0$ , where “zero velocity” means a velocity smaller than the velocity resolution. The probability has a high value around the bottom. We attempt to utilize this value to determine the bottom position as follows:  $Pd$  is almost zero at the flow area, but rapidly increases near the bottom. We make a threshold for the probability density suitable to determine the bottom. The bottom is determined as a position at which  $Pd$  first passes this threshold at each measuring line.

Figure 2 shows the detected bottom position of the open channel. The horizontal axis represents the spanwise position of the channel and the vertical axis is the depth of water. The continuous line represents the actual bottom measured by scale. Threshold is chosen as 0.3. The detected points are very close to the actual bottom measured by scale at every measure line. Error for the detected bottom is less than 3 mm. In this case, the spatial resolution of UVP is 1.78 mm, so this method might be practical.

**2.2 Measurement**

We obtained a data in a small river; of which a width is about 1600 mm. It flows out from a small lake in the Hokkaido University campus. Figure 3 is a photograph of measurement configuration in the river and Figure 4 shows the schematic of coordinate system and measurement location with some typical scale in the river. The interval between

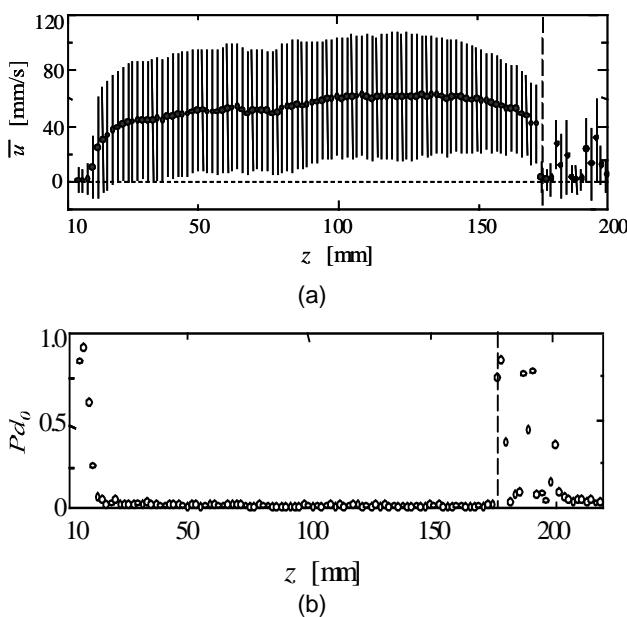


Figure 1: (a) Velocity distribution and (b) Probability

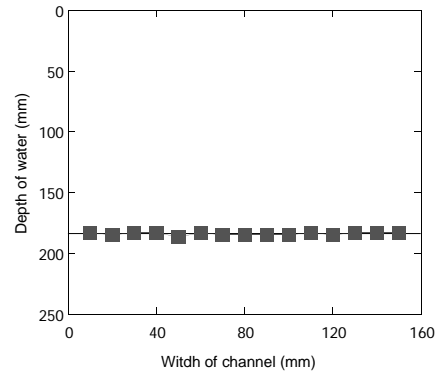


Figure 2: Bottom of the open channel determined by established probability density method

density for zero velocity in the open channel each measurement line is 100 mm. There is a big stone at upstream of the measurement location for  $y = 800$  to  $1000$  mm. The depth at  $y = 0$  to  $1300$  mm is comparatively deeper and the bottom is covered by small stones, whose size is around 10 mm. The area around  $y = 1300$  to  $1600$  mm is shallow and waterweed covers the bottom. Reference depth was measured by a scale at each measuring line. The rectangular weir was located at the inlet of the river from the lake and the reference discharge was determined by an empirical equation with the water level over the weir.

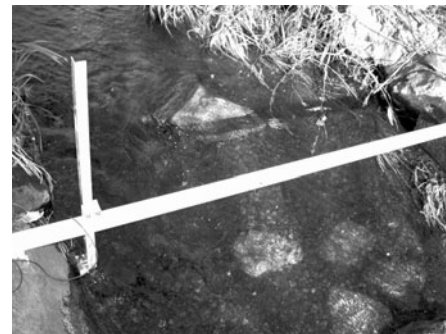


Figure 3: Photograph of the measurement configuration in river

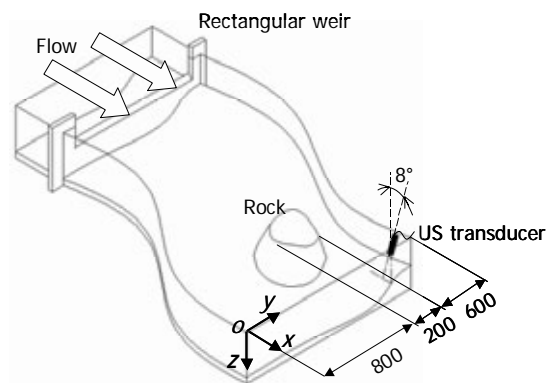


Figure 4: Coordinates and measurement location at the river

The number of profiles measured by UVP is 1024 and the sampling period is 100 ms. The number of measurement points on a measurement line is 128. The distance between each point is 1.48 mm. The velocity resolution is 30.6 mm/s.

### 2.3 Result

Figure 5 shows the form of the cross section in the river determined by the both method; the probability density method explained above and a scale measurement. The horizontal axis represents  $y$  and the vertical axis is  $z$ . The average of the difference between the results obtained by the both methods is negligibly small, 8 mm. In the range of  $y = 1400$  to 1600 mm, corresponding to the waterweed condition, the bottom position is detected shallower than the position measured by the scale, because the ultrasonic beam is scattered by waterweed and cannot reach actual bottom through the waterweed.

Cross sectional mean velocity distribution of the river is shown in Fig.6. as estimated being based on the both of the obtained velocity profiles and the detected bottom. The flow discharge can be estimated by integrating the velocity distribution. The distribution shows a reverse flow region around  $y = 800$  to 1000 mm due to the wake behind the big stone. The obtained discharge is 48.5 l/s. Reference discharge measured by the rectangular weir is 55.0 l/s and thus the error of the provided measurement is 12%. This value is comparably smaller than

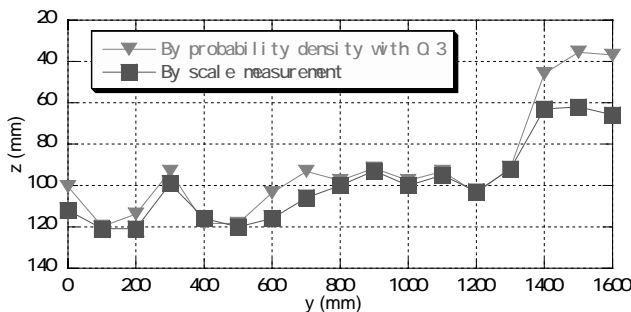


Figure 5: Bottom position of the river determined by the probability density method

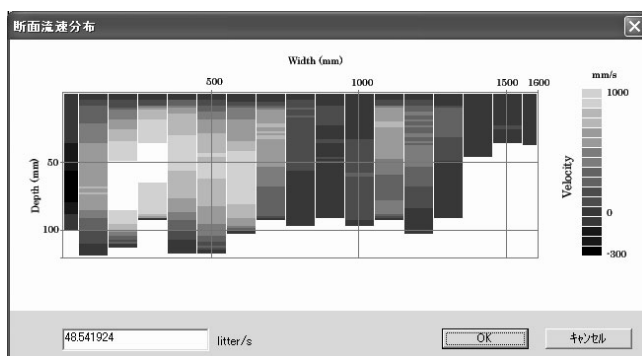


Figure 6: Velocity distribution at cross section of river calculated from the obtained velocity profiles and the detected bottom position.

conventional methods although the weir method has large error.

## 3 MEASUREMENT OF FREE SURFACE

### 3.1 Experimental Apparatus

The commercial UVP systems in pulse-Doppler method use information of amplitude of ultrasonic echo only for detecting phase delay. We attempt to utilize the information to determine a moving free surface in flow accompanying free surface. We constructed UVP system by ourselves based on pulser/receiver board (Matec, TB-1000) and A/D board (Aqiris, DP105) to obtain temporal variation of ultrasonic echo.

We measured the flow in an open channel with the constructed UVP system to establish the method to detect moving free surface. Figure 7(a) shows the schematic illustration of the experimental setup. An US transducer is mounted under the open channel and the US pulse goes upward through the bottom plate. Measured amplitude of US echo is transferred to PC. At the same time, US displacement meter, which can measure the distance from the sensor to

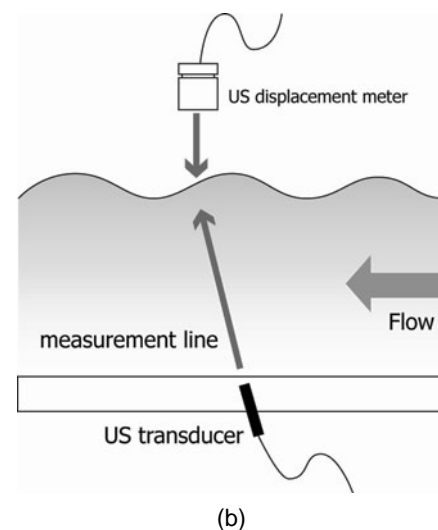
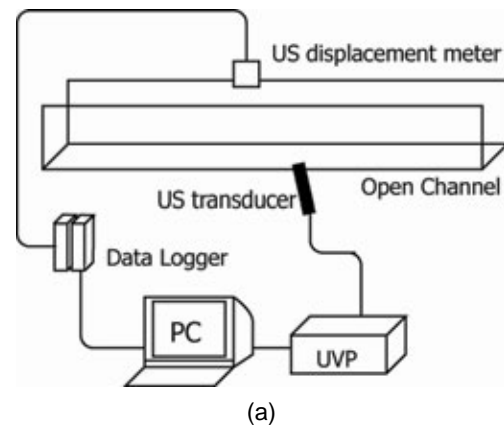


Figure 7: Schematic illustration of experimental setup; (a) overview of the setup and (b) location of measurement lines

the free surface, is located the top of the open channel to obtain a reference data of moving free surface. Its spatial resolution is 0.15 mm. The US displacement meter and the UVP system were synchronized by using a trigger signal. Figure 7(a) shows the positional relationship of the measurement lines. The measurement was repeated 100 times and the interval between each measurement was 10 ms.

### 3.2 Result

Figure 8 shows the amplitude of US echo obtained by the UVP system. The vertical axis represents the distance from the US transducer. The gray scale represents the amplitude of US echo and black area means strong US echo. Strong echo due to multiple reflections of US pulse in the wall and the US transducer exists near the US transducer. The peaks of US echo around 30 mm in the distance represents the free surface of the open channel. We attempted to determine the free surface position by making a threshold and detected the position at which the echo first passes the threshold. Figure 9 shows the variation of the position of the moving free surface measured by two methods; the US displacement meter and the developed system. The position of the free surface slightly varies by wavelet and the displacement is around 5 mm. In comparison with the both results, determined position by the present method is more sensitive because of smaller measurement volume and of no averaging on raw data. We can observe that there is clear error for deformed free surface. Condition of ultrasound reflection at the free surface depends on the inclination of the surface and the echo signal from such a curved free surface changes from the flat condition. Currently, the variation of US echo due to the deformed free surface is a problem on measurement accuracy. But we might utilize the variation of US echo in order to detect the deformation of the free surface with the variation of the position.

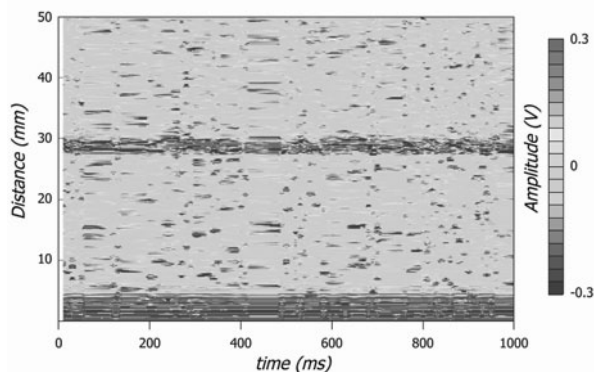


Figure 8: The amplitude of US echo recorded by UVP

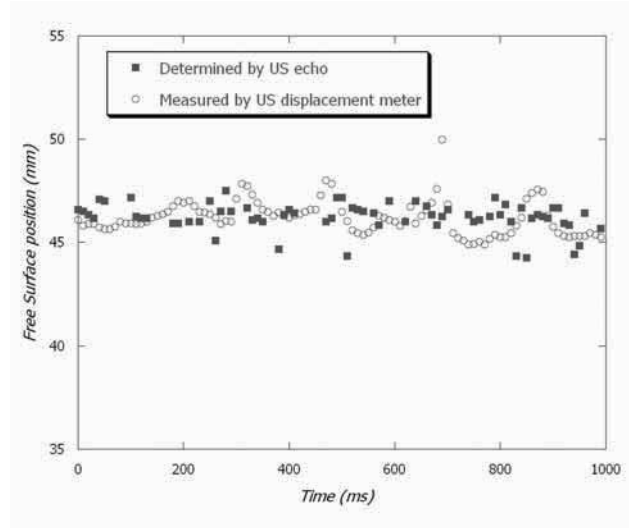


Figure 9: The displacement of the position of free surface measured by US displacement meter and determined by US echo

## 4 SUMMARY

1. We established the method to detect the bottom position of an open channel by using the probability density for zero velocity and applied this method to measure a small river. We confirmed that the measurement of discharge of the river by UVP has high accuracy and more efficient than the conventional measurement methods.
2. Amplitude information of US echo in UVP measurement was utilized to detect moving free surface. To establish the method for detecting free surface, temporal variation of the US echo was simultaneously recorded with surface position measured by US displacement meter.

Current UVP system uses US echo information only for determining instantaneous velocity profile. In the echo, however, other useful information remains. In the future, we attempt to advance UVP system to more useful measurement tool, e.g., simultaneous measurement of the instantaneous velocity profile and the position of moving free surface in an open channel flow.

## REFERENCES

- [1] Takeda, Y., Velocity Profile Measurement by Ultrasonic Doppler Method, EXPERIMENTAL AND FLUID SCIENCE, 10-4(1995), pp. 444-453.
- [2] Yokoyama, K., et al., Flow Measurement in an Open Channel by UVP, 4<sup>th</sup> ISUD(2004), pp. 55-58.
- [3] Okubo, T., et al., Vector Measurement of Environmental Flow Field by UVP, 4<sup>th</sup> ISUD(2004), pp. 59-62.

## Flow Pattern Visualization of Combined Sewer Overflow

Vojtěch Bareš, Jaroslav Pollert, Petr Srníček

Department of Sanitary and Ecological Engineering, CTU Prague, Thákurova 7, 166 29, Prague 6, Czech Republic, email: bares@fsv.cvut.cz; pollertj@fsv.cvut.cz; petr.srnicek@fsv.cvut.cz

Presented paper deals with 2D flow visualization using Ultrasonic Doppler Method (UDM). The flow patterns in the axes of plane symmetry of designed combined sewer overflow (CSO) were measured on the hydraulic model made of plexiglass using Ultrasonic Velocity Profile (UVP) Monitor. The experiments were focused on both, the optimalization of CSO geometry and the verification of the 3D CFD model. The results show great potential of the UDM in combination with numerical analysis to visualize 2D flow field. Moreover, the optimal geometrical configuration with respect to the gravitational separation of suspended solids content and separation of floatable solids was found as well. The comparison between experimental values and CFD simulations introduces sufficient agreement.

**Keywords:** CFD, flow visualization, receiving water, sewer, ultrasonic Doppler method, velocity profile

### 1 INTRODUCTION

Combine sewer overflow (CSO) represents a crucial sewer structure related to wet-weather pollution in urban areas. A tremendous number of CSOs geometrical configurations were developed during last decades worldwide. Often, the geometry of CSO is given by regional development routine and varies in the wide range even in the particular countries. The CSO design itself should take into account different criteria as hydraulic behavior, discharge distribution, energy losses, separation of floating solids, cost-effectiveness etc. In addition, the efficiency of the separation of suspended solids content should be increased using the optimal hydraulic condition and flow pattern distribution. Therefore, the authors deal in the presented study with an evaluation of new prefabricated CSO unit made of fiberglass tubes based on the methods of hydraulic and numerical simulations.

Today, Particle Image Velocimetry (PIV) is most often used method for instantaneous flow pattern visualization. However, various measuring techniques are applicable as well. Mavros (2001) discussed application of wide spectra of methods (hot-wire anemometry, laser Doppler anemometry, laser-induced fluorescence or PIV) with the respect to their usefulness for particular situations. The usability of ultrasonic Doppler method (UDM) for flow visualization was demonstrated e.g. by Murai et al. (2004) at vortex ring dynamics or Hersberger (2003) at curved channel flows, who in fact mainly determined 2D or 3D time-averaged velocity vectors only, when distinctively more simple measuring configuration can be used.

Therefore, the paper deals with simple technique of 2D time-averaged flow field visualization using UDM, particularly UVP method [4]. The flow patterns in the axes of plane symmetry of designed CSO were measured on the hydraulic model made of plexiglass under laboratory condition. The technique

is based on measurements with one ultrasonic probe only, its variable spatial positioning and affine matrix transformation. The obtained velocity vector maps were used for both, the optimalization of CSO geometry and the verification of the 3D mathematical model.

### 2 CSO DESIGN AND OPERATING PRINCIPLES

Due to both manufacturing and construction expenses a very simple principle for CSO design was applied.

In fact, CSO consists of two pipes positioned one above the other (Fig. 1). The outlet with flow regulator is connected at the end of the lower inlet pipe. The upper pipe with slit gate at the bottom along the whole connection of both pipes serves as wastewater overflow into receiving waters. Upstream the slit gate, downflow baffle was installed to prevent the wash-out of floatable solids to natural water environment. Three basic shapes (width) of the slit gate were tested (hereafter lettered as ST1-ST3).

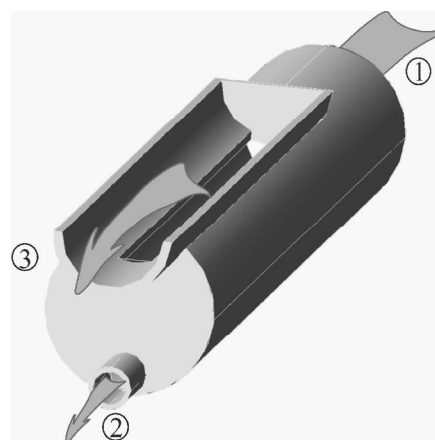


Figure 1: Axonometric projection of CSO chamber (1. inlet; 2. outlet to waste water treatment plant (WWTP); 3. overflow cross slit gate to receiving waters).

## 2 METHODS

### 2.1 Experimental setup

Experimental apparatus (Fig.2) was assembled by hydraulic model of CSO itself, electronically controlled valve, mixed tank with pump for injection of tracking particles and devices for measurement of hydraulic quantities.

Particularly, two MID flowmeters were installed at the inlet and outlet of CSO. Free-surface longitudinal profile was measured using water level point gauge and US water level transducers.

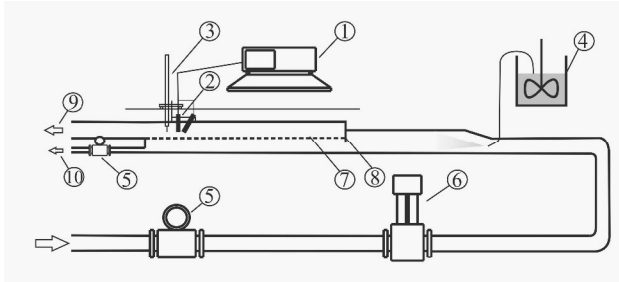


Figure 2: Experimental setup (1. UVP unit; 2. US transducers; 3. movable point gauge and US water level probe; 4. mixing tank; 5. flowmeters; 6. valve; 7. overflow crest; 8. downflow baffle; 9. CSO overflow; 10. CSO outlet towards WWTP).

### 2.2 Velocity measurements

The instantaneous information about velocity distribution in mid-vertical plane of symmetry of CSO was obtained using UVP Monitor (Met-Flow, S.A.). By reason that only time-averaged value of the velocity vectors were analyzed, one US transducer in 3 different geometrical position was used (hereafter: lettered as  $S_{1,2,3}$ ).  $S_1$  was mounted vertically within Cartesian coordinates  $[x_K, y_K]$  and others ( $S_{2,3}$ ) under angle  $\beta = \pm 25^\circ$  from vertical axis (Fig. 3). Moving longitudinal drive along horizontal axis in 50 mm step 24x3 radial velocity profiles  $V_{1,2,3}(y_K)$  were measured.

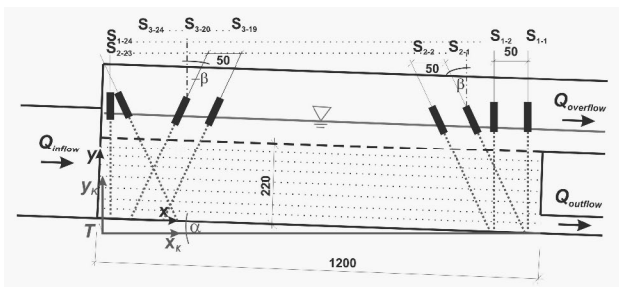


Figure 3: Detail of probe positioning.

### 2.3 CFD simulation

CFD simulations of 3D flow field of CSO were executed in FLUENT environment. Free surface was simulated as a wall without friction. Experimentally evaluated longitudinal profile of free surface along the overflow pipe was considered as

boundary condition. Tetrahedral mesh with different density was used due to increasing precision in overflow silt gate. Further, one geometrical configuration of CSO of the model was simulated using various types of turbulence models to choose optimal one (standard k- $\omega$  model). As a criteria, RMS of horizontal and vertical velocity components related to UVP measurements at mid-vertical plane of CSO symmetry over whole measured flow field were chosen.

## 3 DATA ANALYSIS

### 3.1 Velocity vectors decomposition

Velocity vectors decomposition takes into account several specific aspects of experimental setup as follows: *i*) coordinates of discrete measuring elements given by each US probes  $S_{1,2,3}$  are unequal; *ii*) velocity vectors in discrete measuring elements are measured in direction of radial axis of US probes  $S_{1,2,3}$ ; *iii*) coordinate system of CSO model  $[x, y]$  is different from Cartesian coordinate system  $[x_K, y_K]$ .

Considering above mentioned aspects leads to necessity to transform coordinates of discrete measuring elements from Cartesian  $[x_K, y_K]$  to CSO  $[x, y]$  coordinate system (Figure 3). In case of probe  $S_1$  one can write:

$$[x_1, y_1] = \mathfrak{R} \cdot [x_{K1}, y_{K1}] + T \quad (1)$$

$$\mathfrak{R} = \begin{bmatrix} \cos a & -\sin a \\ \sin a & \cos a \end{bmatrix} \quad (2)$$

where  $\mathfrak{R}$  is rotation by angle  $\alpha$  and  $T$  is shift vector of the origin (Fig. 3).

Whereas the US probe  $S_2$  is rotated from the vertical by angle  $\beta$  eq. (1) is expressed as:

$$[x_2, y_2] = D \cdot \mathfrak{R} \cdot [x_{K2}, y_{K2}] + T \quad (3)$$

where  $D$  is a diagonal matrix expressing skewing of measured matrix  $[x_{K2}, y_{K2}]$  by angle  $\beta = 25^\circ$  (Fig. 3) given as:

$$D = \begin{bmatrix} 1 & \sin b \\ 0 & 1/\cos b \end{bmatrix} \quad (4)$$

Similarly, one can write eq. (3-4) for probe  $S_3$  with  $D$  related to negative value  $\beta = -25^\circ$  (Fig.3).

Consequently, 2D bilinear interpolation [5] of radial velocity vectors  $V_{1,2,3}$  from matrices  $[x_{1,2,3}, y_{1,2,3}]$  to arbitrarily defined rectangular grid is required (herein: measured element size 1220x220 mm; grid spacing 10x10 mm; nr. of grid points 2783).

Finally, one can define total velocity vector and its components in all nodes of the grid. At least couple of measured radial vectors (either  $[V_1, V_2]$  or  $[V_1, V_3]$ ) is known in each grid point. Therefore, following expressions for  $[V_1, V_2]$  can be defined:

$$V_1 = v_{yK} \quad (5)$$

$$V_2 = v_{YK} \cos b - u_{XK} \sin b \quad (6)$$

For total vector  $U$  one can simply write:

$$U = \sqrt{u_{XK}^2 + v_{YK}^2} \quad (7)$$

Accordingly, replacing  $V_2 \rightarrow V_3$  in eq. (6) provides solution for  $[V_1, V_3]$ .

### 3.2 Numerical model data transformation

The 3D grid of modern computational tools is created by irregular elements which created 2D triangular mesh with variable density in mid-vertical plane of CSO symmetry. Therefore, resampling of the hybrid triangular mesh  $[x_f, y_d]$  to defined rectangular mesh  $[x_s, y_s]$  is required to proper calibration and verification of CFD model using experimental data sets.

In fact, the transformation can be described by 2D interpolation of vector components  $u, v$  in random distributed nodes  $[x_f, y_d]$  to defined rectangular mesh  $[x_s, y_s]$  using both the Delaunay triangulation [5] and the triangular interpolation itself [6].

## 4 RESULTS

### 4.1 Evaluation of CSO geometry using UVP

Different geometrical configurations of CSO were evaluated with respect to minimized vertical velocity components (minimizing sewer solids wash-out). Flow patterns of measured element of CSO were analyzed using above described methodology. Fig. 4 presents velocity colour map with total vector field.

Developing sweep region ( $x = 200 \div 400$  mm) can be clearly seen (Fig. 4, Fig. 5) for silt gate shapes  $ST1$  and  $ST2$ . Horizontal velocity profiles of vertical velocity  $v(x)$  (Fig. 5) well demonstrate this effect. The difference between maximal vertical velocity components for all at the end of the silt gate ( $x = 1200$  mm,  $y = 210$  mm) is however negligible.

Moreover, in accordance with previous assumptions the formation of eddy structure can be observed at  $x = 300 \div 500$  mm for  $ST1$  (Fig. 4, Fig. 6).

On the other side, the change of slit gate geometry influences significantly the size of the dead zone downstream of the downflow baffle. Fig. 4 and Fig. 6 demonstrate developing of dead zone. Velocity profiles  $u(y)$  are almost identical at  $x = 700$  mm, but upstream profiles are strongly affected.  $ST3$  shows the worst results (almost 40 % of the slit gate is useless).

### 4.2 Calibration of CFD model

Beside that, obtained data sets were used for numerical model calibration and verification. However, preliminary experiments shows only weak possibilities to optimize model parameters e.g. wall friction etc. due to low sensitivity of tested parameters.

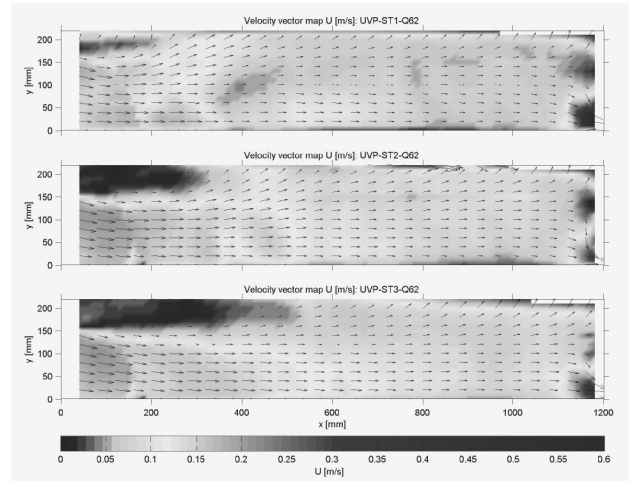


Figure 4: Flow pattern visualization with total vector map of CSO element for different geometrical configurations of slit gate ( $ST1$ ,  $ST2$  and  $ST3$ ).

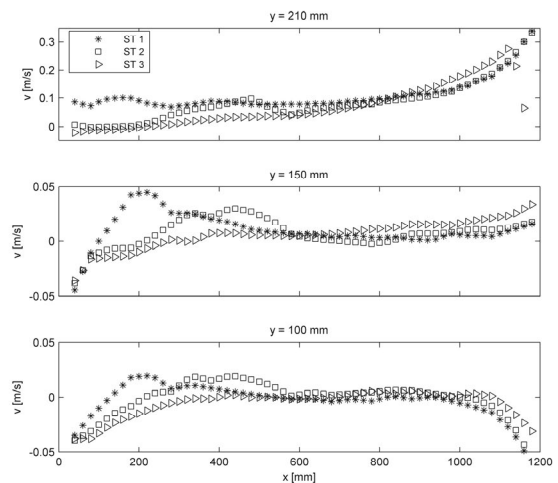


Figure 5: Horizontal profiles of vertical velocity components  $v(x)$  for coordinates  $y = 100 \div 210$  mm and different geometrical configuration.

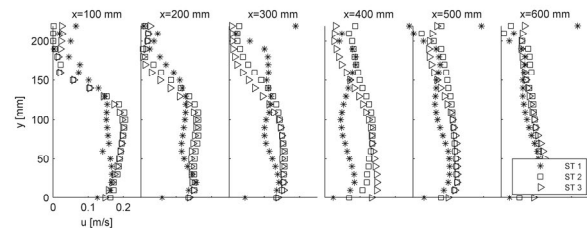


Figure 6: Developing of vertical profiles of longitudinal velocity components  $u(y)$  for coordinates  $x = 100 \div 1100$  mm and different geometrical configuration.

Therefore, attention was called to compare different turbulence models supported by FLUENT (standard  $k-\epsilon$ , RNG  $k-\epsilon$ , realizable  $k-\epsilon$ , standard  $k-\omega$ , shear stress transport (sst)  $k-\omega$ , Spallart-Allmaras (SA)) with respect to best results. Generally, all simulations provide comparable results to UVP measurements. However, one can find significant deviations in specific regions. Particularly, in the

dead zone downstream the downflow baffle standard k-ε,realizable k-ε and SA significantly overvalue real horizontal components  $u$  (Fig. 7). It can be also demonstrated on vertical components  $v$  (Fig. 8). On the other side, second group of models overestimates results in a bulk flow (Fig. 7). Further, all models significantly overestimate vertical components of velocity  $v$  (Fig. 8).

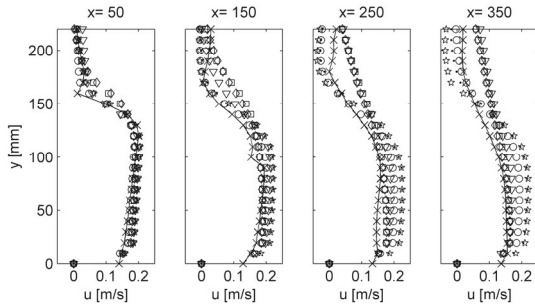


Figure 7: Vertical profiles of horizontal velocity component  $u(y)$  for UVP (✕) and CFD simulations (▽ - SA; ◇ - standard k-ε; ☆ - RNG k-ε; □ - realizable k-ε; ○ - standard k-ω; ● - sst k-ω).

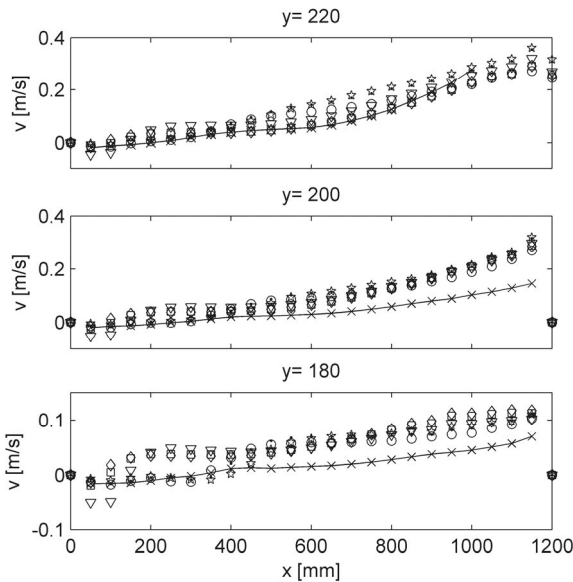


Figure 8: Horizontal profiles of vertical velocity component  $v(x)$  for UVP (✕) and CFD simulations (▽ - SA; ◇ - standard k-ε; ☆ - RNG k-ε; □ - realizable k-ε; ○ - standard k-ω; ● - sst k-ω).

Calculating RMS of horizontal and vertical components deviation between CFD simulation and hydraulic modeling (Fig. 9) best fitted turbulence model was chosen (standard k-ω) for further optimization of CSO geometry.

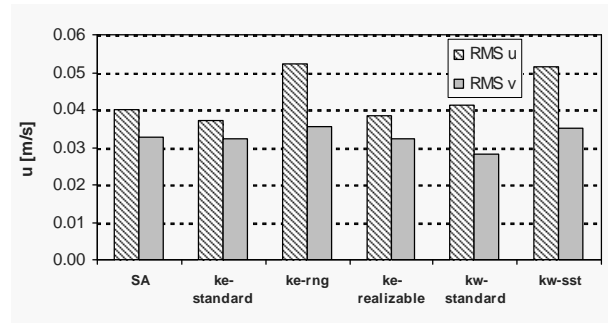


Figure 9: RMS of  $u$  and  $v$  for applied turbulence models.

## 6 SUMMARY

The optimal geometrical configuration of proposed CSO with respect to the gravitational separation of suspended solids content and separation of floatable solids was found using combination of hydraulic and CFD simulations.

The results show great potential of simple application of the ultrasonic Doppler method in combination with numerical data analysis and affine matrix transformation to visualize 2D flow field. However, presented methodology allows obtaining the time-averaged velocity flow field only.

The comparison of experimental data with CFD turbulence models shows wide range of possible simulation results. It's obvious, that "blind" CFD application without careful validation can lead to results misinterpretation.

## ACKNOWLEDGEMENT

This work was supported by the Czech Science Foundation; project No.103/04/1350, by the project of Czech Ministry of Education, Youth and Sport No. MSM6840770002 and by HOBAS CZ, Ltd.

## REFERENCES

- [1] Mavros P: Flow visualization in stirred vessels - A review of experimental techniques, Chemical Engineering Research and Design, 79 (A2) (2001) 113-127.
- [2] Murai Y, Kitaura H, Xiao Z, Thomas PJ, Takeda Y: Study of Vortex Ring Dynamics using UVP, Proceedings 4th ISUD, Sapporo, (2004) 3-8.
- [3] Hersberger DS: Wall roughness effects on flow and scouring in curved channels with gravel bed, PhD thesis, EPFL Lausanne (2003).
- [4] Takeda Y: Instantaneous Velocity Profile Measurement by Ultrasonic Doppler Method, JSME International Journal (1995) 8-16.
- [5] Sedgewick R: Algorithms in C, Part 5: Graph Algorithms, Addison-Wesley, Reading (2002).
- [6] Press WH, Flannery BP, Teukolsky SA, Vetterling WT: Numerical Recipes in C. The Art of Scientific Computing, Cambridge University Press (1993).

# Interface tracking and velocity profile in an oil-water two-phase flow

Azin Amini, Giovanni De Cesare, Anton J. Schleiss

Laboratory of Hydraulic Constructions, Ecole Polytechnique Fédérale de Lausanne, station 18

1015 Lausanne, Switzerland

The main aim of this study is to assess the velocity distribution profiles in oil and water behind a containment barrier. A simultaneous study of the velocity profile in a two phase flow and the interfacial waves was performed in a laboratory flume using ultrasonic velocity profile (UVP) measurements. The increasing of the echo of ultrasonic pulses in the interface of two liquids was used to detect the interface and its fluctuations. Knowing the location of interface the velocity profile can be measured in each liquid phase.

**Keywords:** Velocity profile, oil water interface, interfacial waves, pulse echo, oil spill containment boom, droplet entrainment

## 1 INTRODUCTION

### 1.2 Applications of the UVP method

Velocity measurements are used in various fields of research. In hydraulics, different velocity measurement methods exist (spinner, Pitot-tube, electromagnetic field, laser technology (LDA), Particle Imaging Velocimetry (PIV), and Ultrasonic Velocity Profiling (UVP). The ultrasonic velocity profile (UVP) measurement (Takeda, 1995) was developed to measure an instantaneous velocity profile of liquid flows, using Doppler shift frequency in echoes reflected at small particles flowing with the liquid.

Thanks to the UVP Method one can obtain velocity fields in space and time with a rapid data acquisition. This technique with its advantages compared to more classical measuring methods is now being widely exploited in the Laboratory of Hydraulic Constructions (LCH) of the Ecole Polytechnique Fédérale de Lausanne (EPFL). Among the first performed studies at the LCH was the flow mapping of turbidity currents in a laboratory flume (De Cesare and Schleiss, 1999), where the suspended sediments gave very good ultrasound echo. The interface between the turbidity current and the ambient clear water could also be detected using UVP. Other studies used either steady state measurement allowing a long acquisition time of several seconds or were performed in rather dirty water (De Cesare, 1999).

The applicability of the UVP method to the flow with large fluctuation both in the velocity and orientation of gas-liquid interface was confirmed by Nakamura et al. (1998). However, the capability of this method has not been verified to detect the interface of a two-phase flow.

### 1.2 Frame of the study

The main aim of an ongoing research project is to investigate the efficiency of oil spill containment booms. Oil spills represent a major environmental

concern in coastal regions. The movement of oil slicks can cause long-term environmental damage by contaminating shoreline and marine life. Thus, it is important to improve techniques and equipments that facilitate spill cleanup in the water. Oil spill booms are known as an effective equipment to contain slicked oil and avoid its spreading over water surface. A schematic view of the Cavalli oil containment system is shown in Figure 1. In this system oil is trapped by the reservoir and can be pumped later using skimmers.

Several mechanisms can cause (a part of) the oil slick to pass under the barrier. One of these mechanisms is droplet entrainment failure. A high relative oil-water velocity may cause interfacial waves and oil droplets to be entrained from oil water interface (Wicks, 1996, and Jones, 1972).

In order to investigate the efficiency of an oil boom, it is important to evaluate the oil-water interfacial waves and velocity distribution in oil and water interfacial layers.

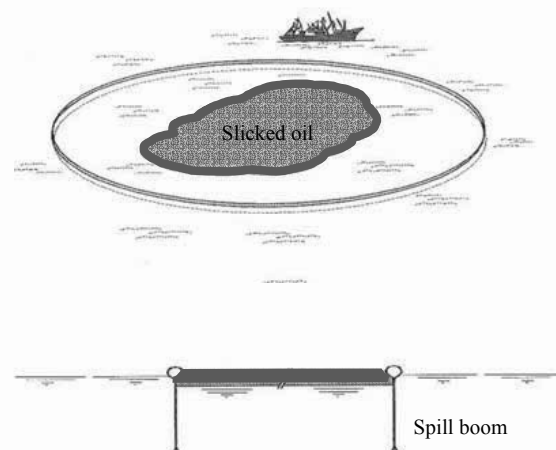


Figure 1: Schematic view of the Cavalli oil containment system; top: perspective of the system, bottom: cross section of the system.

## 2 EXPERIMENTAL SET UP

### 2.1 Channel

Experiments are undertaken in a 0.12 m wide, 6.5 m long and 1.1 m deep flume. For all experiments the water depth is fixed at 0.9 m. A rigid barrier is located in the middle of the flume and a certain volume of rapeseed oil is contained behind it (Figure 2).

The rapeseed oil has a viscosity of 88.8 cSt ( $\text{mm}^2/\text{s}$ ) at room temperature (about 85 times the viscosity of water) with relative density of 0.91.

### 2.2 Measurements

As it is schematically depicted in Figure 2, the ultrasonic transducer is installed on the top of the oil, and it is inclined looking upstream with an angle  $\beta=20^\circ$ . It is located at the point of maximum oil thickness.

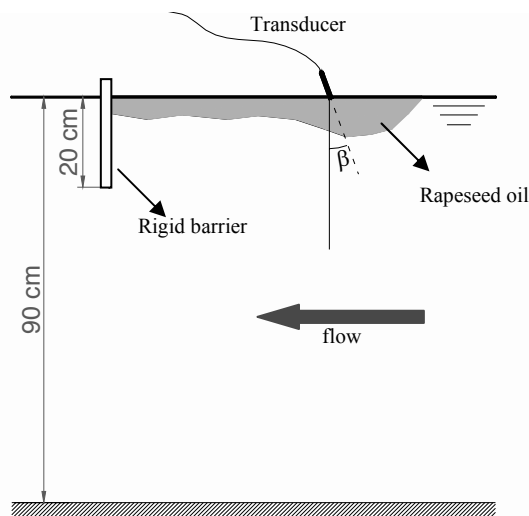


Figure 2: Experimental setup

The flow is not disturbed by the transducer as it just touches the oil surface. The main measurement parameters are listed in Table 1.

Table 1: Main measurement parameters

Parameter	Value
Number of channels	148
Number of profiles	2048
Sampling period	22 ms
Window start	3.7 mm
Window end	228.57 mm
Channel-distance / -width	1.02 mm / 1.48 mm
Frequency	2 MHz
Cycles / Repetitions / Noise level	4 / 32 / 4

## 3 SELECTED RESULTS

The power spectrum showed a high value for the channels in the vicinity of the observed oil-water interface. For all of those channels the pick is observed for a frequency of about 2.5 Hz (Figure 3). Assuming that the maximum echo is produced in the oil-water interface, one can conclude that the high power spectrum value corresponds to the frequency of interfacial waves. It means that the interfacial waves fluctuate with a similar frequency.

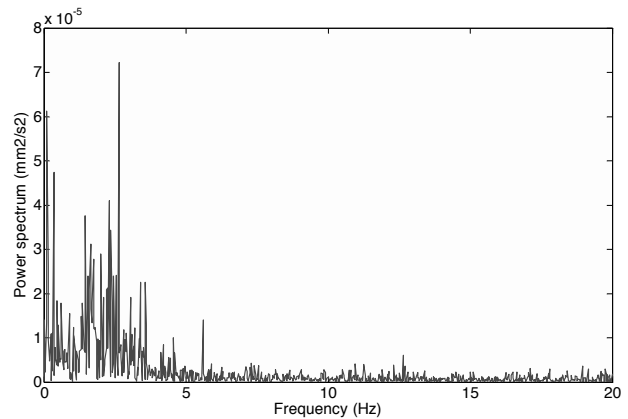


Figure 3: Power spectrum of the 22<sup>nd</sup> channel

In Figure 4 a series of picture during 0.8 s (with sequences of 0.2 s) are shown. Considering the white reference point, it can be seen that an interfacial wave forms in about 0.4 s. This means two consequent images.

Knowing the distance at which the high echo reflects, the location of oil-water interface is derived and illustrated in Figure 5 for duration of about five seconds. This figure confirms a frequency of about 2.5 Hz (period of 0.4 s) for oil-water interfacial waves. The values are smoothed with moving average method in order to remove the noise.

Figure 6 shows the interface derived from the US echo intensity superimposed on the velocity density plot. As shown on the pictures in Figure 4, smooth and breaking interfacial waves could be observed at a regular interval. The smooth waves induce an almost zero horizontal interfacial velocity, whereas the breaking waves move oil downstream with an intrusion of the velocity profile from the uniform flowing water.

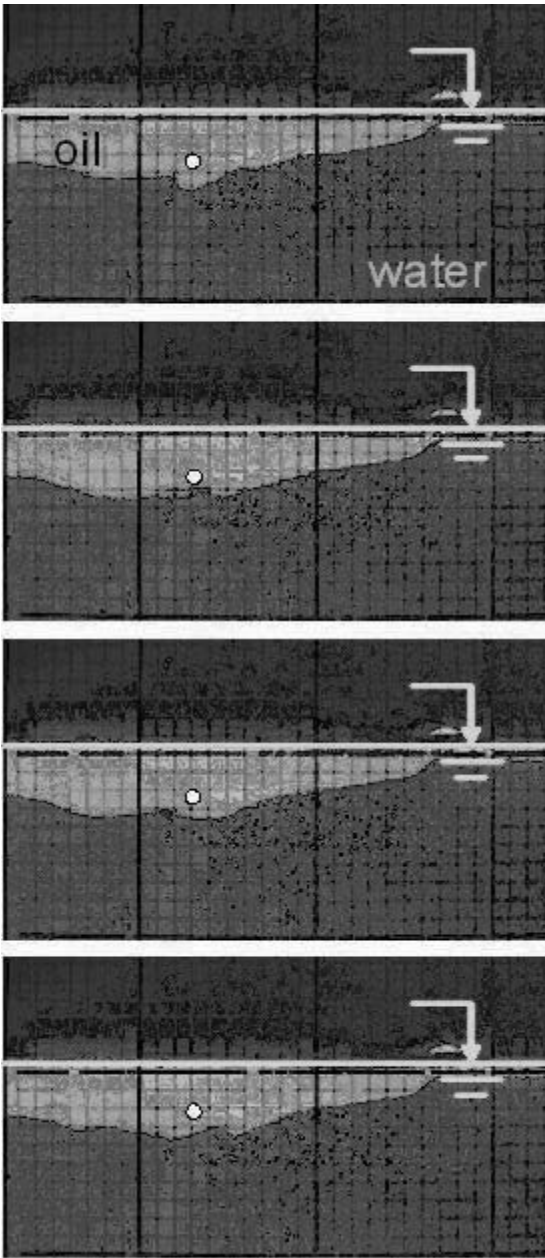


Figure 4: Sequence of pictures 0.2 s, grid size 10\*10 mm, the white point is a reference point to follow the interfacial waves

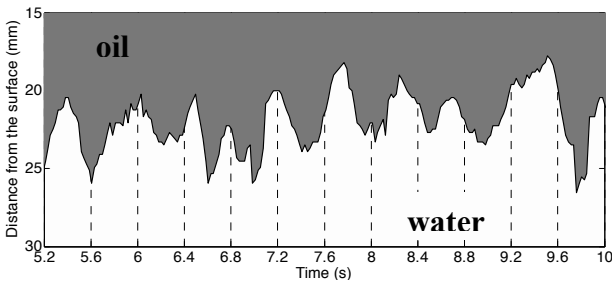


Figure 5: Oil-water interface derived from US echo

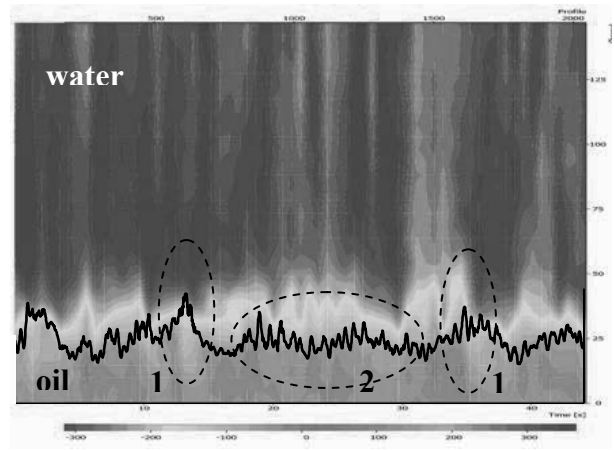


Figure 6: Velocity density plot in oil and water for a duration of 45 seconds; 1: breaking interfacial waves, 2: smooth interfacial waves.

To obtain the velocity profile in oil and water, the interface channel position is detected during a certain time and the measured instantaneous velocity profile shifted to have a constant position of the interface. Then the mean values of velocity in oil and water phases are calculated (Figure 7). As expected the friction layer happens in the water, since it is less viscous.

The visually observed weak circulation in the oil layer could not be measured by UVP.

A schematic velocity profile is shown in Figure 8.

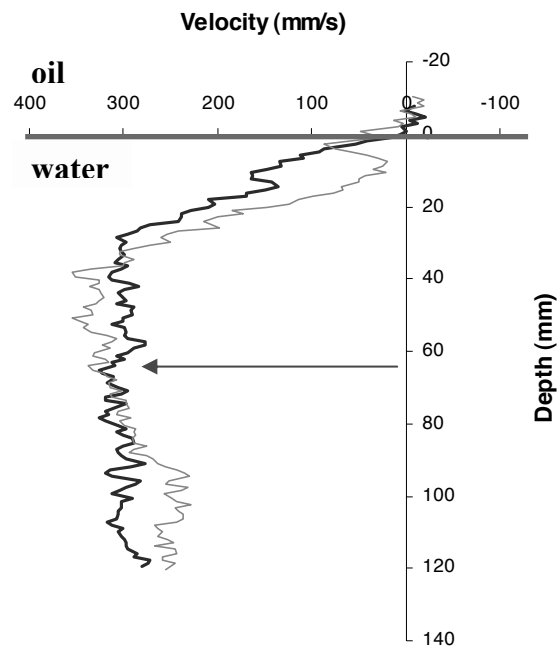


Figure 7: Mean velocity profile in water and oil; thick (blue) line: smooth waves, narrow (red) line: breaking waves

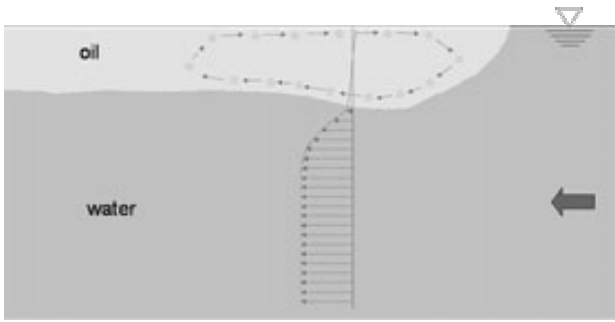


Figure 8: Schematic velocity profile in oil and water, a weak circulation of water bubbles was observed in the oil

#### 4 CONCLUSIONS

In the framework of oil spill booms efficiency study the velocity profile in a two-phase flow was investigated. The oil-water interface is derived from ultrasonic echoes intensity and the velocity profile is determined in oil and water phases.

The capability of the UVP measurements was confirmed for detecting the velocity profile in interface of a two-phase fluid.

#### 5 ACKNOWLEDGMENTS

The research project is financed by the Swiss Petroleum Union (Grant No. 4'09'02). The authors express also their appreciation to Dr. Y. Takeda for his helpful comments on the measurements and data analyses.

#### 6 REFERENCES

- [1] Amini, A., Bollaert, E., Boillat, J.L. and Schleiss, A., Preliminary Design Criteria for Oil Spill Containment Booms, Proc. Coastal Environment V incorporating Oil Spill Conf., pp. 411-420, 2004
- [2] De Cesare, G.: Use of UVP monitor in applied hydraulics, Proc. XVI. Symposium on Anemometry, Brno, Czech Republic, 12-13, 1999
- [3] De Cesare, G., Schleiss, A.: Turbidity current monitoring in a physical model flume using ultrasonic Doppler method, Proc. 2<sup>nd</sup> International Symposium on Ultrasonic Doppler Methods for Fluid Mechanics and Fluid Engineering, Villigen PSI, Switzerland, pp. 61-64, 1999
- [4] Jones, W.T., Instability at an Interface between Oil and Flowing Water, Journal of Basic Engineering, 94 (4), 874-878, 1972
- [5] Nakamura, H., Kondo, M., Kukita, Y., Simultaneous measurement of liquid velocity and interface profiles of horizontal duct wavy flow by ultrasonic velocity profile meter, Nuclear engineering and design, 184, 339-348, 1998
- [6] Takeda, Y., Velocity profile measurement by ultrasonic Doppler method, Exp. Therm. Fluid. Sci. 10, 444-453, 1995
- [7] Wicks, M., Fluid dynamics of floating oil containment by mechanical barriers in the presence of water currents. In: Joint Conference on Prevention and Control of Oil Spills, pp. 55-106, 1969

# Flow Field Investigation in a Rectangular Shallow Reservoir using UVP, LSPIV and numerical model

SAMEH KANTOUSH, ERIK BOLLAERT, GIOVANNI DE CESARE,  
JEAN-LOUIS BOILLAT and ANTON SCHLEISS

Ecole Polytechnique Fédérale de Lausanne (EPFL), Laboratory of Hydraulic Constructions (LCH), CH - 1015 Lausanne, Switzerland,

Low velocity and shallow-depth flow fields often are a challenge to most velocity measuring instruments. In the framework of a research project on reservoir sedimentation, the influence of the geometry of the reservoir on sediment transport and deposition was studied. Inexpensive and accurate technique for Large Scale Particle Image Velocimetry (LSPIV) was developed to measure velocity field in 2D. An Ultrasonic Doppler Velocity Profiler (UVP) and numerical simulation were used for verification and validation for LSPIV technique. The velocities were measured by means of UVP, which allows an instantaneous measurement of the 1D velocity profile over the whole flow depth. The turbulence large scale structures and jet expansion in the basin have been developed from the 3D velocity measurements by UVP, LSPIV and numerical simulations. Vertical velocity distributions were developed to study the vertical velocity effect. UVP measurements confirms 2-D flow map in shallow reservoir. LSPIV has potential to measure low velocity. The comparison between LSPIV, UVP and numerical simulation give sufficient agreements.

**Keywords:** Shallow flow, Reservoir sedimentation, UVP, 3D-flow field, LSPIV, CCHE2D.

## 1 INTRODUCTION

### 1.1 Background

In the framework of a study on the influence of reservoir geometry on the process of sedimentation in shallow reservoirs by suspended load was studied [8]. Two measuring techniques were applied for velocities and instantaneous flow pattern visualization.

Several applications for 1D, 2D and 3D velocities measurements by using UVP have been carried out at Laboratory of Hydraulic Constructions (LCH). The influence of the ribs on the maximum scour depth at a curved channel flows by 3D time averaged flow field have been studied by [5]. Of course there are a lot of different applications by using UVP for velocities measurement (as example [2]).

PIV offers a simple method of measurement in areas with complicated geometry and flow conditions. Surface flow measurements with PIV are described for e.g. in [1]. In hydraulic engineering, however, this technique has so far mainly been applied for surface velocity measurements of water and ice flow in very uniform flow fields [3]; [4].

Numerical simulation of flows in shallow reservoirs has to be checked for its consistency in predicting real flow conditions and sedimentation patterns. Typical flow patterns may exhibit flow separation at the inlet, accompanied by several recirculation and stagnation regions all over the reservoir surface. In this paper, numerical simulations were carried out by CCHE2D [6].

### 1.2 Aim of the study

This study focuses on the sedimentation of shallow

reservoirs by suspended sediments with the objective to gain insight into the physical process in shallow reservoirs. By investigation of 2D surface velocity fields and profiles of vertical velocity components, a better understanding of the mechanism governing the sediment exchange process between the jet entering the reservoir and the associated turbulence structures is attempted. The present paper focuses on:

- 1- The effect of the vertical velocity components on shallow reservoir sedimentation patterns.
- 2- A comparison between 2D-velocity obtained from two different techniques (UVP and LSPIV).
- 3- Validation of numerical model by use of LSPIV and UVP tests results.

3D velocity measurements are part of test series prepared to investigate the ideal reservoir geometry, minimizing the settlement of suspended sediments.

## 2 EXPERIMENTAL MEASUREMENTS

### 2.1 Experiment facilities

The experiments were carried out in a specific test facility at the Laboratory of Hydraulic Constructions (LCH) of the Swiss Federal Institute of Technology (EPFL). A schematic view of the experimental setup is shown in Figure 1. The setup consists of a rectangular inlet channel 0.25 m wide and 1.0 m long made of PVC, a rectangular shallow basin with inner dimensions of 6.0 m length and 4.0 m width, an outlet rectangular channel 0.25 m wide and 1.0 m long, a flap gate 0.25 m wide and 0.30 m height at the end of the outlet (see Figure 1). A sediment supply tank is mounted above the mixing tank. The mixing tank is equipped with a propeller

type mixer to create a homogenous sediment concentration. After filling the experimental reservoir with water, the water-sediment mixture will flow by gravity into the rectangular basin through a flexible pipe with 0.10 m diameter. On the basin side walls a 4.0 m long, movable aluminium frame is mounted which carries the measurement instruments can move in three directions.

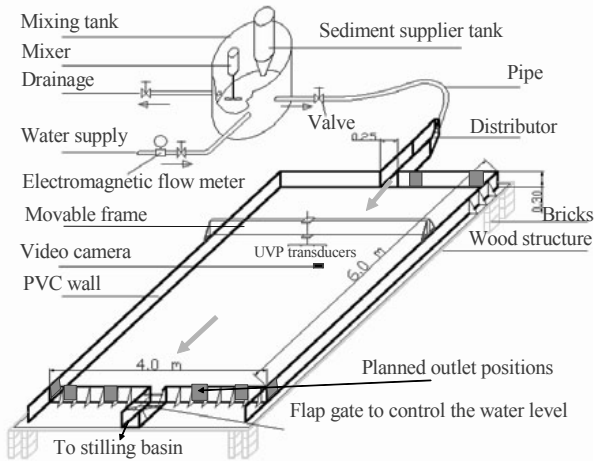


Figure 1: Schematic drawing of the experimental installation

## 2.2 Measurements and data acquisition system

Several parameters were measured during every test; namely: surface velocities, 3D flow velocity, water level and water temperature.

### 2.2.1 Ultrasonic Doppler Velocity Profiler (UVP)

The velocities were measured by means of an Ultrasonic Doppler Velocity Profiler (Metflow SA, UVP-DUO), which allows an instantaneous measurement of the 1D velocity profile over the whole flow depth [8]. The measurement probes were mounted on a support in groups of three, allowing the measurement of the 3D flow field (Figure 2). Since the number of measurement points was high, four PVC plates mounted on the measurements frame, allowing to record four groups of three 1D profiles (constituting one 3D profile) simultaneously to accelerate the data acquisition (see Figure 2). To cover the whole cross section of the basin, 4 positions were chosen along the cross section; each position has four groups of three probes (see Figure 2). All twelve probes were mounted on a frame which moves in the two horizontal directions. The probes were inclined at 20° to the vertical and had an emitting frequency of 2 MHz. A multiplexer shown in Figure 2 allowed switching between the different UVP-probes. Velocity profiles were recorded for all points on a 25\* 50 cm grid in transversal and with flow direction respectively. In order to extract the 3D velocity field in twelve cross sections over the whole reservoir, the acquired binary velocity file needed some

treatment. First the twelve 1D records were read from the raw data file. Then calculation of the velocity time-averaged measured components (average of 24 profiles). Then projection for these values and obtained velocity components cover the whole measurement depth. After rearrangement of the velocity profile, the data was exported to a text file for future automatic treatment with Matlab.

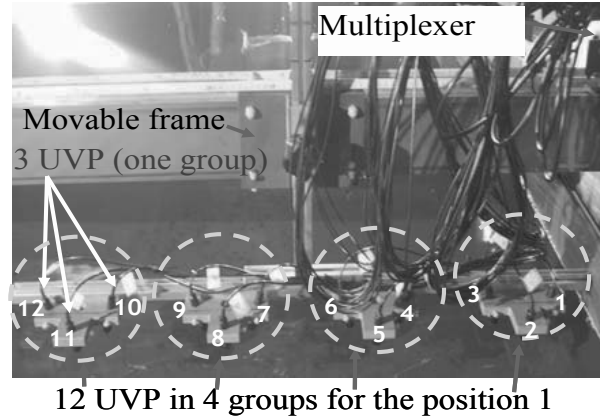


Figure 2: Above: Scheme of UVP installations and data acquisition, Below: Plane view and dimensions of UVP

### 2.2.2 Large-Scale Particle Velocimetr (LSPIV)

Large-scale particle image velocimetr (LSPIV) is an efficient and powerful technique for measuring river surface velocities. LSPIV is an extension of conventional PIV for velocity measurements in large-scale flows. While the image and data-processing algorithms are similar to those used in conventional PIV, adjustments are required for illumination, seeding, and pre-processing of the recorded images. A digital camera connected to a computer was used to record images, white plastic particles and reasonable lights as shown in Figure 3 were used for velocities measurements. Transformation of the images to remove perspective distortion from the objective lens using PTLens software and the image processing were conducted using FlowManeger software. The camera fixed perpendicular on the basin covering the plane basin area (the whole width 4.0 m and 5.0 from the length, missing 0.5m from upstream and downstream ends).

The flow is seeded with plastic particles (with average diameter 3.4 mm and specific weight 960 kg/m<sup>3</sup>) which are then illuminated. The dispersed light allowed recording their positions at two successive instant by video (SMX-155, monochrome, 1.3 megapixel, CMOS camera with USB2.0 interface and frame rate up to 33 FPS). The plan view (measurement plan) is divided into several small sub-areas, known as interrogation areas, IA. In each IA the cross-correlation algorithm is applied

in order to calculate the shift of the particles  $\Delta X$  in the time between two images  $\Delta T$ .

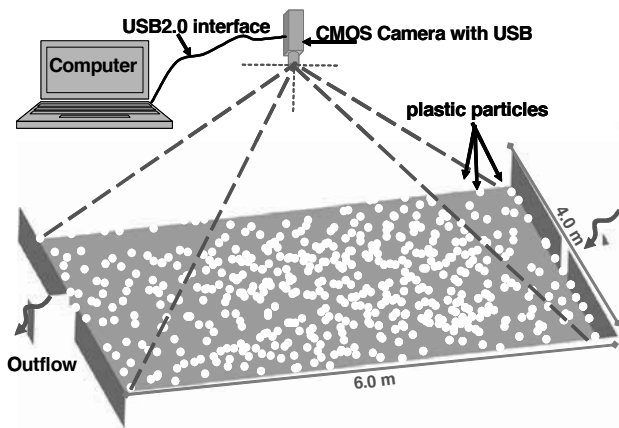


Figure 3: Scheme of LSPIV installations and data acquisition

### 2.2.3 Numerical simulations

Numerical simulations have been performed by using the CCHE2D software with the objective of comparing with the laboratory experiments. CCHE2D is two-dimensional hydrodynamic and sediment transport model for unsteady open channel flows over loose bed. Further details can be found in [6] & [7]. CCHE2D is a depth-integrated 2D hydrodynamic and sediment transport model based on a variant of the finite element method. Simple reservoir geometry has been simulated in order to study whether the relevant processes can be reproduced mathematically, and what features are controlling the phenomena. The model has been represented by a simple rectangular grid spacing of about 0.10 m in the flow direction and 0.05 m in the transverse direction. A total discharges of 7.0 l/s, a flow depth of 0.20 m and a bed roughness  $n = 0.01$  have been used as boundary and initial conditions. For detailed study of the boundary conditions and the results about these simulations see [7].

## 3 RESULTS

### 3.1 Velocity distribution by UVP

Distribution of vertical velocity for alluvial river is particularly important to know the transport of suspended sediment. For the analysis of the 3D velocities measured by UVP one cross section (CS11) near the downstream end of the basin ( $x=5.5$  m) have been chosen. Due to the following reasons the first data point of the velocity profile is located at 18 mm from the free water surface (Figure 4). After 1.50 hour experiment time, regular and uniform velocity profile in vertical depth and friction near zero along the cross section are observed in the downstream cross section shown in Figure 4.

Velocity distributions in stream wise, transversal and vertical directions (U, V, W respectively) at cross

section11 (CS11), located at x-distance 1875 mm; are shown in Figure 5. Vertical velocity are rather small comparing with the other two which it could be negligible and consider the reservoir as a shallow 2D. Moreover, the vertical eddies can be seen clearly from both Figures 4 and 6. So in the same time with horizontal circulations there is a vertical circulation is interaction with the horizontal one. The measurements showed that the velocity has a uniform distribution in vertical direction which confirms that the shallowness of the flow and vertical velocity is so low and uniform comparing with the other directions.

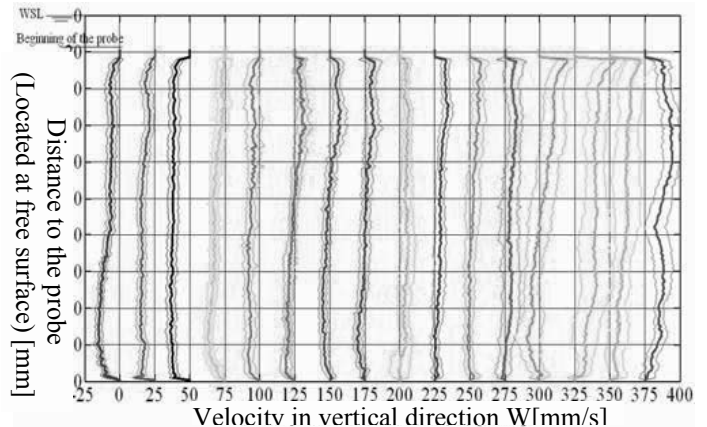


Figure 4: Velocity profiles and standard deviation measured by UVP (CS11)

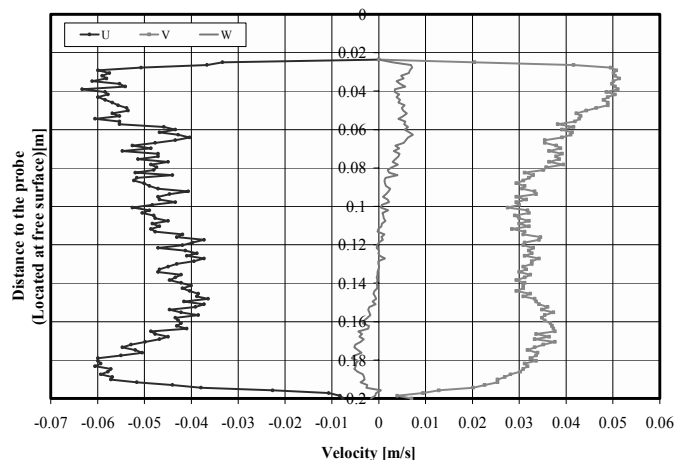


Figure 5: Velocity profiles in three directions U, V & W at x-distance 1875 mm from the left bank of cross section 11

Figure 6 shows the vertical velocity W contours distributed across the reservoir section (twelve cross sections every 0.5 m). The measurements shows that the higher velocity is shifted to the right hand side and the maximum velocity occurs near the wall; gyres and eddies are shown clearly in Figure 6. The maximum velocity is around the centerline and increases towards the walls which indicate that there is no friction in the bed.

### 3.2 Velocity vector map

Averaged flow fields have been obtained by using

UVP, LSPIV and CCHE2D software; are depicted in Figure 7(a), (b) & (c) respectively. Figure 7 shows that the flow enters as a plane jet issuing from the narrow leading channel to the wide basin. After jet issuance, the main flow tends towards the right hand side, generating a large and stable main gyre rotating anticlockwise and two small 'triangular' gyres rotating clockwise in the two upstream corners of the basin. The jet appears to be attracted to one of the side-walls. Its preference for the right side is weak since a stable mirror image of the flow pattern can easily be established by slightly adapting the initial conditions.

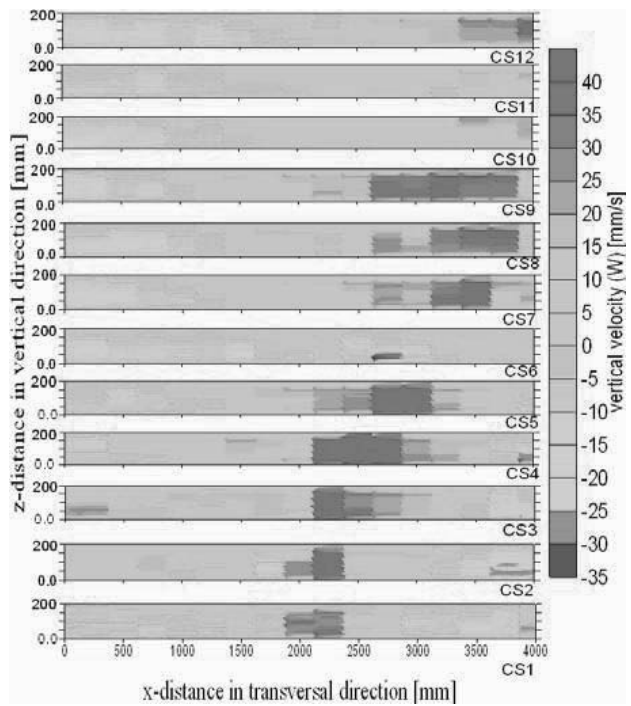


Figure 6: Vertical velocity contours at different cross sections (every 500 mm distance)

By following floating particles, it is noticed that in the first meter from the entrance the particle is straightly entering and, in the next two meters, it deflects to the right until it arrives at the stagnation points near the right wall at the middle (3m from the entrance). The particles that do not leave the basin through the outlet channel circulate with the main gyre to arrive near the separation zone at the farthest left side wall. There, a small gyre has formed at the left corner of the basin with a triangular shape 1.2mx1.2m. The circulation pattern sustains itself because the inertia of the main gyre pushes the incoming jet aside. By comparing the three techniques similar gyre patterns are obtained even with different measuring techniques and calculating program. It's clear that the flows structures by UVP and LSPIV in Figures 7(a) & (b) respectively are similar in magnitude and sharing the same position for the gyres centers. Numerical simulation for that kind of complex flow structure is rather difficult. In spite of that a good agreement velocity vectors and

magnitude are obtained with CCHE2D as shown in Figure 7(c). Figure 8 compare the simulated (computed by CCHE2D) and measured (measured by UVP and LSPIV) velocity vectors overall the basin. The measured vectors by UVP and LSPIV are in excellent agreement. By comparing the two method small difference (see Figure 8) exist at the middle part of the reservoir due to low number of the measured points by UVP and low velocity in the large circulation. Figure 8 shows that the velocity vectors by CCHE2D are acceptable and generally in a good agreement with the two other techniques. It could be explained by the complexity of that type of flow and the possibility that the turbulence model is too diffusive and may be the related to the inadequacy of the eddy viscosity models.

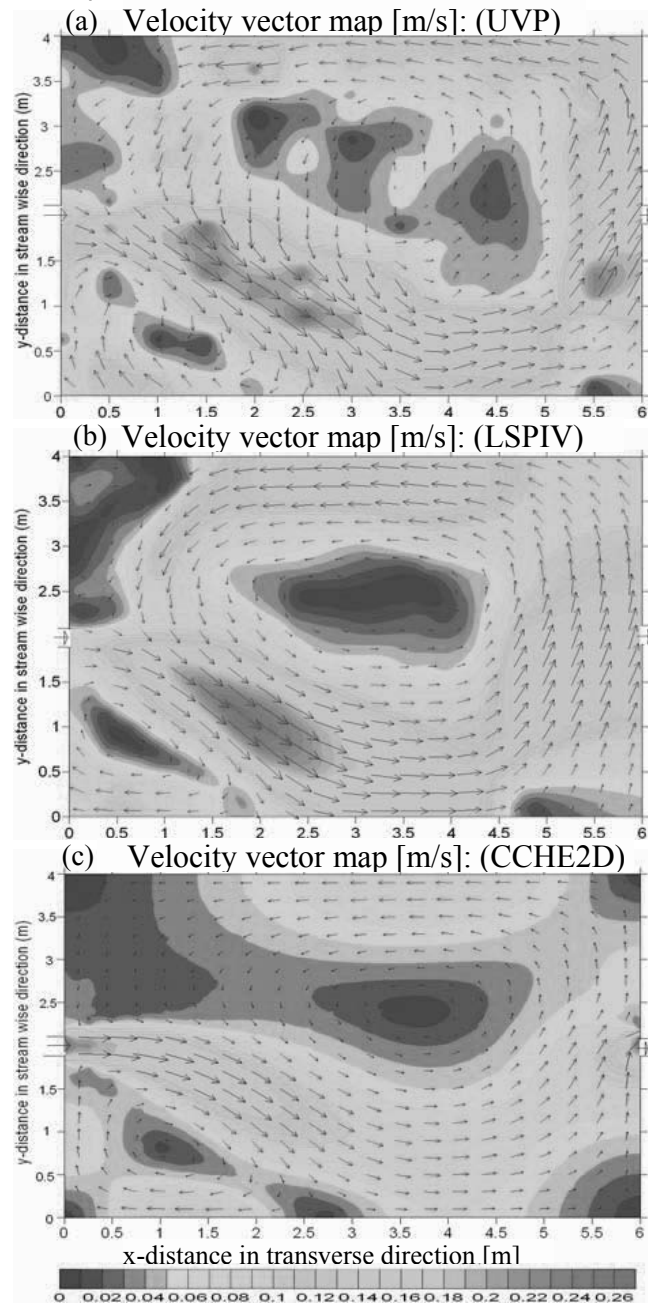


Figure 7: Stationary flow field from three different techniques a) UVP b) LSPIV c) CCHE2D

Figure 9 compares the computed and measured axial velocity magnitude at the basin centerline. Velocity distributions for UVP and LSPIV are approximately the same in the inlet channel. At the interface between inlet channel and basin, a sudden velocity increase may be observed, followed by a gradual decrease throughout the whole basin length. The sudden increase in velocity might be due to the sudden influence of the recirculation eddy that produces significant shear between the jet and the stagnant water, influencing so the horizontal velocity distribution of the jet, before jet diffusion becomes more important.

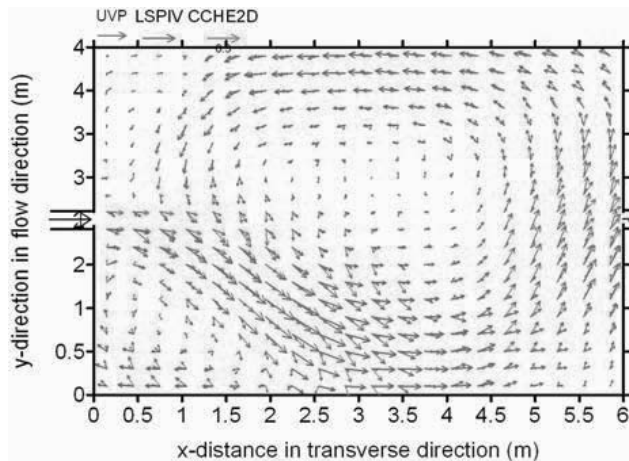


Figure 8: Comparison of velocity magnitude vectors from UVP, LSPIV, and CCHE2D program.

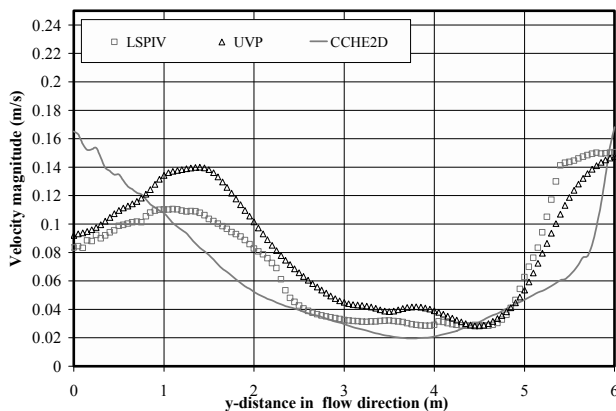


Figure 9: Comparison of longitudinal velocity magnitude along the basin centerline from UVP, LSPIV and numerical model (CCHE2D).

## 6 SUMMARY AND CONCLUSIONS

The first results of ongoing research on the influence of the geometry of a shallow reservoir on suspended sediment transport and deposition have been presented. It was found that the flow is quite sensitive to the boundary and initial conditions. The flow structures for shallow reservoir have been successfully measured using two different techniques LSPIV and UVP. Moreover; low and near zero velocities successfully measured by LSPIV were validated with UVP measurements and

numerical simulations by CCHE2D. The following points could be confirmed:

- (1) The two-dimensional velocity vector field in shallow reservoir can be reconstructed by combining three measurement data sets of UVP.
- (2) The LSPIV efficiency as a surface velocity measurement tool reveals efficient in low velocity shallow water that present numerous difficulties and challenges to existing instruments.
- (3) This particular behavior could also be reproduced by a two-dimensional depth-averaged flow and sediment transport model (CCHE2D). The numerical simulation indicates that the flow pattern can easily switch to different directions, depending on the boundary and initial conditions.

The comparison with UVP measurements allow to conclude that LSPIV has potential for measuring low velocities and is believed to be applicable in field tests as well. Moreover; it could be used for verification of the numerical model. Regarding the continuation of this research project the major goal is to find out which reservoir geometry leads to minimum sediment deposition. This requires experiments of long duration combined with numerical modeling techniques that include all the processes related to water and sediment.

## ACKNOWLEDGMENTS

Authors thanks for Metflow SA, Lausanne, Switzerland for support and providing UVP probes.

## REFERENCES

- [1] Adrian, R. J. Particle-imaging techniques for experimental fluid mechanics. *Annu. Re. Fluid Mech.* 23, 261-304 (1991).
- [2] De Cesare G. Use of UVP monitor in applied hydraulics, *Proc. XVI. Symposium on Anemometry*, (1999).
- [3] Emttea R., Fujita I., Muste M., Kruger A. Particle Image Velocimetry for whole field measurement of ice velocities. *Cold Regions Science and Technology* Vol. 26, 97-112 (1997).
- [4] Fujita I., Muste M., Kruger A. Large scale Particle Image Velocimetry for flow analysis in hydraulic engineering applications, *Journal of hydraulic Research*, Vol. 36, No 3, 397-414 (1998).
- [5] Hersberger, D.S. Measurement of 3D flow field in a 90° bend with ultrasonic Doppler velocity profiler. *Third International Symposium on Ultrasonic Doppler Methods for Fluid Mechanics and Fluid Engineering. PSI Proceedings 02-01, ISSN 1019-6447: 59-66. (EPFL), (2002).*
- [6] Jia, Y., and Wang, S. S. Y., 1999. Numerical model for channel flow and morphological change studies. *J. Hydraulic. Eng.* Vol. 125(9), 924-933.
- [7] Kantoush, S. A., Bollaert, E. F. R., Boillat, J.-L., Schleiss, A. J. Suspended load transport in shallow reservoirs. *Final Proc. XXXI IAHR Congress. Korea Water Resources Association, Seoul, South Korea, 1787-1799 (2005).*
- [8] Metflow. UVP Monitor – Model UVP-DIO. Users guide, Metflow SA, Lausanne, Switzerland, (2002).



# Flow Measurements in a Suction Sump by UVP

Katsuya Hirata, Masakatsu Hattori, Masashi Neya and Jiro Fuanaki.  
Dept. Mech. Engng., Doshisha Univ., Kyoto 610-0321, Japan

Hiroya Tanigawa

Dept. Mech. Engng., National College of Technology, Maizuru 625-8511, Japan

In the present study, to reveal the air entrainment mechanism into a suction pipe in a suction sump, the authors conduct flow-velocity measurements by UDM (Ultrasonic Doppler Method). Here, we consider the simplest geometry as a suction sump, that is, a straight channel with rectangle-cross section and a simple suction pipe near the end of the channel. Ultrasonic transducers are fixed outside the side, bottom and back walls with near-right angle and, we get three-dimensional time-mean velocity distributions and equi-vorticity contours. At first, measurement accuracy is checked by comparing velocity profiles by UDM with hydrogen bubble method. As a result, the authors show typical flow fields in the sump, and show the relation between flow pattern and air entrainment. Especially, we compare two cases where the air entrainment is often observed.

**Keywords:** suction sump, open sump, two-phase flow, vortex, pump, water tank

## 1 INTRODUCTION

In power generation plants, irrigations, drainages, and so on, the optimum designs of suction sumps are needed to get low cost, compact size and high efficiency. As well, in recent years, we often require miniaturization of suction sumps. In such situations, the air entrainment often induces vibrations and noises, which may result in pump's low efficiency or collapse, or which may stop water-vein managements of rivers (for example, see reference [1]).

Hirata et al [2] have conducted series of air entrainment experiments, and revealed the critical conditions to occur the air entrainment. However, for precise prediction of the air entrainment, we have to understand the flow field in the sump accurately and in detail.

Concerning the flow in the sump, Tagomori and Ueda [3] carried out qualitative observations, namely, flow visualization using aluminum flakes or polyethylene particles. Constantinescu and Patel [4] carried out three-dimensional numerical simulations with a  $k-\varepsilon$  turbulent model, and reveal a steady flow field at a Reynolds number of 60000.

Till now, there is no quantitative observation on actual flow in the sump. Then, in the present study, we show velocity vectors and vorticity contours using an ultrasonic-velocity-profile monitor [5] (hereafter, referred to as UVP), and reveal the time-mean three-dimensional flow structures. Specifically speaking, we study two cases, that is, cases A and B. In both cases, we often observe the air entrainment from a free surface into the suction pipe. In the case A, we see two air strings, whose position is in the leeward of the suction pipe with small fluctuation. In the case B, we see the air entrainment from anywhere on the circumference of

the suction pipe. The position where the air entrainment occurs is unstable in random manner.

## 2 EXPERIMENTAL METHOD

### 2.1 Experimental apparatus

Figure 1 shows the present model, that is, a suction sump and a suction pipe with the simplest geometries. And, table 1 shows basic dimensions of the model. Tested cases are two, cases A and B. The difference between two cases is only  $Z/D$ . Here,  $D$  is the outer diameter of the suction pipe, and is used as a length scale. A velocity scale is the mean flow velocity  $V_b$  at the bell-mouth-type intake of the suction pipe, which is defined as

$$V_b = 4Q/(\pi D^2) \quad (1)$$

where  $Q$  is the flow rate into the suction pipe.

Table 1 shows governing kinetic parameters, as well. As the Froude number is the most important parameter, we show the value calculated using another definition where a velocity scale is the mean velocity  $U_c$  at a cross section of the sump channel, for reference.

Figure 2 shows a schematic diagram of the present

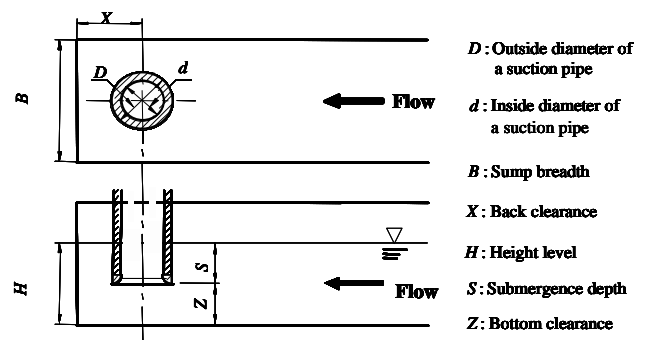
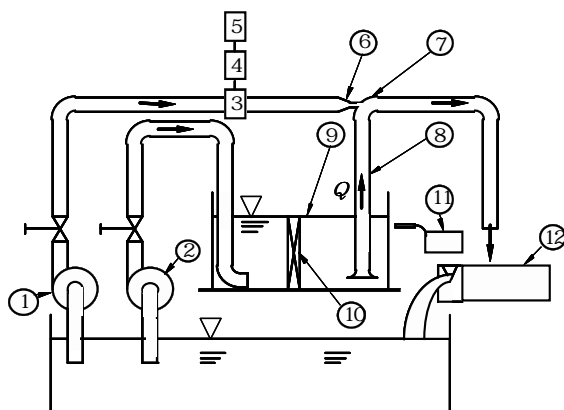


Figure1: Suction sump and suction pipe

Table1: Experimental parameters

	Case A	Case B
$D$ [mm]	38	←
$d$ [mm]	34	←
$B/D$	3.16	←
$X/D$	1.58	←
$Z/D$	0.39	1.18
$H/D$	1.58	←
$V_b$ [m/s]	0.6	←
$U_c$ [m/s]	0.095	←
$Fr=V_b/(gD)^{0.5}$	0.98	←
$Fr(U_c)=U_c/(gD)^{0.5}$	0.156	←
$Re=V_bD/\nu$	$2.2 \times 10^4$	←
$Bo=\rho_w g D^2/\sigma$	200	←
$We=V_b(\rho_w D/\sigma)^{0.5}$	14	←

experimental apparatus. A pump B (No.2 in the figure) feed working fluid (water) to a suction sump (No.9) from a reservoir tank. We control the flow rate from the pump A by a control valve, and then control the water level in the suction sump. At the upstream of the suction sump, namely, at 0.84 [m] upstream from the back wall of the suction sump, we put a strainer (No.10) to get a uniform flow. The strainer consists of unwoven fabric sandwiched between two wire meshes with diameter of 0.001 [m] and gap of 0.001 [m]. A bend-type jet pump (No.6 and 7) pump up water in the suction sump into the suction pipe (No.8). Here, the jet pump has less swirling component, than ordinary pumps. The jet pump is driven by a pump A (No.1). We measure its primary flow rate using an electro-magnetic flow meter (No.3, 4 and 5). And, we measure the total sum of the primary and secondary flow using a triangle weir (No.12). Water from the weir falls into the reservoir tank, then, a water-circulation system is closed. We measure velocities in the suction sump using a UVP monitor (No.11) through side walls, a bottom wall or a back wall.



- 1. Turbo pump A
- 2. Turbo pump B
- 3. Electro Magnetic Flow Meter
- 4. Converter
- 5. Digital multi meter
- 6. Nozzle
- 7. Bend-type jet pump
- 8. Suction pipe
- 9. Suction sump
- 10. Filter
- 11. UVP monitor
- 12. Triangle weir

Figure 2: Schematic of experimental apparatus

2.2 Velocity measurements by UVP monitor

In the present study, the number of measuring points is 128 in one profile, and then, the space resolution on the profile is 0.75 [mm]. As the diameter of the ultrasonic beam is 5 [mm], one measuring volume is a disc with a diameter of 5 [mm] and with a thickness of 0.75 [mm]. We get consecutive 1024 profiles at each measurement with an interval of 32 [ms] or more.

When we get time mean velocities, we average more than 200 profiles, which is enough for the present cases, as the present flow is almost steady with weaker turbulence. Owing to the air entrainment, there often exist free surfaces under the mean water level. As accurate UVP measurements are impossible near free surfaces, we avoid such measurements.

Tracer is polyethylene particle with a mean diameter of  $1.2 \times 10^{-5}$  [m]. As the particle's density lighter than water (its specific gravity is 0.918), we coat particles with surface-active agent to be suspended into water.

Figure 3 shows the definition of the present coordinate system. At each measurement point in the suction sump, we get three velocity components  $u$ ,  $v$  and  $w$ .

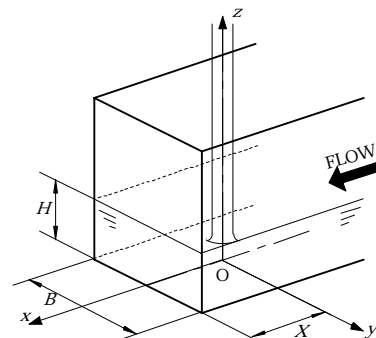


Figure 3: Definition diagram for coordinate system

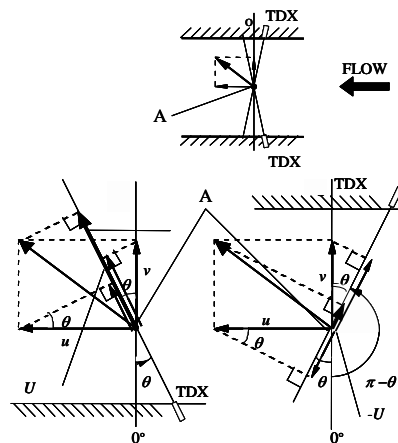


Figure 4: Definition diagram for measurements by UVP

Especially at the upstream of the suction sump, it becomes difficult to get fine measurements, as such place is far from the back wall. For example, when we get  $u$  components at a point A, we measure two velocities  $U$  and  $U$  as shown in figure 4. Then we calculate  $u$  according to the following.

$$u = (U + U) / 2 \sin \theta \quad (2)$$

In the present, transducer's tilting angle  $\theta$  is fixed to  $10^\circ$ .

### 3 RESULTS AND DISCUSSION

#### 3.1 Accuracy check

In order to confirm the accuracy of velocity measurements, we compare a UVP result with a time line by the hydrogen bubble method. Figure 5 shows a comparison between velocity distributions by two methods for the same channel flow. As a result, we can confirm good agreement as shown in figure 5.

#### 3.2 Case A

Now we show some typical results for the case A. Figure 6 shows velocity vectors and vorticity contours on the  $x$ - $y$  plane at  $z/D=0.95$  (near free surface). Flow is almost symmetrical concerning the centre line  $y/D=0$ . And, there is a pair of swirls with the opposite rotation. The position of these swirls' centre almost coincide with the positions of two string-like air bulks accompanied with the air entrainment from the atmosphere into the suction pipe.

Figure 7 shows velocity vectors and vorticity contours on the  $y$ - $z$  plane at  $x/D=-1.58$  (upstream of the suction pipe). As well as figure 6, flow is almost symmetrical concerning the centre line  $y/D=0$ . And, we can see a pair of swirls with the opposite rotation, which is longitudinal vortex pair with stream wise axis.

Figure 8 shows velocity vectors and vorticity contours on the  $x$ - $z$  plane at  $y/D=-0.63$  (in front of the suction sump). At  $x/D=0.2$ , there is a strong downward flow. Besides, in the downstream of the suction sump, we can see a swirl with anti-clockwise strong vorticity. This swirl centre also coincides with the position of the string-like air bulk.

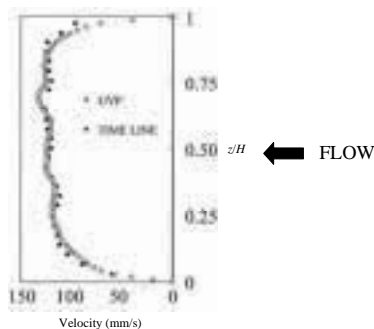


Figure 5: Calibration of UVP by hydrogen bubble method

#### 3.2 Case B

Next, we show some typical results for the case B. Here, flow in the case B strongly fluctuates with time, and the flow symmetry about the sump centre is frequently and randomly broken. So, in order to make the flow almost steady, we slightly tilt the upstream strainer. In such condition, mean velocity on the positive  $y$  side is a little bit faster than the negative  $y$  side.

Figure 9 shows velocity vectors on the  $x$ - $y$  plane at  $z/D=0.63$  (near the sump bottom below the suction pipe). We can see only one swirl on the negative  $y$  side in the downstream of suction pipe. Such clear swirl exists not on the  $x/y$  plane near or above the suction intake, but on the  $x/y$  plane below the intake.

Figure 10 shows velocity vectors on the  $y$ - $z$  plane at  $x/D=0.63$  (leeward of the suction pipe). We can see only one swirl with anti-clockwise vorticity in the negative  $y$  side.

Figure 11 shows velocity vectors on the  $x$ - $z$  plane at  $y/D=0.47$  (behind the suction pipe). In the downstream of the suction pipe near the free surface, we can see reversed flow, corresponding to a complicated three-dimensional flow structure.

In summary, the case B is in the category "[6] column vortex" in the conventional classification. If we consider the flow structure under the free surface, the case B is not properly characterized by the concentric flow around the suction pipe axis.

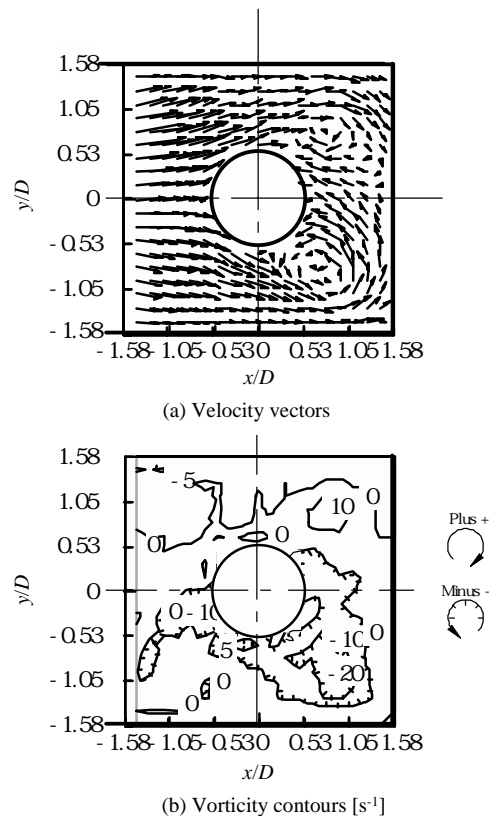


Figure 6: Velocity vectors and vorticity contours on the  $x$ - $y$  plane at  $z/D=0.95$  (case A)

### 4 CONCLUSIONS

We have conducted UVP measurements in a suction sump, and revealed the mean three-dimensional flow structures quantitatively. Both tested cases have complicated flow structures under the free surface, which are difficult to be expected only from surface observations.

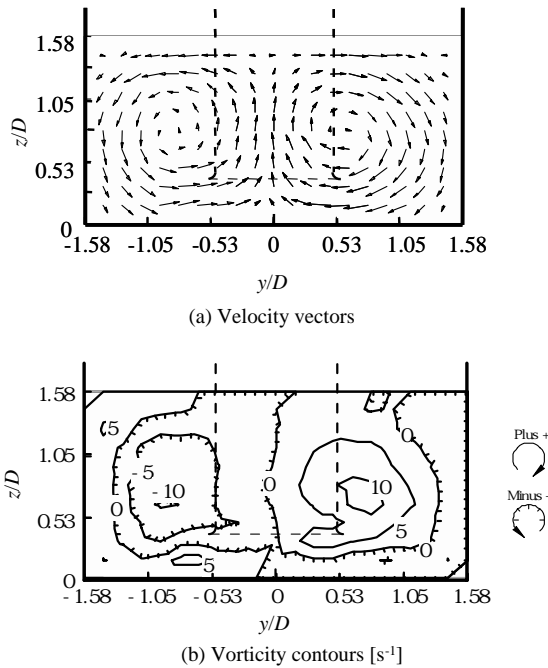


Figure 7: Velocity vectors and vorticity contours on the y-z plane at  $x/D = -1.58$  (case A)

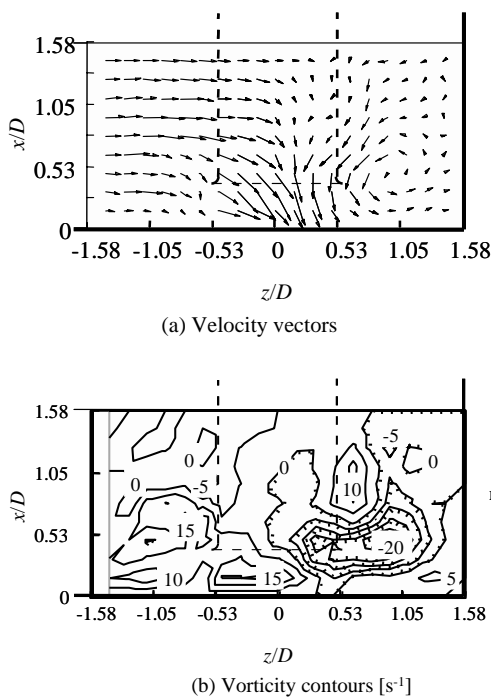


Figure 8: Velocity vectors and vorticity contours on the x-z plane at  $y/D = -0.63$  (case A)

### REFERENCES

[1] JSME standard, standard method for model testing the performance of a pump sump, JSME S 004 (1984) (in Japanese).  
 [2] Katsuya H., Jiro F. and Masashi N.: On the critical submergence for air entraining vortices in a suction sump, JSCE Journal of Hydraulic, Coastal and Environmental Engineering, Vol.65 No.747 (2003) 61-69 (in Japanese).  
 [3] Masashi T. and Haruo U.: An experimental study on submerged vortices and flow pattern in the pump sump, Transaction of JSME, series B, Vol.57 No. 543 (1991) 3641-3646 (in Japanese).  
 [4] G. S. Constantinescu and V. C. Patel: Numerical model for simulation of pump-intake flow and vortices, Journal of Hydraulic Engineering, Vol.4 No.2 (1998) 123-134.  
 [5] Yasushi T.: Velocity profile measurement by ultrasound Doppler shift method, Int. J. Heat and Mass Flow, Vol.7 (1986) 313-318 (in Japanese).  
 [6] H. W. Iversen: Studies of submergence requirements of high-specific-speed pumps, Transaction of ASME, Vol.75 (1953)635-641.

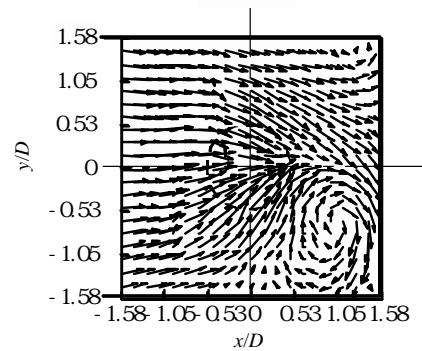


Figure 9: Velocity vectors on the x-y plane at  $z/D = 0.63$  (case B)

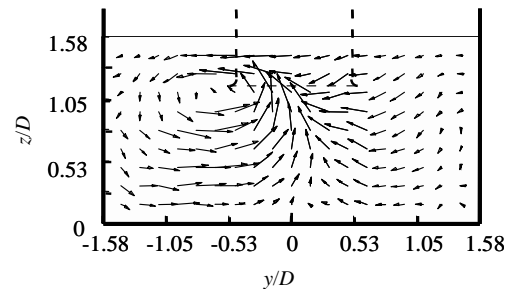


Figure 10: Velocity vectors on the y-z plane at  $x/D = 0.63$  (case B)

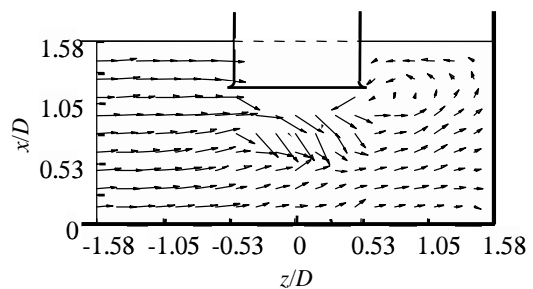


Figure 11: Velocity vectors on the x-z plane at  $y/D = 0.47$  (case B)

# Measurements of Bubble Jets by 3D PTV and UVP

Atsushi Shintani, Jiro Funaki and Katsuya Hirata  
Dept.Mech.Engng., Doshisha Univ., Kyoto 610-0321, Japan

To show three dimensional flow structures is useful and effective when we treat with complicated flows such as bubble jets. A three-dimensional particle tracking velocimetry (3D PTV) is one solution, but has unknown factors. In the present study, we conduct the simultaneous measurements of 3D PTV with an ultrasonic velocity profiler (UVP) using the common tracer particles. The simultaneous measurements have other applicable possibilities, as well as accuracy check of 3D PTV. We tested four conditions - of tracer particles. As a result, UVP is not applicable for small number of the tracer particles. On the other hand, 3D PTV is not applicable for large number of the tracer particles. We have found the optimum condition for both measurements, and confirm the accuracy of measurements. In addition, we apply 3D PTV technique to bubble jets using air bubbles as tracer particles.

**Keywords:** PTV, UVP, Three Dimension, Bubble, Jet

## 1 INTRODUCTION

Recently, we have often suffered from water pollutions caused by eutrophication in lakes, ponds, harbors and so on. Engineers have developed a simple method to improve water quality, using bubble jets which are called aeration to make oxygen in water to resolve water pollution. As well, bubble's motion becomes important in many applications, such as chemical bubble columns, chemical reactors, gas absorbers, fermenters, bubble pumps and nuclear power plants. But each bubble motion in such flows is not sufficiently understood yet.

The authors' final aim is to reveal basic features of air-bubble jets into water. Concretely speaking, we try to measure the movements of bubbles one by one, quantitatively and simultaneously, and to show three-dimensional bubble-jet characteristics precisely and statistically.

Yamamoto et al. [1] have studied the concerning fluid motions using a three-dimensional particle tracking velocimetry (referred to as 3D PTV, for example [2]). Bergmann et al. [3] have studied the concerning fluid and bubble's motion in two dimensions.

Here, for above the purpose, we focus not on fluid motion but on bubbles' motion, and we develop the 3D PTV technique using bubbles as tracer particles. This technique has the following advantages. The technique can give us the information of many bubbles' velocity at each time. There exists no sensor which disturbs the flow. And we get three-dimensional information of a whole flow area successively. However, generally, this method has a disadvantage in accuracy.

In the present study, at first, we check the accuracy of 3D PTV. Namely, we carry out simultaneous measurements of 3D PTV with an ultrasonic velocity profiler [4] (referred to as UVP), which is more accurate in general. So, we conduct the simultaneous measurements in a turbulent and

spatially-complicated flow, that is, a swirling flow in a cylindrical container. We will find the suitable condition of particle's density and particle's size to conduct simultaneous measurements by both 3D PTV and UVP, and then confirm the agreement. Next, from the certified 3D PTV method, we study the bubble-jet features.

## 2 EXPERIMENTAL METHOD

### 2.1 Experimental apparatus

To check the accuracy of 3D PTV, we measure a swirling flow by both 3D PTV and UVP simultaneously. Fig. 1 shows an experimental apparatus. A cylindrical container made of transparent acrylic resin is filled with water. We put the cylindrical container on a magnetic stirrer. A stirring object on the cylindrical container bottom drives a swirling flow.

A 3D PTV system consists of the following: a YAG laser as a light source, two sets of high-speed video cameras with a frame rate of 1/500 [s], camera interfaces and a personal computer on which we conduct 3D PTV analyses. For accurate 3D PTV measurements, we have to diminish the image distortion due to the cylindrical container's surface curvature. We put a rectangular-prism container which covers the cylindrical container, and we fill the space between the containers with water as well.

An UVP system consists of the following: an ultrasonic transducer as an UVP probe, which is placed outside the cylindrical container, and an UVP monitor for simultaneous measurements with 3D PTV.

Fig.2 shows the present coordinate system, with the position of an UVP probe. We put the probe between the rectangular-prism and cylindrical containers.

3D PTV needs more than two cameras, and here we use a pair of cameras A and B. As shown in

Fig.1, the camera A is above the cylindrical container, the camera B is on the side. Fig.3 shows a sample stereo photo by the cameras A and B. Here, the fluid is in a swirling motion, and we can confirm that tracer particles are uniformly scattered.

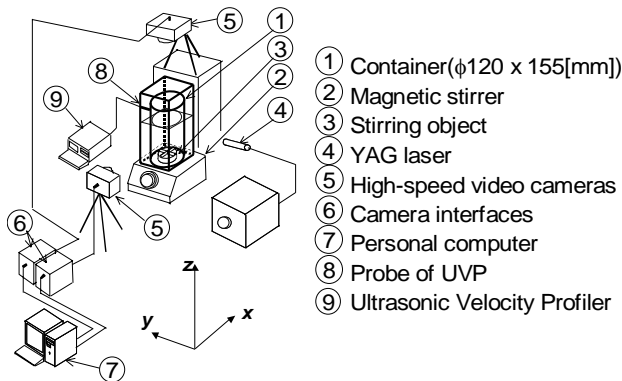


Figure 1: Schematic view of experimental apparatus.

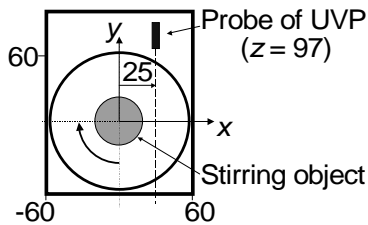


Figure 2: Coordinate system and the position of a UVP probe [mm].

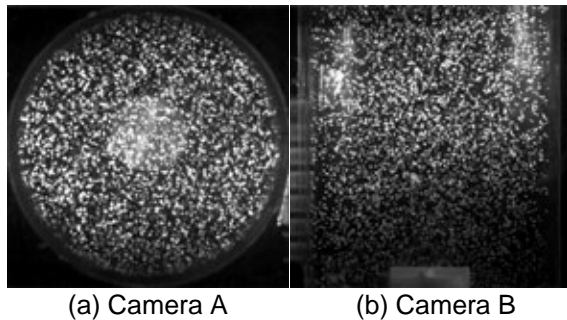


Figure 3: A pair of sample stereo photos for 3D PTV.

Table 1: Tested conditions.

Condition				
$D_p$ [mm]	0.6-1.2	0.6-1.2	0.3-0.6	0.3-0.6
$V_p$ [mm <sup>3</sup> ]	925	1851	444	1851
$C_{VP}$ [%]	0.05	0.11	0.03	0.11
$N_p$	2500	5000	9300	38800
$C_{NP}$ [mm <sup>-3</sup> ]	0.001	0.003	0.005	0.022
$C_{NP} V_{UVP}$ [mm <sup>-3</sup> ]	0.041	0.083	0.15	0.64

As the tracer particles, we use chemical-bridged polyethylene-resin particles with a mean diameter of 0.18 [mm], which is coated with fluorescent paint. Actual particles' diameter  $D_p$  is controlled by the thickness of the paint layer. Tab.1

shows four tested conditions , , and , with different  $D_p$  and different particles' number  $N_p$ . Namely, condition has the smallest  $N_p$ , the second, and the third. The condition has the largest  $N_p$ . The condition and have larger  $D_p$ , and the condition and have smaller  $D_p$ .

### 2.2 Experimental apparatus for bubble jets

Fig.4 shows an experimental apparatus for bubble-jets measurements. A container is a cube of 1 [m] x 1 [m] x 1 [m], and made by acrylic resin. We fill the container with water, whose depth is 0.8 [m]. A compressor makes air flow through a flow control valve and pipe into a stainless-steel chamber. The chamber is placed on the bottom of the cubic container. An air nozzle is on the top of the chamber, through which air bubbles are generated into water. Pressure and temperature in the chamber are measured by a pressure transducer and thermocouple, respectively. These signals through a sensor interface are converted in digital data on a PC. Using two high-speed video cameras with a frame rate of 1/500 [s], two images of bubble flow are taken at the same time. We use a halogen lamp as lighting.

We test two kinds of nozzles. Namely, one is a straight-pipe nozzle with an inner diameter of 0.3 [mm] and a length of 15 [mm], and the other is a convergent nozzle with an inner diameter of 0.1 [mm].

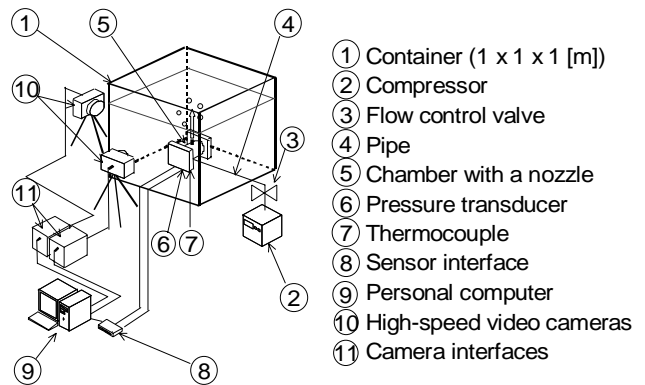


Figure 4: Schematic view of experimental apparatus for bubble jets.

### 2.3 Outline of 3D PTV analysis

For 3D PTV analysis (see [5]), we regard bubbles as tracer particles. First, using two high-speed video cameras, which are calibrated in advance, we take two simultaneous images of bubbles in a measurement volume. Second, we calculate three-dimensional positions of bubbles from a pair of stereo images. Velocity vectors of bubbles are obtained from 4 successive informations of position. All data processings have been done in a PC.

### 3 RESULTS AND DISCUSSION

#### 3.1 Simultaneous measurements of 3D PTV with UVP

Figure 5 shows time history of flow velocity by UVP for each condition at  $y=0$  [mm]. On the condition , we can see scattered data between  $v_y/\overline{v_y}$  of 0 to 1. Then, the standard deviation  $\sigma$  becomes large. As is seen later, small  $v_y$  is considered to be the error due to the lack of tracer particles in UVP-measurement volume. As the total number of tracer particles  $N_p$  increases, the value of  $v_y$  concentrates its mean value  $\overline{v_y}$  (see the condition , and ). One exception is  $v_y = 0$ . However, even the condition , the number of data with  $v_y = 0$  is very small, therefore, time-mean value  $\overline{v_y}$  has negligible effect. So, for appropriate UVP measurements, we need  $N_p$  per unit volume  $C_{NP}$  greater than that on the condition . And we confirm that the conditions , and are in good accuracy.

About the size of tracer particles, we compare the conditions , . Here, the particles on the condition is two-times bigger than the condition . So, we can see no effective size effect of the tracer particles. And the tested particle diameter  $D_p$  is in a suitable range for UVP measurements.

Fig.6 shows comparisons between 3D PTV and UVP about spatial profiles of time-mean velocity  $\overline{v_y}$ . On the condition  $\overline{v_y}$  by UVP is lower than that by 3D PTV. As is shown in Fig.5 (a), UVP data includes many errors with lower values of  $\overline{v_y}$ . Then UVP data in Fig.6 (a) is considered to be lower than the actual data.

In Fig.6 (b), namely, on the condition , 3D PTV is in good agreement with UVP. So, the condition is considered to be suitable for the simultaneous measurements by both 3D PTV and UVP.

In Fig.6 (c) and (d), namely, on the condition and , 3D PTV results are lower than UVP. In general, 3D PTV is not suitable for a large number of tracer particles. And the conditions and are considered to be those with excessive tracer-particle numbers.

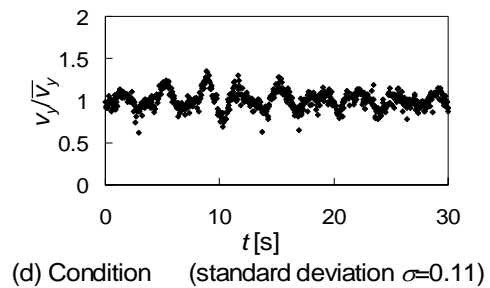
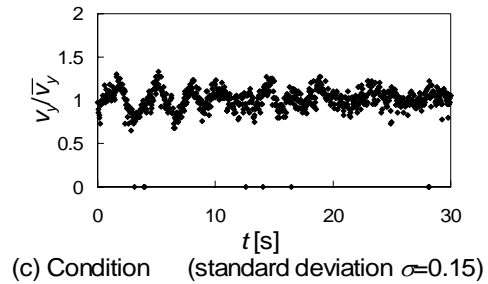
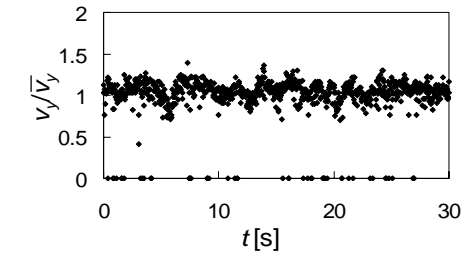
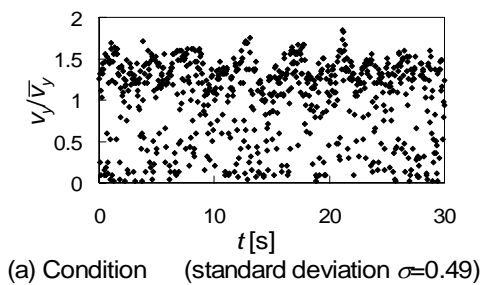
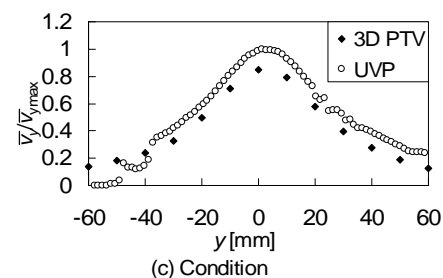
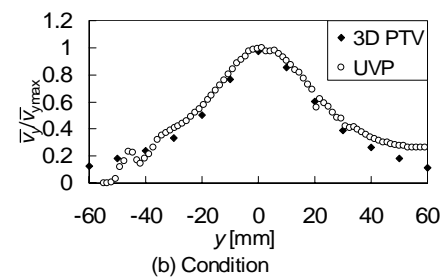
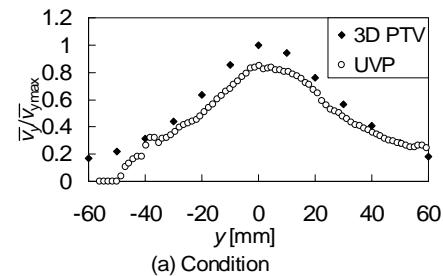


Figure 5: Time history of flow velocity by UVP ( $y=0$  [mm]).



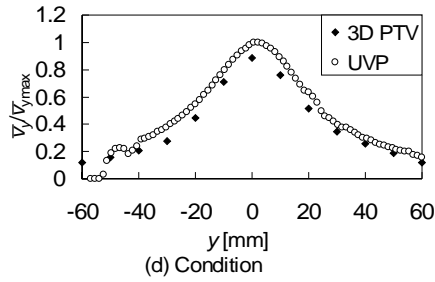


Figure 6: Profile of time-mean velocity  $\bar{v}_y$ .

### 3.2 Results of 3D PTV measurements of bubble jets

Now, we apply the 3D PTV to bubble jets, where air bubbles are used as the tracer particles. The parameter is the pressure ratio  $p/p_0$ , where  $p$  is the surrounding static pressure at the nozzle exit and  $p_0$  is the chamber static pressure. Fig.7 is a sample of velocity vectors of air bubbles, which is obtained by a sequence of stereo photos.

Fig.8 shows the relation between the pressure ratio  $p/p_0$  and the ensemble average of time mean bubbles  $V_b$ . Fig.8 (a) is for the near-centre area (at  $r = 0-5$  [mm]) and Fig.8 (b) is far-centre area (at  $r = 35-40$  [mm]). In the near-centre area, there exists the minimum value at  $p/p_0 \cong 0.6$ , which is near the choke boundary. On the other hand, in the far-centre area, as  $p/p_0$  decreases, the value almost monotonously decreases. But, near the chock-boundary pressure, the value changes rapidly. So, these seem to be a qualitative difference between the choked bubble jets and the non-choked ones. The above features are common on both two different nozzles.

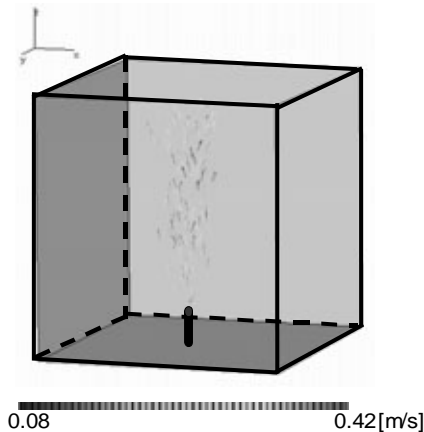


Figure 7: A sample of velocity vectors of bubbles (straight-pipe nozzle;  $p/p_0=0.791$ ).

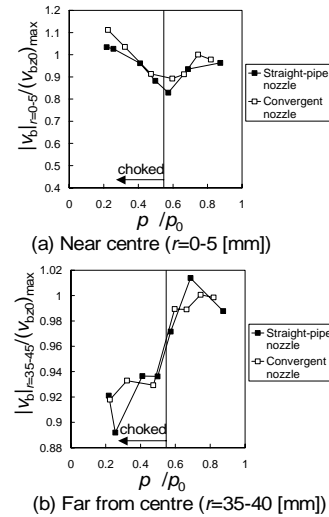


Figure 8: Pressure-ratio effect on mean bubble's velocity ( $z=220-260$ [mm]).

### ACKNOWLEDGEMENTS

This study was partly supported by the Academic Frontier Research Project on "Next Generation Zero-emission Energy Conversion System" of Ministry of Education, Culture, Sports, Science and Technology.

### 5 CONCLUSIONS

The authors conducted simultaneous measurements by 3D PTV and UVP, and obtain the following conclusions.

1. UVP is not applicable for smaller  $C_{NP}$ , and 3D PTV is not applicable for larger  $C_{NP}$ . The condition  $0.001 < C_{NP} < 0.01$  is suitable for UVP, and the condition  $0.001 < C_{NP} < 0.01$  are suitable for 3D PTV.
2. A suitable condition for the simultaneous measurements is the condition  $0.6 < p/p_0 < 1.2$ , where  $D_p = 0.6-1.2$  [mm] and  $C_{NP}=0.003$  [mm<sup>-3</sup>].
3. We have developed time-successive 3D PTV on air-bubble jets into water from a bottom nozzle using the bubbles as tracer particles.

### REFERENCES

[1] Yamamoto F, Iguchi M, Ohta J, and Koketsu M: Measurement of Bubbling-Jet Two-Phase Flow Using 3-D PTV Based on Binary Image Cross-Correlation Method, Flow Visualization and Image Processing of Multiphase Systems ASME 209 (1995) 131-136.  
 [2] Adrian R. J: Particle-Imaging Techniques for Experimental Fluid Mechanics, Ann. Rev. Fluid Mech. 23 (1991) 261-304.  
 [3] Bergmann C, Seol D G, Bhaumik T and Socolofsky S A: Entrainment and mixing properties of a simple bubble plume, 4th International Symposium on Environmental Hydraulics (2004) 403-409.  
 [4] Takeda Y: Measurement of Taylor-Couette Flow by the Pulsed Ultrasonic Doppler Method, Phys. Soc. Jpn. 49 (1994) 994-1001.  
 [5] Doh D H, Kim D H, Cho K R, Cho Y B, Lee W J, Saga T and Kobayashi T: Develop of Genetic Algorithm Based 3D-PTV Technique, J. Visual. 5 (2002) 243-254.

## Discharge estimation by continuous measurement of water velocity by Doppler instrument

Andrej Vidmar, Luka Štravs, Simon Rusjan, Sašo Petan and Mitja Brilly

Chair of Hydraulics Engineering, University of Ljubljana, Jamova 2, 1000 Ljubljana, Slovenia, E-mail: avidmar@fgg.uni-lj.si

Accurate discharge estimation is crucial for an efficient river basin management and especially for flood forecasting and issuing warnings related to possible extreme flood events. The traditional way of estimating the discharge in hydrological practice is to measure the water stage and to convert the recorded water stage values into discharge by using the single-valued rating curve, which is a relationship between the stage and discharge derived from direct measurements of discharge, which are done at convenient times with measurements of flow velocities at different points over the gauging cross section, and hence the discharge values of the rating curve for the extreme events are usually extrapolated by using different mathematical methods and are not directly measured. By using the Starflow ultrasonic Doppler instrument we recorded the actual relation between the water stage and the flow velocity at the occurrence of flood waves. Unsteadiness in the water stage  $\varphi$  water velocity relation causes the trajectory of the flood event to appear as a loop on the stage  $\varphi$  velocity diagram. Results of the 3-year time measurements at different water stations on different Slovenian rivers (the Sava, Dragonja, Gradascica, Reka, etc.) show non-negligible differences in water velocities on the rising and falling limbs of the flood waves at the same water stage. Neglecting the influence of different water flow velocities on the rising and falling limbs of the flood waves can result in underestimation of peak discharges during highly dynamic floods and less accurate estimation of the time of the flood peaks. Measurements of velocity increase also accuracy of estimation of water balance significantly and make more transparent hydraulics regime in particular cross-section of the river.



# Application of in-line ultrasound Doppler based UVP-PD method to concentrated model and industrial suspensions

Johan Wiklund<sup>a</sup> and Mats Stading<sup>a,b</sup>

<sup>a</sup>SIK - The Swedish Institute for Food and Biotechnology, Göteborg, Sweden

<sup>b</sup>Chalmers University of Technology, Materials and Manufacturing Technology, Göteborg, Sweden

Address<sup>a</sup>: PO Box 5401, SE-402 29 Göteborg, Sweden. E-mail: johan.wiklund@sik.se

The applicability of the non-invasive UVP-PD method (Ultrasound Velocity Profiling and Pressure Difference) to concentrated model and polydisperse industrial suspensions was investigated. The UVP-PD method was successfully applied to a large number of model and industrial suspensions containing suspended soft to hard particles of different sizes and shapes. The particle size distributions ranged from sub-microns up to large solid pieces of 3-4 cm. In addition, investigated suspensions differed in solids concentrations, particle composition and fluid matrix. Both model and food suspensions were analyzed in-line in pressure driven, steady shear flow at different volumetric flow rates in an experimental flow loop where rheological flow properties were determined, directly in-line. The ability of the UVP-PD method in combination with measurements of the sound velocity in-line to determine concentration of solids and to monitor a gradual change in rheology with structure degradation directly in the flow loop was demonstrated. A comparison with conventional off-line measurements showed that the UVP-PD method is more versatile and off-line techniques only are valid for suspensions containing particles smaller than the gap width.

**Keywords:** Rheology, suspensions, non-Newtonian, in-line, ultrasound

## 1 INTRODUCTION

Understanding the rheological behavior of concentrated suspensions is of outmost importance in the analysis and control of many industrial processing operations. With processes becoming more continuous and with rapid product changes there is an increased need to switch from conventional off-line rheometers to new in-line techniques, Roberts [1]. However, industrial concentrated suspensions often contain particles with size distributions ranging from microns up to several cm in length which show non-Newtonian behavior over wide ranges of shear rates. Commercial process rheometers generally unable to cope with large particulate suspensions and unreliable when non-Newtonian fluid systems are considered according to recent review articles, Barnes [2] and Roberts [1].

The pulsed Doppler Ultrasound Velocity Profiling (UVP) technique has become an important tool for measuring velocity profiles in research and engineering during the last decade, Takeda [3]. UVP has now been successfully applied to many industrial fluid flows ranging from environmental-, biomedical, pulp, hydraulics and food process flows.

A novel method for in-line rheometry employing the pulsed ultrasound-Doppler velocity profiling (UVP) technique combined with Pressure Difference (PD) has been developed and is described in literature, Ouriev [4] and Wiklund et al [5]. Recently, UVP has recently been successfully tested for transient flows and turbulent flows and the UVP-PD method has been extended to include determination of wall slip

and yield stress in-line, Ouriev [4] and Wiklund et al. [6]. Recently, transient two-phase flows with displacement of fluids has been studied and compared with CFD simulations, Regner et al. [7].

A literature survey over existing UVP and UVP-PD studies was presented by Wiklund [8]. According to literature, all published UVP and UVP-PD studies on model and industrial suspensions have contained either small monodisperse particles or particle distributions almost exclusively in the micrometer range.

In the present study, the applicability of UVP and the UVP-PD method to concentrated model- and polydisperse industrial suspensions with size distributions ranging from microns up to cm was investigated. The suspensions contained suspended soft- to hard particles of many different concentrations, sizes and shapes. In addition, the investigated suspensions differed in solids concentrations, particle composition and fluid matrixes.

All suspensions were analyzed in-line in pressure driven, steady shear flow at different volumetric flow rates in an experimental flow loop and rheological flow properties were determined, directly in-line. Obtained rheological parameters were then compared with off-line measurements using conventional rotational rheometers. In addition, the added benefits of extending the methodology to include measurements of the sound velocity in-line and the use of flow adapter wall membranes were investigated. Detailed information about the UVP-PD method is given in Wiklund et al. [5].

## 2 MATERIALS

### 2.1 Model suspensions

The first set of model suspensions consisted of glass beads suspended in Glycerol. The average particle diameter of the smallest particles was  $4\mu\text{m}$  and  $15\mu\text{m}$  for the largest. The second set of model suspensions consisted of starch particles with particle size distribution of  $30\text{-}300\mu\text{m}$  suspended in a syrup with viscosity ranging from  $49\text{mPas}$  to  $1.2\text{Pas}$  at  $20^\circ\text{C}$ . The third set of model suspensions consisted of polyamide 12 (PA 12) particles suspended in rapeseed oil ( $\eta=66\text{mPas}$  at  $20^\circ\text{C}$ ). The particles had a very narrow particle size distribution. The average particle diameter of the smallest particles was  $11\mu\text{m}$  and  $90\mu\text{m}$  for the largest.

### 2.2 Industrial suspensions

Several industrial suspensions were investigated in-line using the UVP-PD method ranging from cellulose pulp to slurries and several kinds of foods. They differed in solids concentrations, particle composition and fluid matrix. Soft and hard particles with size distributions from submicron, microns to large solid pieces of up to  $3\text{-}4\text{cm}$  in length were used, e.g. aggregating clay particles, spherical glass beads, rod-like pulp and fruit fibers, kidney shaped seeds, odd shaped herb-, fish-, and vegetable pieces. In addition, the investigated industrial suspensions differed significantly in flow behavior from strictly Newtonian to shear-thinning and slightly shear-thickening. A summary of the investigated fluid systems' approximate concentrations and particle sizes/distributions is given in Table 1.

## 3 EXPERIMENTAL METHODS, SET-UP AND INSTRUMENTATION

### 3.1 Off-line viscometry

The flow behavior of the model suspensions and industrial suspensions were analyzed off-line using conventional rheometers, Bohlin VOR and Rheologica Stresstech. Concentric cylinder geometries with a bob diameter of  $20\text{-}25\text{mm}$  were used. The viscosity was measured at several temperatures and shear rates corresponding to those in the experimental flow loop. Particles larger than a  $\text{mm}$  were removed prior to measurements due to gap restrictions.

### 3.2 Flow loop and experimental equipment

The flow loop is shown in Figure 1 and is described in detail together with the methodology elsewhere, [5]. It consists of a closed stainless steel piping circulation system with an inner pipe diameter of  $35.5\text{mm}$ . A positive displacement pump, On-line OL2/0025/10, Johnson Pump, UK was used to recirculate the sample fluids through the piping from a stainless steel product tank with an agitator. Several temperature transmitters, mass and volumetric flow

meeters were installed in order to accurately monitor and characterize the flow. Two pressure sensors, ABB ETP80, Sweden, separated  $2.42\text{m}$  apart, were used to measure the pressure difference. Four ultrasound transducers,  $2\text{-}4\text{MHz}$ , TX-line, Imasonic, France were installed in a novel flow adapter cell, described in section 3.4.

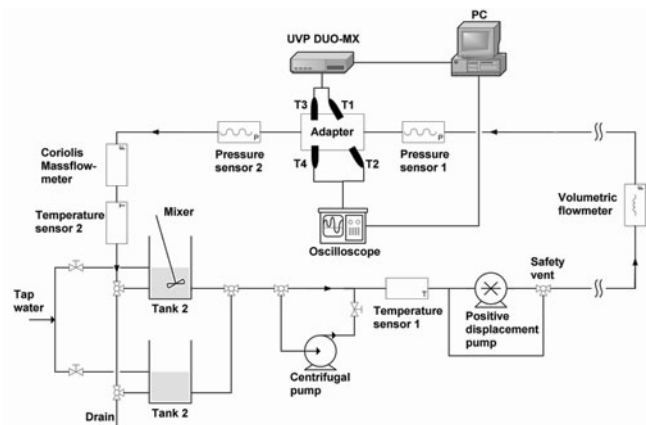


Figure 1: Schematic of the experimental flow loop and instrumentation.

### 3.3 Data acquisition and UVP-PD software

Velocity profiling was performed using the latest available UVP-Duo-MX model with a Multiplexer, Met-Flow SA, Switzerland, [9]. The UVP-Duo instrument and all hardware devices are connected to a master PC for data acquisition, data processing and analysis using novel Matlab-GUI based software developed within this project. Communication with UVP hardware is implemented with an Active X library supplied by Met-Flow SA. All ultrasound signals are continuously monitored using a 4-channel digital oscilloscope, Agilent Technologies, model 54624A, USA. Velocity profiles, pressure difference, mass or volumetric flow rates, temperature and velocity of sound as function of e.g. time, temperature were recorded and processed in-line.

### 3.4 Flow adapter and in-line sound velocity measurements

A novel ultrasound transducer flow adapter cell, shown in Figure 2, was developed and fitted with two transducer pairs. All transducers were installed with a membrane in front of the transducers in order to eliminate the near field problem, increase the signal quality close to the wall and to enable true non-invasive measurements. The membranes were made of aluminium, steel or Plexiglas and the thickness were optimized for maximum transmission of ultrasound. The first transducer pair was used for in-line signal amplitude measurements and sound velocity determination based on time-of-flight method ( $\Delta t$ ), between transducer T1 and T2. The second transducer pair was used for non-invasive measurements of velocity profiles. Detailed information is given in Wiklund et al. [5]. The methodology for in-line sound velocity determination

was developed together with Birkhofer et al. [10].

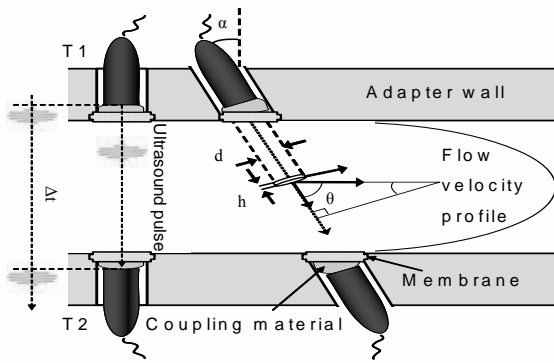


Figure 2: Schematic of the flow adapter fitted with two transducer pairs for non-invasive measurements of velocity profiles and principle of in-line sound velocity determination based on time-of-flight measurements.

## 4 RESULTS AND DISCUSSION

### 4.1 Velocity profiles and effects of particle size, shape and concentration

The results show that UVP could successfully be applied to a large number of highly concentrated bimodal and polydisperse model and industrial suspensions. In this study, we have covered a much wider range of suspension characteristics than what has so far been reported in literature.

Results further showed that instantaneous and complete velocity profiles could be obtained in all investigated suspensions after optimization. It was concluded that polydisperse suspensions containing large amounts of small particles up to approximately  $10\mu\text{m}$  have the strongest influence on the signal quality, discussed in section 4.3. It was shown that UVP can be used for particle concentrations up to approximately 45% by weight for more or less spherical particles in suspensions where hydrodynamic forces dominate. In addition, UVP technique can be used for particle concentrations up to at least 8% by weight for suspensions containing network-building rod-like fibers, Wiklund et al. [6].

### 4.2 UVP-PD In-line viscometry

Experimental results show that a rapid or gradual change in both rheology and shape of the velocity profiles over time, e.g. from pronounced flat plug-flow non-Newtonian behavior into more Newtonian behavior can be monitored. Results from our work on seafood chowder and vegetable soup have also shown the UVP-PD method capable of monitoring a gradual change in rheological behavior with structure degradation directly in the process line.

An example of UVP-PD in-line monitoring of structure degradation in a vegetable sauce containing large solid particles of up to 3-4 cm is shown in Figure 3. It is shown how the power-law flow exponent  $n$  and consistency index  $K$  changes with increasing shear rates and thus increasing structure degradation in the flow loop.

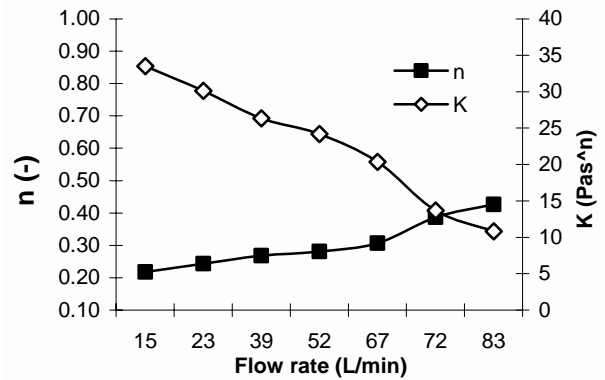


Figure 3: UVP-PD in-line monitoring of structure degradation in a vegetable sauce with increasing shear rates in the flow loop.

Figure 4 shows a comparison example between shear viscosities for two food suspensions, a low-fat strawberry yoghurt and a cheese sauce measured in-line using UVP-PD with off-line measurements using a Bohlin VOR rheometer.

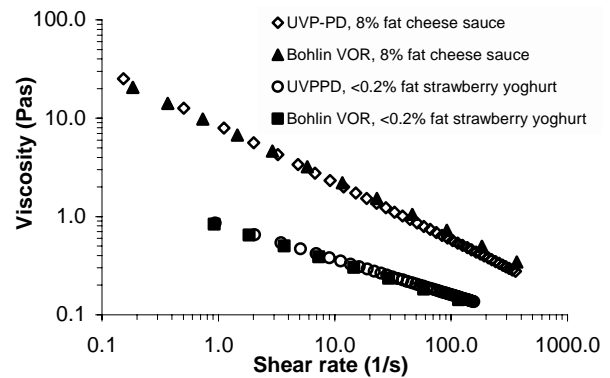


Figure 4: Comparison between shear viscosities for two food suspensions measured in-line using UVP-PD with off-line measurements using a Bohlin VOR rheometer.

As shown in Figure 4, good agreement between the methods is generally found for suspensions containing particles smaller than the gap width, in the concentric cylinder geometries. These experimental results are consistent for all investigated highly concentrated bimodal and polydisperse model- and industrial suspensions.

In addition, results further showed that off-line measurements using conventional rotational rheometers produce unrealistic results for suspensions containing larger particles since the standard measurements are performed on rheologically different systems containing no large particles and under different flow conditions.

### 4.3 Flow adapter and in-line sound velocity measurements

An extension of the UVP-PD method to involve in-line sound velocity measurements and attenuation was shown to be beneficial. The sound velocity is generally found to be a linear function of concentration of solids and temperature. Attenuation was found to be stronger in hydrophobic continuous

phases compared to hydrophilic, aqueous phases.

Experimental results on model and industrial suspensions showed that polydisperse suspensions containing large amounts of small particles up to approximately 10 $\mu$ m have the strongest influence on the signal attenuation probably due to signal deletion caused by multiple scattering. Recently, it was shown that microscopic (crystal size/shape) information in cocoa butter, Birkhofer et al. [10]. In this work, we have shown that also structure degradation can be monitored using in-line sound velocity measurements. In addition, macroscopic information (concentration of solids) information can also be obtained, e.g. in pulp, Wiklund et al. [6].

In addition, it was showed that the signal quality close to the pipe walls can be significantly improved by using novel flow adapters with membranes in front of the transducer.

Table 1: Summary of investigated fluid systems with particle shapes and sizes.

Investigated systems	Particle shape	C <sub>Max</sub> % <sub>(w/w)</sub>	Particle sizes
Glycerol+ glass beads	spherical		4-15 $\mu$ m
Rapeseed oil+ nylon particles	spherical	~ 45	8–90 $\mu$ m
Syrup + starch particles	~spherical	~ 40	30–300 $\mu$ m
Slurries	agglomerates	~ 40	100nm –1 mm
Tomato sauce	rodlike fibers	~ 30	~1 mm
Strawberry Yoghurt	seeds,kidney shaped	~ 8	1-1.2 mm
Fruit jams, marmalades	rodlike fibers		0.2–2 mm
Pasta sauce	mixture		~1-4 mm
Cellulose pulp	rodlike fibers	~8	2-2.4 mm
Cheese sauce + vegetables	cubic		0.5-1 cm
Seafood Chowder	mixture		-> 2-3 cm
Vegetable sauces	mixture		-> 3-4 cm

## 6 SUMMARY

UVP and the UVP-PD method were successfully applied for non-invasive in-line measurements of velocity profiles and rheology of both model and industrial suspensions. Results were consistent for highly concentrated bimodal and polydisperse model and industrial suspensions containing particles ranging from soft to hard. A much wider range of particle sizes, distributions, shapes and suspension characteristics was covered compared to what has so far been reported in literature.

UVP-PD method in combination with in-line sound

velocity measurements enabled determination of concentration of solids and the possibility to of monitor a gradual change in rheological behavior with structure degradation directly in the process line. Comparison with off-line measurements using conventional rotational rheometers revealed that off-line measurements often produce unrealistic results since they are performed on rheologically different systems containing no solid particles larger than a few millimeters and under different flow conditions.

## ACKNOWLEDGEMENTS

This work is part of a PhD project financed by Vinnova, the Swedish Agency for Innovation Systems and Tetra Pak Processing System AB. Met-Flow SA, Switzerland, Beat Birkhofer, Jeelani Shaik and Erich Windhab from ETH-Zürich, Switzerland, are gratefully acknowledged for technical support and scientific collaboration. Yasushi Takeda, Hokkaido University in Sapporo, Japan, and Boris Ouriev, Bühler AG, Switzerland are acknowledged for their technical input.

## REFERENCES

- [1] Roberts I.: In-line and on-line rheology measurement, in: Kress-Rogers & Brimelow (Eds), Instrumentation and sensors for the food industry, Woodhead Publishing Limited, Abington Hall, Cambridge, (2000), 1-403.
- [2] Barnes HA: On-Line or Process Viscometry - A Review. *Appl.Rheol.* 9(3), (1999), 102-107.
- [3] Takeda, Y.: Development of an ultrasound velocity profile monitor. *Nuc. Eng. & Design*, 126, (1991), 277-284.
- [4] Ouriev B: Ultrasound Doppler Based In-line Rheometry of Highly Concentrated Suspensions, PhD Thesis No. 13523, (2000), Zurich, Switzerland.
- [5] Wiklund J, Shahram I, Stading M: Methodology for in-line rheology by ultrasound Doppler velocity profiling- and pressure difference techniques. *Chem. Eng.Sci.*, (2006), In press.
- [6] Wiklund JA, Pettersson AJ, Rasmuson A, Stading M: A Comparative Study of UVP and LDA Techniques for Pulp Suspensions in Pipe Flow. *AIChE J.*, 52(2), (2006), 484-495.
- [7] Regner M. Regner M., Henningsson M., Wiklund J., Östergren K., Trägårdh C.: On the prediction of displacement of yoghurt by water in a pipe using CFD. *Comp. & Chem. Eng.* (2006). In press.
- [8] Wiklund J: Rheological In-line techniques based on ultrasound Doppler methods for the food industry- A literature survey. SIK-Report SR-710, Göteborg, Sweden, (2003), 1-142.
- [9] Met-Flow SA: UVP-Monitor-Model UVP-DUO-MX, User's Guide. Met-Flow SA, Lausanne, Switzerland (2002).
- [10] Birkhofer B, Jeelani SAK, Ouriev B, Windhab EJ: In-Line Characterization and Rheometry of Concentrated Suspension Using Ultrasound. *Proceedings - 4th ISUD*, Sapporo, Japan, (2004), 65-68.

## Monitoring of fat crystallization process using UVP-PD technique

Beat H. Birkhofer, Shaik A. K. Jeelani and Erich J. Windhab

Institute of Food Science and Nutrition, Laboratory of Food Process Engineering, ETH Zurich, Switzerland, E-mail: beat.birkhofer@ilw.agrl.ethz.ch

Boris Ouriev, Klaus-Jochen Lisner, Peter Braun, Yuantong Zeng

Bühler AG, Uzwil, Switzerland, E-mail: ouriev@buhlergroup.com

The response of the cocoa butter shear crystallization process to a step change in flow rate and temperature was investigated by measuring the instantaneous pulsed ultrasound Doppler based velocity profile (UVP) technique and pressure drop (PD) in a pipe section. In addition, the velocity of sound, attenuated amplitude of the transmitted signal and temperature were recorded. The temporal variation in rheological properties such as the shear rate dependent viscosity and the central plug radius in the pipe were determined by fitting the velocity profile and pressure drop to Power-law model. The linear dependence of sound velocity on the solid fat content in the cocoa butter crystal suspension previously determined using Nuclear Magnetic Resonance (NMR) technique was used to characterize solidification or melting behaviour. A new software developed was used to integrate on-line measurement of flow profiles, pressure difference, temperature, velocity of sound and the attenuated amplitude of the transmitted signal. The software also calculates velocity profiles from demodulated echo amplitude using Fast Fourier Transformation (FFT), determines the rheological properties, and provides a graphical user interface and tools for data visualization. The cocoa butter suspension was found to be shear thinning depending on the solid fat content and it was demonstrated that the cocoa butter shear crystallization process can be monitored and controlled using the UVP-PD methodology.

**Keywords:** Flow profiling, in-line rheometry, suspensions, fat crystallization, velocity of sound

### 1 INTRODUCTION

A novel method for in-line rheometry involving the measurement of an Ultrasound based Velocity Profile (UVP) and Pressure Difference (PD) in a pipe section was developed and tested at our laboratory for the flow of a wide variety of opaque model and industrial suspension systems such as chocolate, fat, shampoo and cellulose fibres in water suspensions. The in-line rheological results were compared with those measured by conventional off-line rheometers [1–5].

A shear crystallization process developed at our lab [6], which is meanwhile applied in the chocolate industry, was chosen to demonstrate the UVP-PD in-line rheometry measurement methodology. As it was suitable for the fat crystallization process, the UVP-PD technique is combined with measurements of velocity of sound, attenuation and temperature [7]. This allows an in-depth in-line investigation of the temporal behaviour of the cocoa butter crystal suspension in the process.

### 2 MATERIALS AND METHODS

#### 2.1 Ultrasound transceiver and adapter cell

Transducers with 4 MHz and 5 mm active diameter from Imasonic (Besançon France) were used. The pipe adapter made from hard PVC allows positioning two transducers opposing each other to enable the simultaneous measurement of flow velocity profiles, velocity of sound and attenuation (at the given frequency)[7]. The Doppler angle is 30°. The trans-

ducers are in direct contact with the liquid but pulled back from the actual pipe wall so that the measurement starts at the end of the near field at the focal point of the ultrasound beam. In order to avoid the accumulation of air in front of the transducer, the whole adapter is fixed in a box and submerged in cocoa butter, which also provides a temperature control of the adapter.

#### 2.2 Data acquisition hardware and software

A UVP-Duo instrument from Met-Flow (Lausanne, Switzerland) with a modified firmware that allows the access to the demodulated echo amplitude (DMEA) was used for the flow profile measurements. The two Kulite (Leonia, NJ, USA) pressure transducers and the thermocouples were connected using a National Instruments (Austin, TX, USA) FieldPoint. Velocity of sound (time of flight) and throughput amplitude were measured using a Yokogawa (Tokyo, Japan) DL 1520 oscilloscope.

The data acquisition from those entire instruments was controlled from software written with MATLAB (MathWorks, Natick, MA, USA). This software had a modular structure to allow a quick adaptation to different data acquisition hardware. Data from the UVP can be acquired using the Met-Flow ActiveX library either as DMEA or profile data as calculated with a time domain algorithm on the DSP in the UVP. Besides on-line data acquisition it is also possible to read files stored in various formats containing measurement data.

If the flow profile data is acquired as DMEA, the FFT algorithm is used to calculate the Doppler shift fre-

quencies. Besides data acquisition and signal processing, the software also provides a graphical user interface to set the various measurement parameters and tools for the visualization of the data.

### 2.3 UVP-PD method

The UVP-PD method allows the estimation of rheological parameters for Newtonian and Non-Newtonian liquids or suspension by combining profile measurement, pressure difference and a flow model such as Power-Law ( $\tau = K\dot{\gamma}^n$ ). Details on the technique can be found elsewhere [1-5]. The fitting procedure is also an integral part of the software described in the previous section.

### 2.4 Cocoa butter fat crystal suspension

Cocoa butter used for chocolate production is a mixture of triglycerides with a polymorphic crystallization behaviour that has a melting temperature around 32 °C. The crystal content is increased up to 25% during the shear crystallization developed at our laboratory [6].

### 2.5 Flow loop and crystallization process

The fully temperature controlled flow loop shown in figure 1, discussed in detail in [6], consists of a stirred cocoa butter feed tank, a two stage shear crystallizer and the measurement pipe section. The two pressure sensors are 1 m apart from each other.

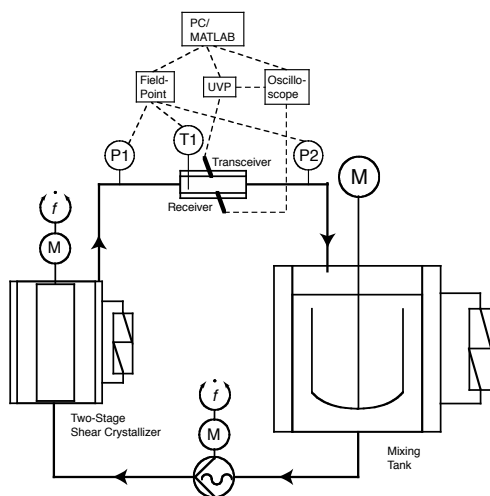


Figure 1 Scheme of the crystallizer flow loop, its instrumentation and data acquisition devices. P1, P2: pressure transducers; T1: thermocouple; M: motor; f: frequency transformer.

## 3 RESULTS

Normally the shear crystallizer operates at steady-state at a given flow rate of the cocoa butter crystal suspension with a constant concentration of the cocoa butter crystals. In order to investigate the changes in the rheological behaviour with time due to changes in the process operating variables, a set of experiments were carried out as described below.

Figure 2 shows an overview of the time dependent variation in the parameters measured over 2 h due to the following three phases of variations in process conditions starting with liquid cocoa butter flowing at steady-state with a throughput of 19.3 kg/h at 43 °C.

### 3.1 Crystallization process parameters

(1) The two-stage shear crystallizer unit was started when the flow loop was operating at a cocoa butter flow throughput of 19.3 kg/h. The first and second stages of the shear crystallizer unit were cooled to 15 °C and 27 °C respectively. The head and spindle of the shear crystallizer, and the pipes were cooled to 32 °C. (2) At 2500 s, the cocoa butter crystal suspension flow rate was reduced to 11.3 kg/h, which resulted in increase in the solid fat content up to about 20–25 %. The temperatures of the first and second stages of the crystallizer are the same as in phase 1. (3) At 8430 s, the cocoa butter crystal suspension was melted by switching off the shear crystallizer and heating the pipes to 43 °C resulting in the flow of liquid cocoa butter at a flow rate of 11.3 kg/h.

### 3.2 Measured parameters

The measured parameters can be broadly classified into four categories: (i) the process parameters such as the pressures and temperatures at the inlet and outlet of a pipe section after the shear crystallizer, (ii) the acoustic parameters such as the sound velocity and the amplitude of the transmitted ultrasound signal through the cocoa butter suspension, (iii) the flow velocity profile along the pipe diameter, and (iv) the rheological parameters such as the shear rate, shear stress, apparent viscosity determined based on the fitted Power-law model parameters  $n$  and  $K$  obtained using the velocity profile and pressure drop in pipe section.

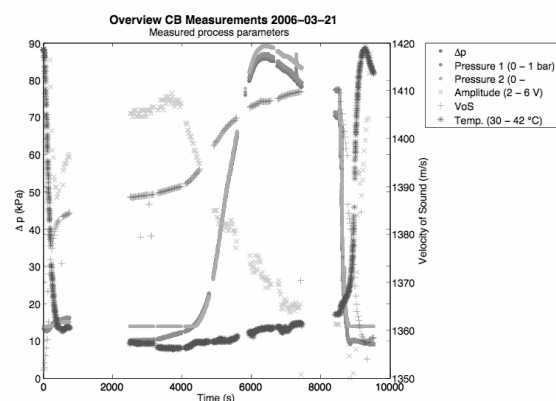


Figure 2: Overview for all the measured values of the crystallization process.

In the first phase (for less than 2500 s), it can be seen from Figure 2 that the temperature decreased from 41 °C to 32 °C while the velocity of sound increased from 1352 m/s to 1384 m/s.

In the second phase (between 2500 s and 8430 s) involving reduction of flow rate to 11.3 kg/h, the concentration of cocoa butter crystals (referred as solid fat content SFC) increased. This resulted in an increase in the sound velocity from 1390 to 1410 m/s and a steep rise in the pressure drop from 10 to 90 kPa. The SFC was not directly measured but under similar process conditions a value of around 20 % was reached in this flow loop. The attenuation increased with the increase of the SFC, thus the amplitude of the signal received with the second transducer was reduced by a factor of two from 5.5 to 2.75 V. The calibration of the amplifier of the sensor at the pipe upstream was not optimally adjusted, thus the pressure difference until about 4300 s was not exact, which could influence the value of  $K$ .

In the third phase of the process condition variation (later than 8430s) involving switching off the shear crystallizer and heating of the pipe, the temperature, and the amplitude of ultrasound signal received increased until their values corresponded to those for the liquid cocoa butter at about 43 °C. The pressure drop and the velocity of sound also decreased until becoming equal to those for the liquid cocoa butter.

### 3.3 Calculated results

Figure 3 shows the development of the root mean square of the DMEA (normal) over the whole measurement. The echo intensity increased during the first four measurement blocks after the flow rate reduction (between profiles 75 and 475) in region near the transducer. After profile no. 450 the intensity in the first 10 channels dropped suddenly from the maximum to the minimum.

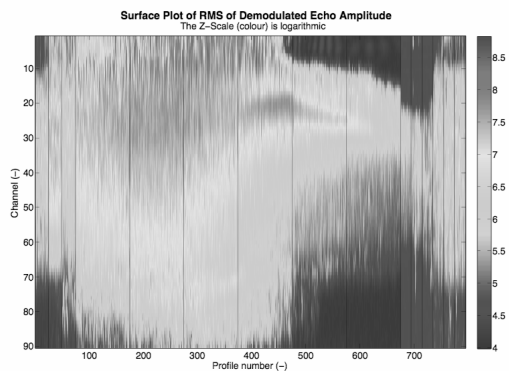


Figure 3: Surface plot of the root mean square of the demodulated echo amplitude with a logarithmic scale in Z (Color) direction. The measurement blocks are marked with vertical lines.

The drop in pressure coincided with the drop of the demodulated echo amplitude. At the same time the slope of the velocity of sound became nearly zero. The pressure continued to drop subsequently while the velocity of sound continued to increase at a slower rate than before.

Figure 4, 5 and 6 show the development of the flow velocity profiles during the process. The first three measurement blocks (before profile no. 100) were measured with a higher flow rate, therefore the drop afterwards. Then, during the next six measurement blocks, until after profile no. 600 the crystallization took place. The minimum velocity was reached at the end of the fourth measurement block before profile no. 500. An interesting point was the non-zero velocities that were measured from this point onwards in front of the transducer (the actual pipe starts only around channel 15). This was probably caused by a lack of signal (see Figure 3). This artefact disappeared when the cocoa butter became mostly liquid in the last three blocks.

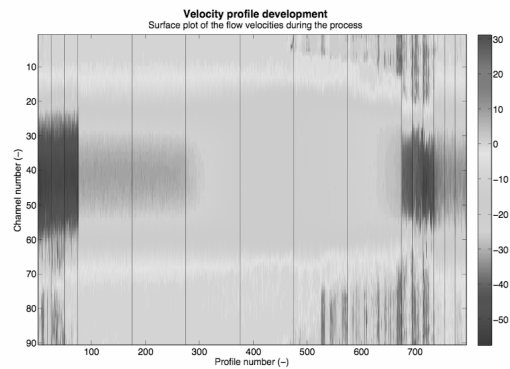


Figure 4: Surface plot of the flow velocities during the crystallization process. The development of velocity profiles along the diameter of the pipe is shown in Figures 6.64 and 6.65 during the three phases of the variation in process conditions.

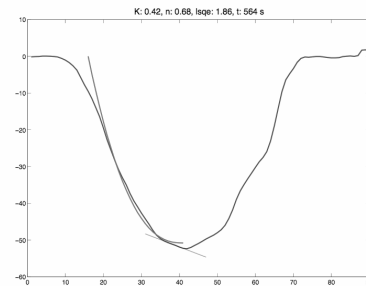


Figure 5: Measured (full curve) and fitted (half curve) velocity profiles after 564 s (liquid cocoa butter).

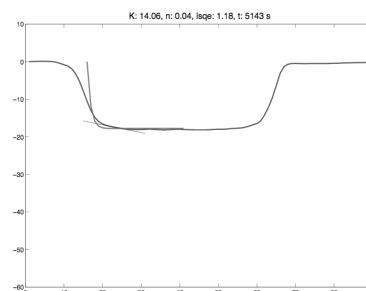


Figure 6: Measured (full curve) and fitted (half curve) velocity profiles after 5143 s (crystal suspension).

Figure 7 shows the values of power-law rheological model ( $\tau = K\dot{\gamma}^n$ ) parameters  $n$  and  $K$  determined by fitting the velocity profile equation. Initially, the cocoa butter was in liquid state so that  $n$  is equal to 1 as expected for Newtonian liquids. Then, in the first phase of the crystallization (until 1000 s) the value of  $n$  drops quickly (corresponding to the temperature reduction) to a value around 0.6. In the first phase after the reduction of the flow rate (after 2500 s) the values of  $n$  and  $K$  change slowly. This is due to the time of approximately 20 min it takes for the passage from the vessel through the shear crystallizer to the profile measurement. Then after 4000 s there is a kink in the value of  $K$ , this is probably due to the problem with the lower threshold of the measurement of the upstream pressure. So before this point the real pressure difference is smaller than the measured one, and thus the calculated value of  $K$  is too high and goes down to the real value when the pressure difference is actually measured after 4500 s. The value of  $n$  is independent of the pressure difference.

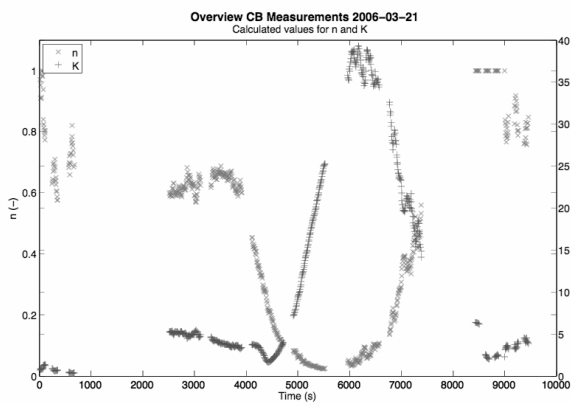


Figure 7: Development of  $K$  and  $n$  during the crystallization process.

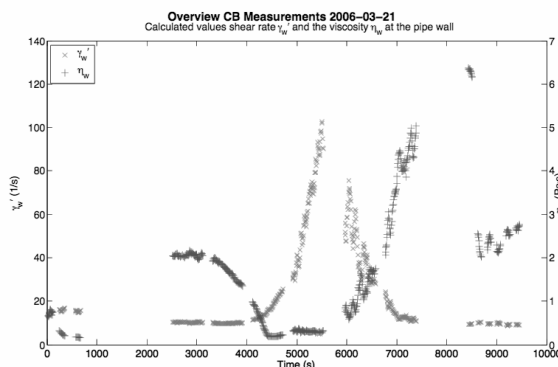


Figure 8: Calculated shear rates ( $\dot{\gamma}_w$ ) and viscosity ( $\eta_w$ ) at the wall.

At the pipe wall we find the highest shear rates and thus (shear thinning character of the crystal suspen-

sion) the lowest viscosities. Figure 8 shows the estimate of the corresponding values calculated from the fitted velocity profile with  $\dot{\gamma}_w = (R\Delta P/2LK)^{1/n}$  and  $\eta_w = \tau_w/\dot{\gamma}_w = K(R\Delta P/2LK)^{1-1/n}$ .

The wall viscosity begins dropping already after 3000 s while the apparent shear rate remains constant until 4000 s. This is due to the difference in the exponent. For  $\dot{\gamma}_w$  it is  $1/n$  while for  $\eta_w$  it is  $1 - 1/n$ .

The radius of the region in the middle of the pipe where the velocity profile is virtually flat, is estimated by analysing the derivative of the profile. This radius  $r_p$  and the corresponding shear stress  $\tau_p = r_p\Delta P/2L$  are shown in Figure 9. The distribution of  $r_p$  is discrete because its possible values correspond to the measurement channels.

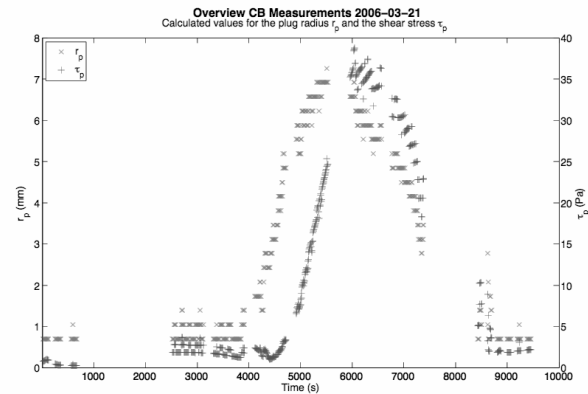


Figure 9:  $\tau_p$  and the estimated radius of the plug  $r_p$ .

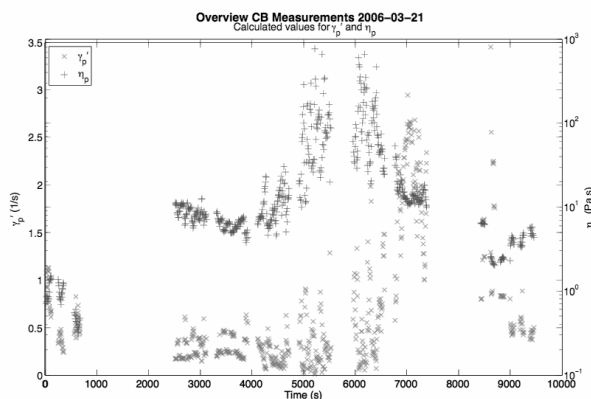


Figure 10: Calculated shear rates  $\dot{\gamma}_p$  and viscosity  $\eta_p$  for the plug.

Figure 10 shows  $\dot{\gamma}_p = \dot{\gamma}_w (r_p/R)^{1/n}$  and  $\eta_p = \tau_p/\dot{\gamma}_p$ . As discussed earlier, the value of  $n$  decreased with time as the crystal concentration increased resulting in an increase in pressure drop. This implied that the crystal suspension became

more shear thinning gradually. At any instant of time, the shear rate increased along the radius of the pipe being maximum at the pipe wall and minimum at the plug radius. Consequently, the viscosity is minimum at the wall of the pipe while it is maximum at the radius of the plug. As time increased, the radius of the plug increased so that the corresponding viscosity also increased resulting in increased pressure drop.

### 3.4 Limitations of the current setup

In order to avoid measurements in the near field of the ultrasound beam the transducer were pulled back 17 mm. As for this experiment the pipe diameter is 16 mm and the diameter of the transducer housing is 8 mm there are three major drawbacks: (i) the actual flow field is influenced by the geometry of the adapter and (ii) especially with the crystal suspension there is the disadvantage of possible crystallization in the cavities in front of the two transducers where there is no flow. Because the transducer adapter block is made from Hard PVC it is also not possible to control the temperature precise and fast enough. (iii) In the presented measurement both transducers were pulled back 17 mm, thus two third of the velocity of sound measurement are not inside the actual pipe diameter. Consequently, sound velocity and throughput signal amplitude are not fully representative for the situation in pipe flow. (iv) Since average sound velocity is measured, its precise value between transducer front and the start of the pipe radius is not determinable. Due to the assumed crystallization in front of the transducer, the velocity of sound is not distributed evenly between the two transducers and thus the distances are not determinable precisely.

A new transducer type that is under development should solve these limitations. This transducer features a so called «delay line» that is fixed to the transducer front and is in flush with the pipe wall. So the delay line contains the near field and at the same time focuses the beam inside the pipe so that the divergence angle is minimized and thus the measurement would be more precise.

## 4 CONCLUSIONS

It was shown that the UVP-PD technique combined with the measurements of velocity of sound and attenuation is an interesting approach for the in-line monitoring of a fat crystallization process. It is possible to monitor crystal content (by the velocity of sound) and the flow behaviour simultaneously. By adapting the transducer to the specific pipe diameter and adapting the UVP electronics for the specific needs it should be possible to implement an automatic in-line process control system for the cocoa butter shear crystallization and other similar applications.

## 5 ACKNOWLEDGEMENTS

We would like to thank Innovation Promotion Agency (CTI) Switzerland for the financial support, Met-Flow SA and Bühler AG for the collaboration and Johan Wiklund from SIK Sweden for providing scientific information.

## NOMENCLATURE

$K$	Pa s <sup><i>n</i></sup>	Flow consistency index
$L$	m	Length of pipe for pressure drop
$n$	–	Flow behaviour index
$\Delta P$	Pa	Pressure difference
$r$	m	Radius
$R$	m	Pipe radius
$\dot{\gamma}$	1/s	Shear rate
$\eta$	Pa s	Viscosity
$\tau$	1/s	Shear stress

Indices:

$\rho$	Plug
$w$	Wall

## REFERENCES

- [1] Ouriev B: Ultrasound Doppler based in-line rheometry of highly concentrated suspensions, Ph.D. Dissertation ETH No. 13523, 2000, Swiss Federal Institute of Technology, Zurich.
- [2] Ouriev, B, et al: Industrial application of UVP-PD technique: Steady shear pipe flow of chocolate suspension in pre-crystallisation, Review of Scientific Instruments 74 (2003), 5255-5259.
- [3] Ouriev B, Windhab E: Transient flow of highly concentrated suspensions investigated using UVP-PD method, Measurement, Science and Technology 14 (2003), 1963-1972.
- [4] Ouriev, B, Windhab E: Novel ultrasound based time averaged flow mapping method for die entry visualization in flow of highly concentrated shear-thinning and shearthickening suspensions, Measurement, Science and Technology Journal 14 (2003), 140-148.
- [5] Wiklund, J, et al.: 3rd-International Symposium on Ultrasonic Doppler Methods for Fluid Mechanics and Fluid Engineering, 2002, 69-76, EPF Lausanne.
- [6] Zeng Y: Impf- und Scherkristallisation von Schokoladen, Ph.D. Dissertation ETH No. 13798, 2000, Swiss Federal Institute of Technology, Zurich.
- [7] Birkhofer B, et al.: 4th International Symposium on Ultrasonic Doppler Method for Fluid Mechanics and Fluid Engineering, 2004, 65-68, Sapporo.



## In-line ultrasonic device for flow and rheology measurements of complex fluids

Robert L. Powell, Nihan Dogan

Department of Chemical Engineering and Materials Science, University of California, Davis, California, USA

Michael J. McCarthy

Department of Food Science and Technology, University of California, Davis, California, USA

Ultrasound pulsed Doppler velocimetry imaging has been implemented to study the flow and rheological properties of complex fluids undergoing steady pressure driven tube flow. The rheological measurements are based on the principles of velocimeter-based rheometry. The shear rate is determined as a function of radius by differentiating the velocity profile and the conservation of linear momentum theory provides a relation between shear stress and radius that is independent of the constitutive relation. The fluids studied include Microcrystalline cellulose gel, Xanthan gum solution, modified and unmodified starch gels, fruit concentrates, diced particles in fruit juice, hardwood and softwood fiber suspensions, and a polymer melt. A comparison of results with those of conventional rheometers showed that this method has the potential to be used as a process rheometer as it provides shear viscosity data over a wide range of shear rates with a single measurement. The shear rate limitations were investigated and a design curve was generated to predict the deviation of the shear viscosity from the rotational rheometers at low shear rates.

**Keywords:** Ultrasonics, rheology, viscosity, in-line viscometer, rheometry, shear dependent, complex fluids

### 1 INTRODUCTION

Many materials are conveyed within a process facility by means of pumping and flow in a circular pipe. From a conceptual standpoint, such a flow offers an excellent opportunity for rheological measurement. In pipe flow, the velocity profile for a fluid that shows shear thinning behavior deviates dramatically from that found for a Newtonian fluid, which is characterized by a single shear viscosity. This difference can be exploited experimentally to determine the shear viscosity at each radial position. From an experimental standpoint, the question we address is what measurements must be made and how to make those measurements in order to ascertain the shear viscosity variation in the pipe. Our goal is to obtain spatially resolved data and to show that from a single set of such data, the viscosity of a complex fluid can be obtained over the range of shear rates in the pipe. This hypothesis is enabled by the capability to measure the velocity and the pressure drop simultaneously. The velocity is used to determine the shear rates and the pressure drop allows the variation of the local value of shear stress. The measurements can be obtained in a standard process flow, without the need for additional pumping capacity or inducing flow in a side stream. We call this approach "pointwise" viscosity measurements. The shear rates are obtained from non-invasive flow measurements, ultrasonic pulsed Doppler velocimetry (UPDV), while the stress distribution can be readily calculated using standard transducers for pressure drop measurements. Therefore, this method can potentially be employed as an in-line or on-line

viscosity probe for process control purposes to improve both process efficiency and end product quality.

### 2 THEORY

The theoretical basis for pointwise rheological measurements rests with the traditional theory of viscometric flows [1,2]. Such flows are kinematically equivalent to unidirectional steady simple shearing flow between two parallel plates. For a general complex liquid, three functions are necessary to completely describe the properties of the material: two normal stress functions,  $N_1$  and  $N_2$  and one shear stress function,  $\sigma$ . All three of these depend upon the shear rate. In general, the functional form of this dependency is not known *a priori*. However, there are many accepted models that can be used to approximate the behavior, such as the power-law model.

Viscometric flows used for measurements include well-known flows such as flow in a narrow gap concentric cylinder device and between a small angle cone and a flat plate. In both of these cases, the flows established in these devices approximate almost exactly simple shearing flow. There are other viscometric flows in which the shear rate is not constant throughout, these include the wide gap concentric cylinder flow and flow in a circular pipe.

Viscometric flow theories describe how to extract material properties from macroscopic measurements, that are integrated quantities such

as the torque or volume flow rate. For example, in pipe flow, the standard measurements are the volume flow rate and the pressure drop. The fundamental difference with pointwise measurements is that the local characteristics of the flows are exploited. Here, we focus on one such example, steady, pressure driven flow through a tube of circular cross section. The standard assumptions are made, namely that the flow is unidirectional and axisymmetric, with the axial component of velocity depending upon the radius only. The conservation of mass is satisfied exactly and the z-component of the conservation of linear momentum reduces to

$$\frac{dr\sigma(r)}{dr} = r \frac{dP}{dz} \quad (1)$$

where P is the pressure and r is the radial coordinate. The pressure gradient is assumed to be constant and is characterized by a pressure drop, ΔP over a length L. Along with the requirement that the stress cannot be singular at r=0, this allows Eqn. (1) to be integrated as

$$\sigma(r) = -\frac{\Delta P}{2L} r \quad (2)$$

Here, ΔP=P<sub>2</sub>-P<sub>1</sub>, where P<sub>2</sub> is the pressure downstream of P<sub>1</sub> and ΔP<0. Equation (2) shows that the local shear stress in a tube is determined by the pressure drop. Recalling the definition of the shear rate, Eqn. (2), it is seen that both the shear stress and the shear rate are functions of radius. To obtain the shear stress as a function of shear rate, in principle we can solve for the radius as a function of the shear rate and substitute this into the shear expression for the shear stress versus radius. From an experimental standpoint, we measure w(r) in order to calculate the radial dependence of the shear rate,  $\dot{\gamma}(r)$ , and, then, at each value of r, determine the shear stress from Eqn. (2). The shear stress versus shear rate is obtained by choosing different radial positions and finding each corresponding value. The shear viscosity,  $\eta(\dot{\gamma})$ , is defined through

$$\sigma(\dot{\gamma}) = \eta(\dot{\gamma})\dot{\gamma} \quad (3)$$

and can be obtained by dividing  $\sigma(\dot{\gamma})$  by  $\dot{\gamma}$ .

The power of this technique is twofold. First, the

viscosity can be measured over a wide range of shear rates. At the tube center, symmetry considerations require that the velocity gradient be zero and hence the shear rate. The shear rate increases as r increases until reaching a maximum at the tube wall. On a theoretical basis alone, the viscosity variation with shear rate can be determined from very low shear rates, theoretically zero, to a maximum shear rate at the wall,  $\dot{\gamma}_w$ . The corresponding variation of the viscosity was described above for the power-law model where it was shown that over the tube radius, the viscosity can vary by several orders of magnitude. The wall shear rate can be found using the Weissenberg-Rabinowitsch equation

$$\dot{\gamma}_w = \frac{Q}{\pi R^3} \left( 3 + \frac{d \ln Q}{d \ln(\Delta P)} \right) \quad (4)$$

where R is the tube radius and Q is the volume flow rate. Since Eqn. (4) requires the measurement of Q for different ΔP, an estimate can be obtained by

$$\frac{d \ln Q}{d \ln(\Delta P)} = 1$$

assuming that fluid is Newtonian with and

$$\dot{\gamma}_w = \frac{4Q}{\pi R^3} \quad (5)$$

The second important feature of this technique is that it is independent of the constitutive relation of the material. This is a direct reflection of its rigorous foundation in viscometric flow theory.

In addition to the measurement of the viscosity, this technique also allows the yield stress to be estimated. For a typical yield stress type material, there is a critical shear stress below which the material does not deform and above which it flows. In pipe flow, the shear stress is linear with radius, being zero at the center and a maximum at the wall. Hence, the material would be expected to yield at some intermediate position, where the stress exceeds the yield stress. The difficulty with this method is in the determination of the point at which yielding occurs and, indeed, whether the material is appropriately modeled as having a yield stress or is better considered as having a highly shear thinning viscosity. For example, if a fluid could be modeled as a power law material with an exponent of 0.25,

the velocity profile from  $\frac{r}{R} = 0$  to  $\frac{r}{R} = 0.4$  varies

by 1%. From a purely experimental standpoint data showing such an effect could either be interpreted through a low power-law exponent or through a yield stress. The latter interpretation can result in robust estimates of this difficult to measure parameter.

As we shall see, the limitation on this technique stems from two related sources. First, the velocity data must be differentiated at each radial position to obtain the local shear rate. If the velocity data are not sufficiently smooth, large errors can result. Secondly, near the tube center, the velocity gradient is nearly zero. The precision of the measurement is particularly critical to obtain meaningful data in this region.

### 3 EXPERIMENTAL

The velocity measurement was performed by emitting multiple ultrasound pulses through the pipe and recording the echo, which was scattered from the particles in the fluid. After demodulation and low pass filter, the signals were stored and analyzed in a desktop computer. The position was calculated from time of flight of the sound wave and the velocity was calculated using the Doppler shift frequency effect, in which a wave scattered from a moving particle is subject to a frequency shift proportional to the velocity of that particle.

Signal analysis was carried out using a fast Fourier transform program and velocity profiles were monitored. The average velocity values used in velocity profiles were calculated by power weighted averaging. Each velocity profile was plotted by averaging of eight consecutive velocity profiles to increase accuracy.

Two types of flow loops were used. One was primarily for suspensions of foodstuffs and materials which generally could be easily pumped. This flow loop consisted of a 53.2mm internal diameter acrylic tube, a positive-displacement pump and two pressure transducers. To provide steady fully developed laminar flow conditions, the ultrasound probe was placed 5 m from the loop bend and the ratio of the length between pressure transducers to tube diameter was 67.

The second flow loop was used for polymer melts. This flow system consisted of 5.5 m long, 2.04 cm diameter acrylic tubing and 1.5 m long, 2.54 cm diameter stainless steel tubing and a gear pump. Stainless steel tubing was used at the exit of the pump to handle the high pressure in this section. The pressure drop was measured using two flush mounting pressure gauges P-1550 (Ametek, U.S. Gauge, PMT Products) that were placed 1 m apart.

All measurements were performed at room temperature and the temperature of the fluid was measured by a digital thermocouple in the storage tank. Two different flow rates studied were 4ml/sec and 13ml/sec. It was not possible to increase the flow rate higher than 13ml/s due to the limitations of the flow system.

The ultrasound probe was a 6.35 mm diameter piezo-electric transducer, which was clamped to the pipe wall with an angle of 45°.

From the velocity profiles of a fully developed laminar flow and simultaneous pressure drop measurements, shear rate and shear stress can be calculated, respectively [3].

### 4 RESULTS

Typical results for these experiments are shown in Figure 1. Here data are shown for the shear viscosity as a function of shear rate for various suspensions of tomato solids. The upper curve represents data for a 17% suspension, the middle curve, a 12.75% suspension and the bottom an 8.75% suspension. For the top and the bottom curves, the data were obtained from a single measurement of the velocity profiles. In each case, it is observed that data over nearly two decades of shear rate were measured. Also, over the entire shear rate range, the viscosity is strongly dependent upon the shear rate. The middle set of data contains two other features. First, there are two sets of UPDV data that were obtained at two different flow rates. The data are essentially indistinguishable. However, the data do access somewhat different ranges of shear rates. That is, the lower the value of the flow rate, the lower the range of shear rates that can be accessed during a UPDV experiment. Secondly, there are four data points represented by triangles. These data were obtained using a capillary viscometer and applying the standard formulas for calculating viscosity. Excellent agreement is found between the UPDV data and those obtained by the conventional method.

These results and similar studies on a wide range of fluids clearly demonstrates that usefulness of UPDV for viscosity measurements of complex fluids. For example, Fig. 2 shows velocity profiles obtained for paper pulp suspensions using UPDV. In this case, the velocity profiles are nearly constant over a most of the pipe. This can either indicate that the suspension is behaving as a power law fluid with a low power law exponent or it is behaving as a material with a yield stress. In the latter case, the yield stress can be associated with the radial position at which the velocity begins to decrease from its constant value. The yield stress measured

in this way is  $13.6 \pm 3.1$  Pa. An alternative means of determining the yield stress is with a vane viscometer. The value that we obtained for this same suspension was  $10.3 \pm 2.6$  Pa. The similarity between these two techniques is quite good. The yield stress itself is typically difficult to determine and there are very few studies that show agreement between the values obtained by different methods.

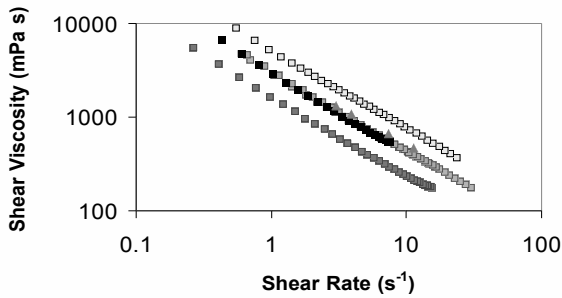


Figure 1. Shear viscosity versus shear rate for tomato suspensions obtained using UPDV (17%, top; 12.75%, middle; 8.75%, bottom; also shown by triangles are capillary data)

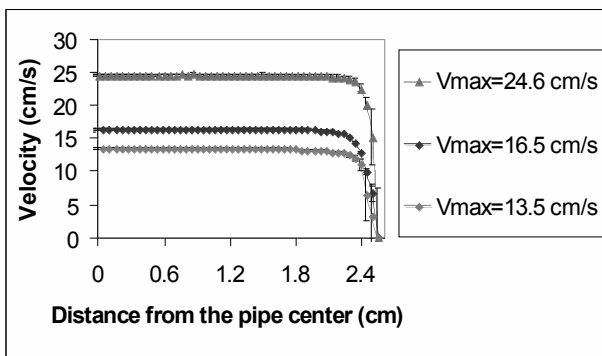


Figure 2. Velocity profiles for a pulp suspension measured by UPDV. The different profiles represent data obtained at different maximum velocities.

#### 4 CITATIONS AND BIBLIOGRAPHY

1. B. D. Coleman, H. Markovitz and W. Noll, *Viscometric Flows of Non-Newtonian Fluids*, Springer, Germany, **1966**.
2. K. Walters, *Rheometry*, Chapman and Hall, UK, 1975.
3. R. L. Powell, R. L., J. E. Maneval, J. D. Seymour, K. L. McCarthy, M. J. McCarthy, *J. Rheol.* **1994**, 38, 1465-1470.